THE UNIVERSITY *of* EDINBURGH

The Rheology of a binary suspension

Yujie Jiang

Doctor of Philosophy
The University of Edinburgh
May 2021

Abstract

Suspensions are widely encountered in industrial processes. So it is important to fundamentally understand how they flow. While progress has been made on monodisperse suspensions, most realistic suspensions are composed of multiple constituent particles. Among a variety of multi-component suspensions, this work concerns a specific class consisting of large repulsive grains suspended in a viscoelastic gel. In such system, we highlight a unique solid-liquid transition which is triggered by external flow. Rheo-imaging reveals the correlation between the rheological transition and the structural change. This state transition is the focus of this thesis.

We first establish a model binary suspension of large repulsive particles and small attractive particles. We mix two species of silica particles together, with the smaller (Brownian) ones being hydrophobically attractive and the larger (non-Brownian) ones stabilised via surface charge. Using a water-glycerol-ethanol mixture as the suspending solvent, we match the refractive index which, along with the fluorescent labelling of both particles and solvent, enables confocal microscopy. Remarkably, this model system is well-characterised, tuneable and transparent (imageable).

Through extensive rheological studies, we observe a flow-switched transition between a solid state and a liquid state. Specifically, the binary suspension solidifies upon cessation of vigorous flow, while prolonged gentle flow results in a liquid state which permanently persists at rest. We demonstrate that this state transition is reversible and has memory.

Rheo-confocal microscopy reveals distinct structure in the two states. The solid state consists of a gel matrix of small particles with large particles embedded inside, whereas in the liquid state, the small particles phase separate into disjoint, globular blobs. While there exists two states, detailed observation identifies three

flow regimes. By varying the particle composition, we construct a state diagram to map out the extent of these regimes.

The three regimes are demarcated by two transition boundaries, which are closely related to the macroscopic property of each state. We verify that the solid state is essentially a particle-filled gel and the lower boundary is its yield stress. Moreover, we show that the blobs in the liquid state are solid 'droplets' whose strength directly determines the upper transition boundary. Beyond the state diagram, we further explore the parameter space of the binary system. We confirm that the small-small attraction and the large particle size are two key factors to the state transition. However, we still do not understand the microscopic mechanism. We illustrate several possible research lines, whose results may fill important gaps for the fundamental understanding.

Our system contributes more than a model system. By comparing the rheology and microstructure, we reveal the similarity between a Li-ion battery slurry and our suspension. Moreover, the flow-switched solid-liquid transition, which is reversible and has memory, sheds new light on the smart material design. We identify our suspensions as a memory mechanorheological (McR) fluid, whose rheology is mechanically tuneable and can persist upon removal of mechanical stimuli.

Lay Summary

Particulate suspension consists of solid particles suspended in a liquid medium. Such mixtures are closely related with our daily life, since many commercial products in the kitchen and bathroom are suspensions, e.g. toothpastes, cosmetics and ketchup). Their flow properties directly determine their performance. For example, toothpaste flows like a liquid when squeezing the tube, but we do not want it to immediately flow off after squeezed on the toothbrush. For efficient and effective manufacturing, therefore, it is important to understand and control the flow of suspensions.

Progress has been made. People have identified the vital role of interparticle force: a suspension can be switched from a liquid to a solid by tuning the interaction from repulsion to attraction. However, such progress is mostly confined to suspensions comprised of a single type of particles. To date, understanding on multi-component suspensions remains far less developed, even though most realistic suspensions fall into this category.

Among the diverse array of complex suspensions, this work focus on a specific class where granular particles are dispersed in a gel. Due to the lack of proper model systems, there are few studies on such class despite of its ubiquity in industry (such as Li-ion batteries and fresh concrete). We therefore establish a model suspension consisting of two species of particles disparate in size and interparticle force.

In this binary suspension, we highlight a unique solid-liquid transition which is triggered by external flow. In general, a fast flow can solidify the composite upon flow cessation, whereas a gentle flow fluidises it. This solid-liquid transition is reversible and has memory. These two features enable us to freely tune a binary suspension from a liquid to a solid with both states persisting until further agitated.

We show that the solid-liquid transition results from a clear change in the microstructure. We therefore define two states based on the structure and map out the state behaviour at various compositions. The flow-switched state transition is tunebale by several parameters, among which the interparticle attraction and particle size are two key factors.

Apart from the intrinsic interest to fundamental physics, studying this composite system sheds light on the smart material design. The unique solid-liquid transition may open up the possibility of a new generation of smart fluids. Moreover, by mapping the behaviour of our model suspension to similar industrial suspensions, one can improve the efficiency of industrial processing by means of tuneable flow.

Declaration

I declare that this thesis was composed by myself, that the work contained herein is my own except where explicitly stated otherwise in the text, and that this work has not been submitted for any other degree or professional qualification except as specified.

(*Yujie Jiang, Oct 2021*)

Acknowledgements

This work would not have been possible without the help of many people over the past four years in Edinburgh. I sincerely appreciate what they have done to support my study.

First, I would like to thank my two supervisors, Wilson Poon and John Royer. Their supervision throughout my PhD study lays a solid foundation of this work. Wilson taught me how to think as a real physicist, while John spent tons of time teaching me experimental skills in the lab and discussing my results in the office. I really benefit a lot from their writing lessons and the Friday morning discussion.

A big thanks to my colleagues in JCMB who helped me along the PhD journey. In particular I would like to thank Andy Schofield, who guided me to synthesise my own silica particles. Thank you for being tolerant when I spilled the pinky solvent in the fume hood, thank you for being patient when I occupied the centrifuge all the time. I would also like to thank Soichiro, Nick and everyone in the dense suspension group for all their helpful suggestions and fruitful discussion.

I am also grateful for my SOFI mates. When I first came to the UK, thank you all for your kindness and patience. It would have been a tough time for me without your friendliness. Thank Dan for teaching me the first British joke (and so far the only one) that I completely understand.

For my Chinese pals, Yangge, Yankai and Xuemao, I would like to thank you for all your practical advices and support. You guys made me feel no longer lonely a thousand miles away from homeland. A special thanks goes to EUCBC and inch park basketball crew: thank you for saving my spare time which should have been boring.

I also acknowledge the industrial partner who partly funded my PhD project, Schlumberger, and my two industrial supervisors, Louise Bailey and Andrew

Clarke.

Finally, I would like to say thank you to my family. Your support is the strongest backup for me. Thanks my wife Suzy for remotely comforting me during the lockdown. 2020 is a tough year, and there is no way I can accomplish this work without your support.

Contents

Chapter 1

Introduction

When studying physics, it is important to get an idea of how big things are, as different length scales d correspond to different physics. For traditional condensed matter, where the constituents are atoms or molecules ($d \sim$ Å), thermal equilibrium can be easily reached within laboratory timescales as the structural relaxation is usually fast. Besides, these conventional materials are usually rigid in solid state because of the high energy density ($k_BT/d^3 \sim 10\,\mathrm{GPa}$) [1]. As d increases to the mesoscopic regime (1 nm to 1 µm), materials become deformable and even flowable under small loads ($\sim$ Pa). Such materials, composed of mesoscale constituents, are known as soft matter, examples including polymers, suspensions and emulsions [2].

Soft materials are easily driven out of equilibrium. Even in an undisturbed, quiescent state, thermal equilibrium may not be reached. Dependent on constituent properties like size and interaction, relaxation timescales in soft materials are often comparable to or longer than experiments. Therefore, to understand soft matter, one must go beyond classical thermodynamics and instead focus on dynamics far from equilibrium, such as rheology – the study of flow. Despite the lack of a generic thermodynamical description, the typical colloidal length ($\sim$ µm) and relatively-slow time scale ($\sim$ s) in soft matter physics enable direct observation in real-time with present microscopy technologies [3]. This remarkable advantage is fully taken of in this work.

1.1 Limited understanding in suspensions

As a typical soft matter system, suspensions of solid particles dispersed in fluid are widely encountered in natural and industrial processes, e.g. mud, cosmetics and pharmaceuticals [4]. Since most of them are in the flowable form, therefore, understanding what affects the suspension flow and how it can be manipulated is crucial in practical applications. Studies have shown that the property of constituent particles plays a vital role, and to date, there has been considerable progress understanding the rheology of 'model' suspensions. For instance, the yielding behaviour of colloidal glasses and gels has been mapped in detail by experiments and simulations [5–7], and some features can be predicted by *ab initio* theories [8]. In addition, deep connection has been found between suspension rheology and dry granular mechanics [9, 10], while a constraint-based model has been recently proposed to explain both yielding and shear thickening in non-Brownian suspensions [11, 12].

However, such progress in fundamental understanding has been limited to suspensions of monodispersed particles, whereas polydisperse suspensions are somewhat ignored. The fact is, even a small departure from monodispersity may have dramatic consequences. For example, crystallisation, a common phenomenology in monodispersed colloids, is absent in suspensions with polydispersity $\gtrsim 10\,\%$ due to symmetry breaking [13, 14]. Besides, polydispersity may also introduce the interplay between the Brownian dynamics in small colloids and the athermal behaviour in large grains, which is of intrinsic interest to statistical physics. Compared with the progress on quiescent phase behaviours, the treatment of polydispersity in rheology still remains on the level of *ad hoc* models [15].

The above is just about size polydispersity. In the real world, suspensions are mostly comprised of multiple species of particles, which may differ in several aspects like size, shape and interaction. In industry, a common class consists of stabilised (repulsive, or at least non-attractive), granular (non-Brownian) particles suspended in a viscoelastic gel of attractive colloidal (Brownian) particles. Three typical examples are battery slurries, concretes and toothpastes [16–18]. Despite wide occurrence, very few studies have probed the flow behaviours of such binary class in depth.

The lack of a proper model system is the main reason. Much of the progress understanding single-component suspensions was underpinned by well-characterised

experiment model systems, such as index-matched particle/solvent combinations that enable direct imaging of stabilised suspensions [19, 20] and depletion gels [6, 21]. However, there is no existing model system for examining this binary class. Establishing such a model system requires particles with both disparate sizes and interactions, ruling out many common approaches for inducing attraction (e.g. depletion and van der Waals force).

Under such context, we develop an experimental model system for granular-gel composites. The system consists of a binary mixture of **large (granular) repulsive particles** and **small (colloidal) attractive particles**. While the small particles form a yield-stress gel on their own, the addition of large particles enables a flow-switched solid-liquid transition. For the binary system, imposing a vigorous flow can switch it into a yield-stress solid upon flow cessation, whereas moderate shear 'permanently' fluidises the system until further agitation. *In situ* rheo-imaging reveals that the macroscopic transition originates from a clear change in the microscopic structure. While the solid state exhibits a homogeneous gel matrix with large particles embedded inside (i.e. particle-filled gel), in the liquid state, the small gel particles aggregate into larger, disjoint 'droplets'.

These results set up an empirical reference for all suspensions in this class. Besides illustrating a strong implication in its industrial counterparts, our suspension surprisingly presents a new paradigm for designing smart fluids with wide-ranging structural and kinetic control. Beyond that, studying the tripartite coupling between arrested gel, non-Brownian grains and external energy input in such a mixture sheds light on the non-equilibrium statistical physics.

1.2 Thesis outline

This thesis explores the rheological and structural behaviours of a binary suspension under shear flow. To help readers better understand our results, we first introduce the requisite background in rheology in Chapter 2, including the formal framework, practical rheometries and experimental concerns relevant to this work. The set-up of rheo-confocal microscopy is introduced in the end.

The suspension rheology is then reviewed in Chapter 3. We start with general physics of suspensions, followed by possible interactions between suspended particles. Based on the interparticle forces, we classify particles into two categories:

repulsive hard-particles and attractive colloids, which exactly correspond to the two components in our binary model system. We give a global introduction of their quiescent phase behaviours, non-equilibrium dynamics and rheology respectively.

Our results are divided into four parts. Chapter 4 mainly reports the establishment of our model system. The system is composed of two species of particles: large repulsive particles and small attractive particles. We first discuss them individually, including particle synthesis and functionalisation, sample preparation and characterisation. The two species of particles are then mixed together to fabricate binary suspensions, in which the inter-species interactions are briefly discussed.

In such a binary suspension, we highlight a unique, flow-switched transition in Chapter 5. Laboratory demonstration shows that fast mixing leads to a yield-stress solid which can then be fluidised by gentle mixing. This solid-liquid transition is quantitatively investigated with a rheometer. Through rheo-confocal microscopy, we correlate the transition in rheology with the change in microstructure. Based on the structural signature, we define two states: homogeneous (H) state of particle-filled gel matrix and phase-separated (PS) state of disjoint 'droplets'. Through systematical experiments, we map out a state diagram.

Given the two structural states, Chapter 6 respectively explores their macroscopic properties. We identify an H state as a particle-filled gel. Compared with an unfilled gel, the addition of large particles strengthens the bulk system and leads to higher yield stress. By processing 3D confocal stacks, we confirm that a PS state consists of globular, solid-like 'droplets' with a characteristic size $\sim 20\,\mu m$. We also estimate the small particle concentration inside these 'droplets', which is found to increase with the addition of large particles. Although the mechanism of 'droplet' formation/breakage is still unclear, our study sets the stage for future investigation.

We further explore the parameter space in Chapter 7. In particular, we vary the three pair interactions and two particle sizes, and identify the attraction between small particles and the size of large particles as two key factors in binary suspensions. These findings may fill important gaps for the fundamental understanding on the state transition.

In Chapter 8, we summarise conclusions as a whole. To manifest the connection

between industry and our study, we compare a lithium-ion battery slurry [16] with our binary suspension, which exhibit similar history dependence. Moreover, the PS state with globular 'droplets' in our suspension is also observed in another system which is more industrially relevant. The application in smart materials is also highlighted. Based on present results, we illustrate several interesting lines for future work in the end.

Chapter 2

Basics of Rheology

Rheology, derived from the Greek phrase πάντα ῥεῖ (everything flows), is the study of deformation and flow, and by extension the response of materials to applied stresses [22]. Technically, people do rheology everyday. For example, toothpaste flows like a liquid when you squeeze the tube, but sits on your toothbrush like a solid until you start brushing. Using a butter knife, solid-like butter can be easily spread on bread like a liquid. Serious rheology quantifies how these materials, and many others, behave within a unified framework. By means of precision instruments and well-defined flow geometries, we can precisely measure the rheological property of various soft materials.

As a fundamental part of material science, rheology has been introduced to the realm of non-equilibrium physics (especially in soft matter [23]) and many other fields ranging from biology to geoscience [24, 25]. Besides the widespread occurrence in academia, rheology also brings practical applications for field engineers, e.g. concrete slump test [26] and examining drilling fluid performance [27]. Sometimes the quality of commercial products is determined by rheology as well, such as foods [28] and plastics [29]. Understanding what affects the rheology of a specific material and how it can be manipulated, therefore, is of great importance.

To systematically explore the flow of a driven system, it is vital to know how to describe flow using the language of rheology. In this chapter, the formal framework of continuum mechanics is firstly outlined. We then narrow the topic down to shear rheology and start with a simple case - Newtonian fluids under laminar shear, and extend the discussion to non-Newtonian behaviours.

Afterwards, we introduce common rheometries as well as some experimental considerations relevant to this work, and detail our set-up of rheo-confocal microscopy in the end. Here we do not confine the discussion to a specific material, while the next chapter focuses on specific considerations in suspension rheology.

2.1 Formal framework

Treating the material as a set of small elements, rheology is principally concerned with continuum mechanics to characterise deformation [22]. The deformation at cubic element P (Fig. 2.1, left) can be defined in the form of a strain tensor $\mathbf{E}$:

$$E_{ij} = \frac{1}{2}\left(\frac{\partial X_i}{\partial x_j} + \frac{\partial X_j}{\partial x_i}\right), \tag{2.1}$$

where $\boldsymbol{x}$ is the position of P and $\boldsymbol{X}(\boldsymbol{x}, t)$ is the displacement of P to the reference state. Similarly, the strain-rate tensor $\dot{\mathbf{\Gamma}}$ can be expressed as

$$\dot{\Gamma}_{ij} = \frac{1}{2}\left(\frac{\partial v_i}{\partial x_j} + \frac{\partial v_j}{\partial x_i}\right), \tag{2.2}$$

in which $\boldsymbol{v}(\boldsymbol{x}, t) = \dot{\boldsymbol{X}}(\boldsymbol{x}, t)$ is the velocity field. In both strain and strain-rate tensors, the diagonal terms ($i = j$) refer to the elongation in i direction, while the off-diagonals ($i \neq j$) describe shearing deformations in i-j plane.

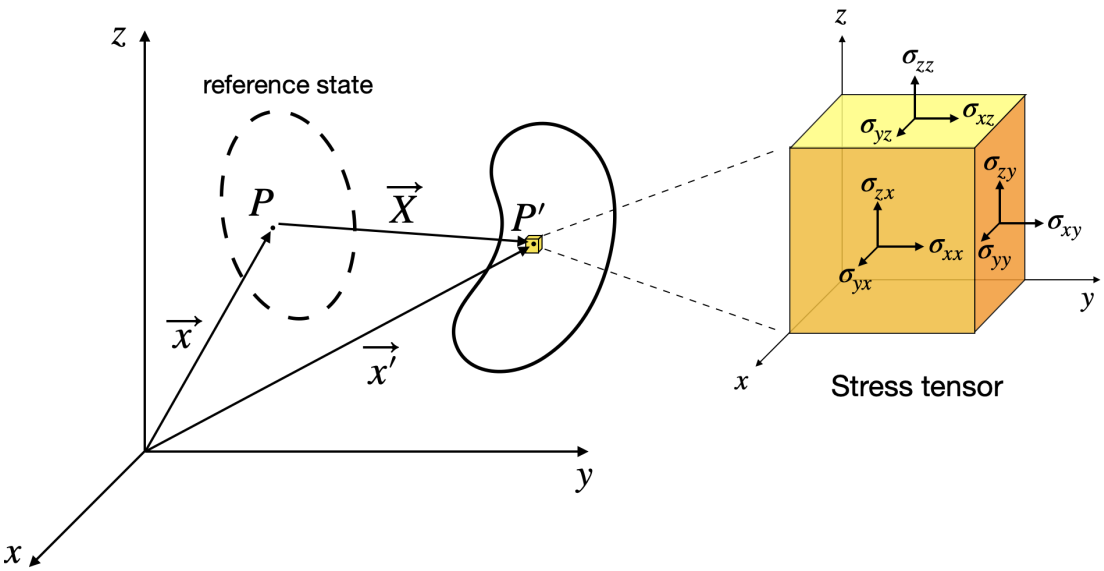

Figure 2.1 Left: sketch of a general deformation. Right: nine components of stress tensor $\mathbf{\Sigma}$.

Relative motion between neighbouring material elements generates stresses, characterised by a stress tensor $\mathbf{\Sigma}$ (Fig. 2.1, right). The components of $\mathbf{\Sigma}$ have units of force/area, or Pa in SI units. Since the force acting on an arbitrary plane of element is not necessarily oriented perpendicular or parallel to that plane, $\mathbf{\Sigma}$ can be written as a second-order tensor σ_{ij} as well, where i refers to the direction of the stress component and j to the plane (normal) the stress acts on, Figure 2.1 (right). As with strain and strain-rate tensors, two different kinds of components can be distinguished: diagonal terms are normal stresses while the off-diagonals are shear stresses. To ensure a zero internal torque, the stress tensor $\mathbf{\Sigma}$ is symmetric ($\sigma_{ij} = \sigma_{ji}$) in most materials. More complete mathematical treatments can be found in [22].

The stress tensor and deformation tensors are related by a constitutive function [30]

$$\mathbf{\Sigma} = \mathcal{F}(\mathbf{E}, \dot{\mathbf{\Gamma}}). \tag{2.3}$$

Specifically, an ideal solid responds only to the strain $\mathbf{E}$ and an ideal liquid responds only to the strain-rate $\dot{\mathbf{\Gamma}}$. Here we first illustrate a simple case - Newtonian liquids under shear.

2.1.1 Newtonian fluids

The stress and strain-rate are linearly related in Newtonian fluids [22]. Given the tensors defined above, the constitutive relation is expressed as:

$$\mathbf{\Sigma} = -P\mathbf{I} + 2\eta\dot{\mathbf{\Gamma}}, \tag{2.4}$$

where $-P\mathbf{I}$ is the hydrostatic pressure (with $\mathbf{I}$ the unit tensor) and η is the viscosity (with SI units of Pa s).

To illustrate a simple shear in x-y plane, here we consider an isotropic fluid contained between two parallel plates with separation H, Figure 2.2. When the top plate slides with velocity V in x direction, the fluid is then dragged to flow with a velocity field $v_x(y)$. Given the 'non-slip' boundary conditions[1], the gradient of v_x in y direction is constant throughout the fluid:

$$\frac{\partial v_x}{\partial y} = \frac{V}{H} = \dot{\gamma}. \tag{2.5}$$

[1]The fluid layer near each plate have the same velocity as that plate.

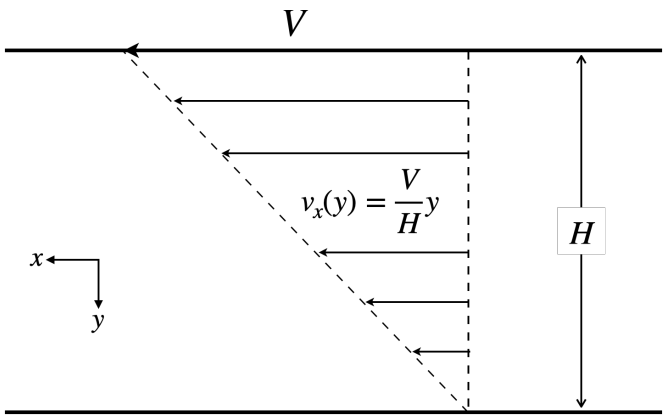

Figure 2.2 Schematic of simple shear flow in x-y plane. x axis: velocity direction; y axis: gradient direction.

Here the velocity gradient $\dot{\gamma}$ is the scalar shear rate with SI units of s^{-1}. The strain-rate tensor is written as:

$$\dot{\mathbf{\Gamma}} = \begin{pmatrix} 0 & \dot{\gamma}/2 & 0 \\ \dot{\gamma}/2 & 0 & 0 \\ 0 & 0 & 0 \end{pmatrix}, \tag{2.6}$$

Combining Eq. 2.4 and 2.6 gives the well-known constitutive equation for Newtonian fluids under shear:

$$\sigma_{xy} = \eta\dot{\gamma}, \tag{2.7}$$

where σ_{xy} is the shear stress (we drop the subscript $_{xy}$ in the following discussion for simplicity). Analogously, one can obtain $\sigma_{xy} = G\gamma$ for Hookean solids, where γ is the shear strain and G is the shear modulus.

Given the shear stress σ and shear rate $\dot{\gamma}$ in a Newtonian fluid, its shear viscosity $\eta = \sigma/\dot{\gamma}$ can be determined. The viscosity η arises from the internal friction between adjacent fluid layers in relative motion, and thereby represents the resistance to flow. As an intrinsic property, the viscosity is constant (rate-independent) in Newtonian fluids. However, for most complex fluids in soft matter science, the stress σ is not proportional to the rate $\dot{\gamma}$ so that their viscosities vary with $\dot{\gamma}$: they are non-Newtonian fluids.

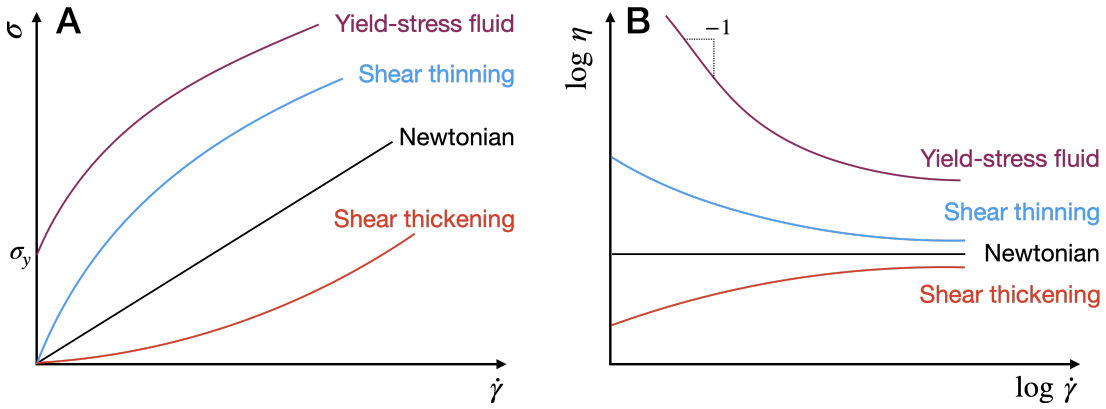

Figure 2.3 Schematic flow curves of possible Non-Newtonian behaviours. A. $\sigma - \dot{\gamma}$ plot. B. $\eta - \dot{\gamma}$ log-log plot.

2.1.2 Non-Newtonian fluids

There is a diverse array of different types of non-Newtonian fluids. Here we mainly focus on those where the shear stress σ is determined by the instantaneous shear rate $\dot{\gamma}$. In these non-Newtonian fluids, σ is not necessarily proportional to $\dot{\gamma}$, and consequently, the apparent viscosity $\eta = \sigma/\dot{\gamma}$ varies as a function of $\dot{\gamma}$ (or σ). Possible shapes of flow curve are shown in Figure 2.3.

Shear thinning and thickening

Fluids with viscosity η decreases with shear rate $\dot{\gamma}$ are termed as shear thinning fluids. For such fluids, σ increases less than proportionally with $\dot{\gamma}$ (Fig. 2.3A, blue), so that η decreases with $\dot{\gamma}$ (Fig. 2.3B, blue). Some common examples of shear thinning fluids are ketchup, paints and blood [31–33]. By contrast, the red curve in Figure 2.3 presents the opposite case, where the viscosity η increases with shear rate $\dot{\gamma}$. This illustrates shear thickening, widely occurring in dense suspensions such as the mixture of cornstarch and water [34]. Shear thinning and shear thickening are the two most common rheological behaviours encountered in complex fluids, and they may coexist in the same material. For instance, suspensions may shear thin at low rates and shear thicken at higher rates [19].

Yield stress

For a number of materials, no flow takes place unless the applied stress exceeds a finite threshold σ_y, Figure 2.3A (purple). Such materials behave as solids under small loads but flow like a liquid beyond σ_y [35]. This solid-to-liquid behaviour is known as yielding and σ_y is the yield stress. For example, toothpaste, once squeezed out, can stay on the toothbrush rather than flowing off as its yield stress dominates gravitation. Since the viscosity η diverges as $\sigma \to \sigma_y$ from above, any yield-stress material inevitably comes with a shear thinning regime at low shear rates.

Many empirical models have been proposed to capture yield stress rheology, such as the Bingham ($\sigma = \sigma_y + \eta\dot{\gamma}$), Casson ($\sqrt{\sigma} = \sqrt{\sigma_y} + \sqrt{\eta_c\dot{\gamma}}$) and Herschel-Bulkley ($\sigma = \sigma_y + k\dot{\gamma}^n$) models [36]. Although it has become customary to describe yielding flow curve with the Herschel-Bulkley equation, neither the consistency index k nor the power law exponent n have a clear physical meaning [37]. In this thesis, we use the Herschel-Bulkley equation:

$$\sigma = \sigma_y + k\dot{\gamma}^n \tag{2.8}$$

only as a fitting tool, by which the value of yield stress can be determined from a steady-state flow curve. The experimental measurement on yield stress will be particularly discussed in the next section.

Other complications

So far, we only refer to non-Newtonian behaviours associated with simple constitutive relation $\sigma = \sigma(\dot{\gamma})$. In practice, there exists a wide spectrum of complex fluids with complicated rheology, e.g. (explicit) time dependence and history dependence. In the presence of these complications, precautions should be taken to ensure reproducible experimental data.

Time-dependent rheology are commonly observed in arrested systems such as thermoreversible gels [39, 40]. Due to thermal fluctuations, the structural evolution in these materials proceeds towards equilibrium slowly. In colloidal gels, this is known as coarsening [38], Figure 2.4A. To minimise such effect, gel samples are usually left undisturbed for a while before measurement until reaching a relatively steady state.

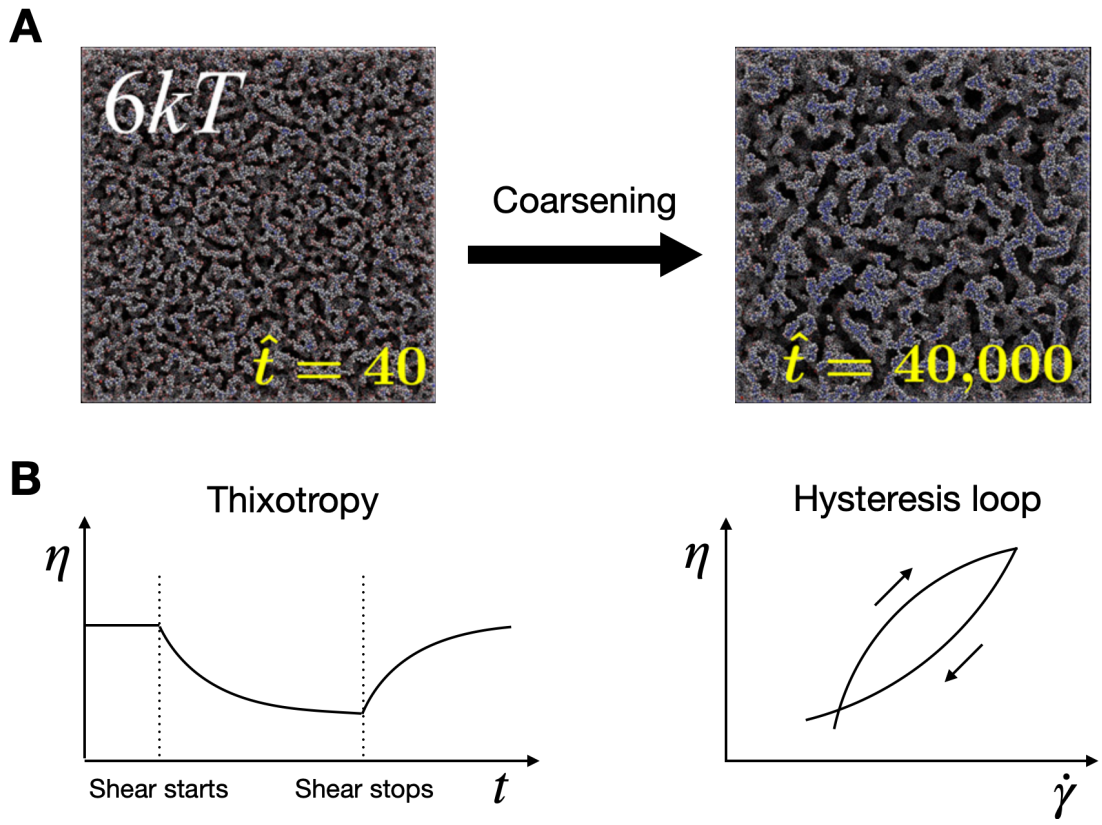

Figure 2.4 A. An example of gel coarsening (simulation). Taken from [38]. B. Schematic thixotropy (left) and consequent hysteresis loop (right).

Thixotropy, the continuous decrease of viscosity (or stress) under flow, is another well-known time-dependent behaviour [41]. Measuring a thixotropic material is challenging, as the result is highly sensitive to the measuring protocol and, frequently, unrepeatable. A typical manifestation is hysteresis loop, Figure 2.4B. When the transient flow curve data are measured, a thixotropic sample will present a loop in the σ-$\dot{\gamma}$ plot as a result of stress lag. To mitigate thixotropic effect, therefore, it is better to record the data at steady (or at least quasi-steady) state.

The rheology of a material may also vary with flow history. For systems constantly away from equilibrium, external flow may have irreversible impact on their microstructure, which in turn causes change in rheology [21, 42]. An effective way to remove history, either from loading or previous experiments, is shear rejuvenation [43]. Imposing a high-rate shear for sufficiently long, rejuvenation can help 'reset' the sample.

2.2 Experimental rheometry

While there are many ways to qualitatively characterise the rheology of a material (e.g. squeezing between fingers), quantitative rheology is mostly carried out on a rheometer. As a precision instrument, rheometer contains the material of interest in a specified flow geometry with controlled environment, and applies and measures strain rate and stress. Rheometers come in various designs, suited to specific types of measurements and materials.

For shear rheology, rotational rheometers are popularly used to generate a steady shear flow. The basic idea is to sandwich the sample between two disks/cylinders and rotate one of them in one direction while quantities like angular velocity Ω (corresponding to shear rate) and torque M (corresponding to shear stress) are measured. During experiments, either shear stress or shear rate can be controlled as demanded. There are several measurement geometries suited to different materials, and cone-plate, parallel plate and Couette cell are three common options, Figure 2.5.

2.2.1 Geometries

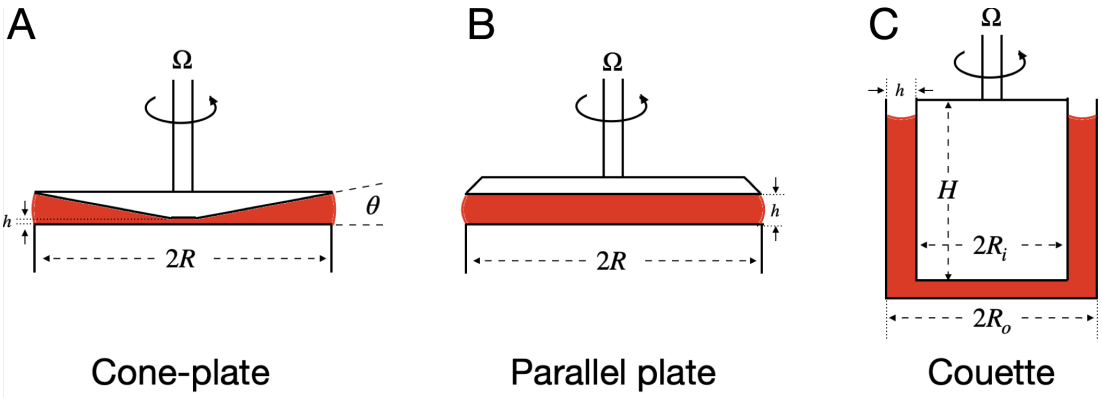

Figure 2.5 Common flow geometries for rotational rheometer.

Cone-plate

The cone-plate geometry consists of a flat bottom plate of radius R and a cone-shaped top plate of small angle θ, Figure 2.5A. With such a geometry, it is possible to impose a constant shear rate throughout the sample. The shear rate $\dot{\gamma}$ and

shear stress σ can be expressed as functions of angular velocity Ω and torque M respectively:

$$\begin{aligned} \dot{\gamma} &\simeq \frac{\Omega}{\theta} \\ \sigma &\simeq \frac{3M}{2\pi R^3}. \end{aligned} \tag{2.9}$$

Strictly, to generate a homogeneous shear flow, the tip of cone should be just in contact with the base plate. Yet in practice, the cone is usually truncated to leave a small gap h (typically $\sim 50\,\mu\text{m}$) to avoid mechanical contact.

Parallel plate

Similar to the cone-plate geometry, shear flow can be generated between two parallel plates (radius R) with a constant gap h, Figure 2.5B. With the upper plate rotating, the shear rate $\dot{\gamma}(r)$ applied is no longer constant and varies linearly with the radial distance r. Hence only apparent quantities can be defined from angular velocity Ω and torque M. For a Newtonian fluid with apparent viscosity η_{app}, the torque M on the plates is written as:

$$M = 2\pi \int_0^R r^2 \sigma(r) dr = 2\pi \int_0^R r^2 \eta_{\text{app}} \dot{\gamma}(r) dr = \frac{\pi R^3}{2} \left(\frac{\Omega R}{h} \right) \eta_{\text{app}}, \tag{2.10}$$

where the item in the bracket refers to the rim shear rate $\dot{\gamma}(R) = \Omega R/h$. If viewing $\dot{\gamma}(R)$ as the apparent shear rate $\dot{\gamma}_{\text{app}}$, the apparent stress can be reported as:

$$\sigma_{\text{app}} = \eta_{\text{app}} \dot{\gamma}_{\text{app}} = \frac{2M}{\pi R^3} \tag{2.11}$$

The discussion above limits to Newtonian fluids whose rheology is rate-independent. To extend to non-Newtonian fluids, one may use a corrected form [44]:

$$\sigma(\dot{\gamma}) = \frac{M}{2\pi R^3} \left(3 + \frac{\mathrm{d}\ \ln M}{\mathrm{d}\ \ln \dot{\gamma}} \right). \tag{2.12}$$

Coutte geometry

Two coaxial cylinders, with one rotating and the other one staying still, can be used to generate shear flow between walls as well. Such geometry, also referred to as Coutte geometry (Fig. 2.5C), is characterised by the inner cylinder radius R_i, outer cylinder radius R_o and height H. Note that the shear rate is not uniform

throughout Coutte geometry. Yet by making the gap h relatively narrow, i.e. $h \ll R_i$, this heterogeneity can be minimised. The shear rate $\dot{\gamma}$ and stress σ are respectively expressed as:

$$\begin{aligned} \dot{\gamma} &\simeq \frac{2\Omega}{1-(R_i/R_o)^2} \\ \sigma &\simeq \frac{M}{2\pi\hat{R}^2 H}, \end{aligned} \tag{2.13}$$

where $\hat{R} = (R_i + R_o)/2$ is the effective radius.

In this work, cone-plate geometry is applied by default unless otherwise stated. This choice is made because cone-plate geometry both applies a uniform (radius-independent) shear strain across the sample and requires the minimum amount of sample[2]. The small truncation gap ($h = 48\,\mu\text{m}$) in the centre is not a problem, since the size of particles we used ($d \lesssim 4\,\mu\text{m}$) is at least ten times smaller than the plate separation.

2.2.2 Oscillatory shear rheology

Conventional condensed matter comes in two forms, elastic solid ($\sigma \propto \gamma$) and viscous liquid ($\sigma \propto \dot{\gamma}$). Yet for soft materials, where the relaxation time is comparable to experiments, there is no clear boundary for solid and liquid. The majority of them behaves in a way that combines viscous and elastic response [2], e.g. yield-stress fluids (a solid below σ_y and a liquid beyond σ_y). These materials are known as viscoelastic materials.

To characterise the viscoelasticity, a useful technique is oscillatory shear rheology [22]. Instead of imposing a steady shear flow, oscillatory rheology applies a sinusoidal strain:

$$\gamma(t) = \gamma_0 \sin(\omega t), \tag{2.14}$$

and measures the real-time stress $\sigma(t)$. In the linear viscoelastic regime (typically small γ_0), the stress signal is also sinusoidal yet with a phase lag:

$$\sigma(t) = \sigma_0 \sin(\omega t + \delta). \tag{2.15}$$

The phase lag δ is the result of viscoelasticity. Indeed, for elastic Hookean solids

[2]Scaling up the synthesis and functionalisation of our small particles is challenging in practice.

$\delta = 0$ and for viscous Newtonian liquids $\delta = \pi/2$. Thus a viscoelastic material displays a phase angle $0 < \delta < \pi/2$.

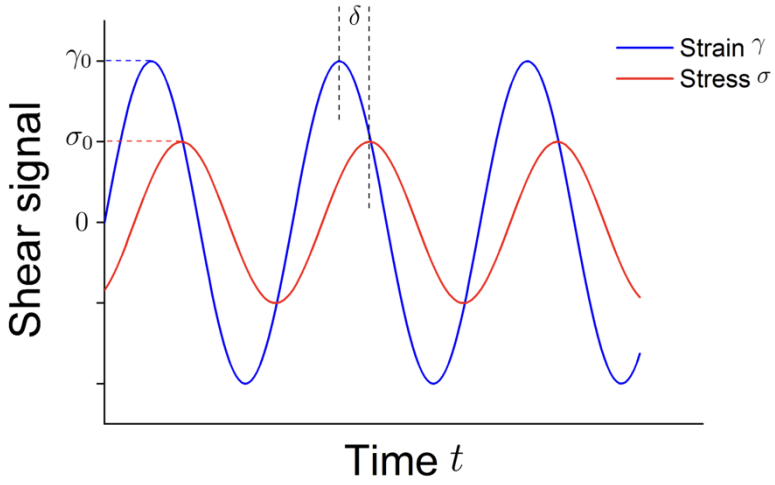

Figure 2.6 Strain and stress signals under oscillatory shear in the linear regime.

By generalising Hooke's law, one can express the constitutive relation in viscoelastic materials as:

$$\sigma^* = G^* \gamma^*, \tag{2.16}$$

where γ^* and σ^* are strain and stress in the complex form, and $G^* = (\sigma_0/\gamma_0)e^{i\delta}$ is the complex shear modulus. For better understanding, this complex modulus is customarily decomposed into elastic (storage) and viscous (loss) components as follow:

$$\begin{aligned} \text{Elastic modulus}: \ G' &= \mathrm{Re}(G^*) = \frac{\sigma_0}{\gamma_0}\cos\delta \\ \text{Viscous modulus}: \ G'' &= \mathrm{Im}(G^*) = \frac{\sigma_0}{\gamma_0}\sin\delta \end{aligned} \tag{2.17}$$

Both the strain amplitude γ_0 and frequency ω can be tuned as free parameters in oscillatory rheology. With the strain γ_0 fixed, one can vary the frequency ω under oscillatory shear. Such experiment is known as a dynamic frequency sweep. Most viscoelastic materials are frequency-dependent, i.e. $G^* = G^*(\omega)$, as oscillatory shear artificially introduces a timescale ω^{-1} that competes with material relaxation. Ideally, a viscoelastic solid tends to be more elastic at lower frequency and more viscous at higher frequency. Yet specific response under oscillatory shear depends on the material property.

The discussion above confines to the linear regime, where γ_0 is so small that the deformation is affine and the responding stress $\sigma(t)$ is as sinusoidal as the imposed strain $\gamma(t)$. The two moduli G' and G'' remain constant in the linear

regime. With the frequency ω fixed, increasing the strain amplitude γ_0 causes the shape of $\sigma(t)$ to distort, Figure 2.7. Such experiment is known as a dynamic strain sweep. For general viscoelastic solids, as γ_0 increases, the elastic modulus G' deviates from linear response and progressively decreases until falling below the viscous modulus G'', Figure 2.7. This crossover indicates a transition from solid to liquid, i.e. yielding [7].

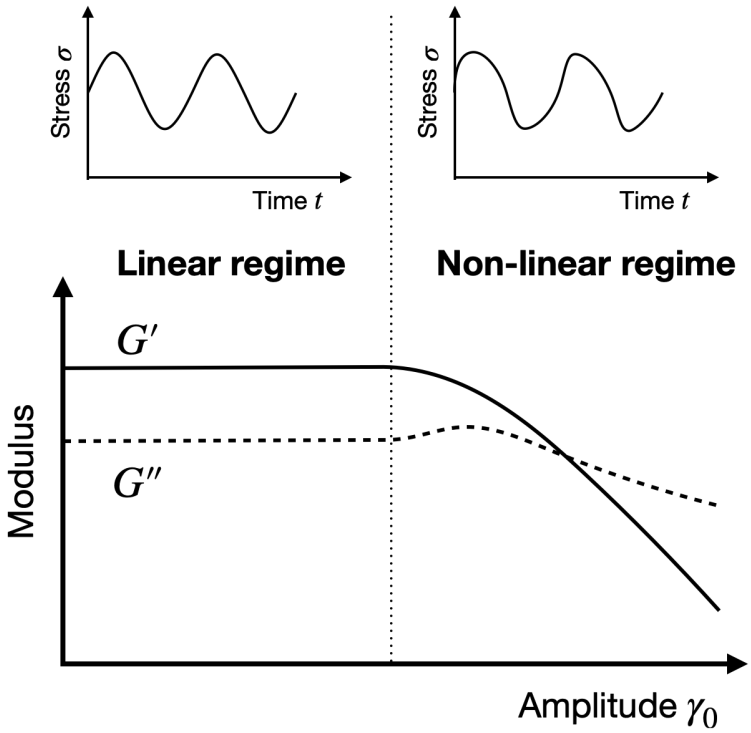

Figure 2.7 Illustration of linear and non-linear regimes in dynamic strain sweep.

The boundary between linear and non-linear regimes (Fig. 2.7, dotted line) depends on the material. For example, polymers may respond linearly up to 1 strain unit [45], whereas for most suspensions, non-linear yielding occurs beyond 1 % strain amplitude [4]. For materials whose microstructure changes under flow, e.g. colloidal gels [21, 46], oscillatory rheology in the linear regime enables non-destructive investigation.

2.2.3 Precautions

Slip and banding

The precise measurement of shear rheology assumes a viscometric flow field (Fig. 2.8A) where the shear rate is spatially uniform. Yet this is not always the

case in experiments, where wall slip and shear banding may occur and obscure measurements [47].

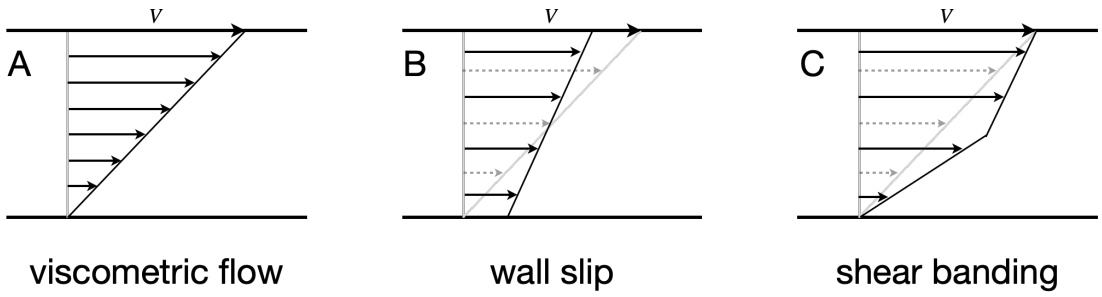

Figure 2.8 A. Ideal flow profile under shear. B. Flow profile with Wall slip. C. Flow profile with shear banding.

Wall slip Caused by various mechanisms, wall slip has been widely observed in driven soft materials [47–49]. In a suspension system, slip usually results from a dilute layer next to the wall, where particles barely interact with boundary [49]. This phenomenology could cause a discrepancy between the applied shear rate (from rheometer) and local shear rate and thus result in invalid data, Figure 2.8B. For example, colloidal gels, supposed to approach its yield-stress σ_y as shear rate $\dot{\gamma}$ decreases, may exhibit a stress drop at low $\dot{\gamma}$ in the presence of wall slip [50].

To data, the best way to minimise wall slip is to use geometries with rough surfaces, such as sandblasted, serrated and cross-hatched plates [47, 49, 50]. Generally, such treatment produces the best result when the plate roughness becomes comparable to or larger than the characteristic length in a sample, e.g the particle size in suspensions or the cluster size in colloidal gels [47].

Shear banding Shear banding refers to the flow where the globally imposed shear is not distributed homogeneously. Figure 2.8C shows a schematic gradient banding, where the sheared sample separates into bands of different shear rates[3]. Shear banding is ubiquitous in yield-stress materials (e.g. colloidal gels [50]) under low shear. This makes sense if we check the constitutive relation $\sigma = \sigma(\dot{\gamma})$. While the stress σ is just a bit higher than the yield stress σ_y, there may exist multiple solutions for $\sigma = \sigma(\dot{\gamma})$. Hence macroscopic regions with different local $\dot{\gamma}$ can persist. The rearrangement of microstructure may also help stabilising these bands [52].

[3]Similarly, vorticity banding, perpendicular to the flow direction, separates the sample into bands with different stresses σ [51].

Unlike wall slip, shear banding appear to occur as a result of inherent material property rather than an artifact. It is difficult to eliminate shear banding in practice.

Evaporation

Despite of the small exposed area in the cone-plate geometry, the sample evaporation still affects rheological measurements. This effect is notorious in suspensions, especially for those using volatile solvents like ethanol. To mitigate evaporation, a sealing hood, also known as solvent trap, can be used to enclose the whole sample geometry in a saturated solvent vapour without touching the rotating shaft. It could also limit the moisture ingress from hygroscopic solvents like glycerol. Meanwhile, using a sealing hood facilitates thermal isolation when the measuring temperature differs from the room temperature.

2.2.4 Yield stress measurement

Precisely determining the yield stress σ_y can be challenging in experiments, since different measuring protocols may give rise to different results [36]. While there is no universally agreed upon method, here we summarise four common approaches (three by steady shear and one by oscillatory rheology) as follow. Figure 2.9 schematically summarises the measuring results on a material with yield stress σ_y.

As previously mentioned, a popular method is to determine the yield stress σ_y from the steady shear flow curve. As shear rate $\dot{\gamma}$ decreases, the stress σ decreases until approaching the yield stress σ_y at low shear rates. Plotting σ versus $\dot{\gamma}$ on a log-log scale manifests a low-shear plateau (Fig. 2.9A), representing a finite yield stress σ_y. The specific value of σ_y can be obtained by Herschel-Bulkley fitting (see Eq. 2.8). Generally, more data at lower shear rates leads to a more precise result. However, in practice, the accuracy may be skewed by problematic flow at low shear, e.g. wall slip and shear banding.

In the second method, one applies a constant shear rate $\dot{\gamma}$ and monitors the stress σ build-up with strain γ, Figure 2.9B. At small strains, the stress σ increases linearly with strain like an Hookean solid. As the material yields, the stress σ rolls over a peak at γ_y followed by a relaxation to the steady state. This is known

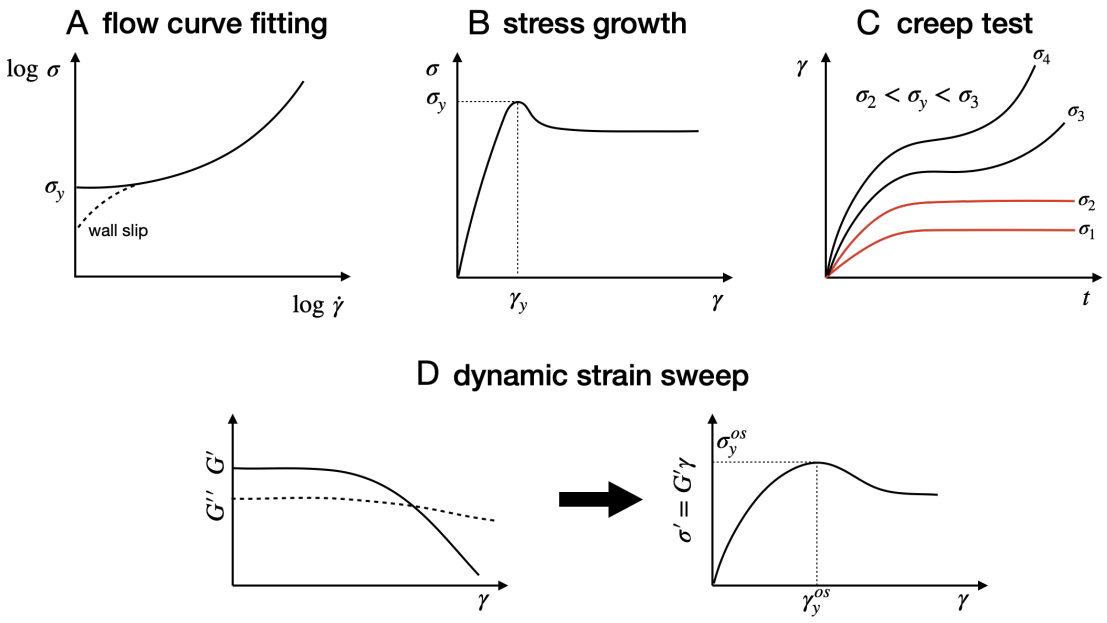

Figure 2.9 Four methods for determining yield stress σ_y.

as stress overshoot, and the peak value represents the yield stress σ_y. The stress growth test is popular for quickly determining the yield stress. However, its result depends on the applied shear rate $\dot{\gamma}$ and thereby may lead to a deviation from the real value.

The third method, known as a 'creep test', uses a series of measurements at discrete shear stresses σ and looks at the long-time behaviour in the strain-time plots, Figure 2.9C. Below the yield stress σ_y, the strain increases with time until reaching a plateau where the material no longer flows, resembling an elastic solid. In contrast, above the yield stress σ_y, the material ultimately flows at a steady shear rate at long times. The creep test directly agrees with the definition of yield stress and thus is supposed to provide the most accurate result. However, it is usually time-consuming.

Apart from these methods under steady shear, the yield stress σ_y can also be determined by oscillatory rheology. A customary way is to apply dynamic strain sweep, by which one can calculate the elastic stress $\sigma' = G'\gamma$. Plotting σ' versus strain γ gives the evolution of stress in the zero-frequency limit, since G' is frequency-independent and $G'' \sim \omega$ in ideal viscoelastic solids. Similar to the stress growth test (Fig. 2.9B), the peak in σ' represents the yielding point, from which the yield stress σ_y can be determined.

In this work, we principally used flow curve fitting and creep test to determine

the yield stress, while other methods were occasionally used as complements.

2.2.5 Rheo-imaging

A rheometer merely measures the macroscopic rheology, whose physics can be better understood if given the microstructure under flow. The conjunction of rheometer and external analytic techniques such as light scattering [53], magnetic resonance imaging (MRI) [54] and confocal microscopy [55] makes it possible to obtain the instantaneous microscopic information under shear. Rheo-confocal microscopy, which combines rheology with simultaneous confocal imaging, is heavily used in this work.

Confocal microscopy

Confocal laser scanning microscopy (CLSM) offers real-space imaging with high resolution and contrast [3]. Using laser as the illumination source, CLSM uses a pinhole to filter the out-of-focus light and scans a two-dimensional area by translating the laser with mirror. To ensure high-quality imaging, fluorescent dyes are commonly used to eliminate background noise, which necessitate matched refractive index in multiphase samples (e.g. suspensions) to minimise scattering.

Three-dimensional images can be achieved for CLSM by mechanically translating the focal plane. Yet when applied to rheo-confocal microscopy, the slow translation along the optical axis would limit the 3D imaging under flow. Hence in most studies (including this work), movies under flow are reported in 2D [21, 50, 55].

Our set-up

Rheo-confocal microscopy was performed using the combination of a rheometer (Anton Paar MCR 301) and a confocal microscope (Leica TCS SP8). Figure 2.10 shows a schematic representation. The upper rheometer geometry was a sandblasted steel cone (cone angle 1°; diameter 25 mm; roughness $\sim$ 10 µm; truncation gap 48 µm), while a semi-transparent roughened glass slide was used for the bottom plate. The glass slide permits confocal imaging from the bottom, while the top cone simultaneously imposes shear and collects rheological data.

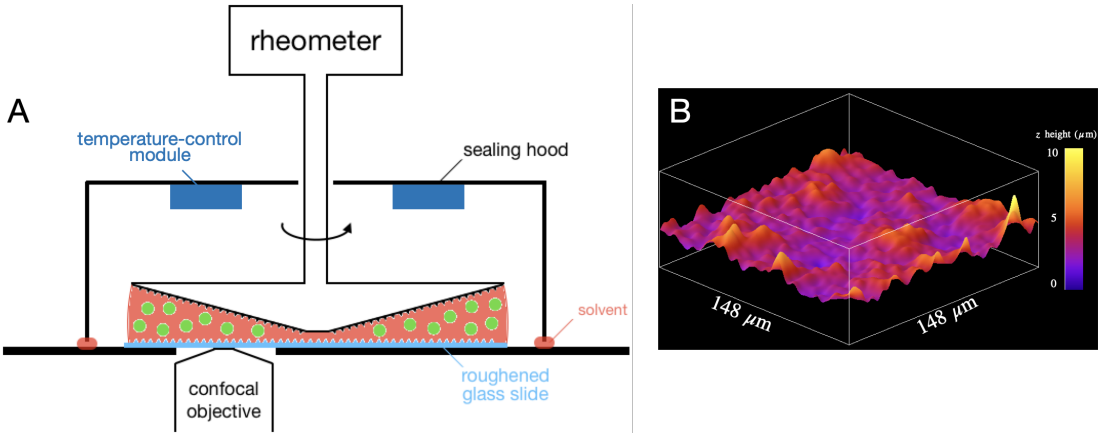

Figure 2.10 A. Sketch of rheo-confocal microscopy apparatus. The extra solvent beneath the edge of sealing hood is for thermal conduct, and it provides a saturated solvent vapour inside the hood as well. B. Colour-mapped surface plot of roughened glass slide. Reconstructed from 3D confocal stack.

In this work, we used a 63× oil objective with NA (numerical aperture) = 1.4 and WD (working distance) = 0.31 mm, and a No. 1.0 (thickness ≈ 0.14 mm) circular coverglass slide as the bottom plate. In principle, this combination gives resolution of ∼ 200 nm and enables imaging to a maximum depth of 170 µm. Yet due to the slight index mismatch between particles and solvent, in practice, it is difficult to identify our colloids ($d \approx 500$ nm) as single particles while clear images are only available up to a maximum height of 80 µm. See detailed discussion in Chapter 4.

While a smooth glass slide would be optimal for imaging, we noticed significant wall slip and heterogeneous crystallisation when using a smooth geometry surface. To remove these effects, we roughened the glass slide with sand paper to induce a roughness of approximately 5 µm, Figure 2.10B. Such degree of roughness is comparable to our particle size ($d \lesssim 4$ µm), and our visual observation confirms that this can effectively mitigate wall slip and eliminate local crystallisation. Though the roughened slide appears optically cloudy in air, the refractive index of our sample ($n \approx 1.45$) is relatively close to that of the cover glass ($n \approx 1.50$). The quality of confocal imaging is thus only slightly compromised with a roughened slide.

As a powerful tool to study flow and deformation in a variety of materials, rheology is widely applied in subjects like physics, geology, biology and engineering. Here we only introduce general rheology and some experimental considerations,

and save the suspension rheology until later. In the next chapter, we classify suspensions into two categories which correspond to the two species of constituent particles in our binary system, and discuss the fundamental physics in them respectively in depth.

Chapter 3

Suspension physics

The term suspension refers to a heterogeneous mixture composed of insoluble solid particles dispersed in a liquid medium. Such systems are ubiquitous in natural, biological and industrial processes and have been of considerable interest for decades, especially in terms of their rheology [4]. For instance, understanding the channel flow of blood, a suspension of blood cells in plasma [56], is important in medical science. For commercial products that are in suspension form, e.g. paints [57] and drilling fluids [58], their rheology directly determines their performance. In industry, moreover, suspensions enable the processing of solids in a flowable form, such as chocolate conching [59] and slot-die coating of battery electrodes [60]. For efficient and effective processing, it is vital to understand how they flow.

While a simple liquid is Newtonian, the addition of solid particles leads to a variety of non-Newtonian behaviours, such as shear thinning [19], shear thickening [34] and viscoelasticity [61]. Suspension rheology is principally determined by the particle-particle interactions, and so are the phase behaviour and particle dynamics [62, 63]. Generally, particles either attract or repel each other via different mechanisms[1] in suspensions, and systems with different particle interactions have different flow properties [5, 11]. For instance, at low concentrations, a gel of attractive colloids possesses a finite yield stress [21] while suspensions of Brownian hard spheres only exhibit shear thinning [64].

In this chapter, we first introduce the general physics in suspensions, including Brownian motion and possible interactions between particles. Based on the

[1] Attraction and repulsion could coexist, e.g. DLVO potential may present repulsion at long range and attraction at short range [4].

interparticle force, here we divide particles into two categories: repulsive hard-particles and attractive colloids. They correspond to the two components in our binary mixture. We then respectively discuss the quiescent phase behaviours and suspension rheology of each category.

3.1 General physics

3.1.1 Brownian motion

When freely suspended in fluid, a particle is constantly bombarded by the thermal motion of fluid molecules and thus driven to move about in a random way, Figure 3.1A. This phenomenology is known as Brownian motion. Such irregular motion has a diffusive character, which can be described by the mean square displacement (MSD) $\langle(\Delta r)^2\rangle$ as a linear function of time t [65]:

$$\langle(\Delta r)^2\rangle = 2N\mathcal{D}t \tag{3.1}$$

where $\mathcal{D}$ is the diffusion coefficient and N the spatial dimension. For simplicity, we set $N = 3$ as default in the following discussion.

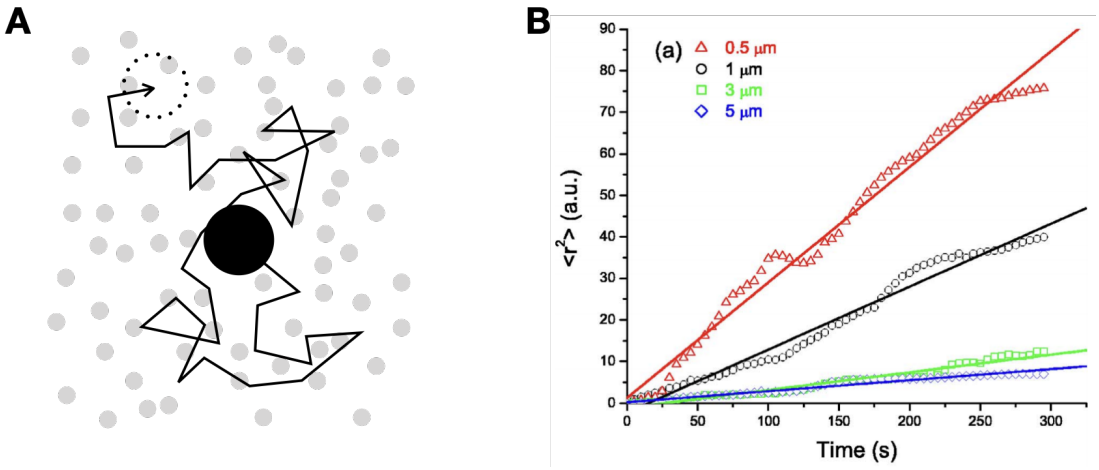

Figure 3.1 A. A sketch of Brownian motion. Gray disks: fluid molecules; Black disk: suspended particle. Not to scale. B. Time evolution of MSD at different particle sizes. Taken from [66]

While a particle is stochastically bombarded and thereby moves in a diffusive manner, its motion is constantly damped by the viscous fluid at the same time. For a spherical particle (of diameter d) moving (with relative velocity v) in a fluid

(of viscosity η_f), the resistive viscous force, also known as Stokes' drag [67], is given by:

$$F_d = 3\pi\eta_f dv. \tag{3.2}$$

Driven by the thermal motion (energy k_BT) and damped by the Stokes' drag, the diffusion coefficient $\mathcal{D}$ is also given by the fluctuation-dissipation theorem[2] [69]:

$$\mathcal{D} = \frac{k_BT}{3\pi\eta_f d}. \tag{3.3}$$

In this way, a characteristic Brownian timescale can be defined as follow:

$$\tau_{\mathrm{B}} = \frac{d^2}{6\mathcal{D}} = \frac{\pi\eta_f d^3}{2k_BT}, \tag{3.4}$$

referring to the time for a particle to diffuse its own size. This Brownian time τ_B determines whether Brownian motion is important in a system. Brownian motion is also associated with a characteristic stress scale $\sigma_B = k_BT/d^3$ [4, 70].

Brownian or not?

It is obvious that the importance of Brownian effect greatly depends on the particle size d, since both τ_B and σ_B follow a cubic power law: $\tau_B \sim d^3$ and $\sigma_B \sim d^{-3}$. The smaller particles are, the more significant Brownian motion is, Figure 3.1B. For example, an 1 µm particle in water diffuses its own size within 4 s, whereas for a 10 µm particle, the same process takes more than 6 min. Based on the Brownian activity, particle size is customarily divided into three regimes [71]: colloidal ($d \lesssim 1$ µm), intermediate (1 µm $\lesssim d \lesssim$ 10 µm) and granular ($d \gtrsim 10$ µm).

From the experimental perspective, telling whether particles are colloidal (Brownian) or granular (non-Brownian) is important. In certain respects, particles behave as 'big atoms' [72], and Brownian motion can drive particles to diffuse and form the configuration at equilibrium [4]. In this way, τ_{B} also represents the relaxation time of a system. Within an experimental timescale, therefore, colloids in suspensions manage to evolve to the equilibrium state, while granular particles barely move and thus are always out of equilibrium.

[2]This expression only applies to dilute systems where particles do not interact with each other. With the presence of more particles, diffusion slows down until arrested in colloidal glasses [68].

There is no absolute size standard to distinguish colloids and grains, since whether Brownian motion is important or not depends on external conditions. While a colloidal suspension can quickly equilibrate at rest, imposing shear flow with $\dot{\gamma} \gg \tau_B^{-1}$ can overwhelm any Brownian effects [64]. Analogously, by simply waiting patiently ($t_{\text{observation}} \gg \tau_B$), we may observe the phase behaviour of neutrally-buoyant granular suspensions as well. In practice, dimensionless quantities are commonly used to determine the relative importance of Brownian effect. For example, the Peclét number $\text{Pe} = \dot{\gamma}\tau_B$ quantifies the ratio of shear flow to Brownian diffusion [4].

3.1.2 Sedimentation

In the presence of gravitation, particles sediment (or cream) if the particle density ρ_p is higher (lower) than the fluid density ρ_f. In suspension studies, gravitational effects can be eliminated by artificially matching the densities. An example is poly(methyl methacrylate) (PMMA) particles in the mixture of cyclohexyl bromide (CHB) and cis-decalin [73]. Yet density matching is not always possible. For our binary system of silica particles in water-glycerol mixture, $\rho_p > \rho_f$ always applies.

A single particle settles down when it is heavier than the ambient fluid ($\Delta\rho = \rho_p - \rho_f > 0$). Balancing the gravitation $F_g = \Delta\rho(1/6)\pi d^3 g$ and Stokes' drag F_d (Eq. 3.2), we find that the steady sedimentation velocity is given by

$$v_{\text{sed}} = \frac{\Delta\rho d^2 g}{18\eta_f}, \tag{3.5}$$

The sedimentation time $\tau_{\text{sed}} = d/v_{\text{sed}}$ ratioed to the Brownian time τ_B gives a gravitational Péclet number Pe_g:

$$\text{Pe}_g = \frac{\Delta\rho(1/6)\pi d^4 g}{k_B T}, \tag{3.6}$$

which quantifies the importance of sedimentation relative to Brownian motion.

3.1.3 Interactions between charged particles

While a single particle in a fluid only interacts with the environment, a pair of or more particles can interact with each other via various mechanisms. Some of the interactions universally exist in suspensions, such as volume exclusion and the van der Waals force, whereas the others depend on the particle surface chemistry and fluid properties [74]. Understanding particle interaction is important, as it controls the macroscopic property of suspensions. Here we confine the discussion to the interactions relevant to this work. The large repulsive particles in our system are charged silica.

Hard spheres

As an idealised model, the concept of hard sphere is widely used in statistical physics and colloid science [2]. Hard spheres refer to non-deformable spheres with volume exclusion. That is, apart from the infinite repulsion at contact, there exists no interaction otherwise. Although hard spheres are impossible to realise in practice, volume exclusion is ubiquitous in real suspensions since solid particles cannot penetrate each other. In this work, we used silica particles with Young's modulus ($E \sim 50\,\mathrm{GPa}$ [75]) far beyond the applied stress ($\sigma \lesssim 1\,\mathrm{kPa}$). Hence the particles in our model system can be regarded as rigid particles.

van der Waals attraction

Unless specifically stabilised, particles inevitably aggregate together in suspensions as a result of van der Waals attraction [2], a dipole-dipole interaction arising from fluctuating atomic polarisation. The attractive force varies with the centre-to-centre distance r. By integrating over all atomic contributions, the van der Waals pair potential $\Phi_{\mathrm{vdW}}(r)$ exhibits a r^{-6} tail at large separations ($r - d \gg d$), where d is the particle diameter. For small separations ($r - d \ll d$), the van der Waals potential has the form:

$$\Phi_{\mathrm{VdW}}(r) = -\frac{Ad}{24(r-d)} \tag{3.7}$$

where A is the Hamaker constant, a material-dependent coefficient that can be estimated using the Lifshitz theory [76].

Theoretically, the depth of van der Waals potential is infinite when $r \to d$, i.e. two particles in contact cannot be separated by finite force. In practice, the particle roughness plays a vital role at small separations and the binding energy is thereby finite. Quantitatively, compared with the smooth spheres with an additional short-range repulsion[3], the surface roughness of less than 1 nm can lower the attraction by 1 to 2 orders of magnitude [77].

Though van der Waals interaction occurs widely in suspensions as a quantum effect, it can be artificially minimised. For example, matching the refractive indices n of particles and solvent can effectively reduce the Hamaker constant A. As a reference, $A \approx 2k_BT$ for silica particles ($n_s = 1.448$) in water ($n_w = 1.33$), whereas for silica in water-glycerol mixture ($n_{wg} = 1.45$), $A \approx 0.5k_BT$ [77]. By introducing polymers or surfactants that imposes a minimum d, van der Waals attraction can also be minimised via steric stabilisation.

Charge stabilisation

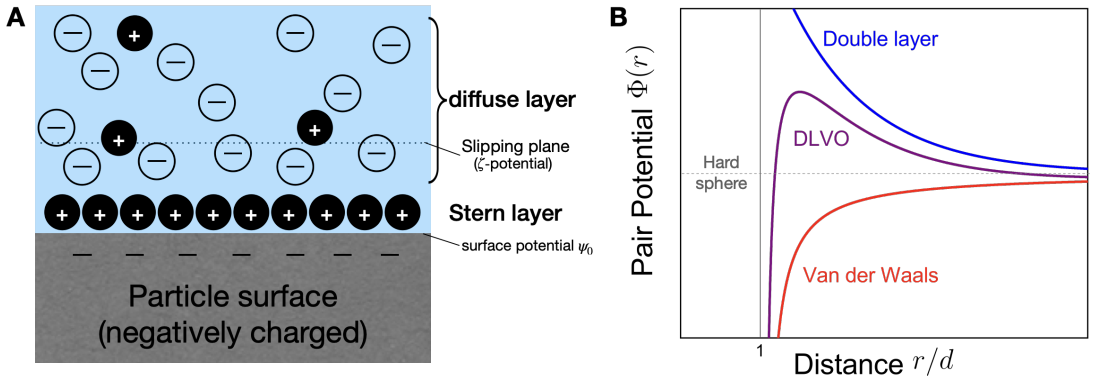

Figure 3.2 A. Schematic double layer on a negatively-charged surface. B. Unscaled pair potentials of hard sphere (gray), van der Waals attraction (red), electric double layer repulsion (blue) and DLVO interaction (purple).

To prevent aggregation caused by van der Waals attraction, an extra repulsion is required to stabilise particles. Charge is one way to impart such stability [74]. When immersed in a solvent, particles with ionisable surface groups gain a net surface charge by releasing counterions to the solvent. For example, as a class of widespread model particles, silica particles are negatively charged via the dissociation of surface silanol group ($\mathrm{Si{-}OH} \longrightarrow \mathrm{Si{-}O^- + H^+}$) when dispersed in a polar solvent [78]. Some of the counterions are tightly bound to the particle

[3]To remove the divergence at contact

surface and form an inner layer called the Stern layer, whereas the rest are loosely associated with the particle as a diffuse layer, Figure 3.2A. This structure is known as the electric double layer [74].

Taking both the Coulomb repulsion and screening from free ions into consideration, the pair potential from the double layer is given by [74]:

$$\Phi_{\mathrm{dl}}(r) = \frac{Zd}{4} \exp\left(\frac{r-d}{\kappa^{-1}}\right), \tag{3.8}$$

where Z is the interaction constant and κ^{-1} is the Debye length, respectively defined as:

$$Z = 64\pi\epsilon_0\epsilon_r \left(\frac{k_B T}{e}\right)^2 \tanh^2\left(\frac{ze\psi_0}{4k_B T}\right) \tag{3.9}$$

$$\kappa^{-1} = \sqrt{\frac{\epsilon_0\epsilon_r k_B T}{\sum_i n_i e^2 z_i^2}}, \tag{3.10}$$

where $\epsilon_0\epsilon_r$ is the solvent permittivity, e is the elementary charge, z is the electrolyte valency[4], ψ_0 is the surface potential[5], n_i and z_i are the concentration and valency of ions i respectively.

Characterising the exponential decay, the Debye length κ^{-1} represents the range of charge screening. According to Eq. 3.10, increasing the ionic concentration (e.g. adding extra salt) can effectively enhance screening effect and shorten the repulsive range κ^{-1}. This is a common way to tune interactions between charged particles in experiments (even from repulsion to attraction [80]).

In practice, it is difficult to directly measure the surface potential ψ_0. Instead, the electrical potential at the slipping plane[6], the ζ-potential, is commonly used to characterise the stability. When the depth of slipping plane (typically $\lesssim 10\,\text{Å}$ [82]) is far shorter than the Debye length κ^{-1}, the ζ-potential roughly equals to the surface potential ψ_0. In experiments, the ζ-potential can be determined from electrophoretic mobility [83].

[4]The case of asymmetrical electrolytes is more complicated, see treatment in [79].

[5]The interaction constant can also be expressed in the surface charge density σ_s alternatively. At low potentials, the surface potential ψ_0 and charge density σ_s are linearly related [74].

[6]The slipping plane labels the interface beyond which fluid is no longer attached to particle surface and thereby mobile [81].

The DLVO theory In suspensions, the van der Waals attraction and double layer repulsion usually coexist in an additive manner. The combined potential, also known as DLVO potential [74], can be written as:

$$\Phi_{\mathrm{DLVO}}(r) = \Phi_{\mathrm{dl}}(r) + \Phi_{\mathrm{vdW}}(r). \tag{3.11}$$

Since the double layer potential Φ_{dl} and the van der Waals potential Φ_{vdW} vary with the distance r differently (see Eq. 3.7 and 3.8), the combined potential $\Phi_{\mathrm{DLVO}}(r)$ usually exhibits an non-monotonic curve, Figure 3.2B (purple). The detailed shape depends on specific parameters. More details about the DLVO theory is outside the scope of this thesis. A systematical review can be found in [84].

3.1.4 Other ways to induce attraction

For both species of particles in our binary suspension, we use silica particles which, if untreated, interact with each other in a DLVO manner. In the discussion above, we have shown that tuning the DLVO potential can induce attraction between particles [80]. In this work, however, we tend to establish a model binary system that has disparate particle interactions. Simply adding salt would make all interactions attractive. Hence in this section, we look for other ways to induce attraction.

Depletion

An alternative method to induce attraction is by means of adding non-absorbing depletants (such as polymers or smaller colloids) , e.g. the PMMA particles-polystyrene polymers mixture [21, 61]. Surrounded by depletants with size d_{dep}, two nearby particles at distance $r < (d + d_{\mathrm{dep}})$ share an overlapped depletion zone (of volume V_o) which is inaccessible for depletants, Figure 3.3. The unbalanced osmotic pressure from depletants then pushes two particles together and results in an effective attraction. The potential is given in the form of [85]:

$$\Phi_{\mathrm{dep}}(r) = -\Pi_p \cdot V_o(r), \tag{3.12}$$

where Π_p is the osmotic pressure of depletants in the free volume[7], and $V_o(r)$ is the overlapped volume (of depletion zone) as a function of distance r.

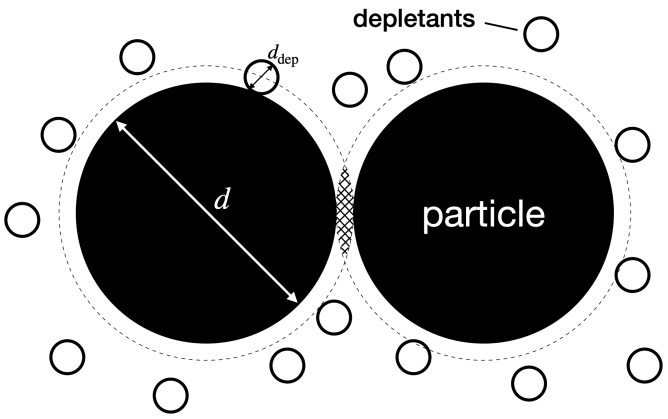

Figure 3.3 Sketch of depletion mechanism. The dashed circles denote the depletion layers and the cross-hatched region is their overlap with volume V_o.

By changing the concentration and size of depletants, both the strength and range of attraction can be tuned in a wide range [6, 86]. Such mechanism is widely used in colloidal gels, and the depletion gel has been a typical model system in soft matter research [61, 87]. Yet similar to van der Waals attraction, if adding depletants to induce attraction between the small particles in our system, the large particles will be inevitably attractive as well.

Hence we do not consider depletion as an option to induce attraction. Yet it is not completely excluded in our system. Technically, depletion force exists in all polydisperse suspensions where smaller colloids work as depletants. In this sense, the large particles may 'feel' depletion from the small particles in our system. Yet such effect will be verified neglectable in Chapter 4.

Hydrophobic interaction

The word 'hydrophobic', literally meaning 'water-fearing', describes the tendency of water and apolar objects to separate. Despite a great deal of research, the physical origin of hydrophobicity is still under debate. Proposed by Frank and Evans in 1945 [88] and accepted by most people to date, the hydrophobic effect is attributed as an entropic result: the cost of free energy for hydrogen-bonded water molecules to accommodate apolar molecules is so high that they prefer

[7]See more comments on free volume in Chapter 6

to separate. In this way, when two or more hydrophobic objects are immersed in aqueous solvent, they tend to stay together to reduce contacts with polar molecules [8], giving an effective attraction [90].

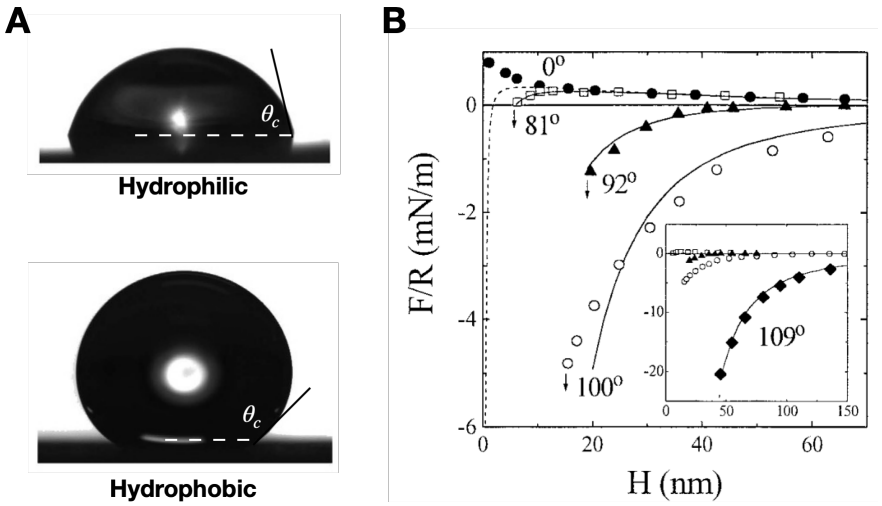

Figure 3.4 A. Contact angles θ_c of water droplet on different surfaces. Hydrophobic surface exhibits higher θ_c. Taken from [91]. B. Direct force measurement between silica plate and glass sphere (15–25 µm radius) with different θ_c in water. Taken from [90].

Hydrophobic attraction can be quite strong. For two hydrocarbon surfaces immersed in water, their adhesion energy, or equivalently the energy cost to fully separate them, is $W \sim 10^2\ k_BT/\text{nm}^2$ [74]. The adhesion energy principally depends on the degree of hydrophobicity, which can be quantified by the contact angle θ_c [91]. Figure 3.4A illustrates the contact angle of water drop on two different surfaces. The more hydrophobic a surface is, the higher the contact angle is.

In principle, hydrophobic interaction should be short-ranged ($\xi \lesssim 10\,\text{nm}$), as it originates from the rearrangement of few layers of solvent molecules near the surfaces. Using equipment like atomic force microscopy (AFM) and surface force apparatus (SFA) [92], nevertheless, people found that two hydrophobic surfaces attract each other within a relatively long range ($\xi \approx 100\,\text{nm}$), Figure 3.4B. Possible mechanisms are discussed in [89].

In our binary system, we use hydrophobic interaction as the attraction mechanism. Importantly, the hydrophobic attraction between small particles does not interfere with the charge repulsion between large silica. While the attraction

[8] This scenario is still controversial and many other theories are proposed in the recent 30 years. See review on hydrophobic interactions in [89].

range ξ, determined by the fundamental physics of hydrophobicity, is more or less fixed, the attraction strength can be tuned by means of silica functionalisation[9]. Details of hydrophobical functionalisation will be presented in chapter 4.

3.1.5 Other interactions

Besides the simple pairwise potential interactions discussed above, particles can interact with each other in a more complicated way. Here we mention two interactions that matter in this work: hydrodynamic coupling and contact forces.

Hydrodynamic interactions

We have considered the translational motion of a single particle in fluid, which is constantly damped by the Stokes' drag. When there are a pair of, or more, particles relatively move in a fluid, hydrodynamic interactions appear between them [94].

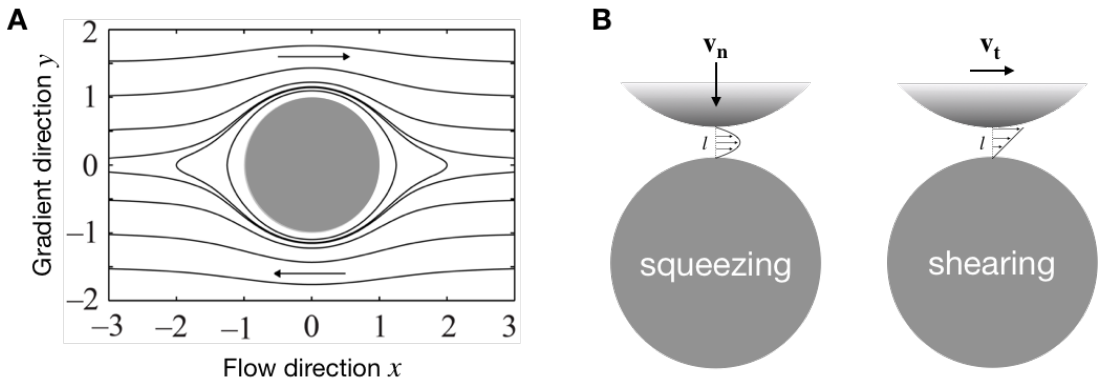

Figure 3.5 A. Schematic 2D profile of streamline around a sphere under simple shear flow. B. Squeezing and shearing lubrication hydrodynamics. Both adapted from [94].

Hydrodynamic interaction manifests under flow. Specifically, while a free particle is driven by the ambient fluid motion in a shear flow, the flow field around it is locally distorted (Fig. 3.5A) and thereby affects other particles involved in this field. In this way, particle motions are hydrodynamically coupled. The magnitude of distortion decays with distance in an inverse-square fashion [94]. Dealing with such far-field hydrodynamics is mathematically difficult, since it involves multiple particles and may be non-radial and asymmetric.

[9] A chemical treatment to coat certain groups on silica particles [93].

Lubrication In concentrated suspensions where the surface separation $l \ll d$ is sufficiently small, short-range lubrication hydrodynamics dominates as a result of large gap pressure [94], Figure 3.5B. For a pair of spheres with relative velocity $\mathbf{v} = \mathbf{v_n} + \mathbf{v_t}$, the normal and tangential components of lubrication force scale as follow:

$$\begin{aligned} f_n &\sim -\eta_f d^2 \mathbf{v_n} l^{-1} \\ f_t &\sim -\eta_f d^2 \mathbf{v_t} \ln l. \end{aligned} \tag{3.13}$$

This implies that a normal force f_n must be applied to make the two spheres approach at speed $\mathbf{v_n}$. As f_n diverges as $l \to 0$, an infinite compressive force is required to squeeze them together. Theoretically, physical contact is impossible for ideal smooth spheres.

Contact mechanics

While lubrication prevents physical contact between smooth spheres, in practice, though, particle surfaces are rough. Such roughness matters at small separation and enables direct contacts even when particles are stabilised [95]. Similar to macroscopic objects, particles interact when they are in contact. Contact forces occur widely in dry granular materials [96], and recent studies revealed the crucial role of interparticle contact in suspension rheology [95, 97].

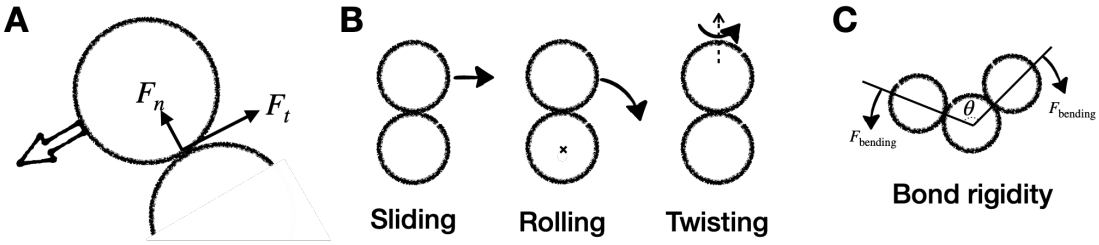

Figure 3.6 Sketches of contact force (A) and basic motions for particles in contact (B) and bond rigidity (C).

Interparticle contact force usually goes with two components: a normal elastic component F_n and a tangential frictional component F_t [96], Figure 3.6A. Unlike ideal hard spheres, the normal force F_n between realistic particles stems from elastic deformation and thereby finite at contact. With the presence of surface roughness [10], the two components are correlated. If Coulomb friction applies, particles either remain static when $F_t < \mu_s F_n$, or slide over each other (in contact)

[10]Note that the tangential force F_t does not necessarily result from roughness [98], although roughness-induced friction dominates in most cases.

when $F_t > \mu_s F_n$ with $F_t = \mu_k F_n$, where μ_s and μ_k are the static and kinetic friction coefficients respectively [99].

There exists three basic motions for a pair of particles in contact, Figure 3.6B. While sliding can be suppressed by tangential friction F_t, particles can still move relatively via rolling and twisting. Such two motions can be constrained by frictional torques in adhesive contacts [11].

Bond rigidity Under simple $U(r)$ attraction, ideal hard spheres aggregate and form contacts with infinitely small area. Particles in such contact can still move freely due to the lack of friction. Yet realistic particles are not perfectly hard and spherical: they are rough and faceted. This leads to finite contact area and non-radial forces and torques. Such contacts are termed as adhesive contacts, and particles with such contacts are adhesive particles [12].

Adhesive contacts constrain bond rotation. For a cluster of three or more particles, bending the bond angle θ in Figure 3.6C requires a finite torque. This is known as bond rigidity, confirmed by direct measurement in experiment [100]. Such rigidity underlies the particle dynamics and thus matters in the macroscopic rheology of suspensions [101].

3.2 Phase behaviours

Colloids behave as 'big atoms' and can somewhat reproduce some of molecular phase behaviours [72]. For example, the phase separation in attractive colloids [87] is reminiscent of the vapour-liquid coexistence in water, which makes sense since both their constituents are attractive [102]. The phase behaviour of a suspension depends on the interaction between particles [63, 86]. Here we start with hard-sphere system first, and then extend the discussion to interacting rigid particles. Note that though the phase behaviour itself does not rely on the particle size, the following discussion only makes practical sense for Brownian colloids.

3.2.1 Hard spheres

Thermodynamics tells us that the equilibrium phase behaviour of a system is determined by the free energy $F = U - TS$, where U is the internal energy, T

the temperature and S the entropy. For hard spheres whose repulsion is infinite when overlapped, U is fixed and proportional to k_BT, so that T only scales the free energy and leaves S the only parameter to minimise F. In this way, all the phase behaviours in hard-sphere system are entropy-driven and controlled by the number density, or equivalently the particle volume fraction ϕ:

$$\phi = \frac{V_{\mathrm{p}}}{V} = \frac{1}{6}\pi d^3 \frac{N}{V}, \tag{3.14}$$

where N is the particle number within a domain of volume V.

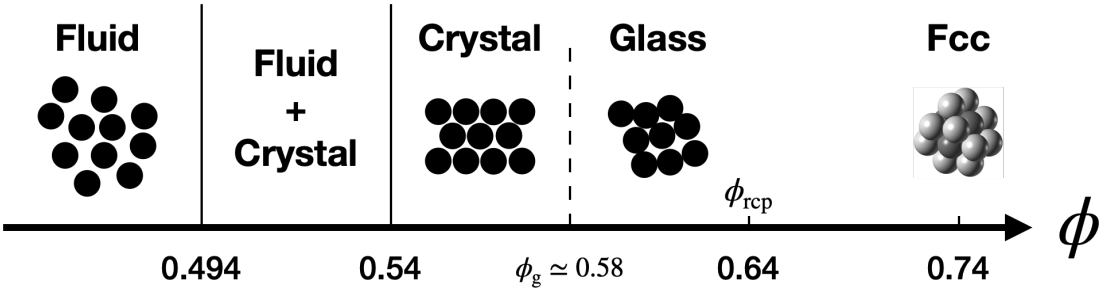

Figure 3.7 Hard sphere phase diagram. The dotted line denotes the non-equilibrium glass boundary ϕ_{g}.

Simulation [103] and experiment [62] give similar phase diagram for (nearly) hard spheres, Figure 3.7. At low volume fractions $\phi < 0.494$, Brownian motion leads to an isotropic configuration of particles at equilibrium, i.e. a fluid phase. When $\phi \geq 0.494$, crystalline domains are formed as an entropic result[11] and the fluid phase coexists with the crystal phase until $\phi \geq 0.54$, where the system is fully crystallised. The closest packing can be achieved by a face-centred crystal (fcc) at $\phi_{\mathrm{fcc}} = 0.74$.

Yet in practice, crystallisation is not always observed above $\phi_{\mathrm{g}} \simeq 0.58$ due to the glass transition [62]. As the volume fraction ϕ increases, the long-time diffusion progressively drops due to the crowding effect and almost vanishes beyond ϕ_{g}. Physically, particles are 'locked' in the cage of their neighbours [12]. The bulk system is then dynamically arrested in an amorphous structure, termed as the colloidal glass [5, 62]. As an non-ergodic state, the colloidal glass is mechanically a solid with a liquid-like structure, since no long-range order is presented yet the relaxation takes infinite time. Such non-ergodic state persists up to a random close packing $\phi_{\mathrm{rcp}} = 0.64$ [105].

[11] Although at first glance, crystallisation reduces the configurational entropy (as it is more ordered), its dense packing creates more free volume so that the bulk entropy still increases.

[12] Glass transition can be induced by both caging and bonding [104], and the latter will be discussed in later section.

Repulsive hard-particles

Apart from volume exclusion, experimental model particles may display a finite-range repulsion. When the repulsion range ξ is small compared to the particle size ($\xi \ll d$), the repulsion can be treated as a perturbation based on hard-sphere potential. It is common to define an effective size by adding a repulsive shell: $d_{\text{eff}} = d + \xi$, so that the solid volume fraction ϕ can be converted to an effective volume fraction $\phi_{\text{eff}} = \phi(1+\xi/d)^3$. Compared with hard spheres, phase (or glass) transitions occur at lower ϕ in repulsive particles [106, 107].

3.2.2 Structure characterisation

To characterise the structure in different phases (or states), a popular way is to measure the pair distribution $g(\mathbf{r})$, defined as:

$$\mathrm{g}(\mathbf{r}) = \frac{1}{n}\left\langle \sum_i \delta(\mathbf{r} - \mathbf{r}_i) \right\rangle, \tag{3.15}$$

where $n = N/V$ is the particle number density, and $\langle \cdots \rangle$ denotes the ensemble average. Given a particle at the origin, the pair distribution offers a measure of the possibility of finding another particle at $\mathbf{r}$ [108]. In an isotropic system, this can be angularly averaged to give:

$$\mathrm{g}(r) = \frac{1}{4\pi} \iint \mathrm{g}(\mathbf{r})\ \mathrm{d}\theta \mathrm{d}\varphi, \tag{3.16}$$

where θ and φ are polar and azimuthal angles respectively.

Peaks in $\mathrm{g}(r)$ characterise the microstructure. For hard spheres in crystalline phase, peaks show up at the lattice spacings [110]. One can determine the crystal system according to the positions of peaks [106]. For hard spheres in fluid phase, while $\mathrm{g}(r)$ presents a flat profile at long distance due to the lack of long-range order, the effect of volume exclusion is manifested by the peaks at short distances, Figure 3.8. The i-th peak corresponds to the i-th shell of nearest neighbour, with the peak height quickly decaying to 1 beyond several particle diameters. Note that $\mathrm{g}(r)$ only includes structural information in radial direction. To account for anisotropy or spatial heterogeneity, a full map of $\mathrm{g}(\mathbf{r})$ is required [34].

As the Fourier-transformed version of $\mathrm{g}(\mathbf{r})$ [108], the static structure factor $S(\mathbf{k})$

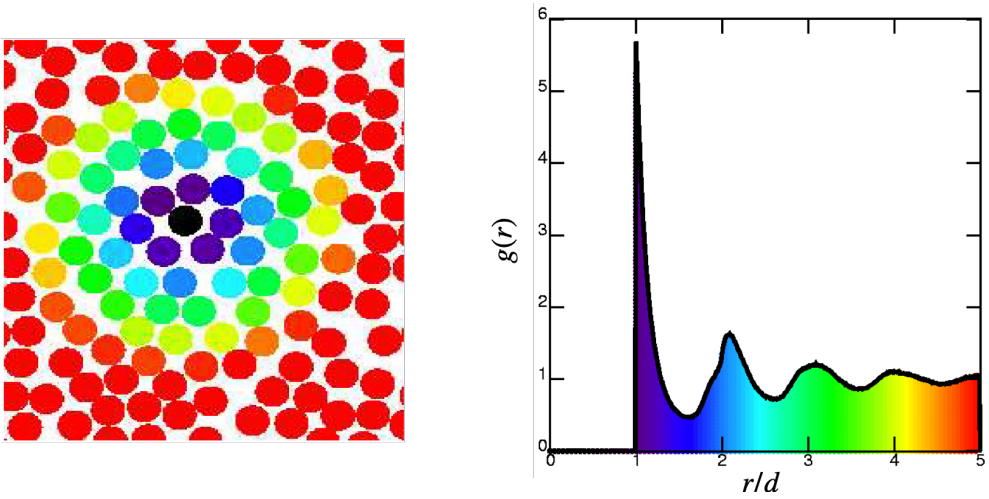

Figure 3.8 A collection of hard disks (left) and its radial distribution function $g(r)$ (right). The colour mapping illustrates the contribution from particles at different distances r. Taken from [109].

is another measure of structure, defined as:

$$S(\mathbf{k}) = \frac{1}{N}\left\langle \sum_i e^{i\mathbf{k}\cdot\mathbf{r}_i} \sum_j e^{-i\mathbf{k}\cdot\mathbf{r}_j} \right\rangle, \tag{3.17}$$

where $\mathbf{k}$ is the wave vector. Compared with g($\mathbf{r}$) which is obtained from real-space configuration, the structure factor $S(\mathbf{k})$ provides information in the frequency domain and correlates more with scattering results [61, 87]. Similarly, taking the angular average gives a radial spectrum $S(k)$, which is widely applied to determine the characteristic length scale in a structure. For example, in colloidal gels, a peak at k_0 indicates a characteristic cluster size of $2\pi/k_0$ [61]. The slope of $S(k)$ also gives information on the fractal information of gel structure [111].

3.2.3 Attractive colloids

Phase behaviours

For a quiescent collection of attractive colloids without bond rigidity, the phase behaviour has been extensively studied by experiments [63, 112] and simulations [113]. The phase behaviour depends on interparticle attraction, which is mainly characterised by the potential depth U_{att} (i.e. the attraction at contact, or binding energy) and interaction range ξ. For short-ranged attractions, or quantitatively $\xi/d \lesssim 0.3$ [114], a schematic diagram is outlined by the normalised attraction

U_{att}/k_BT and the volume fraction ϕ, Figure 3.9A.

There still exists three regions: fluid, solid (crystalline) and their coexistence [112]. As the attraction increases, even at low volume fractions, particles aggregate and form colloid-rich domains which crystallise at equilibrium. The fluid-solid coexistence region broadens with increasing U_{att}/k_BT. In our system, however, the ordered solid phase is always inhibited by gelation. In the following discussion, therefore, we ignore crystallisation.

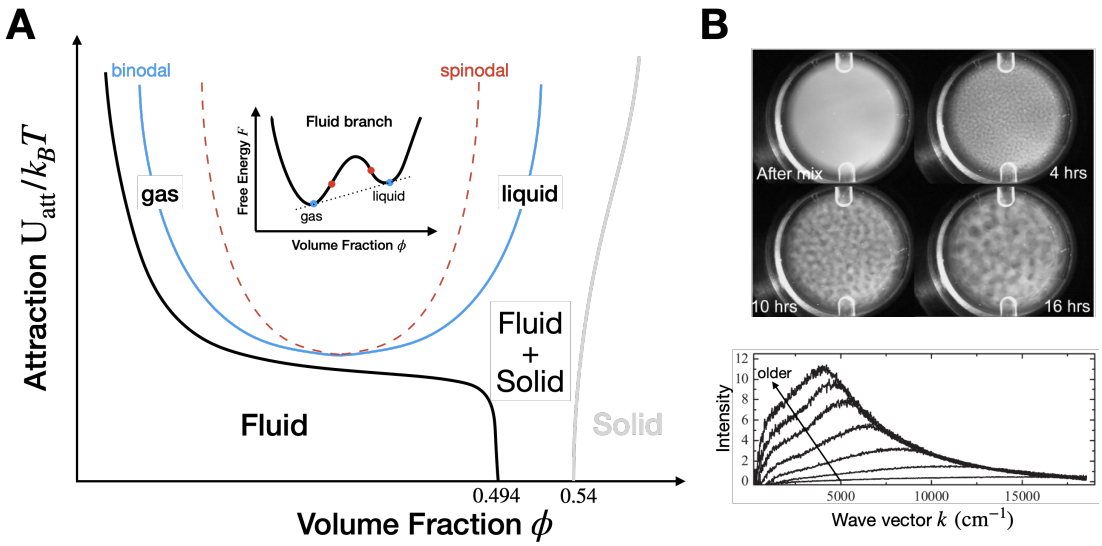

Figure 3.9 A. Schematic phase diagram of colloids with short-range attraction. Inset: free energy curve in fluid branch. Adapted from [61]. B. Spinodal decomposition in a model colloid-polymer mixture [115]. Top: snapshots at different time after mixing; Bottom: small-angle light scattering results. Taken from [115].

Taking away crystallisation manifests a region of gas-liquid coexistence which is originally 'buried' inside the equilibrium fluid-solid coexistence. The gas-liquid coexistence occurs as a result of the 'double-minimum structure' in the free energy [61]. As shown in Figure 3.9A (inset), the coexisting phases are defined by the line that is tangent to the free energy curve, and the locus of the two points of tangency determines the binodal line in Figure 3.9A (blue solid line). Systems within the binodal region tend to separate into gas and liquid phases.

Spinodal decomposition When looking in more detail at the free energy curve, we can notice a region with negative curvature between the inflection points where $\partial^2 f/\partial^2\phi = 0$, Figure 3.9A inset (red symbols). Their locus determines the spinodal line in Figure 3.9A (red dashed line). System in this region is unstable

with respect to any local fluctuations and will immediately phase separate in a characteristic manner, known as spinodal decomposition.

Spinodal decomposition has been widely observed in colloids, polymer blends and alloys [115–117]. Figure 3.9B (top) shows snapshots of a model colloid-polymer mixture during spinodal decomposition. In such depletion system, particles seek to lower their free energy by developing a coarsening bicontinuous texture of colloidal liquid (colloid-rich domain) and vapour (colloid-poor domain).

The dynamics of spinodal decomposition can be characterised by the structure factor $S(k)$, or equivalently scattering results. As the phase separation proceeds, a peak at low wavenumber k appears, grows and shifts to a lower k over time, Figure 3.9B (bottom). That is, a characteristic lengthscale progressively grows until two phases demix. Through dynamic scaling, the evolution of $S(k)$ can be described by the Furukawa form [118].

Experiments [61, 115], supported by simulations [38], show that many attractive systems phase separate via spinodal decomposition. At sufficiently high ϕ, however, such phase separation can be arrested in a ramified network structure [6, 115]. This dynamical arrest originates from the glass transition.

Dynamical arrest

Glass transition occurs at $\phi_{\mathrm{g}} \simeq 0.58$ in hard spheres. Such glass, dynamically arrested due to caging effect, is termed as the repulsive glass (RG) [5]. In the presence of attraction, a new category of glass appears at high U_{att}/k_BT. Unlike RG, such glass results from particle bonding rather than caging and thereby termed as the attractive glass (AG) [5]. As the attraction strength increases, the glass boundary ϕ_{g} decreases quickly so that the dynamical arrest could occur at low volume fractions. The glass lines can be calculated from mode coupling theory (MCT) [119] or determined by simulations [104, 120].

Dynamical arrest even occurs below the glass line ϕ_g. As we mentioned above, attractive systems phase separate via spinodal decomposition. Before this process is complete, however, the liquid branch becomes so dense that it turns into an AG. The structure is then arrested in a bicontinuous texture which spans the system. Such state is known as the colloidal gel [61]. Due to the percolated, ramified network, a gel responds like a soft solid. In this way, gelation can be interpreted as *arrested phase separation*. Such scenario has been verified in a wide

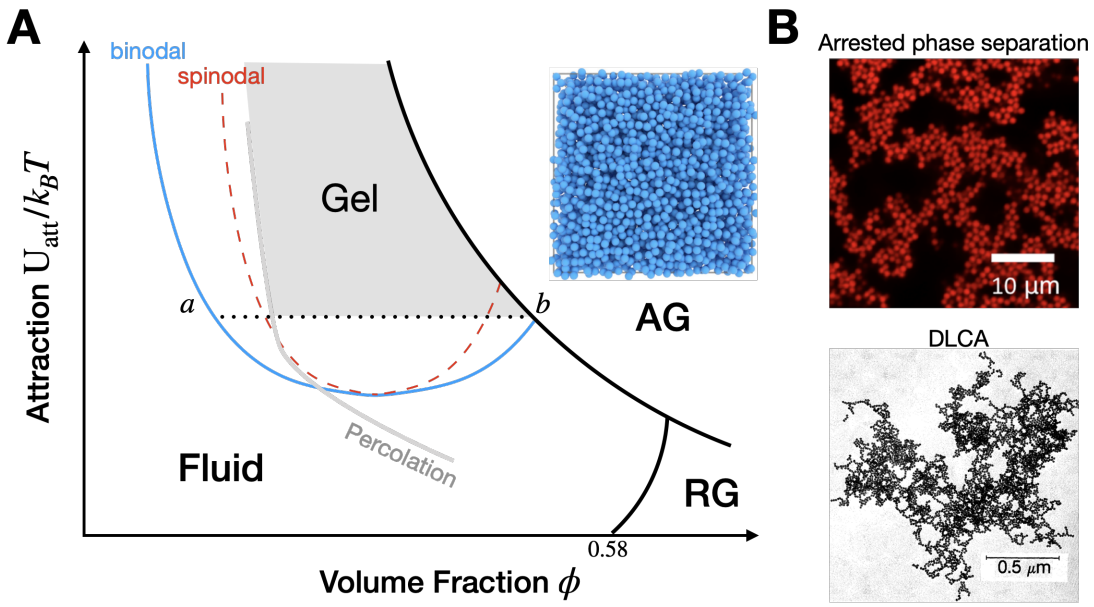

Figure 3.10 A. Schematic non-equilibrium state diagram. AG: attractive glass (inset: 3D rendering of AG from [121]); RG: repulsive glass; Gray area: colloidal gel. Dotted line *ab*: tie-line where the binodal line meets the AG line. Redrawn from[120]. B. Structure of different types of gel. Top: confocal image of *arrested phase separation* gel. Taken from [122]. Bottom: TEM image of *DLCA* aggregate. Taken from [123].

range of gels [6, 38, 61].

Figure 3.10A summarises these non-ergodic states in a schematic state diagram. All arrested systems respond like solids. From the structural perspective, RG and AG (see inset in Fig. 3.10A) are amorphous and relatively homogeneous. In contrast, the colloidal gel, formed within the gray area, exhibits a ramified network with large voids. Figure 3.10B (top) shows confocal image of a model depletion gel [122]. Though we use lines to demarcate these states in the diagram, note that there is no sharp state boundary in reality.

So far, the state diagram has not been fully understood. As ϕ decreases, there comes a point where the formation of an interconnected bicontinuous pattern becomes impossible, and phase separation occurs via nucleation and growth. The kinetic arrest then gives attractive-glass 'beads' rather than a gel structure [124]. Unexpected fluids of clusters are also observed between the gelation and fluid regions [125].

Different gels

For attractive particles, gelation occurs as *arrested phase separation*. Specifically, the phase separation proceeds via spinodal decomposition, where the bicontinuous texture of liquid branch becomes increasingly dense until arrested on the AG line. Figure 3.10B (top) shows a typical *arrested phase separation* gel. Such scenario has been widely verified in experiments by small-angle scattering [61] (or the structure factor $S(k)$ [6]), where a peak grows, narrows and shifts to lower wave vector k. The peak position k_0 decreases with time in a power-law manner until reaching a steady (or say arrested) state [6, 61].

Such interpretation does not include bond rigidity. In practice, however, particles may be not only attractive but also adhesive, i.e. relative motions are constraint once touched [11, 12]. An idealised model, known as *diffusion-limited cluster aggregation* (DLCA), describes the gelation in such case [126]. Brownian adhesive particles move and meet and irreversibly stick to each other. During aggregation, the access to the interior of aggregate is blocked by the earlier arrivals so that free particles can only adhere to the exterior, leading to fractal clusters [123]. We can define the fractal dimension d_f in DLCA as:

$$N \sim \left(\frac{d_c}{d}\right)^{d_f}, \tag{3.18}$$

where d_c is the characteristic cluster size and N the particle number of the cluster. DLCA aggregate has a fractal dimension $d_f \sim 1.7$ to 1.8 in 3D [123].

These clusters grow over time and the volume fraction inside clusters $\phi_c \sim (d_c/d)^{d_f-3}$ decreases accordingly. Once ϕ_c decreases to ϕ, the cluster packing then spans the entire space and a DLCA gel is thus formed. In this way, we have the critical cluster size d_{gel}:

$$d_{\text{gel}} \sim d\phi^{1/\left(d_f-3\right)}. \tag{3.19}$$

The *DLCA* gel is then an assembly of fractal clusters with size d_{gel}.

Figure 3.10B (bottom) shows a TEM image of DLCA gel. Compared to the *arrested phase separation* gel on the top, the network in DLCA gel is highly porous and tenuous. Moreover, the fractal feature enables a DLCA gel to be formed theoretically at arbitrary low ϕ, whereas a finite gel boundary ϕ_{gel} exists in *arrested phase separation* gel [127]. Despite of such difference, similarity

was revealed between DLCA and phase separation in small-angle scattering experiment [128]. In this sense, a DLCA gel may be considered as a variant of *arrested phase separation*, where the dynamics is arrested by bond rigidity rather than attractive glass [129].

We note that other gelation routes are possible (see review by Zaccarelli [129]), and they may lead to different gel properties. But they are beyond the scope of this thesis.

3.3 Suspension rheology

Suspensions under flow display a variety of rheological behaviours, such as the shear jamming in dense suspensions [130]. However, reaching a fundamental understanding on suspension rheology is challenging. The conventional 'mean-field' approach does not work. Each particle only interacts with ~ 10 neighbours, i.e. the local details matter [71]. Yet in some cases, mean-field approximation gives convincing predictions, e.g. the Wyart-Cates model [9] in shear thickening. With the knowledge of rheology and suspension physics, here we again start with hard spheres, and then consider effects from particle interactions.

3.3.1 Hard spheres

Adding solid particles to a liquid enhances the resistance to flow, as the particles distort the flow field [4]. The more particles added in, the more pronounced the resistance becomes. In the language of rheology, the suspension viscosity η increases with the volume fraction ϕ.

We first consider the simplest case: neutrally-buoyant, non-Brownian, smooth hard spheres suspended in a Newtonian fluid. Under a steady Stokes shear flow without inertial effects, there exists only one stress scale - the viscous stress $\dot{\gamma}\eta_f$. So that the relative viscosity η_r can be described by a universal relation [131]

$$\eta_r = \frac{\eta}{\eta_f} = \frac{\sigma}{\dot{\gamma}\eta_f} = f(\phi), \tag{3.20}$$

where $f(\phi) \geq f(0) = 1$.

The relative viscosity η_r linearly increases with ϕ in the dilute regime, and

grows faster and faster with the addition of more particles [4]. Simulations and experiments confirm the existence of a jamming volume fraction ϕ_J, above which no steady flow is possible [51]. With $f(0) = 1$ and $f(\phi_J) \to \infty$, an empirical equation describes the η_r-ϕ relation [132]:

$$\eta_r = f(\phi) = A\left(1 - \frac{\phi}{\phi_J}\right)^{-2}, \tag{3.21}$$

where A is a dimensionless prefactor. The value of ϕ_J highly depends on the property of particles. For monodispersed smooth hard spheres, $\phi_J = \phi_{\mathrm{rcp}} \simeq 0.64$ [133].

Inertial effects Discussion above is confined to inertialess Stokes flow. In a sheared suspension, the importance of inertia is quantified by the Stokes number St and the particle Reynolds number Re_p, defined as follow:

$$\begin{aligned} \mathrm{St} &= \frac{\rho_p \dot{\gamma} d^2}{\eta_f} \\ \mathrm{Re}_p &= \frac{\rho_f \dot{\gamma} d^2}{\eta_f}. \end{aligned} \tag{3.22}$$

Our model system is composed of silica particles ($\rho_p \lesssim 2.0\,\mathrm{g\,cm^{-3}}$ and $d \lesssim 4\,\mu\mathrm{m}$) suspended in a Newtonian solvent ($\rho_f = 1.23\,\mathrm{g\,cm^{-3}}$ and $\eta_f = 0.13\,\mathrm{Pa\,s}$). Within the range of accessible shear rate of our rheometer ($\dot{\gamma} \lesssim 10^4\ \mathrm{s^{-1}}$), $\mathrm{Re}_p \ll 1$ and $\mathrm{St} \ll 1$ always apply. In this work, therefore, we ignore inertial effects.

Brownian effects

Characterised by the timescale τ_{B}, Brownian motion always tends to drive the suspension's structure to an isotropic equilibrium state. Shearing a Brownian suspension would distort the structure and thus generate an internal stress resisting the flow [34]. The competition between imposed shear and Brownian diffusion can be characterised by the ratio of two time scales:

$$\mathrm{Pe} = \frac{\tau_{\mathrm{B}}}{1/\dot{\gamma}} = \frac{3\pi\eta_f \dot{\gamma} d^3}{4k_B T}, \tag{3.23}$$

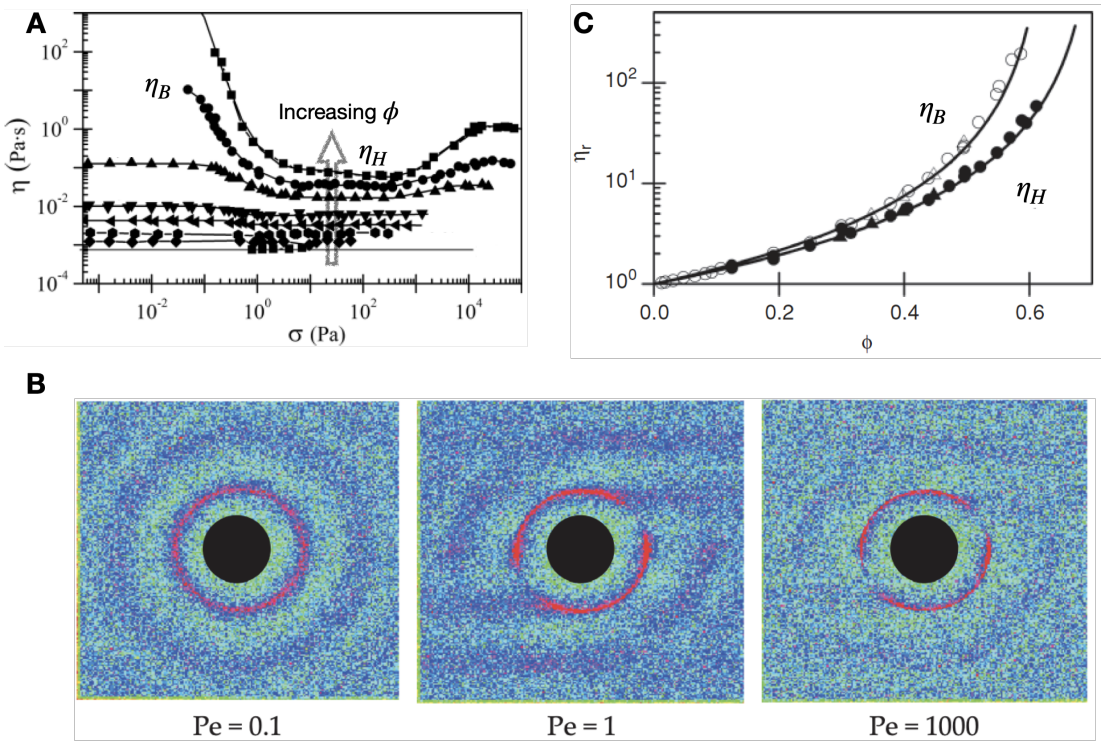

Figure 3.11 A: Viscosity η as a function of shear stress σ in colloidal latex suspensions. Adapted from [134]. B: Low shear and high shear viscosities of colloidal silica suspensions as functions of volume fraction. Taken from [4]. C: Pair distributions at different Pe. Taken from [34].

known as Peclét number. By analogy, this can also be reported in terms of a dimensionless stress [135]:

$$\hat{\sigma} = \frac{\sigma}{\sigma_{\mathrm{B}}} = \frac{\sigma}{k_B T/d^3}. \tag{3.24}$$

Both Pe and $\hat{\sigma}$ represent the importance of shear flow relative to Brownian effect.

In the presence of another stress scale σ_{B}, Brownian suspensions shear thin [134] as shown in Figure 3.11A. At low shear (Pe $\ll$ 1) where Brownian effect dominates, the microstructure is maintained in a quasi-equilibrium state and the system exhibits a strong resistance to flow, namely high viscosity η_{B}. As Pe increases, the isotropic structure is progressively distorted and the suspension shears thins until reaching a lower viscosity η_{H} at Pe $\gg$ 1 [34]. Figure 3.11B shows the pair distribution under different Pe.

The two viscosity plateau, $\eta_{\mathrm{B}}(\phi)$ and $\eta_{\mathrm{H}}(\phi)$, follow the form of Eq. 3.21 with different ϕ_J, Figure 3.11C. In principle, the low-shear viscosity η_{B} diverges at

$\phi_g \simeq 0.58$. This makes sense as colloidal glass with finite yield stress is formed above ϕ_g. By contrast, the high-shear viscosity η_H diverges at approximately random close packing $\phi_{rcp} \simeq 0.64$. In practice, however, the jamming volume fractions ϕ_J for η_B and η_H are sensitive to particle details and fitting method. They may scatter around ϕ_g and ϕ_{rcp} with high uncertainties [10, 135].

3.3.2 Repulsive hard-particles: shear thickening

Shear thickening has been widely observed in dense suspensions [19, 34, 71]. With increasing shear stress, the suspension viscosity lifts from a low Newtonian plateau η_H to a higher viscosity η_F, Figure 3.12 [71]. For decades, theories such as 'hydroclusters' [19, 34] and 'order-disorder transition' [136] have been proposed. Although these explanations offer a qualitative prediction of continuous shear thickening (CST), none of them reproduces discontinuous shear thickening (DST) [13], i.e. the stress jumps suddenly to a higher (or infinite) value above a critical shear rate [138].

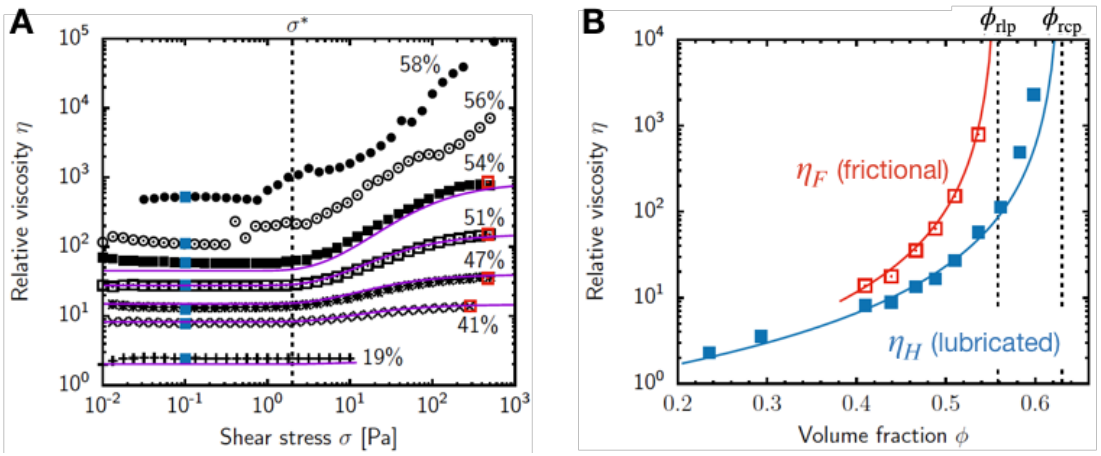

Figure 3.12 A. Flow curves reported in η_r-σ for $d = 3.77\,\mu m$ PMMA spheres in CHB-decalin mixture. The solid lines are fits to the Wyart-Cates theory. B. Two viscosity branches vary as functions of volume fraction ϕ. Both taken from [71].

Recent studies found a deep connection between dense suspension rheology and granular mechanics [139], where the role of interparticle friction in shear thickening was progressively revealed [97, 140]. In short, it is the transition from frictionless to frictional contacts that gives rise to shear thickening [95]. A

[13] An extreme example of DST is dense cornstarch-water mixture on which an adult can run [137].

phenomenological model by Wyart and Cates [9] summarised these considerations and proposed an analytic approach by making ϕ_J stress-dependent, i.e. $\phi_J = \phi_J(\sigma)$.

Shear thickening occurs in suspensions of repulsive hard-particles. Stabilising repulsions separate particles with a finite gap where lubricated contacts are maintained. In such frictionless state, $\phi_J = \phi_{\text{rcp}}$ and $\eta = \eta_H$. As the shear stress σ increases beyond an onset stress $\sigma^\star$, the thin lubricated film between particles is ruptured, giving frictional contacts. At the same time, ϕ_J drops to a lower ϕ_{rlp} with the subscript 'rlp' referring to random loose packing[14] [142]. Accordingly, the viscosity η increases to a higher η_F.

The viscosity η can be described by adapting Eq. 3.21:

$$\eta(\sigma) = A\left(1 - \frac{\phi}{\phi_J(\sigma)}\right)^{-2}, \tag{3.25}$$

where $\phi_J(0) = \phi_{\text{rcp}}$ (corresponding to the lubricated state η_H) and $\phi_J(\infty) = \phi_{\text{rlp}}$ (corresponding to the frictional state η_F). To correlate the global macroscopic quantities (σ and ϕ_J) with the local microscopic friction, the Wyart-Cates model uses the fraction of frictional contacts in total contacts f.

As σ increases above $\sigma^\star$, the value of f gradually increases from 0 to 1. A common exponential form is used in [71] to characterise the transition:

$$f(\sigma) = e^{-(\sigma^\star/\sigma)^\beta}, \tag{3.26}$$

where $\beta \leq 1$ is the stretch exponent. Based on the values of ϕ_J at different states, the Wyart-Cates theory assumes ϕ_J as a linear function of f:

$$\phi_J(f) = f \cdot \phi_{\text{rlp}} + (1 - f) \cdot \phi_{\text{rcp}}. \tag{3.27}$$

A recent study probed ϕ_J at a microscopic level by introducing sliding constraint and correlating it with isostaticity [11, 143]. The combination of Eq. 3.25, 3.26 and 3.27 provides a robust fitting for both CST and DST.

Shear thickening, desirable in some cases (e.g. shock absorber) whereas unwanted in others (e.g. pipe clogging) [34], results from interparticle contacts. Hence controlling the contacts holds the key to tunable shear thickening. Externally,

[14] Dependent on the friction coefficient μ, the value of ϕ_{rlp} varies from approximately 56 % ($\mu \to \infty$) to $\phi_{\text{rcp}} \approx 64\,\%$ ($\mu = 0$) [141].

an orthogonal vibration can relax frictional contacts and thereby lessen shear thickening [144]. Besides, tuning the intrinsic onset stress $\sigma^\star$ is also an effective way. The physics of $\sigma^\star$ arises from the interparticle repulsion. To rupture the lubricated film between particles, a repulsive barrier $F^\star$ with force units has to be overcome first. In this way, a critical stress scale $F^\star d^{-2}$ can be defined and correlated with the onset stress as:

$$\sigma^\star \sim F^\star d^{-2}. \tag{3.28}$$

The d^{-2} dependence of $\sigma^\star$ has been verified in [71] and this work. In addition, surface roughness has also been revealed to play a vital role in shear thickening [145, 146].

Thinning? Thickening?

Arising from different mechanisms, shear thinning (Brownian effect) and shear thickening (contact mechanics) are supposed to coexist in repulsive systems. However, colloidal suspensions mostly exhibit only shear thinning [147] and granular suspensions exhibit only shear thickening [71, 148, 149]. The coexistence of shear thinning and thickening is mostly observed in particles with intermediate size ($0.5\,\mu\text{m} \lesssim d \lesssim 5\,\mu\text{m}$) [19, 34, 71].

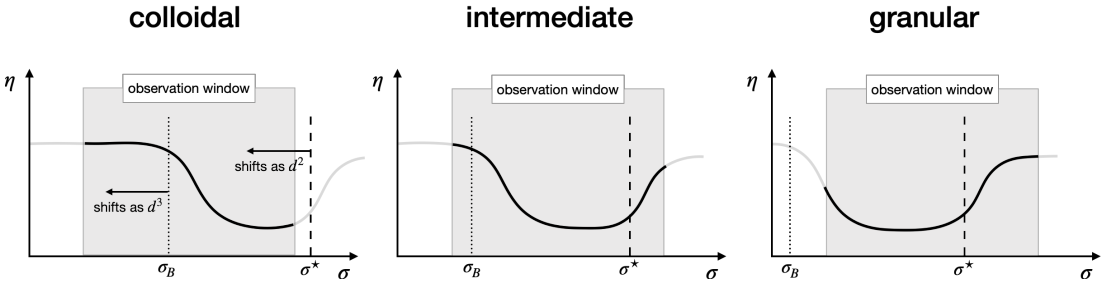

Figure 3.13 Sketches of observable flow curves in different size regimes. Adapted from [71].

This results from the different size scaling in thinning onset $\sigma_B \sim k_B T d^{-3}$ and thickening onset $\sigma^\star \sim F^\star d^{-2}$. With increasing d, the two onsets shift to smaller values at different rates. Given the range of accessible shear stress in rheometers is fixed (typically $10^{-2} \sim 10^4$ Pa), schematic flow curves in different size regimes are shown in Figure 3.13. For colloidal suspensions, the thickening onset $\sigma^\star$ is usually beyond the maximum stress and thus not shown. As d increases to the intermediate range, the two onsets are both in the observation window until the

thinning onset σ_B falls below the rheometer resolution, i.e. only shear thickening is presented [71].

3.3.3 Colloidal gel rheology

Apart from dynamical arrest at quiescence, interparticle attraction also has a significant effect on suspension rheology. With proper concentration ϕ and attraction strength U_{att}, particles tend to aggregate together and form a ramified network which can carry stresses and thereby reacts as a soft solid, i.e. the colloidal gel. Because of the disparate interactions and microstructure, the rheology of gel differs a lot from that of repulsive suspensions.

Linear viscoelasticity

Colloidal gels are viscoelastic materials. The spanning network gives rise to an elastic, solid-like behaviour, whereas the finite bond strength, as well as the liquid component, offers a viscous response. At sufficiently small strains γ (i.e. in the linear regime), the simultaneous stress σ is proportional to γ and thus leads to constant moduli. Such response, occurring prior to yielding, is known as linear viscoelasticity.

In oscillatory rheology, the elastic modulus G' and viscous modulus G'' are two important measures of linear viscoelasticity . The two moduli, especially G', depend on system parameters, such as the volume fraction ϕ which determines the strength of gel network. The more concentrated a gel is, the higher moduli it has [7, 127]. The elastic modulus G' usually increases with ϕ in a power-law manner [7]:

$$G' \sim \phi^n, \tag{3.29}$$

where the exponent n depends on system details, e.g. attraction strength U_{att}, particle size d and gelation mechanism [7, 150, 151]. Theories like MCT can offer *a priori* prediction on modulus scaling [152, 153].

For a colloidal gel, G' and G'' barely vary with the oscillatory strain amplitude γ at small strain amplitudes; yet they do depend on the frequency ω. The frequency dependence is significant around the gelation boundary ϕ_{gel}: the two moduli increase with ω roughly as a power law. As ϕ increases, the relaxation becomes slower so that less dependence is shown within the accessible ω range

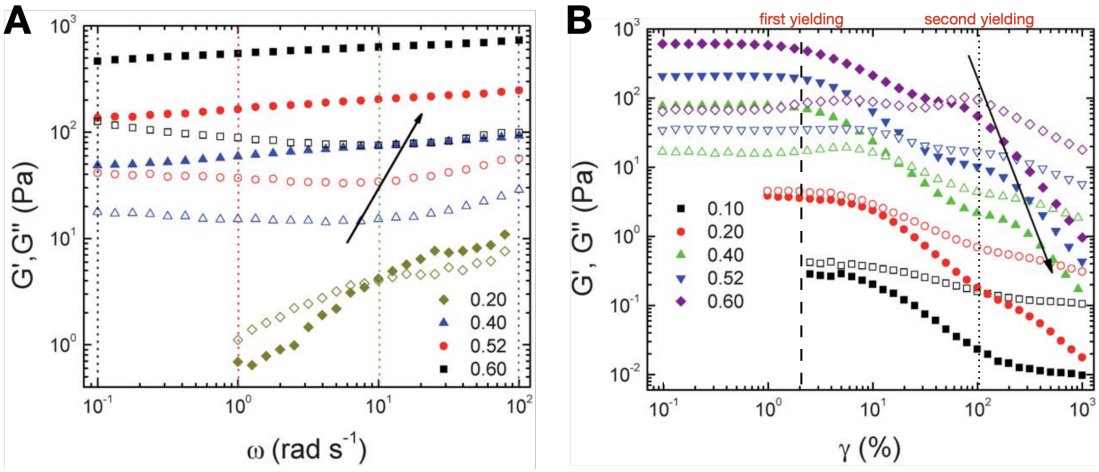

Figure 3.14 Oscillatory rheology of colloidal (depletion) gels at different concentrations, with the elastic modulus G' as solid symbols and the viscous modulus G'' as open symbols. Adapted from [7]. A. Dynamic frequency sweep at $\gamma = 0.1\,\%$. The arrow indicates the minimum of G''. B. Dynamic strain sweep at $\omega = 10\,\mathrm{rad\,s^{-1}}$. The dashed and dotted lines indicate the first and second yielding respectively.

in experiments[15]. Figure 3.14A exhibits frequency sweep results in depletion gels. A generic broad minimum in $G''(\omega)$ is commonly observed at different concentrations, suggesting a characteristic relaxation time scale [154].

Yielding behaviour

As the oscillation strain γ increases, the deformation becomes non-affine at the microscopic level and the responding stress is no longer sinusoidal. In such a nonlinear regime, the elastic modulus G' drastically decreases with γ until falling below the viscous modulus G'', Figure 3.14B. This behaviour suggests a solid-to-liquid transition and is known as yielding. Apart from the moduli crossover, another yielding signature is the peak in $G''(\gamma)$, which results from the decrease of structural relaxation time at large γ [154].

The concept of yielding may include several steps. Two steps of yielding are commonly observed in colloidal gels [7, 155], and Figure 3.14B shows strain sweep results with two-step yielding. In most cases, the first yielding event demarcates the linear and nonlinear regimes and thereby corresponds to the macroscopic solid-to-liquid transition. At a microscopic level, this is attributed to

[15] Typically 10^{-2} to 10^{3} $\mathrm{rad\,s^{-1}}$.

the breakdown of inter-cluster bonds [7]. By contrast, manifested by the 'modulus bulge' as well as the second peak in $G''(\gamma)$ at large γ, the second yielding involves the breakage of gel clusters [7].

In steady state rheology, a colloidal gel yields and flows when sheared beyond its yield stress σ_y. As another measure of mechanical strength, the yield stress σ_y also depends on factors such as volume fraction ϕ, particle size d and attraction strength U_{att}. If view yielding as a result of bond breakage, then σ_y should be positively correlated to the product of bonding force and bond density. In this way, stronger attractions, higher concentrations and smaller particles all lead to stronger gels.

In colloidal gels, the relation between yield stress σ_y and volume fraction ϕ has been extensively studied [7, 21, 153]. However, due to the non-equilibrium nature of gel, an *apriori* prediction on σ_y is difficult. Generally, σ_y scales with ϕ in a power-law manner:

$$\sigma_y \sim \sigma_0 \phi^{\nu}, \tag{3.30}$$

where σ_0 is a prefactor with stress units. The magnitude of σ_0 may offer an empirical estimation of attraction potential depth U_{att}. Similar to the treatment on the thickening onset stress $\sigma^{\star}$, the stress scale σ_0 may be correlated with the attractive force F_{att} as follow:

$$\sigma_0 \sim \frac{F_{\text{att}}}{d^2} \sim \frac{U_{\text{att}}}{\xi d^2}, \tag{3.31}$$

where ξ is the attraction range and d the particle size.

Gels under flow

Upon yielding, gels shear thin under steady shear flow. As shear rate $\dot{\gamma}$ (or stress σ) increases, the viscosity η decreases as a result of cluster breakage. The steady flow curve can be empirically described by the Herschel-Bulkley equation:

$$\sigma = \sigma_y + k\dot{\gamma}^n \tag{3.32}$$

where σ_y is the yield stress, k and n the fitting parameters. This expression indicates that flow (non-zero shear rate) is only possible above σ_y.

The rate-dependent rheology arises from the rate-dependent structure. With the

development of experimental techniques and simulation methods, gel structure under flow has been widely studied [21, 46, 156, 157]. On one hand, shear flow accelerates the aggregation of attractive particles by providing an extra diffusion, known as orthokinetic aggregation [158]. On the other hand, external shear peels aggregates apart and may completely redisperse the particles at sufficiently high shear. With the existence of interparticle attraction and Brownian diffusion, the structural behaviour of gel under flow is complicated. Generally, the higher the shear rate is, the smaller the clusters are.

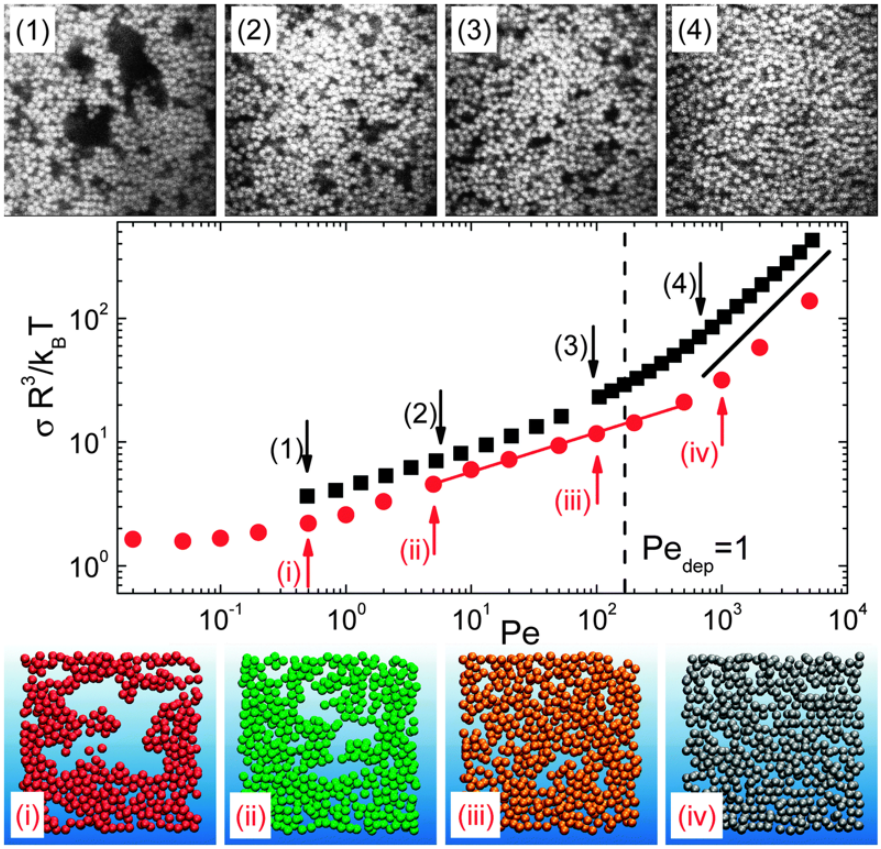

Figure 3.15 Gel rheology and gel structure at different shear rates [21]. Top panel: confocal snapshots of a depletion gel ($\phi = 44\,\%$) under different shears. Middle panel: flow curves from experiment (black) and MD simulation (red). Bottom panel: simulated gel ($\phi = 44\,\%$) under different Pe.

The impact from shear even still manifests upon flow cessation. Shear with high rates can fully breakdown the structure, so that after shear cessation, a more homogeneous and stronger gel can be formed. By contrast, a lower shear rate gives rise to a relatively heterogeneous network with large voids [21, 159]. That is, the re-gelled structure depends on the flow history and cannot be achieved by simple thermal quenching.

For colloidal gel under shear, a minimal consideration involves three factors (reporting in force scales): Brownian motion ($\sim k_BT/d$), viscous drag ($\sim 6\pi\eta_f d^2\dot{\gamma}$) and interparticle attraction ($\sim U_{\text{att}}/\xi$). Similar to the Peclét number Pe, the relative importance of each factor can be represented by the ratio of one to another. For example, the competition between attraction and shear force is quantified by a dimensionless Mason number Mn:

$$\text{Mn} = \frac{F_{\text{shear}}}{F_{\text{attraction}}} = \frac{6\pi\eta_f d^2\dot{\gamma}}{U_{\text{att}}/\xi}. \tag{3.33}$$

This is also referred to as the depletion Péclet number in [21]. Similarly, U_{att}/k_BT measures the importance of attraction to Brownian motion.

Here we consider strong attraction, i.e. $U_{\text{att}} \gg k_BT$. When shear force dominates ($\text{Mn} \gg 1$), most bonds are ruptured and the structure is rejuvenated. After shear stops, the post-shear gelation starts from a suspension of well-dispersed particles and ends up with a homogeneous gel network. As shear decreases until it is comparable to the attraction ($\text{Mn} \sim 1$), particles are allowed to explore possible configurations to a certain extent without breaking most bonds. This gives compact clusters which rearrange into heterogeneous gel network upon flow cessation. Figure 3.15 shows the gel structure induced by different shear rates in experiment (top panel) and simulation (bottom panel). And a recent study interpret such behaviour as a release from dynamical arrest [156]. Yet so far, there is a lack of unified description on shear-induced structure in colloidal gels.

Clearing history before measurement Given the rate-dependent structure, it is not difficult to see that the measurement of gel rheology is sensitive to the flow history. Hence to ensure valid measurement, specific precautions should be taken prior to the experiment. A popular treatment to clear history effect [16] is rejuvenation. By imposing a high-rate preshear, we enable a gel to be formed from a random configuration. The gelation process can be monitored by the evolution of the elastic modulus G'. When G' increases to a (quasi-)steady state, an intact colloidal gel is then formed.

In this chapter, we have reviewed the fundamental physics of suspensions. Based on the interparticle force, we classify suspensions into two categories and respectively discuss their quiescent phase behaviours (including dynamical arrest)

[16] From loading or previous measurements.

and rheology. While there is considerable progress in describing single-component suspensions as reviewed, the understanding on multi-component suspensions remains far less developed. In this work, we focus on a generic composite consisting of large grains suspended in a colloidal gel. In the next chapter, we will establish the model system for such class and characterise each component.

Chapter 4

Establishing a model binary suspension

This work is concerned with the rheology of binary suspensions containing large repulsive grains suspended in a viscoelastic gel of smaller attractive colloids. Such binary system is of specific interest as it occurs widely in industrial suspensions, such as fresh concrete [17, 160], battery slurries [16, 161] and toothpastes [162]. For efficient and effective processing, it is vital to understand how they flow. Despite their ubiquity, there are few studies on suspension of particles disparate in both size and interaction. While many well-established model systems (such as sterically-stabilised PMMA particles) have been used to study size bidispersity [15], it is challenging to achieve different kinds of interparticle forces in one system.

In this chapter, we establish an index-matched model system composed of **small attractive particles** and **large repulsive particles**. We chose silica (SiO_2) spheres for both species. Widely used as model particles in suspensions [10, 163], these have key advantages as follow: (i). they are easy to synthesise (good reproducibility) or purchase (relatively cheap) in bulk quantities [164]; (ii). the refractive index can be matched in a variety of solvent mixtures [165]; (iii). the well-established chemistry enables fluorescent labelling and surface functionalisation [93, 165].

Here we used two batches of silica particles to establish our model binary suspension. The two batches differ in size and surface wetting: the larger particles are non-Brownian and hydrophilic, whereas the smaller ones are colloidal and hydrophobic. Using a mixture of ethanol, water and glycerol

as suspending solvent, the hydrophobic small silica attract each other via hydrophobic interaction, whereas the large silica are charge stabilised. To enable confocal microscopy, small particles and solvent were labelled by different dyes, and the refractive index was roughly matched. We start with synthesising and characterising each species of particles, and then detail the preparation of binary samples and characterise the inter-species interactions in a composite suspension.

4.1 Small attractive particles (S)

4.1.1 Silica chemistry

Synthesis

Our small silica colloids were synthesised in house and hydrophobically functionalised to induce attraction. We followed the Stöber process [166], where the synthesis is accomplished via hydrolysis and condensation of tetraethoxysilane (TEOS). Under the catalysis of ammonia, TEOS molecules are hydrolysed and subsequently condensed in ethanol-water solution to build larger compounds. As the reaction proceeds, these compounds grow and crosslink until they come out of the solution as solid particles. Figure 4.1A shows a schematic representation of synthesis.

To enable confocal microscopy, silica particles are usually labelled with fluorescent dyes during synthesis. Here we use rhodamine B isothiocyanate (RBITC). Specifically, RBITC and the coupling agent (3-aminopropyl)triethoxysilane (APS) are mixed in advance for full coupling [165]. We then transfer the coupled dye (APS-RBITC) to the reaction solution, so that RBITC can be covalently attached to the particles during synthesis, Figure 4.1A.

The particle property highly depends on the surface chemistry. Figure 4.1B displays possible surface groups on RBITC-labelled stöber silica. Siloxane groups are the majority ($\sim 60\,\%$ of total surface groups), whereas silanol and ethoxy groups take up $\sim 20\,\%$ each [93, 168]. Aminopropyl group results from the coupling agent APS. Note that the proportion of each group, as well as the surface chemistry, is sensitive to reaction conditions and could vary from batch to batch [164].

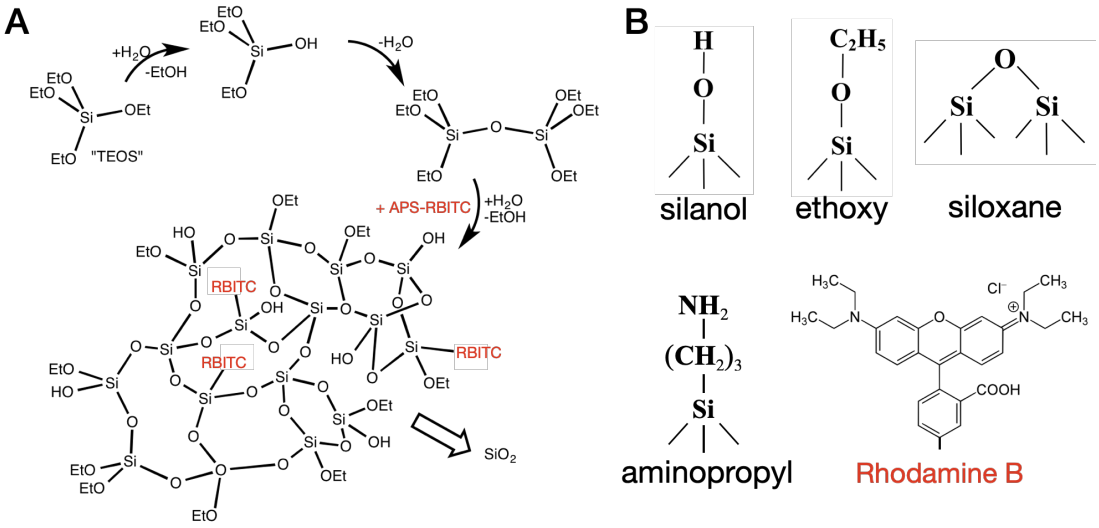

Figure 4.1 A. A simplified representation of RBITC-labelled stöber silica synthesis. Et denotes ethyl group ($-CH_2CH_3$). Adapted from Wikipedia [167]. B. Possible surface groups on RBITC-labelled stöber silica. Part adapted from [93].

When immersed in a polar solvent, the silanol groups on silica particles disassociate and present negative surface charge. Silica particles can thus be stabilised via electrostatic interaction. Though aminopropyl groups produce positive charge, they are relatively rare so that the net charge on particle surface is still negative. This can be verified by ζ-potential measurement. Suspended in water-glycerol mixture (1: 1 by mass) with 1 mM sodium chloride (NaCl), our RBITC-labelled silica colloids have a ζ-potential of $-80\,\mathrm{mV}$ (measured by Malvern Nano-ZS ZEN2600 Zetasizer), which is sufficient for stability [169].

Functionalisation

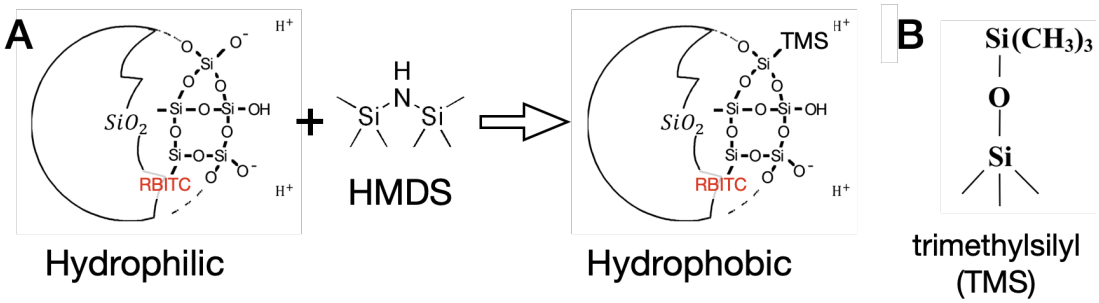

Figure 4.2 A. Schematic HMDS functionalisation. After functionalisation, a fraction of hydrophilic silanol groups are replaced by hydrophobic TMS groups. B. Tri-methylsilyl (TMS) group.

Besides providing surface charge, reactive silanol group also enables modification on the surface chemistry. The basic idea is to replace silanol groups with other groups with desired property. Such treatment is referred to as functionalisation [93]. In this work, we made silica colloids hydrophobic by coating trimethylsilyl (TMS) groups ($-Si(CH_3)_3$, Fig. 4.2B) on the silanol sites. Figure 4.2A shows a schematic functionalisation process.

The functionalisation is based in ethanol solution and accomplished by hexamethyl disilazane (HMDS). Mixing HMDS, silica colloids, ethanol and ammonia solution[1] at a certain ratio, three main reactions occur during the functionalisation [93]:

$$\begin{aligned}
(CH_3)_3Si{-}NH{-}Si(CH_3)_3 + 2\,EtOH &\longrightarrow 2\,EtO{-}Si(CH_3)_3 + NH_3 \\
(CH_3)_3Si{-}NH{-}Si(CH_3)_3 + 2\,{\equiv}Si{-}OH &\longrightarrow 2\,{\equiv}Si{-}O{-}Si(CH_3)_3 + NH_3 \\
(CH_3)_3Si{-}OEt + {\equiv}Si{-}OH &\longrightarrow {\equiv}Si{-}O{-}Si(CH_3)_3 + EtOH.
\end{aligned}$$

After reaction, a fraction of hydrophilic silanol groups are replaced by hydrophobic TMS groups. The functionalised particles thereby become hydrophobic.

The consequent hydrophobicity is important as it directly determines particle interaction. The degree of hydrophobicity depends on factors such as the original surface chemistry, the amounts of reactants and particle surface area. Unfortunately, since we can neither precisely control the property of synthesised silica nor quantitatively characterise the surface chemistry, it is almost impossible to reproduce identical hydrophobicity in different batches even if using the same recipe [164]. We therefore scaled up particle synthesis and functionalisation to prepare a big batch of RBITC-labelled silica colloids with consistent hydrophobicity. See below for detailed procedure.

4.1.2 Materials and methods

Synthesis of hydrophobic silica

Three portions of coupled dye were prepared in advance: 825.9 mg APS and 500 mg RBITC were added to 10 mL ethanol in lightproof glass vials, mixed by magnetic stirrer for 24 h.

[1] Ammonia prompts silanol disassociation to catalyse the reaction [170].

For silica synthesis, 4140 mL ethanol, 135 mL distilled water and 336 mL 35 % ammonia solution were mixed together in a 5 L glass bottle, followed by 183 mL TEOS and prepared dyes. The solution was then briefly shaken well and placed at rest overnight. After separating out of the solution, silica particles were transferred in ethanol by ten rounds of washing[2] at volume fraction $\phi \approx 2\,\%$.

For silica functionalisation, particles were added in ethanol-ammonia solution followed by HMDS, with the mass ratio of silica: ethanol: HMDS: ammonia (35 % solution) being 1: 40: 3: 7. The functionalisation proceeded with magnetic stirring for 24 h in the dark. Afterwards, particles were again repeatedly washed by ethanol. After the final wash, the supernatant was removed and the sediment particles were dried at temperature $T = 120\,^{\circ}\mathrm{C}$ for 2 h. The final product was sealed in a dry form and stored in a desiccator.

Ethanol and 35 % ammonium hydroxide solution were from Fisher Scientific (reagent grade); distilled water was taken from a laboratory distillation system; TEOS, RBITC, APS and HMDS were from Sigma Aldrich (reagent grade). All chemicals were used as purchased.

Basic characterisation

Particles Size, density and refractive index are basic particle properties. Here we measured the diameter of **S**mall attractive particles d_S by dynamic light scattering (DLS). Our DLS apparatus consists of a laser, a sample holder, a detector fixed at 90° angle and a correlator. Auto-correlation on the signal intensity characterises a decay time scale which measures the Brownian motion of colloids. Through the relation between intermediate scattering function and auto-correlation function, we quantitatively determined the small particle size $d_S = 482\,\mathrm{nm}$. This value is visually consistent with the image from scanning electron microscopy (SEM), see Figure 6.13 from Chapter 6.

We also determined the particle density $\rho_S = 2.07\,\mathrm{g\,cm^{-3}}$, with the specific measurement discussed in Sec. 4.1.2. The particle refractive index $n_S \approx 1.42$ was estimated by suspending particles in a series of water-glycerol mixtures with different indices n_f. In the suspension with the greatest clarity (judged by eye), the refractive indices n_f and n_S are considered matched, i.e. $n_S \approx n_f$. The

[2] A series of procedures to replace the original solvent, including centrifuge, supernatant removal, new solvent addition and redispersal.

solvent index n_f was measured by an Abbe refractometer at room temperature.

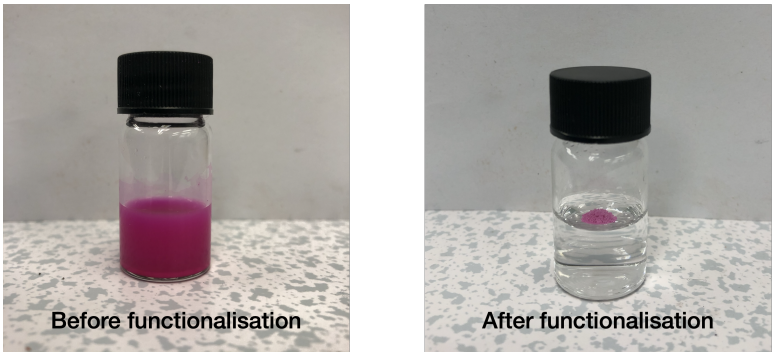

Figure 4.3 Demonstration of hydrophobicity after functionalisation. Here we used water as the suspending solvent.

We simply examined the hydrophobicity by suspending particles in water. Before functionalisation, silica particles are hydrophilic and can be well dispersed, Figure 4.3 (left). By contrast, attempts at mixing functionalised silica with water would only produce clumps at the water-air interface, Figure 4.3 (right).

Solvent In our model system, we used the mixture of ethanol, water and glycerol as the suspending solvent. The binary water-glycerol mixture can induce hydrophobic attractions and roughly match the refractive index. In addition, we use a small amount of ethanol to wet hydrophobic silica before dispersal. This facilitates the mixing of dry hydrophobic particles and aqueous solvent.

Specifically, particles are suspended in the ethanol-water-glycerol mixture with mass ratio 1: 1: 9. The solvent was labelled by $\sim$ 1mM fluorescein (sodium salt, from Sigma Aldrich) and preadjusted with sodium hydroxide (reagent grade, from Fisher Scientific) to pH = 9.0. At $T = 20\,^{\circ}\mathrm{C}$, the solvent viscosity $\eta_f = 0.13\,\mathrm{Pa\,s}$ was measured by rheometer using a 50 cm diameter cone-plate geometry, while the solvent density $\rho_f = 1.23\,\mathrm{g\,cm^{-3}}$ was determined by Anton Paar DMA 4500 density meter. The solvent refractive index $n_f = 1.444$ was from an Abbe refractometer.

Sample preparation

Figure 4.4 shows how to prepare a suspension of small hydrophobic silica. To start with, hydrophobic dry silica of weight m_S was wetted by ethanol of weight m_e. We then added water-glycerol mixture (1: 9 by mass) of weight m_{wg} to the

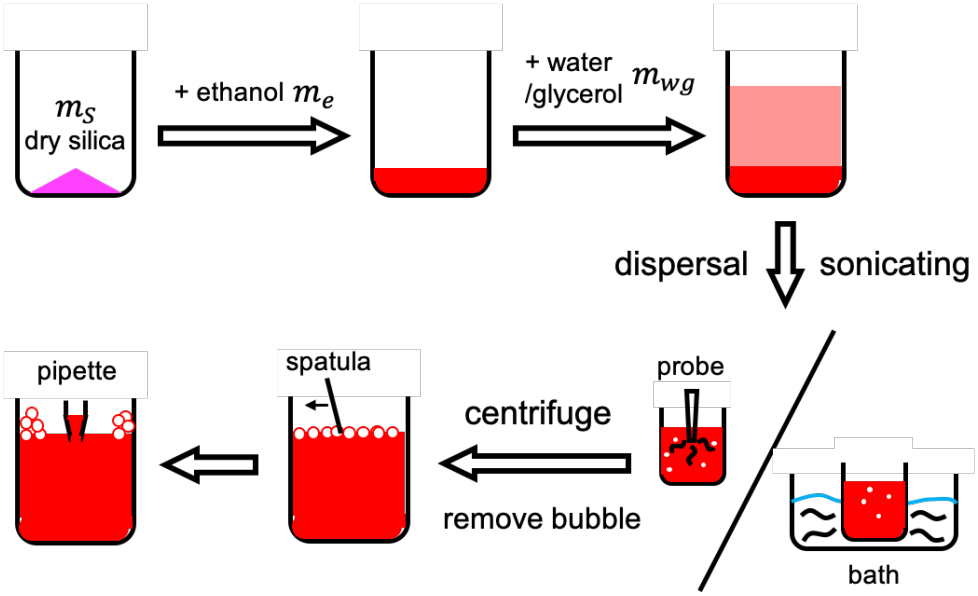

Figure 4.4 Schematic sample preparation of suspensions of hydrophobic small silica.

wetted particles. Note that $m_{wg} = 10m_e$ always applies to ensure a consistent solvent composition (ethanol: water: glycerol = 1: 1: 9 by mass).

The mixture was then sonicated by probe and bath in turn until there exists no visible aggregates. This sonication step may introduce particle-stabilised air bubbles, which are undesired. To remove these bubbles, the sample was quickly centrifuged for 10 s at 330 × g and then briefly sonicated in bath to re-disperse possible sediment. Remaining bubbles on the suspension-air interface could be manually removed by using a spatula to push them to the vial wall. The bubble-free sample was then transferred by pipette. Such bubble removal was confirmed effective by confocal imaging.

Determining particle density ρ_S and volume fraction ϕ Particle concentration is an important parameter in suspensions. From the sample preparation described above, we can determine the weight fraction of small particles ϕ_{wt} as follow:

$$\phi_{\mathrm{wt}} = \frac{m_S}{m_S + m_e + m_{wg}} = \frac{m_S}{m_S + 11m_e}. \tag{4.1}$$

To convert weight fraction ϕ_{wt} to volume fraction ϕ, particle density ρ_S is required.

We determined the particle density ρ_S through the relation between suspension density ρ_{sus} and weight fraction ϕ_{wt}. The suspension density ρ_{sus} can be directly

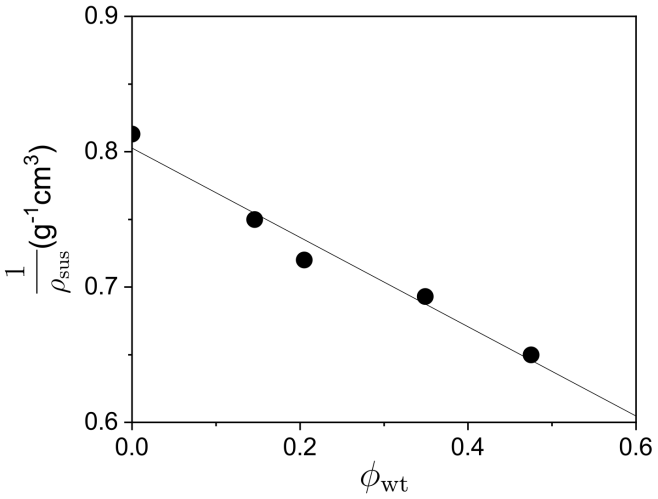

Figure 4.5 The inverse of suspension density $1/\rho_{\rm sus}$ versus the weight fraction $\phi_{\rm wt}$. Here we include four suspension samples and a solvent sample ($\phi_{\rm wt} = 0$). The error bars are smaller than the size of symbols in all cases. The solid line is linear fit, giving the slope of $-0.33\,\rm g^{-1}\,cm^3$ and the intercept of $0.803\,\rm g^{-1}\,cm^3$.

measured by density meter. Alternatively, we can express it in the form of:

$$\rho_{\rm sus} = \frac{m_{\rm sus}}{V_{\rm sus}} = \frac{m_{\rm sus}}{V_{\rm S} + V_f} = \frac{m_{\rm sus}}{\frac{m_{\rm sus}\phi_{\rm wt}}{\rho_S} + \frac{m_{\rm sus}(1-\phi_{\rm wt})}{\rho_f}} = \frac{1}{\frac{\phi_{\rm wt}}{\rho_S} + \frac{1-\phi_{\rm wt}}{\rho_f}}, \tag{4.2}$$

where $m_{\rm sus}$ and $V_{\rm sus}$ are the mass and volume of suspension, V_S and V_f are the volumes of small particles and solvent. This expression (Eq. 4.2) implies a linear relation between $1/\rho_{\rm sus}$ and $\phi_{\rm wt}$ as follow:

$$\frac{1}{\rho_{\rm sus}} = \left(\frac{1}{\rho_S} - \frac{1}{\rho_f}\right)\phi_{\rm wt} + \frac{1}{\rho_f}. \tag{4.3}$$

To determine the particle density ρ_S, we prepared four suspension samples with the weight fractions $\phi_{\rm wt}$ ranging from 0.15 to 0.5, as well a solvent sample where $\phi_{\rm wt} = 0$. We measured their densities $\rho_{\rm sus}$ respectively, and plotted the inverse of density $1/\rho_{\rm sus}$ versus $\phi_{\rm wt}$ in Figure 4.5, which roughly exhibits a linear relationship as expected by Eq. 4.3. The linear fitting result (solid line) goes as follow:

$$\frac{1}{\rho_{\rm sus}} = (-0.33 \pm 0.03)\ \rm g^{-1}\,cm^3 \cdot \phi_{\rm wt} + (0.803 \pm 0.009)\ \rm g^{-1}\,cm^3. \tag{4.4}$$

We thus determined the particle density $\rho_S = 2.07 \pm 0.02 \rm g\,cm^{-3}$.

The measured density is comparable to that of stöber silica without dye yet a

little bit higher than that of fluorescent silica [171]. This may result from the error in the suspension density ρ_{sus}, which is not included in the measurement uncertainty. When measuring ρ_{sus}, we loaded suspension samples to a density meter via a 10 mL syringe. This extrusion process may cause particle migration [172, 173] and give rise to a deviation in the suspension concentration and thereby in ρ_{sus}. However, it is difficult to quantify such effect in practice. Given that the number of silicon atoms attached with APS is small compared to the total number of silicon atoms [171], our measured density is actually acceptable. Hence we still used $\rho_S = 2.07\,\text{g}\,\text{cm}^{-3}$ throughout this work.

Given the particle density $\rho_S = 2.07\,\text{g}\,\text{cm}^{-3}$ and solvent density $\rho_f = 1.23\,\text{g}\,\text{cm}^{-3}$, weight fraction ϕ_{wt} can be converted to volume fraction ϕ as follow:

$$\phi = \frac{\frac{\phi_{\text{wt}}}{\rho_S}}{\frac{\phi_{\text{wt}}}{\rho_S} + \frac{1-\phi_{\text{wt}}}{\rho_f}}. \tag{4.5}$$

These (Eq. 4.1 and Eq. 4.5) enable us to prepare suspension samples with designed volume fractions. The uncertainty on particle density $\Delta\rho_S = 0.02\,\text{g}\,\text{cm}^{-3}$ would propagate an error on ϕ in the form of $(\partial\phi/\partial\rho_S)\cdot\Delta\rho_S$. Yet the magnitude $\Delta\phi \lesssim 0.1\,\%$ can be viewed as neglectable.

Particles in suspension

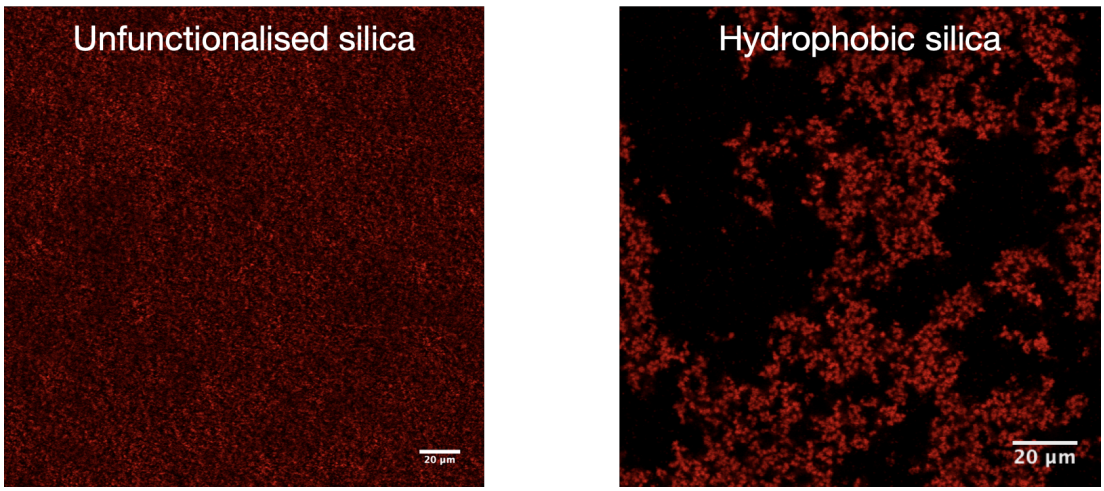

Figure 4.6 Confocal images of unfunctionalised silica (left) and hydrophobic silica (right) suspended in our solvent. The volume fraction $\phi = 10\,\%$.

Interparticle attraction We followed the above protocol to prepare a suspension of small attractive particles, which exhibits clear confocal images (Fig. 4.6). Theoretically, we can resolve our small colloids as single particles. According to the Rayleigh criterion, the resolution limit is given by [174]:

$$d_{\min} = \frac{0.61\lambda}{\mathrm{NA}}, \tag{4.6}$$

where λ is the wavelength in the medium and NA is the numerical aperture of objective. For the confocal imaging of our RBITC-labelled silica, we used a green wavelength 552 nm (so that $\lambda = 552\,\mathrm{nm}/n_f \approx 382\,\mathrm{nm}$) and an immersion 63× objective with NA = 1.4, giving $d_{\min} \approx 166\,\mathrm{nm} < d_S$. Yet in practice, due to the slightly mismatched index, it is challenging for single particles to be resolved when they are clustered, Figure 4.6 (right).

By comparing the microstructure at $\phi = 10\,\%$, we verify that our functionalisation treatment can effectively make charge-stabilised silica into attractive colloids. Specifically, while no visible aggregate was observed amongst unfunctionalised silica, the hydrophobic silica form ramified clusters, Figure 4.6. This confirms the hydrophobic attraction resulting from functionalisation.

Interparticle attraction is mainly characterised by the potential depth U_{att} and interaction range ξ. As previously mentioned (Sec. 3.1.4 in Chapter 3), hydrophobic attraction is typically strong ($U_{\mathrm{att}} \gg k_B T$) and short-ranged ($\xi \ll d_S$). However, quantitatively characterising the attraction would require precision instruments such as colloidal-probe atomic force spectroscopy [175], surface force apparatus [176] or optical tweezer [177], which are all challenging in practice.

Though depending on many factors such as the degree of hydrophobicity, the hydrophobic attraction is typically confined within $\xi \lesssim 10\,\mathrm{nm}$ [89]. Based on the dynamic strain sweep result later shown in Fig. 4.10, we estimate the range of hydrophobic attraction between our small particles $\xi \sim 1\,\mathrm{nm}$. Note that such magnitude, consistent with [89], is just for setting an order of magnitude.

We also estimate the attraction strength U_{att} using two individual methods, with one based on the separation work density and the other one based on the direct force measurement result in [90] (see details in Appendix A). Though both the methods are crude and quantitatively problematic as they rely on numerous assumptions and approximations, they consistently point to a potential depth

$U_{\text{att}} \sim 10^2 k_B T$. Such magnitude agrees with the estimate from yield stress in Sec. 4.1.3.

Sedimentation and Brownian effect Since the particle density ($\rho_S = 2.07\,\text{g}\,\text{cm}^{-3}$) is higher than the solvent density ($\rho_f = 1.23\,\text{g}\,\text{cm}^{-3}$), our small particles sediment in the suspension. Meanwhile, they diffuse via Brownian motion. As discussed in Chapter 3, the two processes (sedimentation and Brownian diffusion) are characterised by two time scales respectively:

$$\tau_{\text{sed}} = \frac{18\eta_f}{(\rho_S - \rho_f)dg} = 396.0\,\text{s} \qquad \tau_B = \frac{\pi\eta_f d^3}{2k_B T} = 6.4\,\text{s}. \tag{4.7}$$

Therefore, our small particles can be considered as colloids, where Brownian diffusion dominates over sedimentation. However, since our small particles are attractive, they form clusters larger than single particles. As the gravitational Péclet number Pe_{g} scales with d^4, the cluster sedimentation may manifest. Actually, for our small particles, $\text{Pe}_{\text{g}} = 0.016$ is slightly beyond the critical $\text{Pe}_{\text{g}} \sim 0.01$ [178]. The absence of G'' peak in dynamic strain sweep may imply the role of gravitation (see discussion in Sec. 4.1.3).

4.1.3 Suspension rheology

$\phi = 10\,\%$ gels

The hydrophobic attraction between small particles is sufficient to induce gelation at low concentrations. We verified this by a sample at volume fraction $\phi = 10\,\%$. After loaded on confocal rheometry, the sample was rejuvenated at high shear rate $\dot{\gamma}_{\text{rej}} = 1000\,\text{s}^{-1}$, and then left undisturbed for 1 h ($\sim 500\tau_{\text{B}}$). *In-situ* confocal imaging shows that the microstructure evolves from an non-flocculated, homogeneous state (Fig. 4.7A) to large ramified clusters (Fig. 4.7B) after 1 h at quiescence.

Oscillatory rheology shows that the $\phi = 10\,\%$ sample is a viscoelastic gel, Figure 4.7C. Just after rejuvenation, the elastic modulus G' (filled circles) is lower than the viscous modulus G'' (open circles). Therefore, the sample is initially a liquid, consistent with the non-flocculated structure in Figure 4.7A. While $G'' \approx 20\,\text{Pa}$ remains almost constant, G' quickly increases with time and exceeds G'' within 30 s, i.e. the elastic response starts to dominate. As the evolution proceeds,

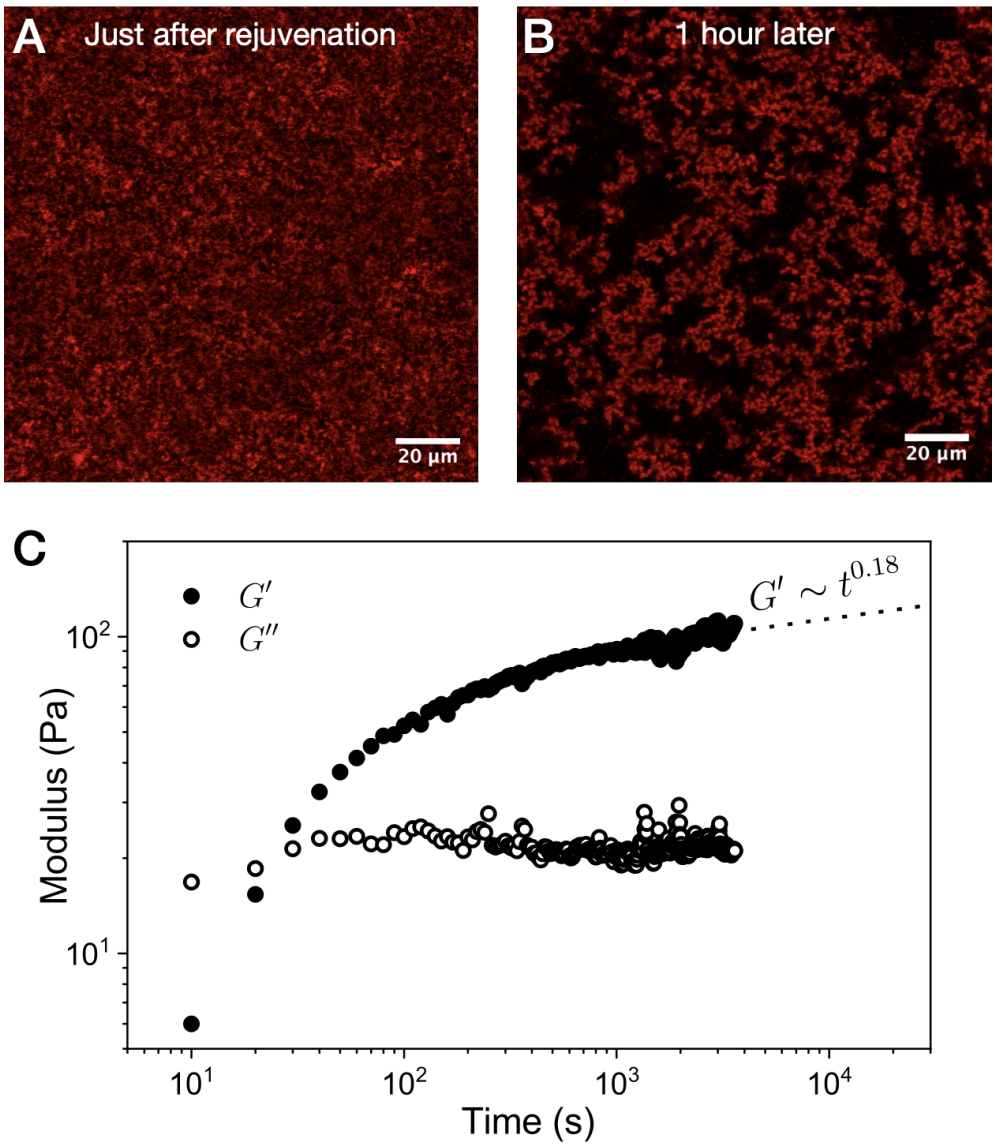

Figure 4.7 Confocal images taken at height $H = 20\,\mu\text{m}$ just after rejuvenation (A) and 1 hour later (B). Here we used the suspension of small attractive particles at $\phi = 10\,\%$. C. Evolution of dynamic modulus after rejuvenation. The elastic modulus G' (filled circles) and the viscous modulus G'' (open circles) were measured at $\omega = 10\,\text{rad}\,\text{s}^{-1}$ and $\gamma = 0.1\,\%$. Each point was measured for 10 s. We fitted the $G'(t)$ data taken after 30 min by power law, giving $G' \sim t^{0.18}$ (dotted line).

G' grows increasingly slow until reaching a quasi-steady state after 30 min. A colloidal gel is formed.

Before measurement As mentioned in Chapter 3, gel rheology depends on the flow history. To clear history (from either loading or previous experiments) and thereby obtain reproducible data, before measurement, we always impose a high shear rejuvenation at $\dot{\gamma}_{\text{rej}} = 1000\,\text{s}^{-1}$ for at least 1 min. Such treatment was chosen to ensure a well-dispersed initial state, as shown in Figure 4.7A.

To study a well-developed gel, the rejuvenated sample is then left at rest for 30 min. Compared with our experimental timescale (~ 6 h), this waiting time is not unacceptably long. Meanwhile, it ensures consistent gel property during the measurement. For the $\phi = 10\,\%$ sample, the evolution of G' becomes exceedingly slow after 30 min ($G' \sim t^{0.18}$, see the dotted line in Figure 4.7C). Such evolution becomes even slower as time goes on, giving the real exponent lower than 0.18. After waiting for 30 min, therefore, the variation in gel is almost neglectable within the experimental timescale.

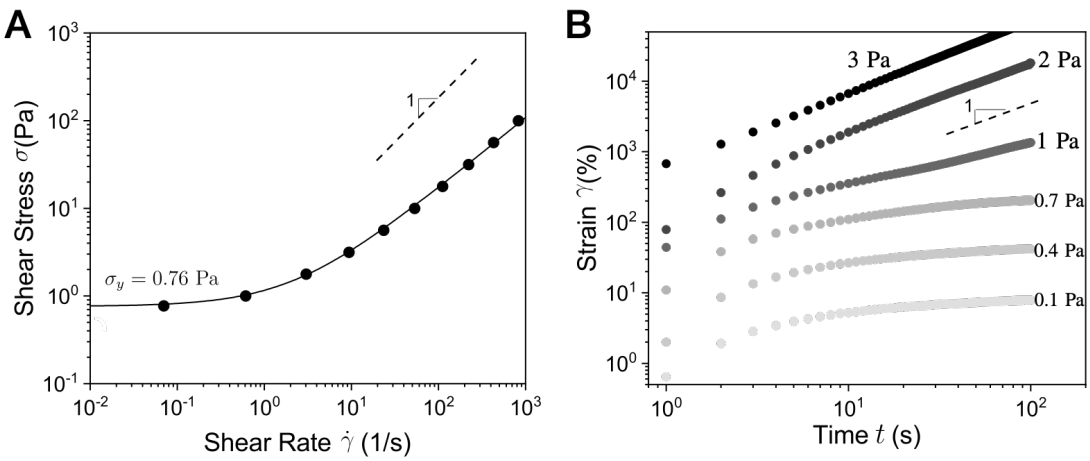

Figure 4.8 Steady shear rheology of $\phi = 10\,\%$ sample. A. σ-$\dot{\gamma}$ flow curve in log-log plot. We ramped down the shear rate $\dot{\gamma}$ and measured the shear stress σ for 5 min at each data point. The solid line is Herschel–Bulkley fit: $\sigma_y = 0.76\,\text{Pa}$, $k = 0.40\,\text{Pa}\,\text{s}^n$ and $n = 0.81$. The dashed line indicates a slope of 1. B. Strain γ versus time t for creep test performed at different stresses. After rejuvenation, we imposed shear stress σ which increases in a stepwise manner and measured the transient strain γ for 100 s. The stresses are annotated on each curve. The dashed line indicates a slope of 1.

We performed extensive rheological studies on a $\phi = 10\,\%$ gel. We start with the

steady shear flow curve, Figure 4.8A, where the shear stress σ is plotted versus the shear rate $\dot{\gamma}$. As the slope is always below one (compared with the dashed line in Fig. 4.8A), the sample constantly shears thin within the $\dot{\gamma}$ range we probed. As $\dot{\gamma}$ decreases, the stress σ appears to approach a low-shear plateau. This implies a finite yield stress σ_y, which is consistent with the fact that $G' > G''$ (Fig. 4.7C). Hershey-Buckley fit ($\sigma = \sigma_y + k\dot{\gamma}^n$) gives a specific value for the yield stress $\sigma_y = 0.76\,\mathrm{Pa}$, with other parameters $k = 0.40\,\mathrm{Pa\,s}^n$ and $n = 0.81$ (Fig. 4.8A, solid line).

We then applied a stepwise increase in the shear stress σ and monitored the evolution of strain γ, Figure 4.8B. Under small loads ($\sigma \leq 0.7\,\mathrm{Pa}$), the sample progressively stops flowing as γ reaches a plateau. Flow occurs when sheared at $\sigma = 1\,\mathrm{Pa}$, since the strain γ constantly increases over time in a power-law manner. Yet the exponent is below 1, implying a creeping gel. Under higher stresses ($\sigma \geq 1\,\mathrm{Pa}$), the exponent approaches 1 and the sample thereby flows with a steady shear rate. The creep test result indicates that our gel has a yield stress σ_y between 0.7 Pa and 2 Pa, which roughly agrees with the Herschel–Bulkley fit above ($\sigma_y = 0.76\,\mathrm{Pa}$).

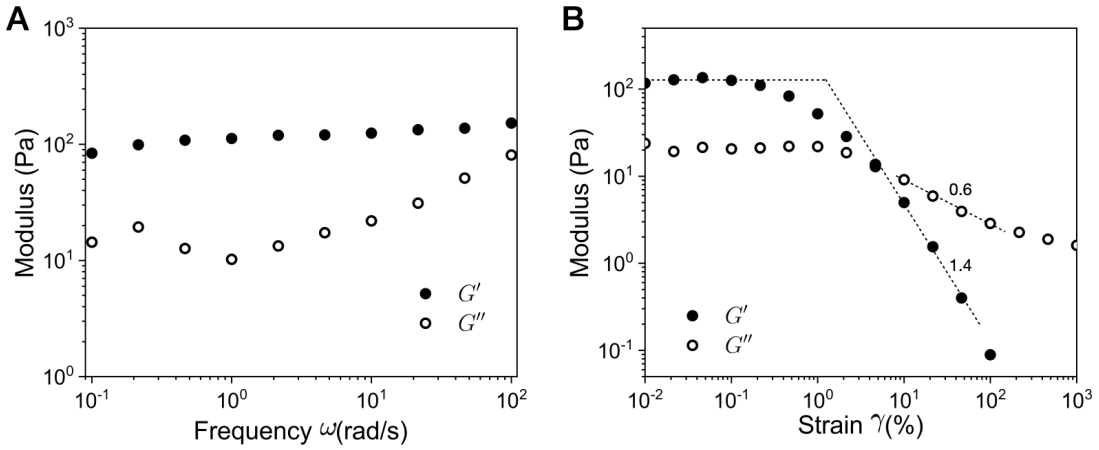

Figure 4.9 Oscillatory rheology of a $\phi = 10\,\%$ gel, where the elastic modulus G' and the viscous modulus G'' are represented by filled and open circles respectively. A. Dynamic frequency sweep at $\gamma = 0.1\,\%$. After rejuvenation and subsequent waiting, the frequency ω was ramped down and each data point was measured over $\gtrsim 10$ oscillation cycles. B. Dynamic strain sweep at $\omega = 10\,\mathrm{rad\,s}^{-1}$. The strain amplitude γ was ramped up and each data point was measured for 100 s. The dashed lines are drawn to guide the eye through the data in the linear regime at small strain and the thinning regime at large strain. The slopes of G' and G'' are annotated in the graph respectively.

Oscillatory rheology also suggests that the $\phi = 10\,\%$ sample is a yield-stress solid.

The dynamic frequency sweep in Figure 4.9A shows that, over the whole range of frequency ω that we probed, the elastic modulus G' is always higher than the viscous modulus G''. In particular, $G'(\omega)$ slightly increases with ω, whereas $G''(\omega)$ presents a broad minimum at $\omega \sim 1\,\mathrm{rad\,s^{-1}}$. These behaviours have been reported in a diverse array of colloidal gels [7, 46, 127].

In addition, we performed dynamic strain sweep at frequency $\omega = 10\,\mathrm{rad\,s^{-1}}$. The two moduli, G' and G'', are nearly constant at small strains ($\gamma \lesssim 0.1\,\%$), suggesting a linear response. As the strain amplitude γ increases, G' starts to deviate from the plateau and quickly drops. Compared with G', the decrease in G'' appears to occur from a larger strain and is less rapid. At large strains, $G' \propto \gamma^{-1.4}$ and $G'' \propto \gamma^{-0.6}$, annotated in Figure 4.9B. Similar scaling has been observed in various systems [179, 180].

As the strain γ becomes larger, G' falls below G'' at $\gamma \approx 5\,\%$, indicating a solid-to-liquid transition (i.e. yielding). By extrapolating the linear plateau at small strain and thinning behaviour at large strain, as indicated by the dashed lines in Figure 4.9B, we determine the yield point at $\gamma_y \sim 1\,\%$. The small yield strain agrees with the short-ranged hydrophobic attraction. Quantitatively, since $\gamma_y \sim \xi/d_S$ [179], we estimate the attraction range $\xi \sim 5\,\mathrm{nm}$. Around the yielding point, we did not observe the generic peak in $G''(\gamma)$ that has been reported in many soft glassy materials [7, 49, 154]. This may imply gravitational effect (see discussion in Sec. 4.1.3).

History dependence

Similar to other colloidal gels [21, 46], the rheology of our $\phi = 10\,\%$ gel is history-dependent. To demonstrate this, we designed a measuring protocol to investigate the preshear effect, Figure 4.10A. Several rounds of experiment were applied to measure the gel after different preshears. In each round, we first rejuvenated the sample at $\dot{\gamma}_{\mathrm{rej}} = 1000\,\mathrm{s^{-1}}$ for 100 s to ensure a reproducible initial state. The rejuvenated sample was then presheared at stress σ_{pre} until a constant viscosity was recorded, followed by a sudden shear cessation ($\dot{\gamma} = 0\,\mathrm{s^{-1}}$). We then waited up to 30 min at rest to obtain an intact gel after preshear.

For the gel formed after the preshear at stress σ_{pre}, we recorded its structure by *in-situ* confocal imaging and then applied non-destructive rheological measurements. Specifically, confocal imaging was performed within the depth of 70 µm from the

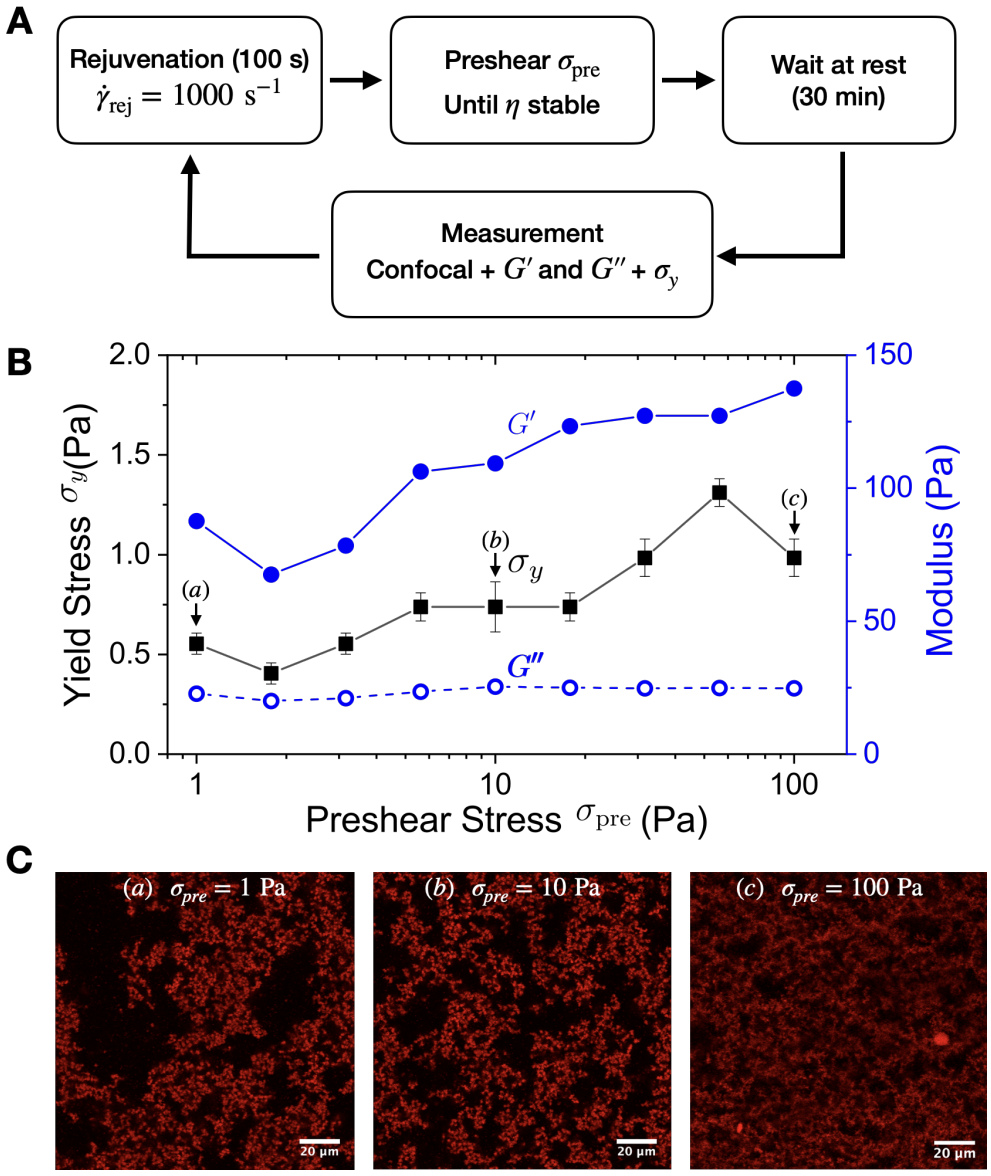

Figure 4.10 A. Measurement protocol of preshear effect. B. Preshear effect on gel rheology. The yield stress σ_y (black squares) and dynamic modulus (the elastic component G' – blue filled circles; the viscous component G'' – blue open circles) vary as functions of preshear stress σ_{pre}. The yield stress was measured by creep test, while the two moduli were measured at $\gamma = 0.1\,\%$ and $\omega = 10\,\mathrm{rad\,s^{-1}}$. C. Preshear effect on gel structure. The confocal snapshots were taken at height of 20 µm after different preshears (σ_{pre} noted on the top).

bottom. Oscillatory rheology was then measured in the linear regime. Finally, we measured the yield stress σ_y by creep tests, where the imposed stress σ was increased from 0.1 Pa in a stepwise manner until $\sigma \gtrsim \sigma_y$. This protocol, repeated for various σ_{pre}, enables us to measure the intact gel formed after different preshears.

We found that the rheology of $\phi = 10\,\%$ gel does depend on the preshear strength. To a certain extent, the elastic modulus G' and yield stress σ_y increase with the preshear stress σ_{pre}, Figure 4.10B. In contrast, the viscous modulus G'' remains almost constant. This means that a more vigorous preshear leads to a stronger gel.

Such preshear dependence is not just confined to the macroscopic rheology. Figure 4.10C displays confocal images after different preshears. Visually, the strongest preshear ($\sigma_{\text{pre}} = 100\,\text{Pa}$) results in the most homogeneous network. As the preshear strength decreases, large voids appear and the microstructure becomes increasingly heterogeneous. This structural behaviour explains the preshear-dependent rheology in some respects. As the preshear increases, the gel structure becomes more homogeneous and the bond density becomes higher, which in turn gives rise to a stronger gel [21].

Such tendency, discovered in various colloidal gels [21, 159], enables one to tune gels. However, the tuneability is limited: a gel will always recover to a solid regardless of flow history. In the next chapter, we will demonstrate that this is not the case for our binary suspensions.

Other concentrations

Our small-particle gels were further studied at different volume fractions ϕ. Using the same protocol as the $\phi = 10\,\%$ gel, we preformed regular rheological measurements including flow curve, dynamic frequency sweep and strain sweep.

Figure 4.11A shows the σ-$\dot{\gamma}$ flow curves. For all the samples with $\phi \geq 6.7\,\%$, the stress σ appears to approach a plateau at low shear, indicating a finite yield stress σ_y. Determined by Herschel-Bulkley fitting (Fig. 4.11A, solid lines), the yield stress σ_y increases with the volume fraction ϕ in a power-law manner (i.e. $\sigma_y = \sigma_0 \phi^{\nu}$), Figure 4.11B. Linear fit to the data (solid line) gives the exponent $\nu = 3.3$, which is comparable to that of other gels [181, 182]. According to the fitted slope $\sigma_0 = 1870\,\text{Pa}$, we can estimate the attraction strength U_{att} by the

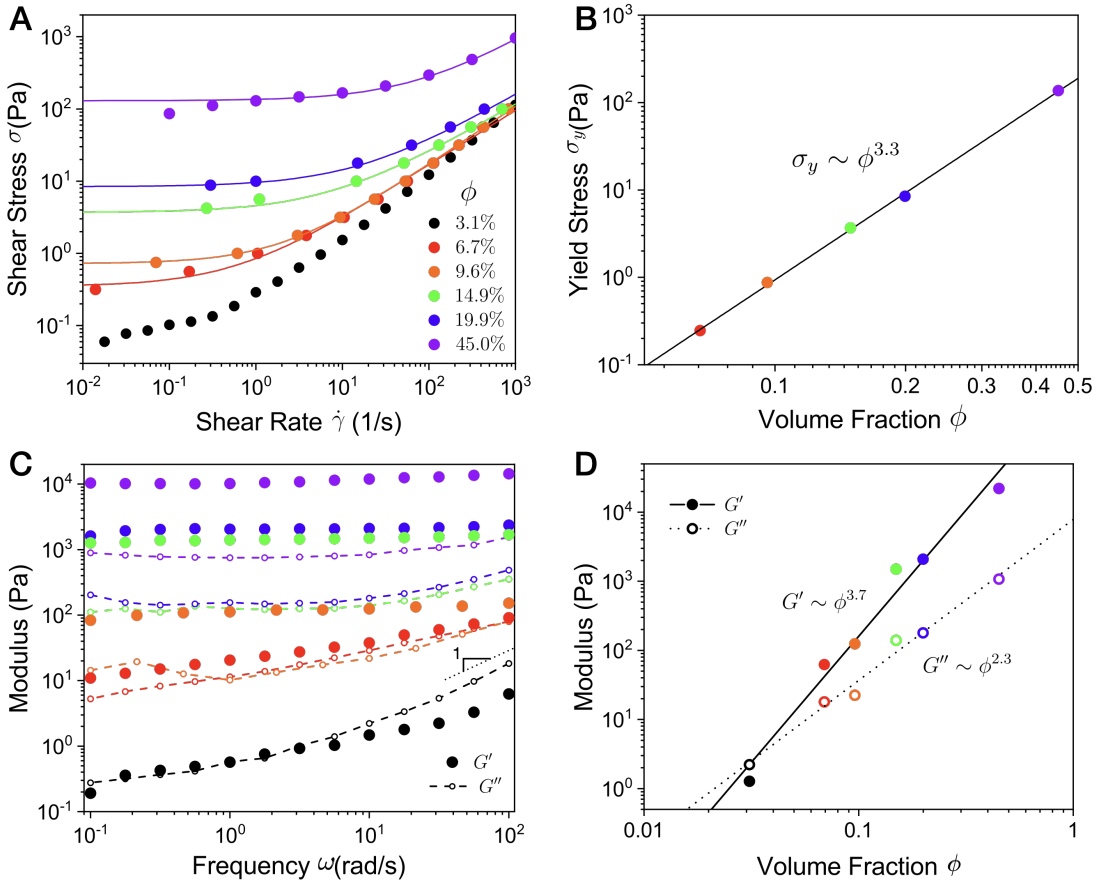

Figure 4.11 Regular rheology at different volume fractions ϕ. A. σ-$\dot{\gamma}$ flow curves. The solid lines are Herschel–Bulkley fits to the data. B. Yield stress σ_y (determined from the Herschel–Bulkley fits in A) varies as a function of volume fraction ϕ. The solid line is power-law fit ($\sigma_y = \sigma_0 \phi^{\nu}$) to the data, giving $\sigma_0 = 1870\,\mathrm{Pa}$ and $\nu = 3.3$. C. Dynamic frequency sweep at $\gamma = 0.1\,\%$. Filled circles: elastic modulus G'. Open circles: viscous modulus G''. The dotted line indicates a slope of 1. The dashed lines are drawn to guide the eye. D. The two components of dynamic modulus (at $\omega = 10\,\mathrm{rad\,s^{-1}}$ and $\gamma = 0.1\,\%$) vary as functions of volume fraction ϕ. The solid and dashed lines are power-law fits to the G' data and G'' data respectively.

relation $\sigma_0 \sim U_{\text{att}}/\xi d^2$ (see Eq. 3.31 in Chapter 3). Our previous discussion on Figure 4.9B estimates the attraction range $\xi \sim 5\,\text{nm}$, which gives $U_{\text{att}} \sim 500 k_B T$. Such magnitude is consistent with our previous estimate in Sec. 4.1.2.

In addition, Figure 4.11B does not exhibit a clear gel boundary ϕ_{gel} below which yield stress vanishes. Although the sample at $\phi = 3.1\,\%$ does not present a noticeable sign of yield stress in Figure 4.11A (black filled circles), this may be because its yield stress is unmeasurably low. By extrapolating the fitted power law in Figure 4.9B (solid line) to $\phi = 3.1\,\%$, we expect a yield stress $\sigma_y \approx 0.02\,\text{Pa}$ at $\phi = 3.1\,\%$, which is below the rheometer resolution ($\sim 0.1\,\text{Pa}$). That is, our sample is still a gel at a such low concentration $\phi = 3.1\,\%$. The absence of gel boundary differentiates our small-particle gels and depletion gels which are formed via arrested spinodal decomposition [127, 153]. We thus infer that our small particles are adhesive particles where bond rigidity applies. Our small-particle gels are therefore fractal gels.

Figure 4.11C shows dynamic frequency sweep at $\gamma = 0.1\,\%$. For the $\phi = 3.1\,\%$ sample, G' and G'' are comparable at low frequencies ($\omega \lesssim 10\,\text{rad}\,\text{s}^{-1}$) and both grow with frequency ω. As ω increases, G'' exceeds G' and approaches a slope of 1 at high frequencies. This corresponds to the Cox-Merz rule [183], where high frequency oscillatory rheology corresponds to high-shear-rate steady flow. Quantitatively, the deduced viscosity ($\eta \sim G''/\omega$) agrees with the measured high-shear viscosity ($\eta \approx 0.1\,\text{Pa}\,\text{s}$) in Figure 4.11A (black filled circles).

This limit has not been reached for all the other concentrations. As ϕ increases to $\phi = 6.7\,\%$, G' and G'' both scale with ω as power law (Fig. 4.11C, red filled circles), while the former exhibits a slightly smaller exponent: $G' \propto \omega^{0.32}$ and $G'' \propto \omega^{0.44}$. Extrapolating the power law to the zero-frequency limit gives $G' > G''$: such scaling indicates a gel. This is consistent with the yield-stress flow curve in Figure 4.11A (red filled circles).

With ϕ increasing, the frequency dependence becomes progressively weak and $G' > G''$ applies within the whole ω range we probed, Figure 4.11C. A broad minimum in $G''(\omega)$ generically occurs at $\omega \sim 1\,\text{rad}\,\text{s}^{-1}$, consistent with other gel systems [21, 46]. At a fixed $\omega = 10\,\text{rad}\,\text{s}^{-1}$, both the two moduli grow with volume fraction ϕ, Figure 4.11D. Power-law fits show that $G' \sim \phi^{3.7}$ (solid line) increases more rapidly than $G'' \sim \phi^{2.3}$ (dashed line). In particular, the G' scaling is comparable to that in other gels with short-range attraction [184, 185].

We also explored the yielding behaviour by dynamic strain sweep, Figure 4.12.

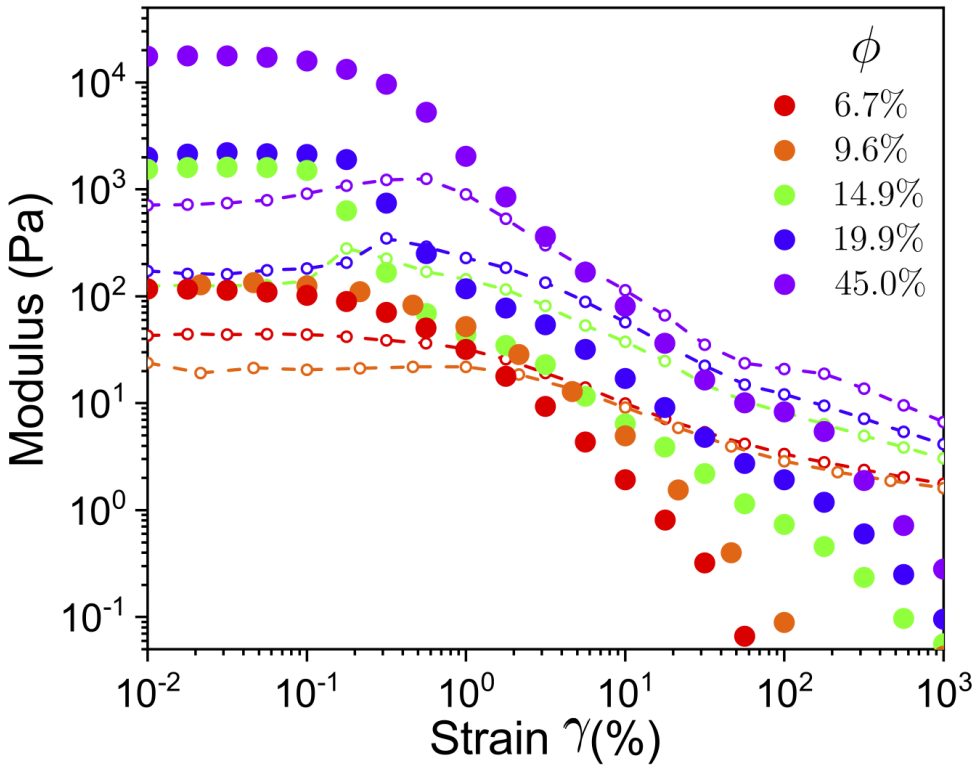

Figure 4.12 Dynamic strain sweep at $\omega = 10\,\mathrm{rad\,s^{-1}}$ with different volume fractions ϕ (see legend). Filled circles: the elastic modulus G'. Open circles: the viscous modulus G''. Dashed lines are drawn to guide the eye.

At all concentrations, linear response confines to small strains ($\gamma \lesssim 0.1\,\%$) beyond which the elastic modulus G' drops rapidly and until falling below the viscous modulus G''. The crossover corresponds to the yielding point, while the yield strain γ_y, ranging between 0.5 % and 5 %, varies from sample to sample. The small yield strain is consistent with the short-ranged hydrophobic attraction [186].

A generic peak in $G''(\gamma)$ has been widely reported in glassy materials [154, 179]. Though not fully understood, it is in general related with modes of energy dissipation and occurs together with yielding [179]. For our gels, however, such peak was only observed at intermediate volume fractions $\phi \gtrsim 15\,\%$, Figure 4.12. We attribute the absence of G'' peak in dilute samples to gravitation.

As discussed in Chapter 3, the size of gel cluster becomes larger with decreasing ϕ. As the gravitational Péclet number $\mathrm{Pe_g}$ scales with d^4 (Eq. 3.6 in Chapter 3), gravitational effect is more significant at lower concentration ϕ. In dilute gels, the density variation in the vertical direction gives rise to various length scales so that energy dissipation no longer manifests at a sole strain amplitude and the

G'' peak is thereby 'flattened'.

At high concentrations $\phi \gtrsim 15\,\%$, G'' peak and deviation from linear response approximately occur at the same strain, ranging between $0.1\,\%$ and $1\,\%$. Such strain scale indicates a short attraction range ξ between 0.5 nm and 5 nm, which is consistent with other work on hydrophobic attraction [89]. As the strain increases up to $\gamma \sim 100\,\%$, both G' and G'' appear to exhibit shoulders in concentrated gels ($\phi \gtrsim 20\,\%$). Such behaviour, widely observed in dense attractive systems [7, 179], has been attributed to a two-step yielding.

All these results establish that our small-particle gel behaves similarly to other model gels with short-range attraction. Based on the yield stress scaling (Fig. 4.11B), we roughly estimate the magnitude of attraction strength $U_{\text{att}} \sim 500\ k_BT$. Though we cannot precisely determine the attraction range ξ, the dynamic strain sweep result (Fig. 4.12) gives an estimate between 0.5 nm and 5 nm. According to the absence of gel boundary ϕ_{gel} in Fig. 4.11B, we suspect that our small-particle gel is fractal and our small attractive particles thereby have bond rigidity. Yet this requires further verification.

4.1.4 Tuneability

Notably, our attractive colloids are of great Tuneability. Tuneability is important for industrial suspensions as it enables process control. The property of suspensions highly depends on that of constituent particles, such as size d, concentration ϕ and pair interaction. For example, stronger colloidal gels are formed with smaller d or higher ϕ or stronger attraction U_{att} [127, 184, 187].

For our small attractive particles, all the three parameters can be tuned. According to the preparation protocol described in Figure 4.4, we can control the particle concentration ϕ when making the sample. And we have shown gel rheology at various ϕ in the previous section. The particle size d_S is tunable by changing the synthesis recipe [164]. However, since the surface chemistry varies from batch to batch, it is almost impossible to synthesise particles of different d_S yet with identical surface wetting. Thus we did not quantitatively study the size effect in this work.

Tuning hydrophobic attraction

The attraction strength U_{att} between our small particles directly depends on the degree of hydrophobicity. Therefore, tunable hydrophobicity enables tunable U_{att}. By using different recipe to functionalise the same batch of silica colloids, we can fabricate particles of different hydrophobicity with otherwise identical properties.

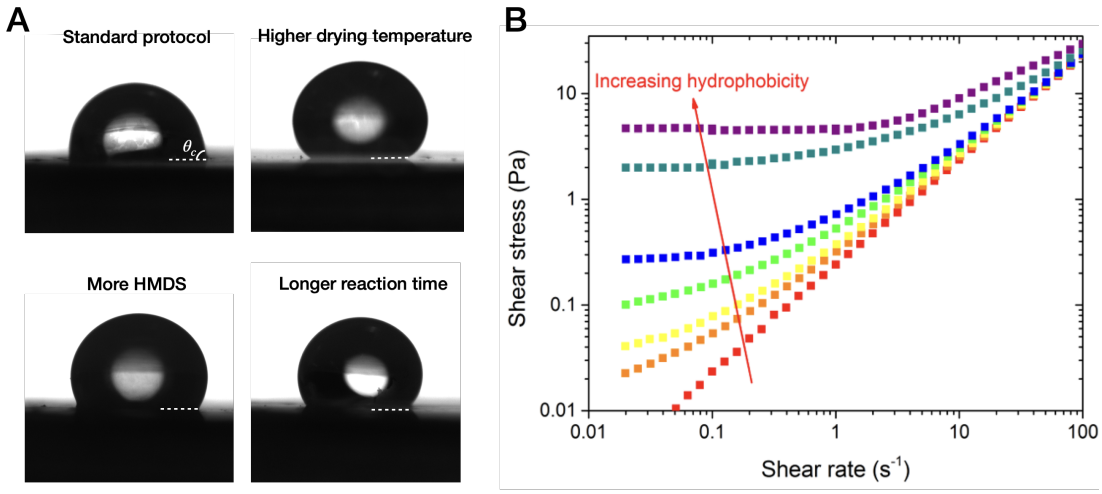

Figure 4.13 A. Contact angle measurement on layers of particles functionalised by different recipe. We used water as the liquid and dried slabs of particles as the substrates. Higher drying temperature: $T = 170\,^{\circ}\text{C}$ (compared with $T = 120\,^{\circ}\text{C}$). More HMDS: additional 100 % HMDS. Longer reaction time: 3 days (compared with 1 day). The dashed lines are to guide the eye. B. Flow curves at $\phi = 10\,\%$ with different particle hydrophobicity. The degree of hydrophobicity was tuned by the amount of HMDS during functionalisation, indicated by the red arrow.

The degree of hydrophobicity can be quantified by contact angle θ_c. Here we measured the contact angle of water on a dried slab of particles by sessile drop method [188]. The particle slab was prepared on a round glass slide ($r = 25\,\text{mm}$) using spin-coating. Specifically, the slide was hold on a Cammax Precima spin-coater by a vacuum and spun at around 2 kRPM, while a suspension of hydrophobic silica in ethanol ($\phi_{\text{wt}} \approx 20\,\%$) was dripped on the slide at the same time. The particle-coated slide was then left to dry for 1 h, after which the contact angle measurement was performed. For the hydrophobic silica from the standard functionalisation protocol described in Sec. 4.1.2, $\theta_c \approx 85°$, Figure 4.13A.

Note that the measurement above is crude, as we ignored many factors such as surface roughness which affect the result [188]. Yet this is sufficient to compare the hydrophobicity from different functionalisation recipe. In this way, we found

that more HMDS, longer reaction time and higher drying temperature all lead to larger contact angles θ_c and thereby greater hydrophobicity, Figure 4.13A. Through controlling the amount of HMDS, we fabricate particles with various hydrophobicity. Their flow curves at $\phi = 10\,\%$ show that the yield stress increases with the hydrophobicity. We thus infer that higher hydrophobicity leads to stronger attraction.

Likewise, the attraction strength U_{att} also varies with the sample age t_{age}. This is confirmed by the decay in yield stress σ_y. We prepared a gel sample at $\phi = 20\,\%$ and kept it well sealed for 2 months. At different ages t_{age}, we transferred an amount of the sample to rheometer and measured its flow curve, Figure 4.14A. As the sample ages, the stress at low shear rate decreases by almost two orders of magnitude, whereas the viscosity at high shear rate is roughly constant, indicating little variation in the sample composition over 2 months.

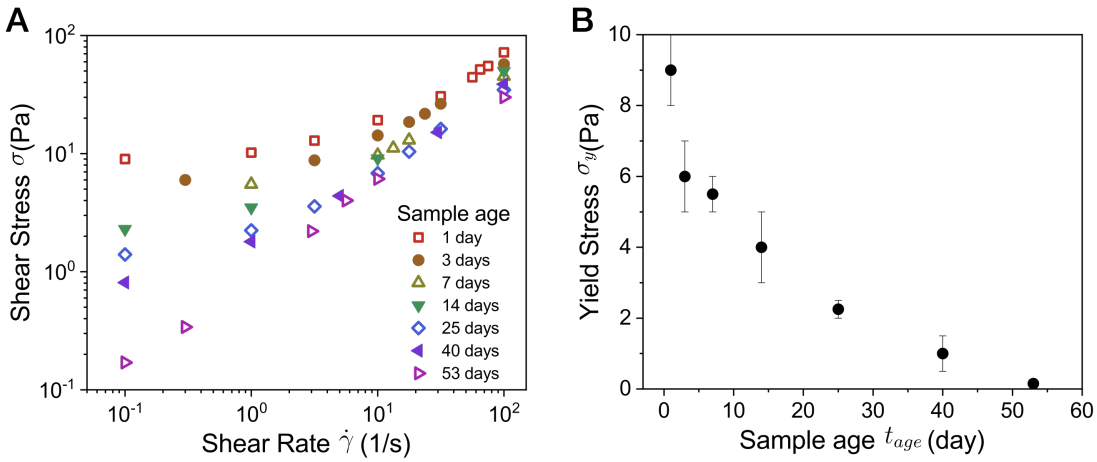

Figure 4.14 A. Flow curves of $\phi = 20\,\%$ gel at different sample ages t_{age}. B. Yield stress σ_y decays as a function of sample ages t_{age}. The yield stresses are determined by Herschel-Bulkley fit to the data in A.

The yield stress σ_y, determined by Herschel-Bulkley fit to the data in Fig. 4.14A, decreases from $\sim$10 Pa to $\sim$0.1 Pa with the sample age t_{age}, Figure 4.14B. Given the little variation in other properties, we infer that our small particles become less attractive over time after dispersed in the solvent. Despite of the unknown mechanism, such ageing is not a problem for our experiments since the decay timescale ($\sim$ weeks) is far longer than the experimental timescale ($\sim$ hours). However, precautions should be taken to ensure identical attraction strength U_{att} in different samples. To prevent possible inconsistency, therefore, all fresh-made samples were aged on roller bank for exactly 3 days (unless otherwise noted) before measurement.

4.2 Large repulsive particles (L)

4.2.1 Materials and methods

Sample preparation

We used silica microspheres (from AngstromSphere®) with diameter $d_L = 4.0\,\mu\text{m}$ as the **L**arge repulsive particles in our binary suspension. Before being dispersed in suspension, the dry particles were firstly washed in sodium hydroxide solution (pH ≈ 9.5) for several times, during which prolonged sonication (probe and bath in turn) was applied. This treatment is to fully induce surface charge and break compact aggregates. When there exists no visible aggregates (judged by eye), we transferred the particles to our solvent by several rounds of washing.

For convenience, we prepared a stock concentrated suspension with known weight fraction ($\phi_{\text{wt}} = 63.4\,\%$) in advance. Such high concentration was achieved by centrifuge and supernatant removal. In this way, samples with lower concentrations can be prepared by simple dilution. Through the same methods as used in small particles, we measured the density $\rho_L = 2.0\,\text{g}\,\text{cm}^{-3}$ and the refractive index $n_L \approx 1.45$ of the large particles.

Basic characterisation

Large silica particles are charge stabilised in aqueous solvent. Hence we expect a DLVO interaction between them. We measured the ζ-potential of large repulsive particles in water-glycerol mixture, giving $-87\,\text{mV}$. Taking the ions from sodium hydroxide and fluorescein (sodium salt) into consideration and using $A \approx 0.5 k_B T$ [77], we estimate the DLVO potential based on Eq. 3.7-3.11 in Chapter 3. Theoretical calculation shows that van der Waals attraction only manifests at very small separations ($r \lesssim 1\,\text{nm}$), beyond which a repulsive barrier with height $U_{\text{rep}} \sim 70\ k_B T$ is presented. The Debye length $\kappa^{-1} \sim 10\,\text{nm}$, indicating that the interaction between our large particles is short-ranged repulsion. This is confirmed by the shear thickening behaviour in the next section.

Compared with small attractive particles, large repulsive particles are considered non-Brownian because of the slow diffusion ($\tau_B \approx 1\,\text{h}$). Because $\tau_{\text{sed}} \approx 74\,\text{s}$, sedimentation may be important for the large particles during experiments.

4.2.2 Shear thickening rheology

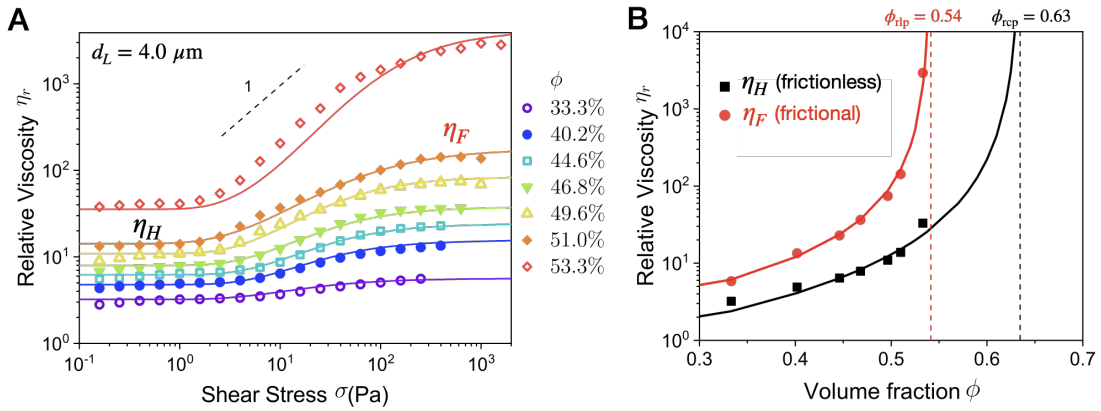

Figure 4.15 A. Relative viscosity η_r versus shear stress σ for 4.0 µm large particles at different volume fractions ϕ. We ramped up the shear stress σ and measured the viscosity η at a steady state. The solid lines are Wyart-Cates fits (see Eq. 3.25-3.27 in Ch. 3), giving the prefactor $A = 0.63$, the stretch exponent $\beta = 0.87$ and the onset stress $\sigma^\star = 7.3$ Pa. B. Two viscosity branches (frictionless η_H – black; frictional η_F – red) vary as functions of volume fraction ϕ. The solid lines are Wyart-Cates fits (see Eq. 3.25 in Ch. 3), giving $\phi_{\rm rlp} = 0.54$ and $\phi_{\rm rcp} = 0.63$.

We measured the flow curve of large particle suspensions at various volume fractions ϕ, Figure 4.15A. While the $\phi = 30\,\%$ sample is nearly Newtonian with the viscosity η slightly increases at high shear stress σ, shear thickening manifests in dense suspensions ($\phi \gtrsim 35\,\%$). In these samples, the viscosity η increases from a lower plateau η_H to a higher one η_F as the shear stress σ increases. At the highest concentration we achieved ($\phi = 53.3\,\%$, open diamonds in Fig. 4.15A), the slope of the η_r-σ curve approaches 1, indicating a discontinuous shear thickening [189].

Suspensions of our large particles appear to shear thicken at a similar stress scale $\sigma \sim 10$ Pa. Quantitatively, Wyart-Cates fits to the flow curve data (Fig. 4.15A, solid lines) gives the onset stress $\sigma^\star = 7.3$ Pa. The shear thickening behaviour suggests repulsive large particles, which form frictional contacts when sheared beyond $\sigma^\star$. We therefore deduce a repulsive barrier $F^\star \sim \sigma^\star d^2 \sim 30\ k_BT$/nm in force units. Such magnitude is approximately consistent with our previous estimate on the DLVO interaction: $U_{\rm rep}\kappa \sim 10\ k_BT$/nm.

The two viscosity branches, η_H and η_F, both increase rapidly with ϕ and appear to possess different jamming volume fractions, Figure 4.15B. According to the Wyart-Cates fits (solid lines), the frictionless branch η_H diverges at $\phi_{\rm rcp} = 0.63$

while the frictional branch η_F diverges at a lower $\phi_{\text{rlp}} = 0.54$. The two jamming volume fractions here are comparable to those in other literature [10, 71].

Other sizes d_L

We also studied silica particles with different sizes d_L. Suspensions of silica particles with $d_L = 0.5\,\mu\text{m}$ and $1.5\,\mu\text{m}$ (from Amstrongsphere®) were prepared and measured in the same way as 4-µm silica particles. Shear thinning occurs at low shear as d_L becomes smaller, Figure 4.16A ($d_L = 1.5\,\mu\text{m}$) and 4.16B ($d_L = 0.5\,\mu\text{m}$), indicating that particles are Brownian colloids [19]. In particular, the 0.5-µm silica even develop a yield stress $\sigma_y \sim 1\,\text{Pa}$ at $\phi = 51.2\,\%$, Figure 4.16B (red open squares).

Moreover, shear thickening was observed in both cases, Figure 4.16A and 4.16B, indicating repulsions between these particles. Compared with $d_L = 4\,\mu\text{m}$, smaller particles appear to shear thickening at a higher stress. The onset stress $\sigma^\star$ decreases with d_L roughly in a power-law manner: $\sigma^\star \sim d_L^{-2}$, Figure 4.16C. Such scaling is consistent with other shear thickening suspensions [71].

Figure 4.16D adds the data of 0.5-µm silica and 1.5-µm silica to the η_r–ϕ plot in Figure 4.15B. Although data points are scattered to a certain extent, approximately, the two viscosity branches do not vary much with d_L despite of the small shifts in the two jamming volume fractions (ϕ_{rlp} and ϕ_{rcp}). These rheological results establish that our large particles are similar to other repulsive hard-particles [71].

4.3 Establishing model binary suspension

We establish our model binary system by mixing the two species of particles - small attractive particles and large repulsive particles. Analogous to single-component suspensions, such binary mixture is characterised by the concentration of each species of particles. Here we use ϕ_S and ϕ_L to respectively denote the volume fraction of small attractive particles and large repulsive particles:

$$\begin{aligned} \phi_S &= \frac{V_S}{V_S + V_L + V_f} \\ \phi_L &= \frac{V_L}{V_S + V_L + V_f}. \end{aligned} \tag{4.8}$$

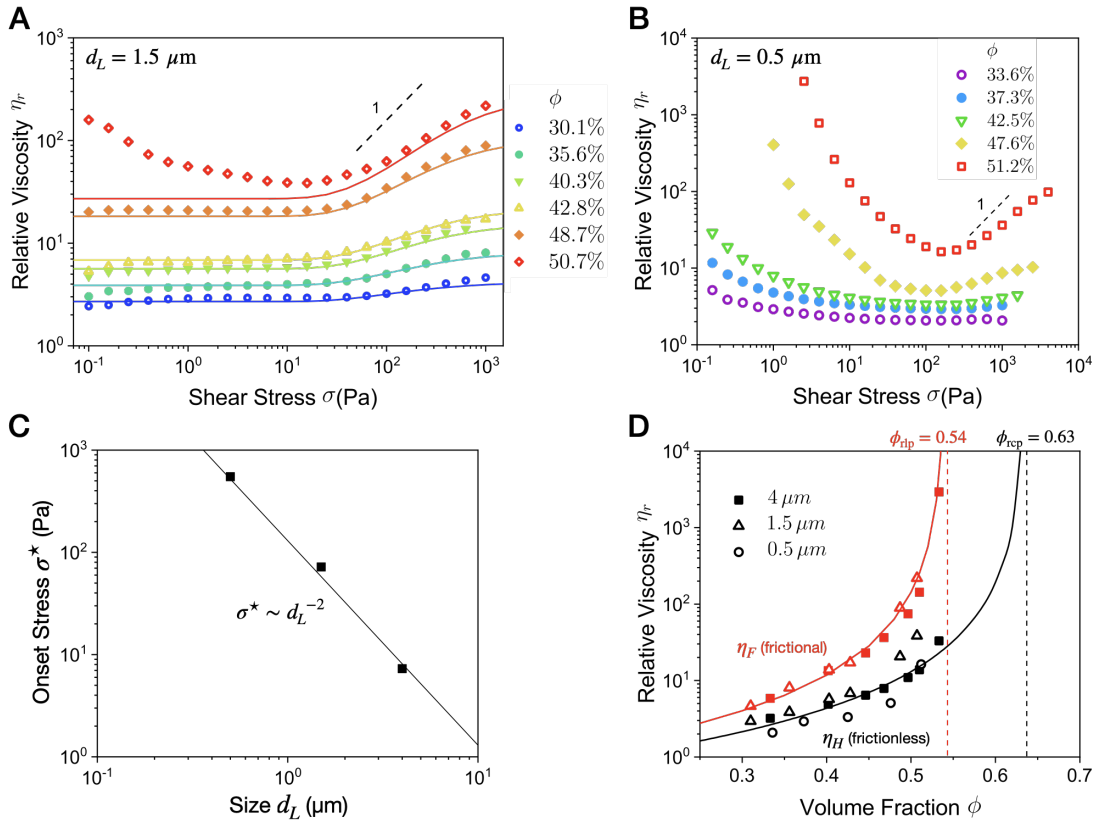

Figure 4.16 η_r-σ flow curves of silica particles with $d_L = 0.5\,\mu m$ (A) and $d_L = 1.5\,\mu m$ (B). C. The onset stress $\sigma^\star$ decreases as a function of the large particle size d_L. The solid line is power law with exponent -2. D. Two viscosity branches (frictionless η_H – black; frictional η_F – red) at three d_L (labelled by different symbols). Solid lines are fits in Figure 4.15B as a reference.

Throughout the thesis, we use ϕ to denote the volume fraction in single-component suspensions, whereas ϕ_S and ϕ_L are only applied to binary suspensions.

4.3.1 Determining ϕ_S and ϕ_L

Given the densities of particles and solvent, both ϕ_S and ϕ_L can be deduced from weight fractions. To prepare a binary suspension, small hydrophobic silica of weight m_S are firstly wetted and dispersed in ethanol of weight m_e by sonication. We then add the stock large-particle suspension ($\phi_{\text{wt}} = 63.4\,\%$) of weight m_{Ls} to the silica-ethanol mixture, followed by the water-glycerol mixture (1:9 by mass) of weight m_{wg}. Again, we fix $m_{wg} = 10m_e$ to ensure consistent solvent composition. Finally, sonication (probe and bath) and subsequent bubble removal

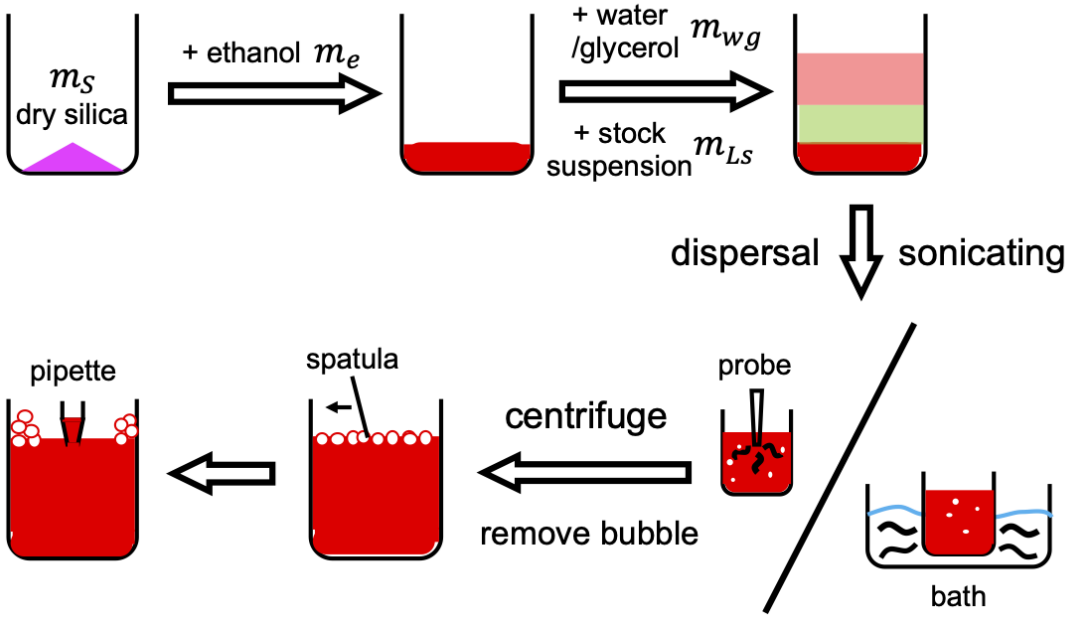

Figure 4.17 Schematic preparation protocol of binary suspensions.

are performed. Figure 4.17 shows a schematic protocol of preparing binary suspensions.

For samples prepared by such protocol, ϕ_S and ϕ_L are expressed as follow:

$$\begin{aligned}\phi_S &= \frac{\frac{m_S}{\rho_S}}{\frac{m_S}{\rho_S}+\frac{m_e+m_{wg}}{\rho_f}+\frac{m_{Ls}\phi_{\mathrm{wt}}}{\rho_L}+\frac{m_{Ls}(1-\phi_{\mathrm{wt}})}{\rho_f}} \\ \phi_L &= \frac{\frac{m_{Ls}\phi_{wt}}{\rho_L}}{\frac{m_S}{\rho_S}+\frac{m_e+m_{wg}}{\rho_f}+\frac{m_{Ls}\phi_{\mathrm{wt}}}{\rho_L}+\frac{m_{Ls}(1-\phi_{\mathrm{wt}})}{\rho_f}}.\end{aligned} \tag{4.9}$$

In this way, we can prepare a binary sample at designed ϕ_S and ϕ_L.

4.3.2 New interactions

Following the protocol above, we first prepared a binary suspension at $\phi_S = 10\,\%$ and $\phi_L = 20\,\%$ as a trial experiment. Even though the refractive index was not perfectly matched, our sample still presents clear confocal image, Figure 4.18A. Large particles (green, resolved as single particles) and small particles (red) were imaged by individual channels, and Figure 4.18A merges them together.

Because of the distinct mechanisms, we expect the hydrophobic attraction

between small particles and the charge repulsion between large particles to do not interfere with each other. The microstructure in Figure 4.18A is consistent with our expectation. In the presence of large particles, small attractive particles attract each other and form clusters. Meanwhile, aggregation between large particles was not observed, implying their repulsive interaction.

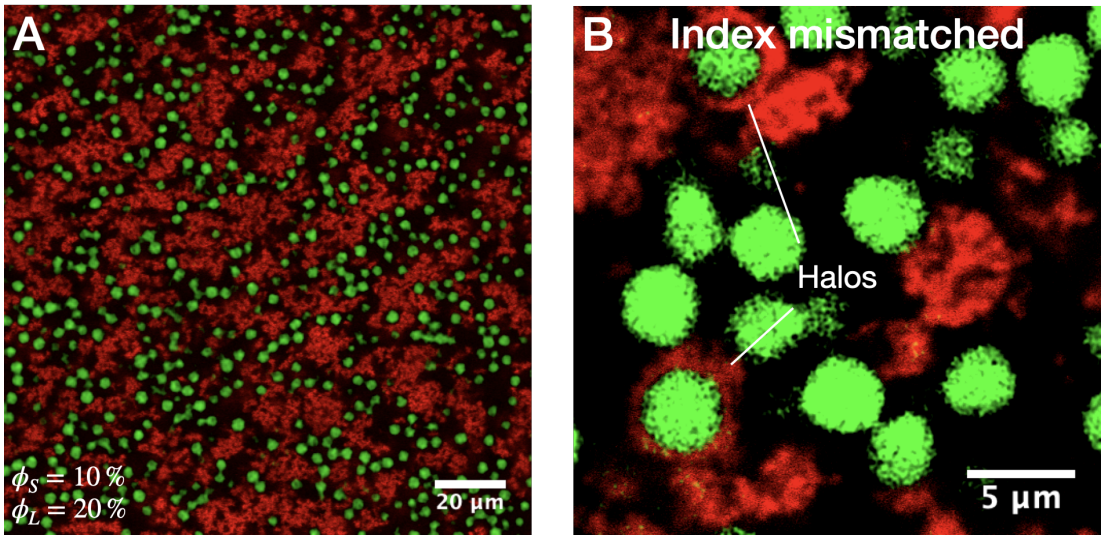

Figure 4.18 A. Confocal image of a binary suspension at $\phi_S = 10\,\%$ and $\phi_L = 20\,\%$. The refractive index is nearly matched by using our solvent ($n_f = 1.444$). Large and small particles are labelled by green and red respectively. B. Zoomed confocal image of index-mismatched system where $n_f = 1.375$. Here we used solvent with ethanol: water: glycerol = 1:5:5 by mass. Small-particle halos are highlighted, implying small-large attraction [190].

Mixing the two species of particles may introduce inter-species interactions. An *apriori* prediction on the nature of these interactions is difficult. Confocal imaging (Fig. 4.18A) does not show evidence of 'halos' of small particles around the large ones, as one would expect if the two species attract each other. Thus we infer that any small-large attraction is either extremely weak or completely absent. Here we list three potential mechanisms that may reduce or eliminate small-large attraction:

1. The grafted hydrophobic TMS groups on small silica repel the hydrophilic silanol groups on large silica.

2. The remaining silanol groups on hydrophobic silica present negative charge and thereby repel the negatively-charged large silica[3].

[3]The charge repulsion is weaker than hydrophobic attraction so that hydrophobic particles still attract each other.

3. The Van der Waals attraction is weakened by the nearly-matched index.

Confocal microscopy demonstrates that small-large attraction is possible if the index is intentionally mismatched, evident in the small-particle halos around large particles in Figure 4.18B. Since precise characterisation on these interactions may require complex apparatus like colloidal-probe atomic force microscope, here we simply classify the small-large interaction as non-sticky in our nearly-index-matched solvent.

Another possible interaction is the depletion force between large particles. Our binary suspension is size-bidispersed, so that the small colloidal particles may work as depletants. However, even if the small particles were well-dispersed, the depletion attraction between large particles would be fairly weak. For a binary mixture at $\phi_S = 10\,\%$ and $\phi_L = 20\,\%$, we estimate the depletion potential at contact $U_{\text{dep}} \sim 5\ k_BT$ (see Sec. 3.1.4 in Ch. 3), which is an order of magnitude lower than the repulsive barrier that we previously estimate ($U_{\text{rep}} \sim 70\ k_BT$, see Sec. 4.2.1). Since small particles usually exist in the form of aggregates, the real depletion force is significantly weaker and thereby neglectable. This agrees with our visual observation that large particles do not stick to each other.

4.4 Conclusions

To conclude, we have developed a model binary suspension consisting of large repulsive particles and small attractive particles. We suspended bare silica microspheres (large particles) and hydrophobic silica colloids (small particles) in an aqueous mixture of ethanol, water and glycerol. On their own, the small particles attract each other and form yield-stress gels at low concentrations, whereas the large particles are repulsive and exhibit shear thickening in dense suspensions. We then proposed a standardised protocol to prepare binary suspensions, in which basic properties are more or less characterised (see Tab. 7.1 as a summary).

Compared with other suspensions disparate in size and interaction [191–193], our model system is well-characterised, tunable and transparent (imageable). Our silica particles are easy to be customised by functionalisation, leading to great Tuneability which enables exploration on the parameter space. Together with rheo-imaging technique, the matched index allows us to probe the relation be-

Table 4.1 *Summary of characterisations in binary system*

	Small particles	Large particles	Solvent
Materials	hydrophobic silica	silica	ethanol/water/glycerol (1:1:9 by mass)
Density	$\rho_S = 2.07\,\mathrm{g\,cm^{-3}}$	$\rho_L = 2.0\,\mathrm{g\,cm^{-3}}$	$\rho_f = 1.23\,\mathrm{g\,cm^{-3}}$
Refractive index	$n_S \approx 1.42$	$n_L \approx 1.45$	$n_f = 1.444$
Size	$d_S = 482\,\mathrm{nm}$	$d_L = 4\,\mu\mathrm{m}$	
Interaction	hydrophobic attraction $U_{\mathrm{att}} \sim 10^3\ k_BT$ $0.5\,\mathrm{nm} \lesssim \xi \lesssim 5\,\mathrm{nm}$	electrostatic repulsion $U_{\mathrm{rep}} \sim 70\ k_BT$ $\kappa^{-1} \sim 10\,\mathrm{nm}$	
Viscosity			$\eta_f = 0.13\,\mathrm{Pa\,s}$
Brownian	$\tau_B = 6.4\,\mathrm{s}$ (Brownian)	$\tau_B \approx 1\,\mathrm{h}$ (non-Brownian)	
Sedimentation	$\tau_{\mathrm{sed}} = 396\,\mathrm{s}$	$\tau_{\mathrm{sed}} = 74\,\mathrm{s}$	
Others	Small-large interaction: non-sticky		

tween macroscopic rheology and microscopic structure in our binary suspension. Moreover, the materials we used (silica and aqueous solvent) are relatively cheap and easily accessible. All these advantages makes our binary suspension promising as a model system.

Chapter 5

Flow-switched transition

Due to their non-equilibrium nature, colloidal gels are sensitive to flow history. In the last chapter, we revealed history dependence in our gel of small attractive colloids. Upon flow cessation, preshear at higher stress produces a stronger gel with greater homogeneity, whereas lower-stress preshear leads to a more heterogeneous gel structure with reduced strength. Such behaviour, widely reported in gel systems [21, 46], enables one to tune a gel and thereby sheds new light on applications in industry and material design. However, our gel, like other gels [21, 194], is tunable only to a certain extent as it always tends to recover to a yield-stress solid regardless of previous flow.

This is not the case for our binary suspension. In the presence of large particles, we found that moderate flow can result in permanent fluidisation. Through laboratory mixing operations, we demonstrate a solid-liquid transition triggered by flow. Specifically, while vigorous vortex mixing produces a solid-like gel after flow cessation, gentle roller mixing gives rise to a flowable liquid which persists when left undisturbed. The sample is switchable between solid and liquid states, and remembers the state into which it has been switched upon the removal of flow. In other words, the transition is *reversible* and has *memory*.

We quantitatively characterised the transition by performing rheo-imaging experiments at a specific composition: $\phi_S = 10\,\%$ and $\phi_L = 20\,\%$. Consistent with the lab demonstration, preshear with high stress leads to a yield-stress solid and that with lower stress eliminates the yield stress. For the solid and liquid states, *in-situ* rheo-imaging revealed differences in microstructure. To distinguish different structural states, we defined a quantitative criterion, based on which

two states and three flow regimes were identified. Finally, we mapped out an non-equilibrium state diagram. Given the full history of a binary suspension, the state diagram allows us to predict whether it is a solid or a liquid.

5.1 Lab demonstration

We followed the protocol in Chapter 4 to prepare a binary sample at $\phi_S = 12.5\,\%$ and $\phi_L = 30\,\%$. An striking flow-switchable bistability, illustrated in Figure 5.1, was observed during routine preparation. The sample coming off the roller bank was initially a flowable liquid that, upon brief vortex mixing ($\sim 30\,\mathrm{s}$), switched into a solid able to support its own weight in an inverted vial. Subsequent roller mixing ($\sim 20\,\mathrm{min}$) of the solid-like sample led to re-fluidisation. In short, upon flow cessation, brief vigorous vortex mixing results in a solid, whereas prolonged gentle roller mixing results in a liquid. This solid-liquid transition is *reversible*.

Solid-liquid transitions are ubiquitous in suspensions. For example, yielding in colloidal gels can be interpreted as a solid-to-liquid transition under load [7]. However, such fluidisation cannot persist, since a yielding gel will recover to a solid after flow ceases [21]. In our binary sample, by contrast, both states remained stable when left undisturbed. We prepared a solid-like sample by vortex mixing and then inverted the vial. As shown in Figure 5.1 (bottom left), at quiescence, the self-supportive sample persists for a week except for a little creep. Similarly, a liquid-like sample (prepared by roller mixing) remained flowable after a week at rest, Figure 5.1 (bottom right). This establishes that our binary sample is bistable and can 'remember' [195] the state into which it has previously been switched. This solid-liquid transition has *memory*.

Further study revealed that the transition generically occurs in binary suspensions. In the rest of this chapter, for simplicity, we study this transition in detail at a specific composition ($\phi_S = 10\,\%$ and $\phi_L = 20\,\%$) unless otherwise stated.

5.2 Rheology

Not surprisingly, the state transition plays a role when measuring the rheology. In this section, we manifest the transition in rheology experiments by designing several measurement protocols.

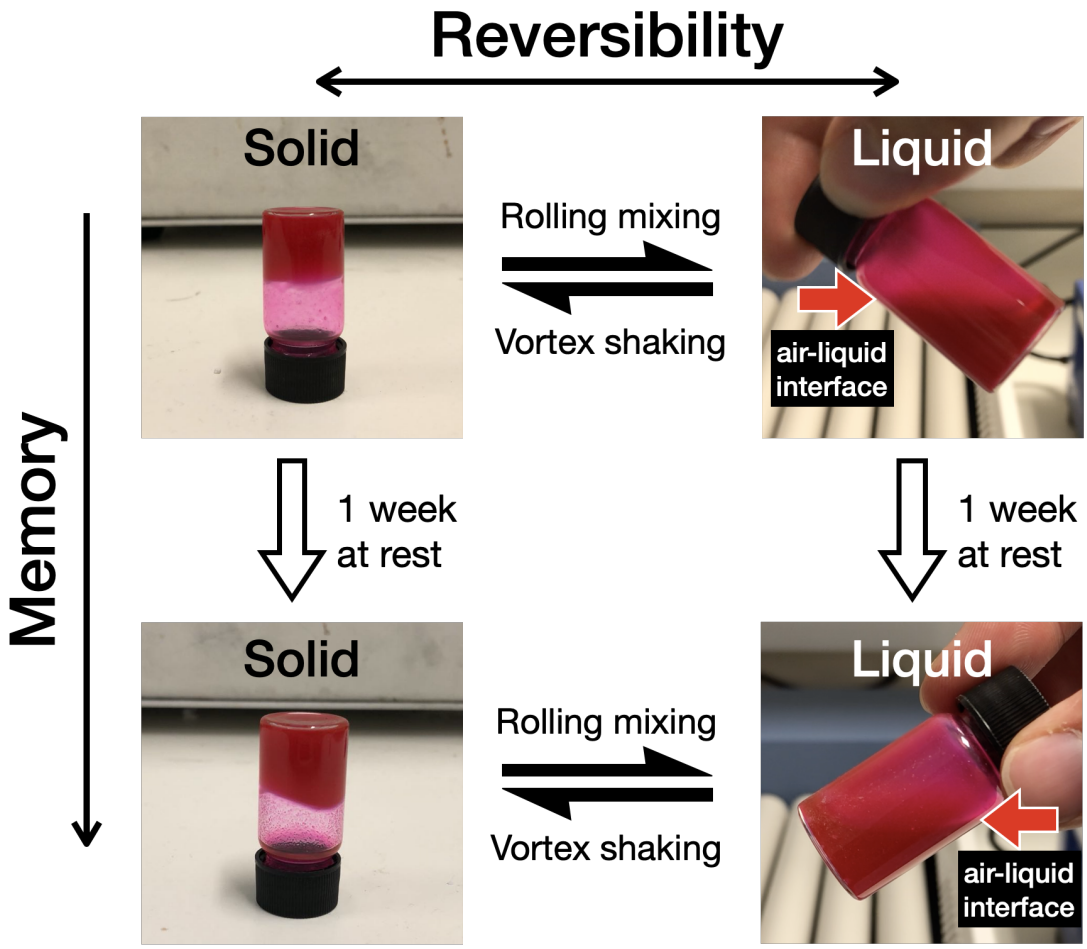

Figure 5.1 Lab demonstration of solid-liquid transition using roller mixer (Stuart Rollermixer SRT9) and vortex mixer (Ika Vortex Genius 3). The sample shown was composed of $\phi_S = 12.5\,\%$ small particles and $\phi_L = 30\,\%$ large particles.

5.2.1 Methods

To highlight the two states in steady-state rheology, we designed two protocols: ramp-down protocol and step-down protocol. The first protocol follows the typical method by ramping the shear rate down after initial rejuvenation, while stress at steady state is measured simultaneously. The step-down protocol, by contrast, measure the transient stress just after rejuvenation, which is applied between each measurement. The second method offers a way to characterise the steady-state rheology of solid state.

We also design a protocol to precisely measure the yield stress of gelled sample formed after various preshears. This has already been mentioned in Figure 4.10. We first rejuvenate a sample by high shear to remove history effect, and then

apply a preshear at a specific σ_{pre} until reaching a steady state. We then stop the preshear and wait at rest for 30 min to enable intact gelation, and then apply stepwise-increasing stress and examine the evolution of strain, i.e. creep test.

For these protocols, detailed values we used can be found in the corresponding sections.

5.2.2 Protocol dependence

Extensive rheological studies were performed on the sample of $\phi_S = 10\,\%$ and $\phi_L = 20\,\%$. When measuring its flow curve, we noticed a remarkable protocol dependence which is absent in the pure colloidal gel ($\phi_L = 0$).

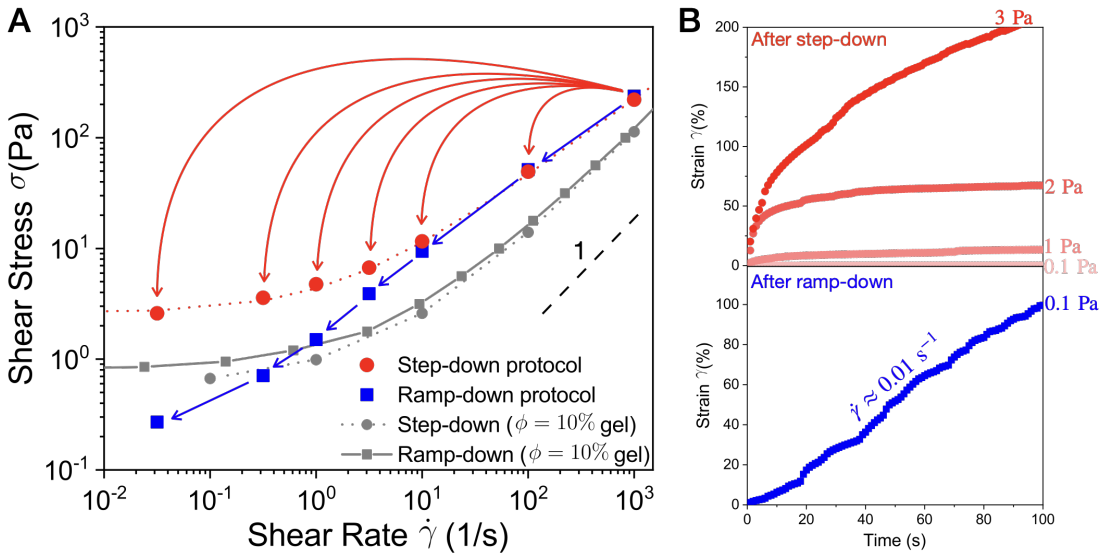

Figure 5.2 Protocol-dependent rheology in the sample of $\phi_S = 10\,\%$ and $\phi_L = 20\,\%$. A. Flow curves measured by different protocols. Red: step-down shear. After rejuvenation at $\dot{\gamma}_{\text{rej}} = 1000\,\text{s}^{-1}$ for 100 s, a lower shear rate $\dot{\gamma}$ was applied and the responding stress σ was measured over 30 s. Such procedure was repeated for various $\dot{\gamma}$, indicated by red arrows. The red dotted line is Herschel-Bulkley fit with $\sigma_y = 2.6\,\text{Pa}$, $k = 1.8\,\text{Pas}^{\text{n}}$ and $n = 0.7$. Blue: ramp-down shear. With descending shear rate $\dot{\gamma}$ (indicated by blue arrows), the steady-state stress σ was measured for 5 min at each data point. Gray: flow curves of a $\phi = 10\,\%$ gel measured by different protocols. The lines are to guide the eye. B. Creep tests after flow curve measurements in A. The imposed shear stresses σ are annotated in the graph.

We used two different protocols in the flow curve measurement. The first protocol follows the typical method by rejuvenating at $\dot{\gamma}_{\text{rej}} = 1000\,\text{s}^{-1}$ and then ramping down and measuring the shear stress σ at steady state. This regular protocol

shows no visible sign of yield stress, Figure 5.2A (blue). As the shear rate $\dot{\gamma}$ decreases, the stress σ constantly decreases as $\sigma \sim \dot{\gamma}^n$ with the exponent $n < 1$. This suggests that the sample is a shear-thinning liquid.

However, using another measuring protocol comes to the opposite conclusion. The second protocol resembles the step-down shear test [41]. We first rejuvenated the sample at $\dot{\gamma}_{\mathrm{rej}} = 1000\,\mathrm{s}^{-1}$ and then abruptly decreased the shear rate to a new value $\dot{\gamma}$ and measured the stress σ for 30 s. The same experiment was repeated for various $\dot{\gamma}$ values. With decreasing $\dot{\gamma}$, the stress σ seems to approach a low-shear plateau, Figure 5.2A (red). The sample is thereby a yield-stress solid with $\sigma_y = 2.6\,\mathrm{Pa}$ from Herschel-Bulkley fit (red dotted line). Intriguingly, whether the sample is a solid or a liquid depends on the measuring protocol.

Such protocol dependence only manifests at low shear. In Figure 5.2A, the two series of data overlap at high shear and diverge from each other when the stress σ drops below $\sigma_2 \approx 10\,\mathrm{Pa}$. Moreover, it only occurs in binary suspension. In a $\phi = 10\,\%$ gel, we did not observe obvious difference when using different measuring protocols, Figure 5.2A (gray).

Since the two protocols disagree in the binary system with each other, we performed creep test after each measurement to further examine the rheology. After the ramp-down protocol, the sample flows under a small load $\sigma = 0.1\,\mathrm{Pa}$ with a steady shear rate $\dot{\gamma} \approx 0.01\,\mathrm{s}^{-1}$, Figure 5.2B (blue). This is consistent with the liquid-like response in Figure 5.2A (blue). After step-down protocol, by contrast, the sample creeps to a finite strain under stresses $\sigma \leq 2\,\mathrm{Pa}$ and flows when sheared at $\sigma = 3\,\mathrm{Pa}$, Figure 5.2B (red). This suggests a yield stress $\sigma_y = 2.5 \pm 0.5$ Pa, which quantitatively agrees with the Herschel-Bulkley fit in Figure 5.2A ($\sigma_y = 2.6\,\mathrm{Pa}$, red dotted line).

This protocol-dependent rheology is consistent with the solid-liquid transition reported earlier. Specifically, the high-shear rejuvenation in the step-down protocol works as the vigorous vortex mixing in the lab demonstration so that the sample solidifies upon shear cessation. By recording the transient data after rejuvenation, we measured the response of solid state. In contrast, ramping down the shear rate inevitably fluidises the sample in the moderate shear regime, which corresponds to the gentle roller mixing.

In the colloidal gel where the solid-liquid transition is absent, we did not observe protocol dependence either. These observations imply that the protocol dependence is a manifestation of the solid-liquid transition. There exists new

effects under flow caused by the presence of large particles.

5.2.3 Preshear effect

To precisely demarcate the high shear regime (resulting in the solid state) and the moderate shear regime (resulting in the liquid state), we studied the preshear effect in the binary sample of $\phi_S = 10\,\%$ and $\phi_L = 20\,\%$. We used the same protocol illustrated in Figure 4.10A from Chapter 4, and compared the rheology result with that of a $\phi = 10\,\%$ gel. As previously shown, the $\phi = 10\,\%$ gel is history dependent and its strength (including the yield stress σ_y and the elastic modulus G') increases with the magnitude of preshear, Figure 5.3A. However, it always tends to recover to a yield-stress solid with $G' > G''$ regardless of the flow history. This is not the case in the binary suspension.

In the binary sample, the yield stress σ_y and the elastic modulus G' vary as functions of preshear as well, Figure 5.3B. As the preshear stress σ_{pre} decreases, however, the yield stress σ_y constantly decreases until becomes unmeasurably low below a critical preshear stress $\sigma_2 = 11\,\text{Pa}$ (dotted line). At the same time, the elastic modulus G' constantly drops until it falls below the viscous modulus G'' below $\sigma_2 = 11\,\text{Pa}$.

This result indicates solid-liquid transition, which has been demonstrated in the lab (Fig. 5.1). Here we classify the preshear that induces solidification as high shear, whereas that producing flowable liquids as medium shear, noted in Figure 5.3B. In this definition, the vigorous flow from vortex mixer is high shear and the gentle flow from roller bank is medium shear. Similarly, the solid-liquid transition is reversible in the rheometer, and each state can be considered as stable at rest since we performed measurement after preshear had ceased for 30 min. The critical stress $\sigma_2 = 11\,\text{Pa}$ demarcates the two shear regimes. This value is almost identical to the stress at which the two curves diverge in Figure 5.2A. We therefore attribute the protocol-dependent rheology to the solid-liquid transition.

The solid states induced by different high preshears are not identical. In this high shear regime ($\sigma_{\text{pre}} > \sigma_2$), the strength of the binary sample increases with preshear, Figure 5.3B. This tendency resembles that in colloidal gels, either as shown in Figure 5.3A or in other literature [21, 159]. In the medium shear regime ($\sigma_{\text{pre}} < \sigma_2$), the yield stress σ_y is constantly below the rheometer resolution

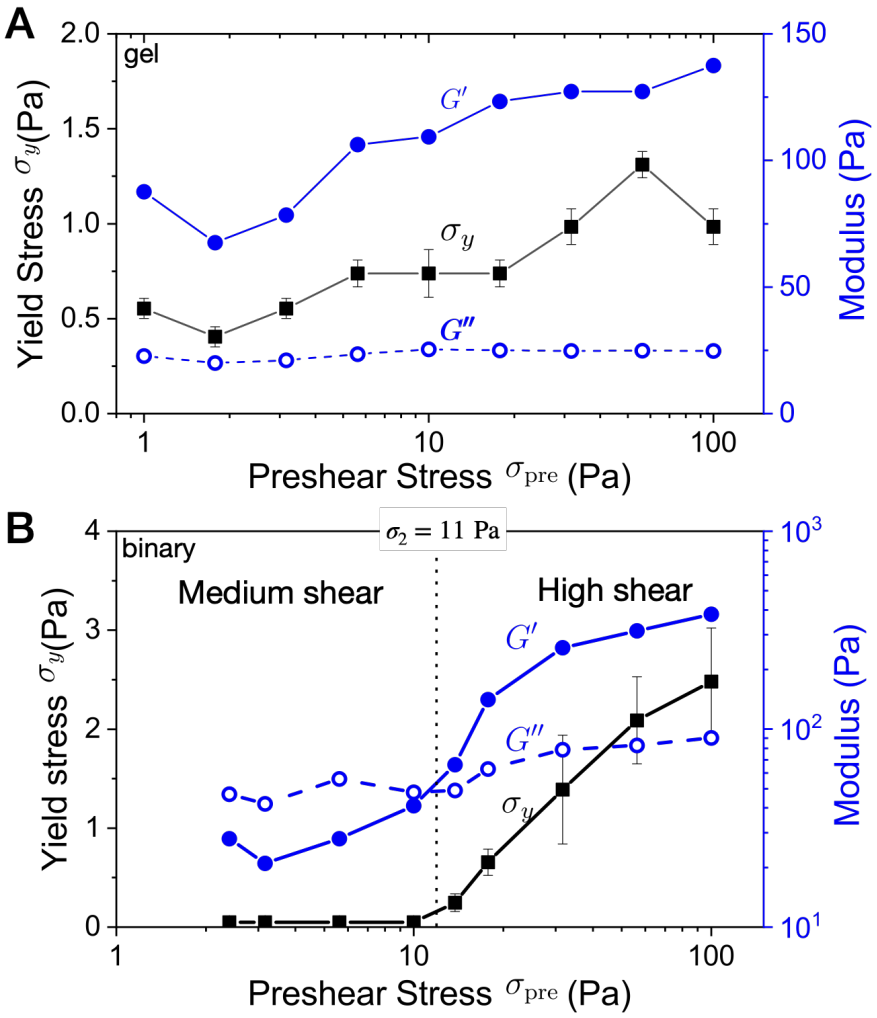

Figure 5.3 Comparison of the preshear effect in a colloidal gel and a binary suspension. A. Colloidal gel at $\phi = 10\,\%$, reproduced from Figure 4.10B in Chapter 4. B. Binary sample at $\phi_S = 10\,\%$ and $\phi_L = 20\,\%$. We used the same protocol for consistency. After rejuvenation at $\dot{\gamma} = 1000\,\mathrm{s}^{-1}$ for 100 s, the sample was presheared at $\sigma_{\rm pre}$ until the viscosity η reaches a steady state. Upon preshear cessation, we waited for 30 min and measured the dynamic modulus at $\gamma = 0.1\,\%$ and $\omega = 10\,\mathrm{rad\,s}^{-1}$ and the yield stress σ_y via creep test. The dotted vertical line ($\sigma_2 = 11\,\mathrm{Pa}$) demarcates the high shear and medium shear regimes.

($\sim 0.1\,\mathrm{Pa}$), whereas the viscous modulus G'', constantly higher than the elastic modulus G', exhibits little variation.

Stress overshoot?

Next we imposed various shear rates $\dot{\gamma}$ immediately after rejuvenation and examined the stress evolution for 10 min. In the pure gel, the stress σ quickly equilibrates at high-rate shear, whereas that under lower $\dot{\gamma}$ increases over time until finally reaching the steady state, Figure 5.4A. Such behaviour is expected in thixotropic gels, corresponding to the build-up of gel structure [196].

Under high-rate shears, the stress σ in the binary sample also stabilises rapidly. However, under shear rate $\dot{\gamma} \lesssim 10\,\mathrm{s}^{-1}$, the stress σ overshoots before decaying to a plateau, Figure 5.4B. This is reminiscent of the stress overshoot in yielding gels [7, 156]. Nevertheless, we did not observe such behaviour in our gel (Fig. 5.4A), presumably because shears were imposed before the gel structure formed after rejuvenation. In addition, the stress overshoot in yielding gels typically occurs at small strains $\gamma \lesssim 1$ [7, 156], whereas the stress peaks in Figure 5.4B are at $\gamma \sim 20$ (solid line) which is an order of magnitude higher. This indicates different physics.

The dashed line in Figure 5.4B, below which the 'stress overshoot' occurs, is again comparable to the critical stress $\sigma_2 = 11\,\mathrm{Pa}$ at which we see the solid-liquid transit on (Fig. 5.3B). Hence we infer that the 'stress overshoot' is another manifestation of the state transition. The subsequent decay implies the transition from a solid state to a less dissipative liquid state. The long duration ($\gtrsim 10\,\mathrm{min}$) is consistent with the lab demonstration where complete fluidisation requires prolonged roller mixing.

5.2.4 Comparing with thixotropy

The stress decay is reminiscent of thixotropy. As shear proceeds, the structure is progressively broken and the dissipation thereby decreases. Thixotropy may also give rise to temporary fluidisation upon preshear cessation [197]. Here we stress that *the solid-liquid transition in our binary suspension is not simple thixotropy.* First and foremost, our state transition is bistable, i.e. each state persists for a long time after flow stops. Thixotropic gels, by contrast, will recover to a solid

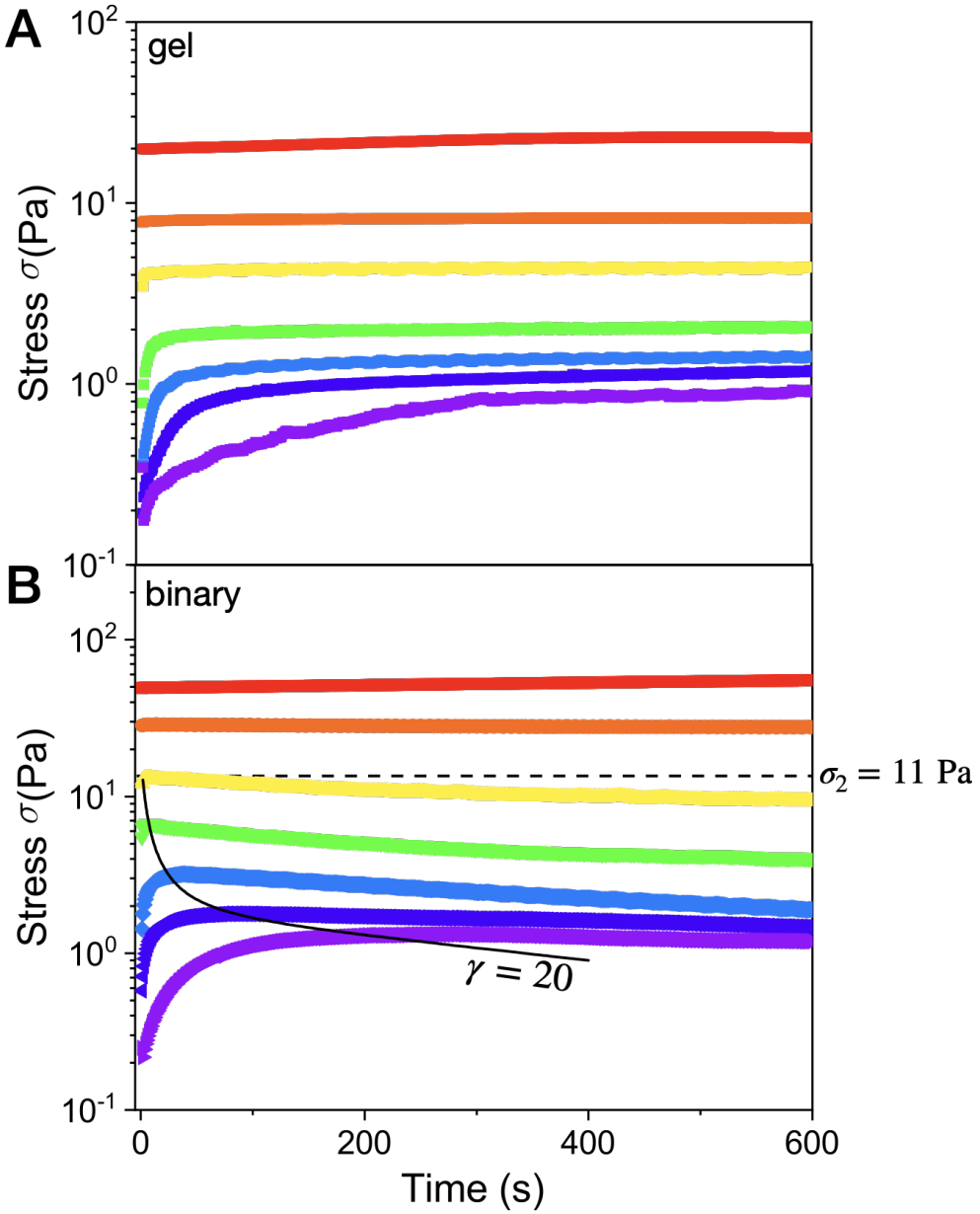

Figure 5.4 Stress evolution in a $\phi = 10\,\%$ gel (A) and a binary suspension at $\phi_S = 10\,\%$ and $\phi_L = 20\,\%$ (B). Following the high-shear rejuvenation at $\dot{\gamma}_{\mathrm{rej}} = 1000\,\mathrm{s}^{-1}$, the imposed shear rates $\dot{\gamma}$ are (from top to bottom) 100, 31.6, 10, 3.16, 1, 0.316, $0.1\,\mathrm{s}^{-1}$. The solid line indicates a constant strain $\gamma = 20$. The dashed line denotes the critical stress $\sigma_2 = 11\,\mathrm{Pa}$.

at rest.

We compare our binary suspension with general thixotropy in two aspects: hysteresis loop and step-down test. When measuring the flow curve of a thixotropic material, hysteresis loop (Fig. 5.5A) appears as a result of stress lag [41]. Such hysteresis is more or less reproducible if using the same measuring protocol. However, when we measured the flow curve in several cycles, our sample only exhibits visible hysteresis in the first round, Figure 5.5B. The 1st ramp-up (open red squares) gives higher stress than the 1st ramp-down (filled blue circles) at low shears, while subsequent loops simply reproduce the lower branch.

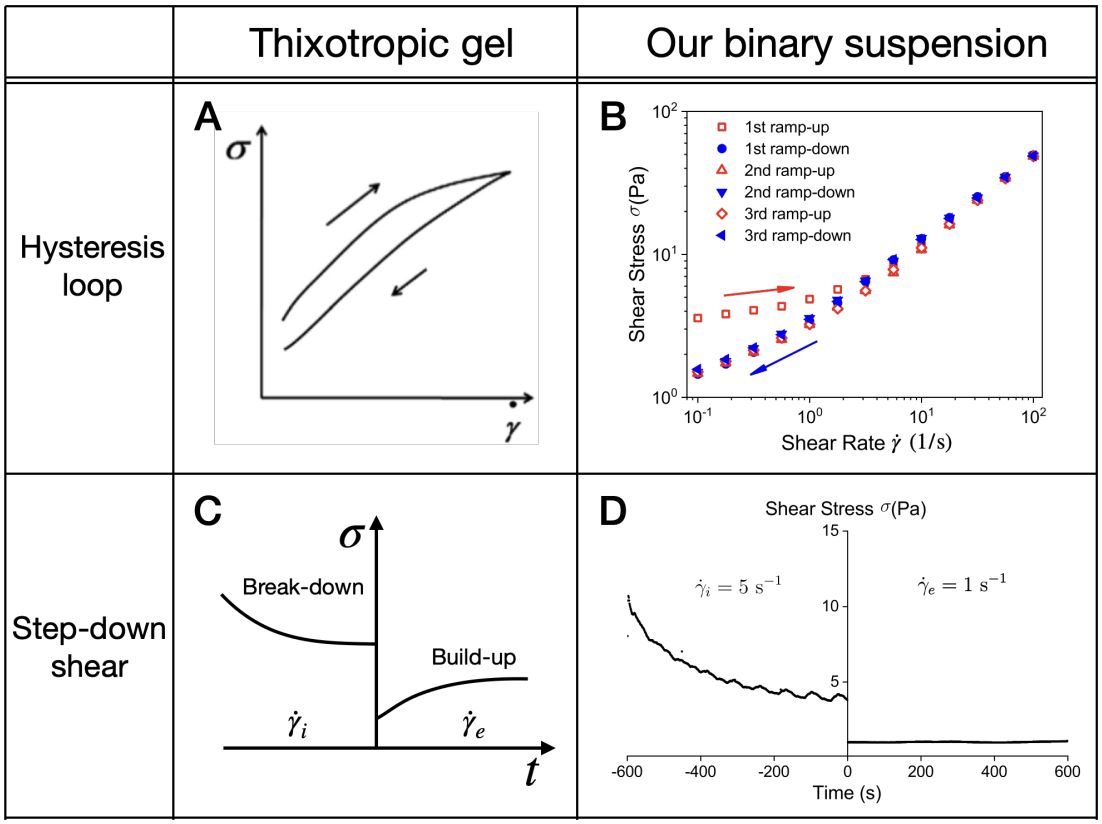

Figure 5.5 Comparison of thixotropy (A and C) and our binary suspension at $\phi_S = 10\,\%$ and $\phi_L = 20\,\%$ (B and D). A. Schematic hysteresis loop in the flow curve (linear-linear scale), taken from [41]. B. Flow curves measured by three rounds of ramp-up and ramp-down. We first rejuvenated the sample at $\dot{\gamma}_{\mathrm{rej}} = 1000\,\mathrm{s}^{-1}$, and then ramped up (red) and down (blue) shear rate $\dot{\gamma}$ for three times. Each data point was measured for 30 s. C. Schematic step-down shear test for thixotropic materials, adapted from [41]. D. Step-down shear in our binary suspension. After rejuvenation at $\dot{\gamma}_{\mathrm{rej}} = 1000\,\mathrm{s}^{-1}$, we imposed $\dot{\gamma}_i = 5\,\mathrm{s}^{-1}$ and subsequently $\dot{\gamma}_e = 1\,\mathrm{s}^{-1}$, with each shear lasting for 10 min.

In a step-down shear test, the stress evolution is tracked after a sudden decrease in shear rate from $\dot{\gamma}_i$ to $\dot{\gamma}_e$. Thixotropic materials usually present a decreasing stress at $\dot{\gamma}_i$ and an increasing stress at $\dot{\gamma}_e$, Figure 5.5C. These respectively correspond to the break-down and build-up process of microstructure [41]. Using $\dot{\gamma}_i = 5\,\mathrm{s}^{-1}$ and $\dot{\gamma}_e = 1\,\mathrm{s}^{-1}$, our binary suspension only presents stress decrease at the initial higher shear rate, Figure 5.5D. In the second stage with $\dot{\gamma}_e = 1\,\mathrm{s}^{-1}$, shear stress σ barely changes over time.

Based on these results, we conclude that the addition of large particles introduces a unique state transition. It differs from typical thixotropy and occurs as a new effect. The binary suspension can be freely switched between solid and liquid states by different flows, and each state permanently persists when left undisturbed. This transition not only manifests itself under routine laboratory operations, but also has an impact on rheological measurements (such as the protocol dependence in Fig. 5.2A and the 'stress overshoot' in Fig. 5.4B). When measuring our binary suspensions, therefore, special caution needs to be taken to ensure reproducible results.

5.3 Microstructure

To better understand the state transition, we investigated the *in-situ* structure under/after shear flow through rheo-confocal microscopy. We used two individual channels to separately image the two species of particles. We verified that the solid-liquid transition originates from a clear change in microstructure. To better distinguish the system state, we proposed a quantitative structural criterion.

5.3.1 Methods

To image the binary suspension after various preshears, we used our confocal rheo-imaging setup and again designed corresponding protocols. Similar to the measurement of yield stress upon preshear cessation, we first rejuvenate a sample and preshear it at a specific σ_{pre} until reaching a steady state. After 30 min at rest so that the sample may be fully gelled, we scan the sample in situ in 3D using confocal microscope. We use red to denote small particles (which are not quite solvable as single particles) and green to denote large particles.

Our suspension shows strong spatial heterogeneity in the microstructure. We used Moran's I, a popular tool in statistics and geography [198], to quantify this heterogeneity as a scalar. It actually has been used in image analysis to characterise spatial auto-correlation such as phase separation [199, 200]. Given the spatial distribution of a set of features, it evaluates whether a pattern is clustered, dispersed, or random. The higher Moran's I is, the more heterogeneous the pattern is. Figure 5.6 shows three typical instances.

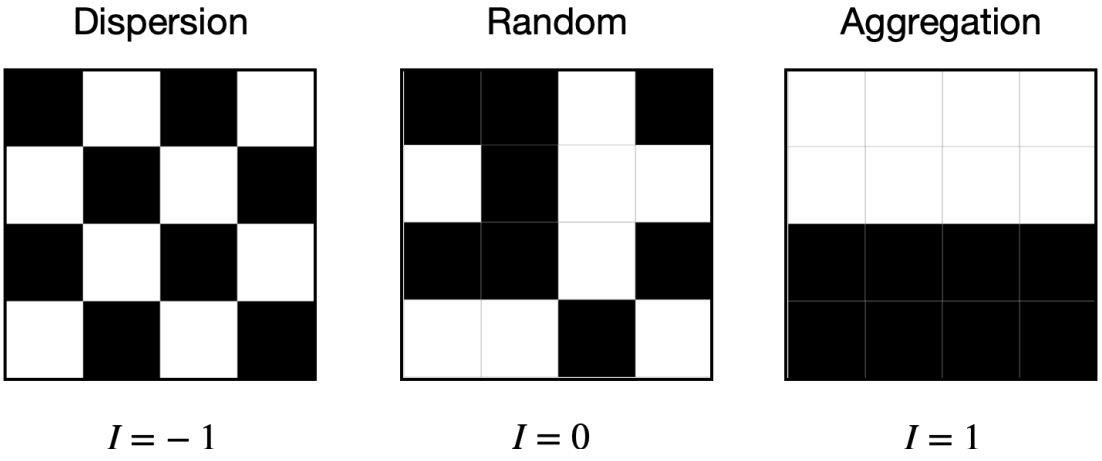

Figure 5.6 Moran's I in three schematic cases.

The calculation of Moran's I is based on feature locations and feature values simultaneously, given by:

$$I = \frac{N}{W} \frac{\sum_{i,j} w_{ij}(x_i - \overline{x})(x_j - \overline{x})}{\sum_i (x_i - \overline{x})^2}, \tag{5.1}$$

where N is the number of spatial units indexed by i and j; x is the feature of interest and $\overline{x}$ is the mean; w_{ij} is the spatial weight and W is the sum of all elements. Since our small particles are not quite resolvable as single particles, we use the pixels of confocal image as the features to calculate Moran's I. Specifically, we use the grayscale value of pixel element i as x_i in Eq. 5.1, and set w_{ij} to be 1 if pixel i and pixel j are neighbours and 0 otherwise. See more comments and details in the corresponding sections.

5.3.2 Structure in different states

For binary sample with $\phi_S = 10\,\%$ and $\phi_L = 20\,\%$, cessation after high preshear $\sigma_{\text{pre}} > \sigma_2 = 11\,\text{Pa}$ results in a solid state whereas medium preshear $\sigma_{\text{pre}} < \sigma_2$ results in a liquid state, Figure 5.3B, To probe the microstructure in different

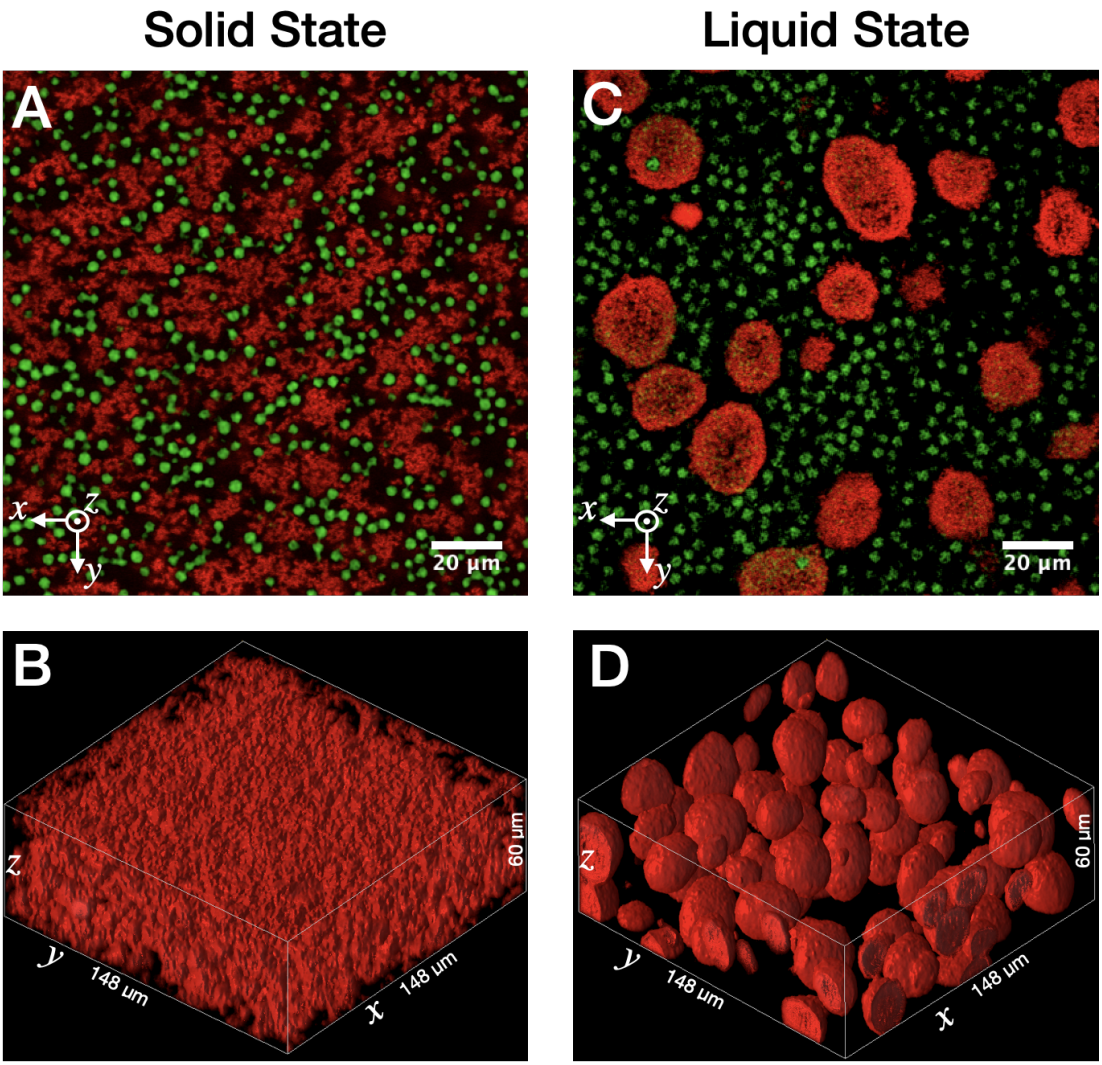

Figure 5.7 Confocal imaging of different states in a sample at $\phi_S = 10\,\%$ and $\phi_L = 20\,\%$. The solid and liquid states were prepared by preshear at $\sigma_{\text{pre}} = 100\,\text{Pa}$ and $\sigma_{\text{pre}} = 5\,\text{Pa}$ respectively, both lasting for 20 min. A. Confocal slice of solid state at height of $z \sim 30\,\mu\text{m}$. Large and small particles are labelled by green and red respectively. B is the 3D rendering of the confocal stack (small-particle channel). C and D are confocal slice and 3D rendering of the liquid state respectively. Velocity direction – x; vorticity direction – y; gradient direction – z.

states, we prepared solid and liquid states by preshears at $\sigma_{\text{pre}} = 100\,\text{Pa}$ and $\sigma_{\text{pre}} = 5\,\text{Pa}$ respectively. Each preshear lasted for 20 min to ensure a well-developed state. Upon preshear cessation, confocal imaging was carried out in three-dimensional space (148 µm × 148 µm × 60 µm), giving 3D stacks of images at different heights (z step interval $\sim 0.3\,\mu\text{m}$).

The two states present distinct microstructure. In the solid state, the small particles (red) form a ramified network with the large particles (green) embedded inside, Figure 5.7A. The 3D rendering of small-particle channel indicates a homogeneous gel matrix, Figure 5.7B. By contrast, the liquid state exhibits a collection of isolated large particles and globular blobs of small particles, in which large particles are occasionally trapped, Figure 5.7C. According to Figure 5.2A, the The solid state exhibits a finite yield stress ($\sigma_y = 2.6\,\text{Pa}$) while the liquid state does not. We thus infer that the gel matrix in the solid state percolates the whole sample, whereas the 'droplets' in the liquid state are disjoint from each other.

Compared with the solid state in Figure 5.7B, the 3D rendering of the liquid state (small-particle channel) in Figure 5.7D suggests a relatively heterogeneous structure. Visually, the blobs have a characteristic size of $\sim 20\,\mu\text{m}$ and are quite globular without obvious anisotropy. Differing from the loose clusters in colloidal gels [125, 201], these blobs are enclosed by sharp interfaces and appear to be more compact. This is reminiscent of typical liquid droplets which are also globular because of surface tension [202]. In this sense, we refer to our small-particle blobs as 'droplets' in the rest of this thesis. However, the lack of coalescence suggests that they are solid 'droplets'. This will be discussed in depth in Chapter 6.

5.3.3 Structure after different preshears

Different preshears lead to different states. As previously reported in Figure 5.3B, a critical stress $\sigma_2 = 11\,\text{Pa}$ demarcates high shear and medium shear, which result in solid and liquid states respectively. The microstructure in the two states are distinct, i.e. the structure of binary suspension is preshear-dependent.

We imaged the binary sample ($\phi_S = 10\,\%$ and $\phi_L = 20\,\%$) upon cessation of various preshears. Below the critical stress σ_2 (Fig. 5.8A, dotted line), i.e. in the medium shear regime, preshear results in the liquid state where the yield stress σ_y is unmeasurably low and 'droplets' with sharp interfaces are formed.

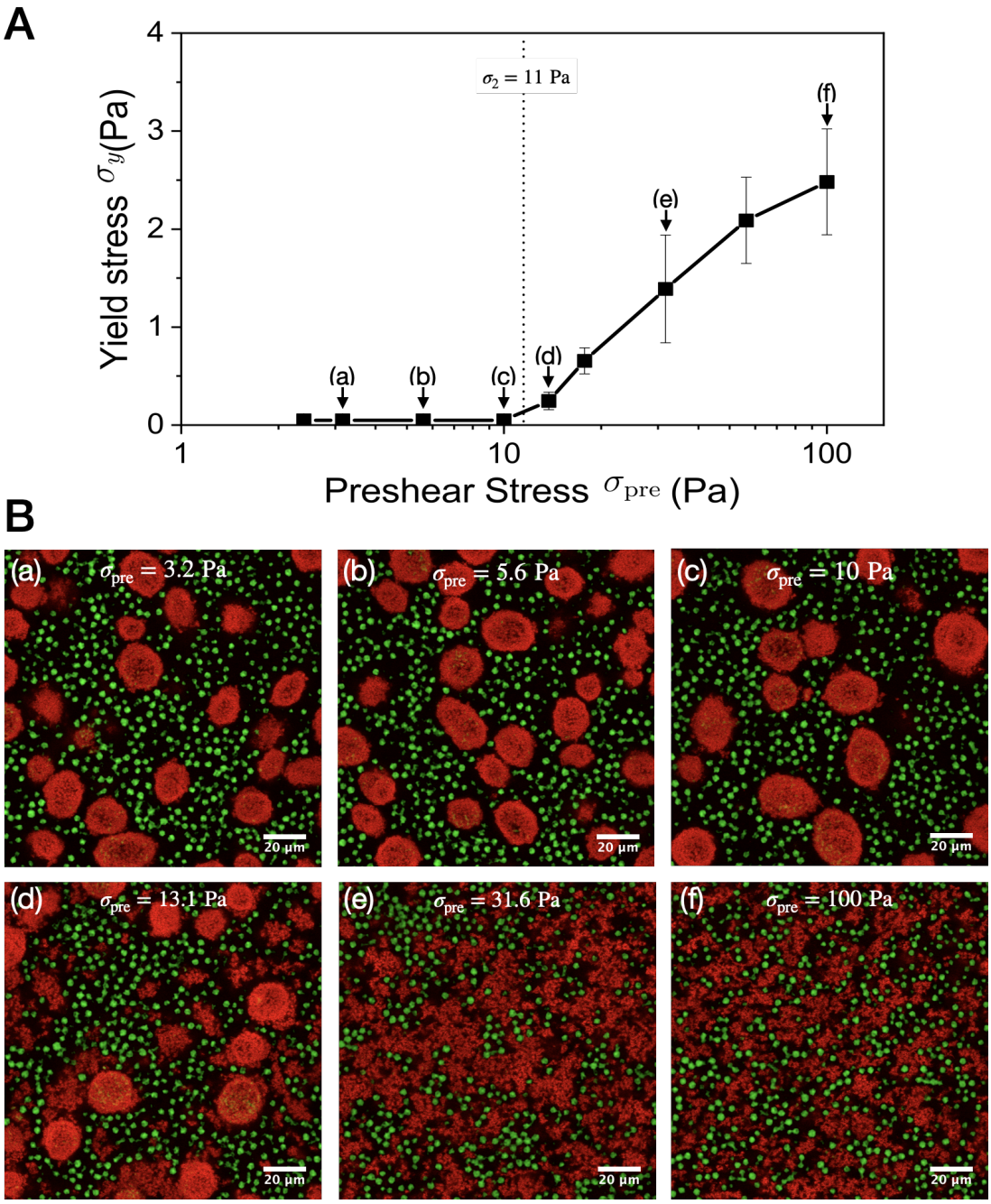

Figure 5.8 Preshear effect on the sample of $\phi_S = 10\,\%$ and $\phi_L = 20\,\%$. A. Yield stress σ_y varies as a function of preshear stress σ_{pre}. The critical stress $\sigma_2 = 11\,\mathrm{Pa}$ (dotted line) demarcates high shear and medium shear regimes. Reproduced from Figure 5.3B. B. Confocal images after different preshears, indicated by the arrows in A. The preshear stress σ_{pre} is annotated on the top of each image.

The structure after preshears at three stresses, $\sigma_{\text{pre}} = 3.2$, 5.6 and 10 Pa, appears visually indistinguishable, Figure 5.8B(a-c). That is, the liquid state has similar structure regardless of the preshear strength.

As preshear increases beyond σ_2, the sample responses like a solid after preshear cessation. The yield stress σ_y increases as a function of the preshear stress σ_{pre}, Figure 5.8A. This correlates with the microstructure. Preshear just above σ_2 ($\sigma_{\text{pre}} = 13.1$ Pa) produces a weak solid ($\sigma_y = 0.3$ Pa) where 'droplets' and tenuous clusters coexist as shown in Figure 5.8B(d). After preshear at $\sigma_{\text{pre}} = 31.6$ Pa, we did not observe 'droplets' within the imaging volume; instead small particles form a gel matrix and the yield stress increases to $\sigma_y = 1.4$ Pa, Figure 5.8(e). For stronger preshear at $\sigma_{\text{pre}} = 100$ Pa, the gel matrix appears to be more homogeneous and exhibits higher yield stress $\sigma_y = 2.5$ Pa, Figure 5.8B(f). Such preshear dependence has been observed in other colloidal gels [21, 159], and the structural behaviour will be quantitatively confirmed later.

5.3.4 Distinguishing between different states

To better characterise the state transition, it is important to precisely determine the state. In the previous discussion, we used the yield stress σ_y to distinguish between the solid state ($\sigma_y \geq 0.1$ Pa) and the liquid state ($\sigma_y < 0.1$ Pa). Yet in some cases, this method is insufficient. For example, in the case where 'droplets' and tenuous clusters coexist, Figure 5.8(d), a finite but small yield stress $\sigma_y = 0.3$ Pa is presented. Simply labelling such case as the solid state obscures important structural information. In addition, using the yield stress σ_y may misjudge the state at small ϕ_S, where σ_y in solid state may be too low to be measured.

Therefore, we use microstructure to distinguish between different states in this work. Since the condensed 'droplets' in the liquid state resembles the structure after phase separation, we thus define the structure with 'droplets' as the **phase-separated (PS) state**. Compared with the 'droplets', the gel matrix in the solid state is more spatially homogeneous. Based on the structural signature, we define the structure consisting of gel matrix and embedded large particles as the **homogeneous (H) state**.

In most cases shown in Figure 5.8, solid states have homogeneous structure and are in the H state, while liquid states are composed of phase-separated 'droplets'

and thereby in the PS state. However, it is difficult to precisely classify an intermediate state (such as the 'droplet'-cluster coexistence in Fig. 5.8B(d)) by direct visual observation. Under this context, we use a measure of spatial auto-correlation, Moran's I, to quantitatively distinguish different states.

We note that this method can be applied to both 2D slices and 3D stacks. Since the major structural change occurs in small particles, we therefore calculate Moran's I only in the small-particle channel. Even for the same sample at the same state, the I value varies from volume to volume. Hence for a specific sample presheared at a specific stress, we perform several imaging at different sites and use the average I. The standard deviation then gives a characteristic uncertainty $\Delta I \lesssim 0.01$. Note that the result is insensitive to the imaging condition (e.g. overall brightness).

Test on Moran's I

We first used two confocal slices of different states to test the validity of Moran's I. Visually, the structure of small particles in Figure 5.9A is less heterogeneous than that in Figure 5.9B. Since the small particles are attractive, the values of Moran's I are quite high in both cases. Compared with the homogeneous network in Figure 5.9C, which has a Moran's I of 0.87, the PS state in Figure 5.9D exhibits higher Moran's $I = 0.98$. This is consistent with our visual judgement, and the difference is significant compared with the characteristic uncertainty $\Delta I \lesssim 0.01$. Therefore, it is feasible to distinguish structural states by Moran's I.

Structural criterion $I_c = 0.95$

Moran's I was further tested in the binary sample at $\phi_S = 10\,\%$ and $\phi_L = 20\,\%$. After cessation of preshears at various σ_{pre}, 3D confocal stacks were imaged within a depth of 60 µm from the bottom, based on which Moran's I was calculated.

Not surprisingly, Moran's I varies as a function of preshear strength σ_{pre}, Figure 5.10 (red). As previously discussed, we defined the solid and liquid states based on the yield stress σ_y (Fig. 5.10, black) and accordingly mapped out the medium and high shear regimes. In the medium shear regime ($\sigma_{\mathrm{pre}} < \sigma_2$), Moran's I remains relatively high with $I \approx 0.97$, suggesting heterogeneous structure in the liquid state. As the preshear stress σ_{pre} increases beyond σ_2, Moran's I progressively

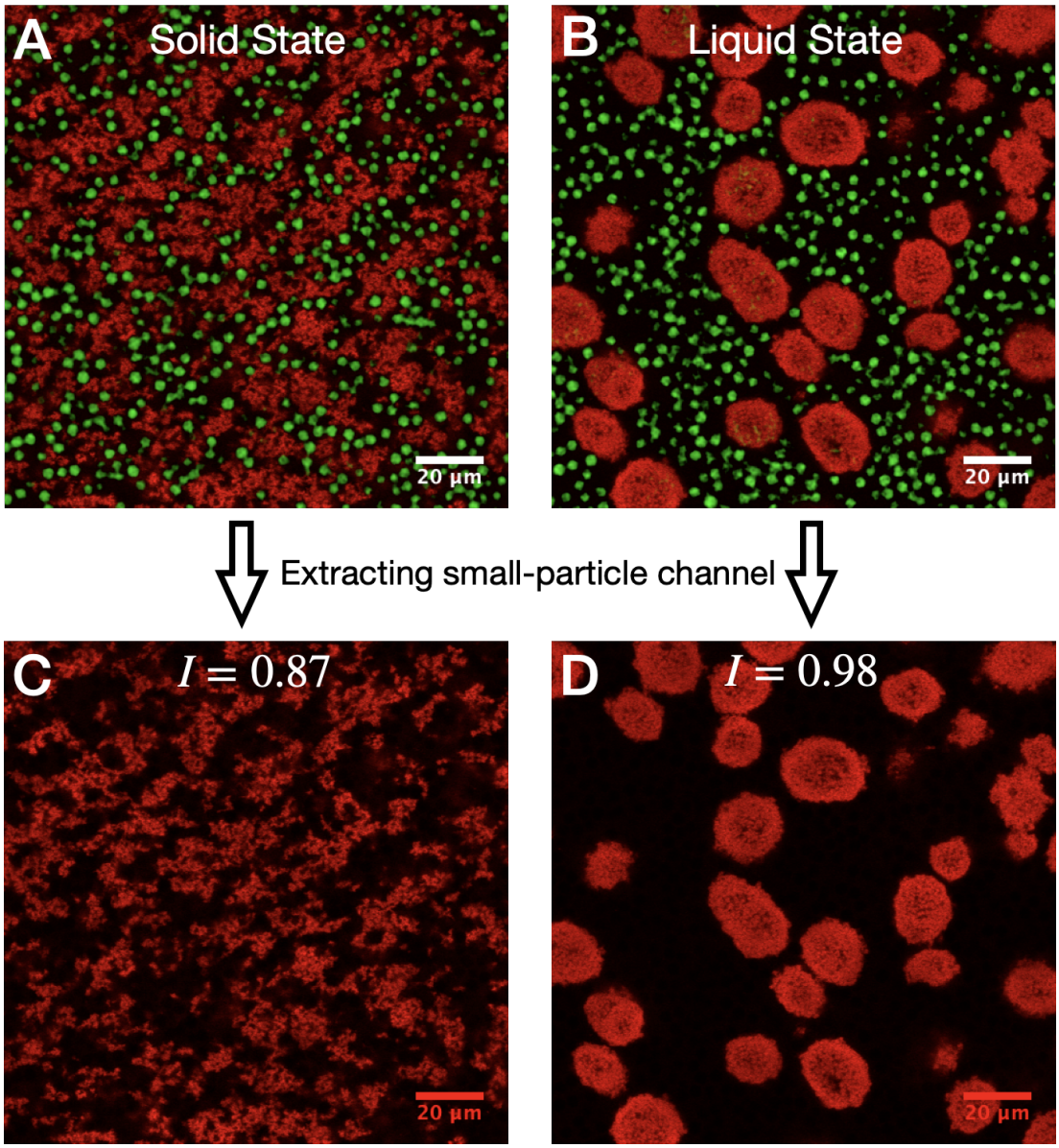

Figure 5.9 Validity test of Moran's I. A and B are confocal images (merged-channel) of the solid and liquid states respectively. To calculate Moran's I, we extract the small-particle channels as presented in C and D. The calculated Is are shown on the top of each image.

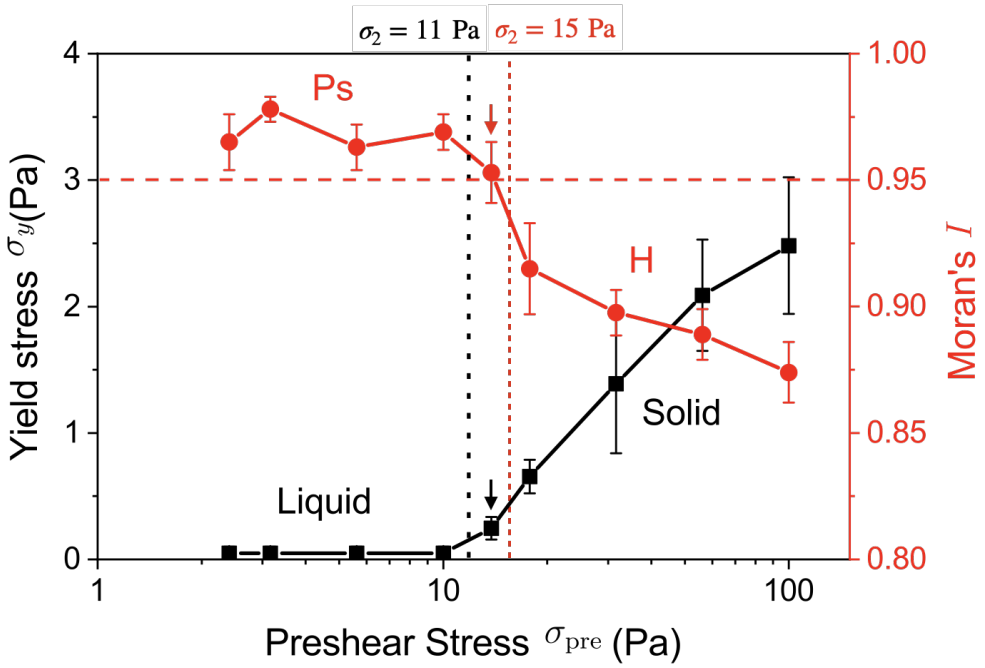

Figure 5.10 Preshear effect on sample of $\phi_S = 10\,\%$ and $\phi_L = 20\,\%$. Yield stress σ_y (reproduced from Fig. 5.3B) and Moran's I (calculated from 3D stacks) vary as functions of preshear stress σ_{pre}. The error bars of Moran's I (red) represent the standard deviation of I values in at least four confocal stacks. The black dotted line denotes the critical stress $\sigma_2 = 11\,\text{Pa}$ determined from rheological criterion, while the red dotted line denotes the critical stress $\sigma_2 = 15\,\text{Pa}$ determined from structural criterion ($I_c = 0.95$, red dashed line). Arrows indicate the sample which responses like a solid ($\sigma > 0.1\,\text{Pa}$ yet with a PS structure ($I > I_c$).

decreases along with the increase in yield stress σ_y. This is consistent with the confocal imaging in Figure 5.8B, where the structure becomes increasingly homogeneous as σ_{pre} increases.

Taking the rheology and the microstructure into consideration, here we define a critical $I_c = 0.95$, Figure 5.10 (red dashed line). In this definition, structure with $I < I_c$ is classified as the H state, whereas that with $I \geq I_c$ is classified as the PS state. As indicated by Figure 5.10, judgements from the yield stress σ_y and Moran's I mostly agree with each other: the H state ($I < I_c$) is solid-like ($\sigma_y \geq 0.1\,\text{Pa}$) and the PS state ($I \geq I_c$) is liquid-like ($\sigma_y < 0.1\,\text{Pa}$). This verifies the synchrony between structural transition and rheological transition.

One exception is the sample after preshear with stress $\sigma_{\text{pre}} = 13.1\,\text{Pa}$, as indicated by arrows in Figure 5.10. This sample exhibits a small yield stress ($\sigma_y = 0.3\,\text{Pa}$) yet a relatively heterogeneous structure ($I > I_c$). The confocal imaging shows

a coexistence of 'droplets' and tenuous clusters in Figure 5.8B(d). To better characterise the structural information, therefore, we use $I_c = 0.95$ as the only criterion to determine the system state (H: $I < I_c$; PS: $I > I_c$) in the rest of this thesis. This will lead to a small shift in the critical stress $\sigma_2 = 15\,\text{Pa}$, Fig. 5.10 (red dotted line), which appears to better characterise the critical point above which Moran's I starts to decrease drastically.

5.4 State diagram

We now demonstrate that there is a third shear regime in addition to the two that we have already described, and then construct a partial state diagram to map out the extent of these regimes in the ϕ_L–σ parameter space.

5.4.1 Three shear regimes

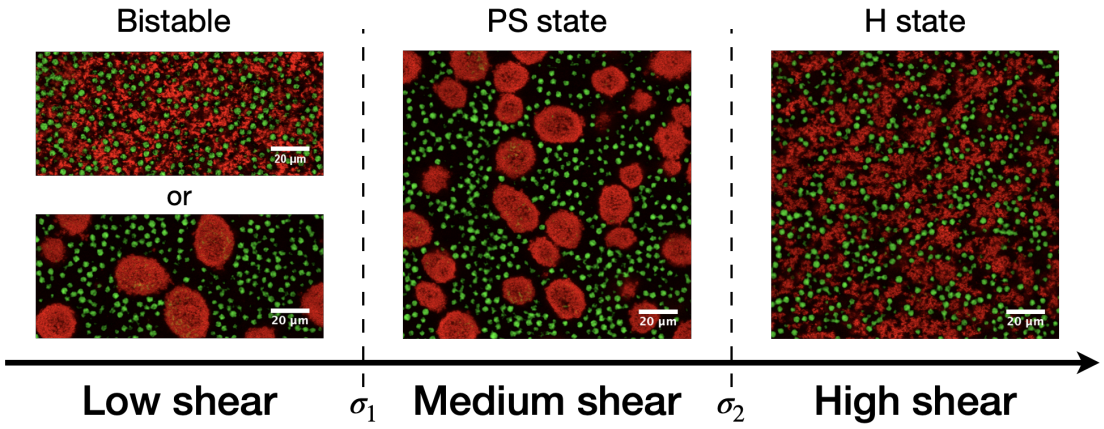

Figure 5.11 A sketch of three shear regimes. The confocal images are from the sample at $\phi_S = 10\,\%$ and $\phi_L = 20\,\%$, where $\sigma_1 = 3\,\text{Pa}$ and $\sigma_2 = 15\,\text{Pa}$.

For our binary suspension at $\phi_S = 10\,\%$ and $\phi_L = 20\,\%$, the magnitude of preshear determines its state. Accordingly, shear flow can be divided into different regimes. In previous sections, we identified two shear regimes demarcated by a critical stress $\sigma_2 = 15\,\text{Pa}$. Shear in the high shear regime ($\sigma > \sigma_2$) results in the H state while that in the medium shear regime ($\sigma < \sigma_2$) leads to the PS state. Moreover, detailed observation identified a bistable low shear regime. The boundary between low and medium shear regimes is denoted as σ_1. In this way, medium shear refers

to the shear with stress $\sigma_1 < \sigma < \sigma_2$, while low shear refers to the shear stress below σ_1. Figure 5.11 illustrates these three shear regimes.

High shear regime ($\sigma > \sigma_2$)

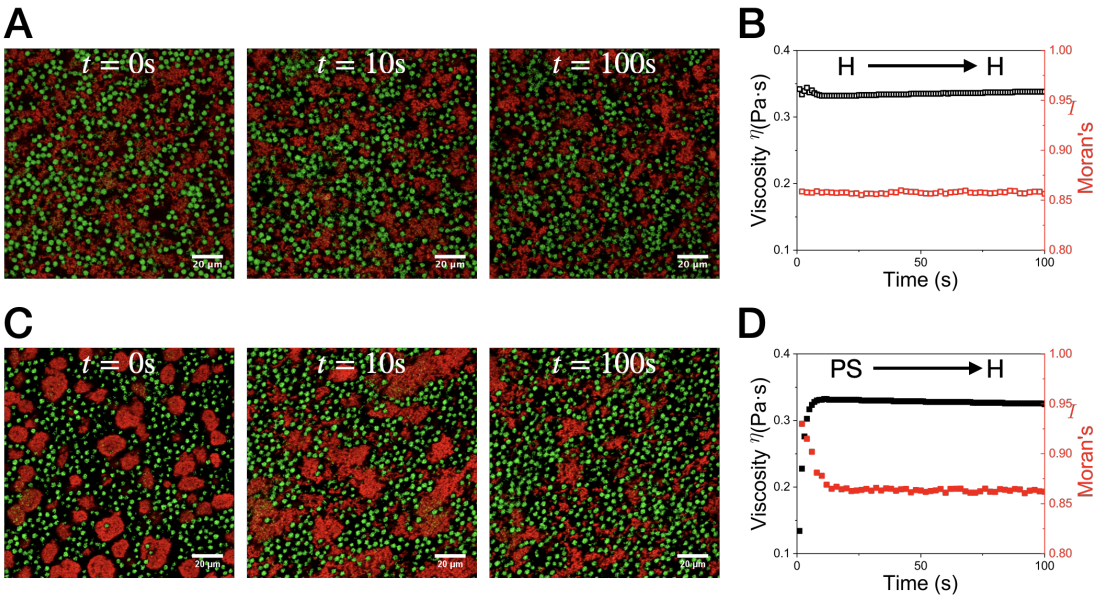

Figure 5.12 Different states under high shear ($\sigma = 100\,\text{Pa}$). The sample composition is $\phi_S = 10\,\%$ and $\phi_L = 20\,\%$. A. Confocal snapshots of an H state (prepared by preshear $\sigma_{\text{pre}} = 100\,\text{Pa}$) under high shear. Taken in the velocity-vorticity plane at a depth of 30 μm from the bottom. B. Evolutions of viscosity η (black) and Moran's I (red) for the H state under high shear. The Moran's I was calculated from the 2D confocal snapshots. Similarly, C and D record the evolution of a PS state (prepared by preshear $\sigma_{\text{pre}} = 5\,\text{Pa}$) under high shear.

Resulting in the solid-like H state, the high shear regime is history-independent and thus monostable. The final steady state upon cessation of high shear is always the H state regardless of history. We confirmed this using the sample of $\phi_S = 10\,\%$ and $\phi_L = 20\,\%$. Different initial states were prepared by different preshears in advance. Upon preshear cessation, we imposed a shear with high stress $\sigma = 100\,\text{Pa}$. Simultaneously, time-lapsed confocal snapshots were taken at height[1] of 30 μm under shear flow.

If the binary sample is initially in H state, high shear firstly collapses the gel matrix into small pieces and then drives them to flow. During the whole

[1]This ensures that we are at least one 'droplet' diameter clear of the bottom plate.

process, the structure remains homogeneous (Fig. 5.12A) and Moran's $I \approx 0.86$ is constantly low (Fig. 5.12B, red). Consistent with the evolution of Moran's I, the viscosity η shows little variation[2] under high shear, Figure 5.12B (black).

For an initial PS state, by contrast, high shear ruptures the 'droplets' in seconds and the suspension is then rejuvenated into the H state, Figure 5.12C. The evolution of Moran's I records the structural change: from heterogeneous to homogeneous (I from high to low), Figure 5.12D (red). Meanwhile, the viscosity η increases rapidly and reaches the steady state almost together with Moran's I, Figure 5.12D. The PS $\rightarrow$ H transition takes around 10 s, which is consistent with the fast solidification by vortex mixer in Figure 5.1. Note that the final steady states in Figure 5.12B and D have similar viscosity $\eta \approx 0.33\,\mathrm{Pa\,s}$ and Moran's $I \approx 0.86$, indicating the history-independence in the high shear regime.

Medium shear regime ($\sigma_1 < \sigma < \sigma_2$)

Leading to the PS state, the medium shear regime is history-independent and monostable as well. Analogous to the experiment above, we studied different states under a medium shear ($\sigma = 5\,\mathrm{Pa}$). As shear proceeds, the microstructure in the velocity-vorticity plane was recorded by rheo-confocal microscopy, whereas the evolution of viscosity η was measured simultaneously.

The H $\rightarrow$ PS transition, i.e. 'droplets' formation, resembles phase separation. Under medium shear, the gel matrix in the H state yields and quickly collapses into small pieces, which move with flow and gradually aggregate into 'droplets' with sharp interfaces, Figure 5.13A. Moran's I, increasing from 0.87 to 0.97, illustrates the structural evolution under medium shear, Figure 5.13B (red). At the same time, the viscosity η decreases over time until reaching a steady state after $\sim 10\,\mathrm{min}$. The long duration is consistent with the prolonged fluidisation on roller bank in the lab demonstration (Fig. 5.1).

If the sample starts from a PS state, the medium shear simply drives 'droplets' to flow without rupturing them, Figure 5.13C. In this way, the final state is exactly the same as the initial state: PS state. The evolution of Moran's I confirms that the structural heterogeneity barely changes under medium shear, Figure 5.13D (red). The viscosity η remains almost unchanged as well, Figure 5.13D (black).

[2]The H-state sample has already yielded by our first measurement, so that the viscosity η is finite.

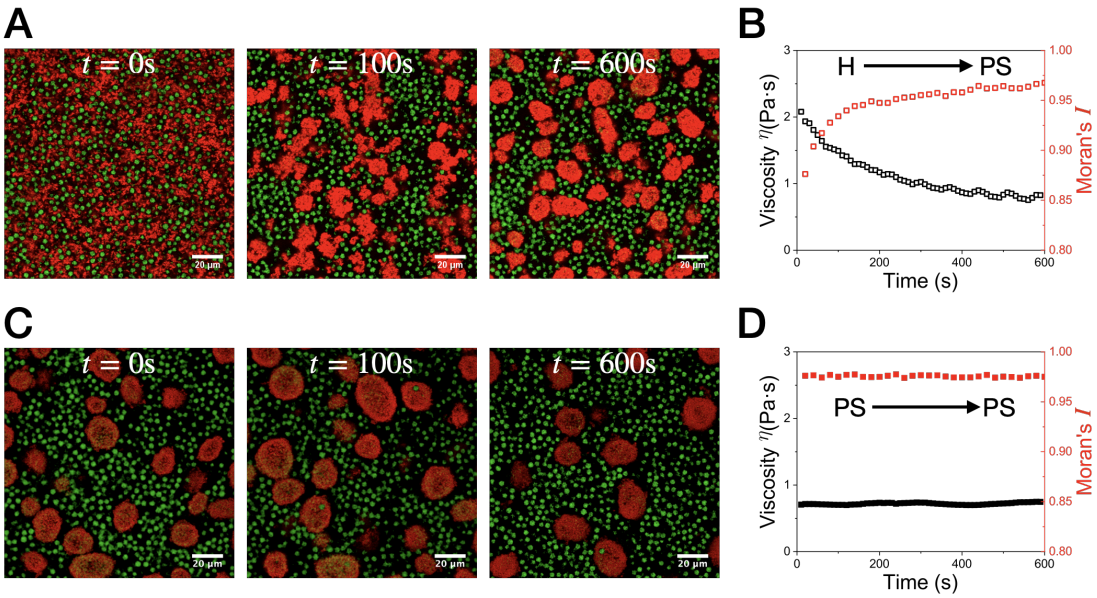

Figure 5.13 Different states under medium shear ($\sigma = 5\,\mathrm{Pa}$). The sample composition is $\phi_S = 10\,\%$ and $\phi_L = 20\,\%$. A. Confocal snapshots of an H state (prepared by preshear $\sigma_{\mathrm{pre}} = 100\,\mathrm{Pa}$) under medium shear. Taken in the velocity-vorticity plane at a depth of 30 μm from the bottom. B. Evolutions of viscosity η (black) and Moran's I (red) for the H state under medium shear. The Moran's I was calculated from the 2D confocal snapshots. Similarly, C and D record the evolution of a PS state (prepared by preshear $\sigma_{\mathrm{pre}} = 5\,\mathrm{Pa}$) under medium shear.

Again, regardless of the initial state, prolonged medium shear gives rise to PS states with similar viscosity $\eta \approx 0.65\,\mathrm{Pa\,s}$ and Moran's $I \approx 0.97$. Medium shear regime does not depend on history state either.

In both high and medium shear regimes, history is not important: the outcome of shear does not depend on the starting state and there exists only one stable state after infinitely long shear. This monostability leads to the reversibility in the solid-liquid transition. Yet the two shear regimes are indeed time-dependent, as state transitions (H → PS or vice versa) take time.

Low shear regime ($\sigma < \sigma_1$)

The system develops memory when the shear stress σ drops below another critical value σ_1. We therefore define a low shear regime ($\sigma < \sigma_1$) in which, unlike the medium and high ones, the properties of a sample depends on history. Specifically,

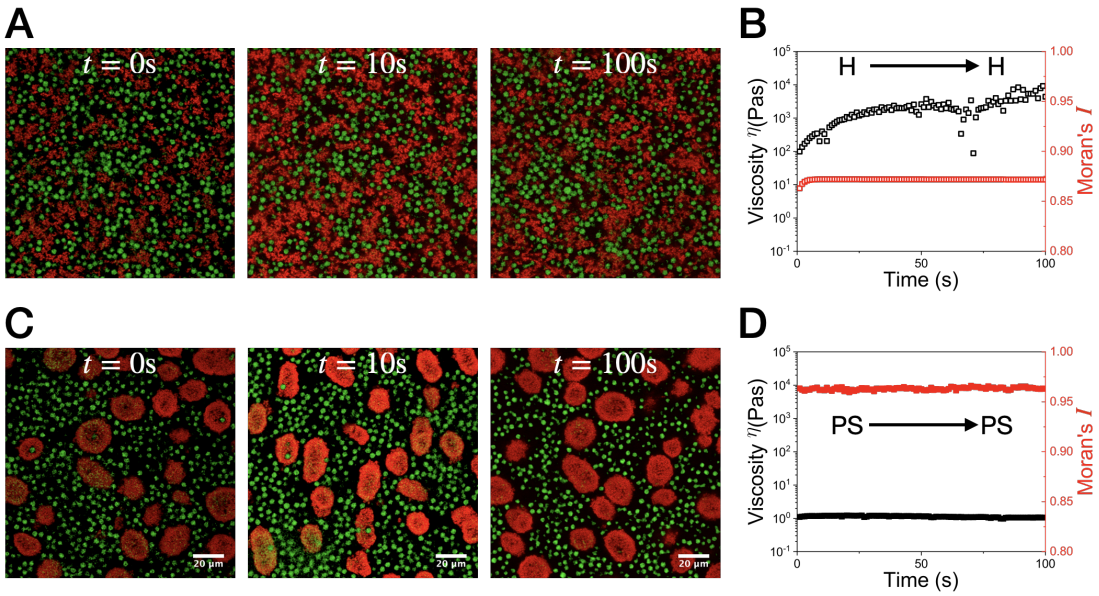

Figure 5.14 Different states under low shear ($\sigma = 1\,\mathrm{Pa}$). The sample composition is $\phi_S = 10\,\%$ and $\phi_L = 20\,\%$. A. Confocal snapshots of an H state (prepared by preshear $\sigma_{\mathrm{pre}} = 100\,\mathrm{Pa}$) under low shear. Taken in the velocity-vorticity plane at a depth of 30 µm from the bottom. B. Evolutions of viscosity η (black) and Moran's I (red) for the H state under low shear. The Moran's I was calculated from the 2D confocal snapshots. Similarly, C and D record the evolution of a PS state (prepared by preshear $\sigma_{\mathrm{pre}} = 5\,\mathrm{Pa}$) under low shear.

shear stress below σ_1 can neither drive an H state to phase separate into a PS state, nor rejuvenate a PS state into an H state. As long as the imposed shear is in the low shear regime, the final state is exactly the same as the initial state regardless of the duration. Since there exists two stable states in binary suspensions, the low shear regime is bistable.

We confirmed the bistability by imposing a low shear ($\sigma = 1\,\mathrm{Pa}$) to an H state and a PS state respectively, Figure 5.14. The sample in the H state is a solid with yield stress $\sigma_y \approx 2.5\,\mathrm{Pa}$. Therefore, 1 Pa shear only drives it to creep without collapsing the gel matrix. The apparent viscosity η remains high under low shear, indicating that the sample is a creeping solid, Figure 5.14B (black). Meanwhile, Moran's I is constantly at a low level (≈ 0.87), Figure 5.14B (red). These results illustrate that the H state persists under low shear.

By contrast, the sample in PS state is a flowable liquid without yield stress. Under 1 Pa low shear, the PS state flows with a steady shear rate $\dot{\gamma} \approx 1\,\mathrm{s}^{-1}$ and thereby a steady viscosity $\eta \approx 1\,\mathrm{Pa\,s}$, Figure 5.14D (black). Such shear is too

weak to rupture the 'droplets' (Fig. 5.14C), and the evolution of Moran's I in Figure 5.14D (red) confirms that the microstructure remains heterogeneous under low shear. If comparing Figure 5.14B and D, we will notice that the consequent steady states after low shear are different in both Moran's I and viscosity η. Unlike medium shear and high shear, the final state depends on the initial state in the low shear regime. This regime is bistable since two stable states exist after infinitely long shear. If viewing quiescence as a special low shear, the memory in the solid-liquid transition (Fig. 5.1) can then be explained by such bistability.

Two transition boundaries

There are therefore three different regimes and two transition boundaries: from bistability to phase separation at σ_1, and from phase separation to homogenisation at σ_2. We now attempt to understand the position of these two transition boundaries.

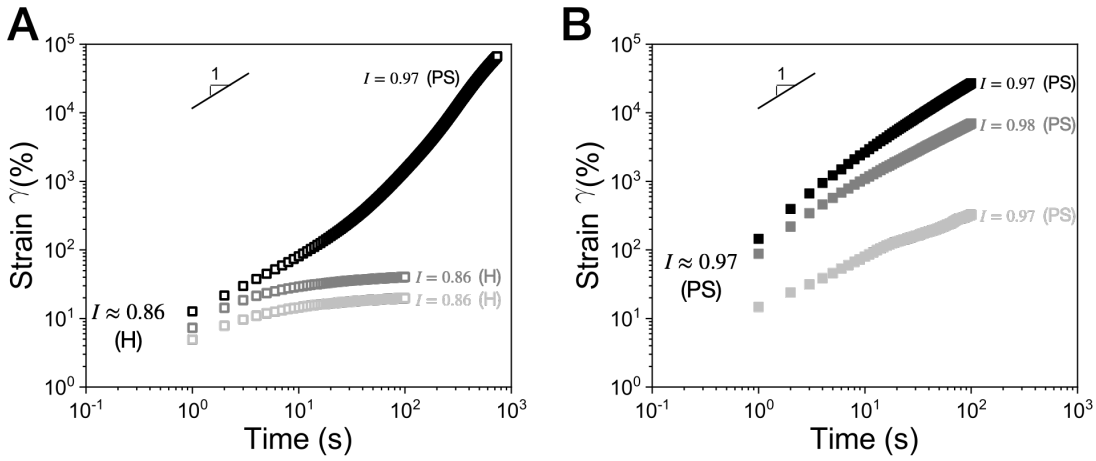

Figure 5.15 Strain evolution of sample at $\phi_S = 10\,\%$ and $\phi_L = 20\,\%$ under low and medium shears. A. H states (prepared by preshear $\sigma_{\text{pre}} = 100\,\text{Pa}$) under shear stresses (from bottom to up) $\sigma = 1$, 2 and 3 Pa. B. PS states (prepared by preshear $\sigma_{\text{pre}} = 5\,\text{Pa}$) under shear stresses (from bottom to up) $\sigma = 1$, 2 and 3 Pa. The initial and final values of Moran's I are noted for each shear stress.

Shears at three different stresses σ were successively imposed on an H-state sample at $\phi_S = 10\,\%$ and $\phi_L = 20\,\%$, Figure 5.15A. At $\sigma = 1$ and 2 Pa, which are below the H-state yield stress σ_y, the sample creeps to a finite strain without yielding. The structure barely changes under shear and the final Moran's I is almost the same as the initial value, Figure 5.15A. When sheared at $\sigma = 3\,\text{Pa}$, the sample yields and continuous flow occurs with the shear rate $\dot{\gamma}$ increasing from $0.1\,\text{s}^{-1}$ to

$1\,s^{-1}$. After around 1000 s, Moran's I increases from 0.86 to 0.97, indicating an H $\rightarrow$ PS transition. By contrast, shearing a PS state at these shear stresses produces only PS state, Figure 5.15B. This suggests that $\sigma = 1$ and 2 Pa are low shear and $\sigma = 3$ Pa is medium shear. The lower transition boundary $\sigma_1 = 2.5 \pm 0.5$ Pa is comparable to the yield stress $\sigma_y = 2.6$ Pa of the solid state (Fig. 5.2A).

The upper transition boundary σ_2 demarcates medium and high shears. In the medium shear regime ($\sigma < \sigma_2$), 'droplets' are formed in the PS state which can be rejuvenated back into the H state if sheared above σ_2. In this sense, σ_2 represents the shear stress beyond which 'droplets' are broken, i.e. the breaking stress σ_b. This agrees with our observation in Figure 5.8B.

These considerations suggest that the lower boundary, σ_1, should be identified with the yield stress of the H state σ_y, and the upper boundary, σ_2, should be identified with the breaking strength of the 'droplets' σ_b. Hereafter, we will therefore use σ_y and σ_b to refer to these boundaries.

5.4.2 State diagrams

Given the bistable state transition, a binary suspension is characterised by the two transition boundaries σ_y and σ_b. Previous results were mostly from the sample at $\phi_S = 10\,\%$ and $\phi_L = 20\,\%$, where $\sigma_y = 2.5$ Pa and $\sigma_b = 15$ Pa. Further investigation reveals that the flow-switched transition occurs at a wide spectrum of ϕ_S and ϕ_L. Studying how the state boundaries vary with particle concentrations would improve fundamental understanding on binary systems. In this section, we illustrate the structural behaviour of binary suspensions by means of state diagram.

$\phi_S = 10\,\%$

Following the protocol in Chapter 4, we prepared binary samples at $\phi_S = 10\,\%$ with various ϕ_L. Through rheo-confocal microscopy, three shear regimes were mapped out for each sample. We summarise the results in the form of state diagram in Figure 5.16A. Since we controlled the shear stress σ and varied the large particle volume fraction ϕ_L during experiments, the diagram has σ and ϕ_L as axes.

At $\phi_L = 0$, the binary suspension reduces to a $\phi = 10\,\%$ gel. Though the gel

structure does depend on shear strength σ, we did not observe phase-separated 'droplets' in the gel regardless of shear stress. The microstructure is always homogeneous with Moran's $I < 0.95$. In this sense, the gel has one stable state with a finite yield stress $\sigma_y \approx 1\,\text{Pa}$. Shear above σ_y results in a homogeneous state (■ in Fig. 5.16) which re-gels upon shear cessation. When sheared below σ_y, no flow (× in Fig. 5.16) takes place. The sample remains monostable up to $\phi_L = 10\,\%$.

Bistability occurs from $\phi_L = 10\,\%$ to $40\,\%$. For a specific point i in the diagram, after shear with stress $\sigma = \sigma_i$, the binary sample at $\phi_L = \phi_{L,i}$ is either in the H state (■), the PS state (●) or bistable (×). As ϕ_L increases, both transition boundaries σ_y and σ_b increases. Compared with the upper boundary σ_b, the lower one σ_y grows faster with ϕ_L. The two boundaries meet each other at $\phi_L \approx 40\,\%$, above which the sample again becomes monostable.

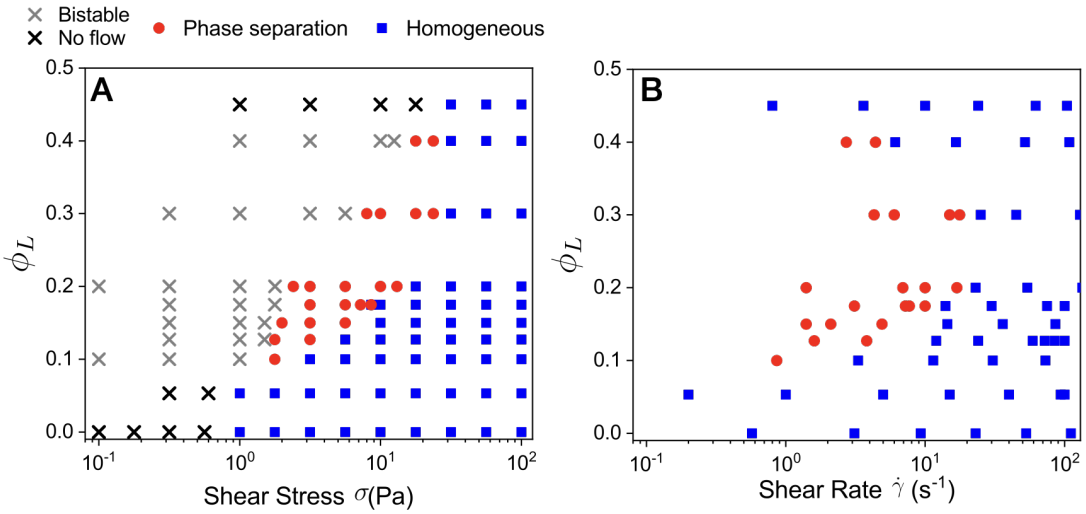

Figure 5.16 State diagram at $\phi_S = 10\,\%$. A. σ–ϕ_L diagram. For each data point, we first rejuvenated the sample at 100 Pa and then imposed the corresponding shear stress σ for sufficiently long until reaching the steady state. Upon flow cessation, confocal imaging was performed in 3D and Moran's I was calculated from the 3D stacks to determine the state. B. $\dot{\gamma}$–ϕ_L diagram converted from A. We replot the H (■) and PS (●) states in A using the steady state shear rate $\dot{\gamma}$ versus ϕ_L.

The absence of PS state at high concentration $\phi_L = 45\,\%$ can be interpreted as σ_y exceeding σ_b, i.e. putative 'droplets' cannot survive a stress needed to yield the gel in the first place. This may also explains the monostability at low ϕ_L. In this way, the state diagram (Fig. 5.16A) is mainly characterised by the two boundaries, which vary as functions of the large particle concentration ϕ_L.

Stress σ or rate $\dot{\gamma}$?

So far, we have reported our results in terms of stresses. This was partly in anticipation of our identification of the lower boundary as the yield stress σ_y. However, using stress σ as the control variable introduces complications in the bistable regime of low shear. In principle, this regime can be skipped by using shear rate $\dot{\gamma}$, since any non-zero $\dot{\gamma}$ induces stress $\sigma > \sigma_y$. In this way, only the two monostable shear regimes are left, and the two stress boundaries σ_y and σ_b reduce to one rate boundary $\dot{\gamma}_2$ which demarcates medium and high shears. We expect the $\dot{\gamma}$–ϕ_L state diagram to be like Figure 5.16B.

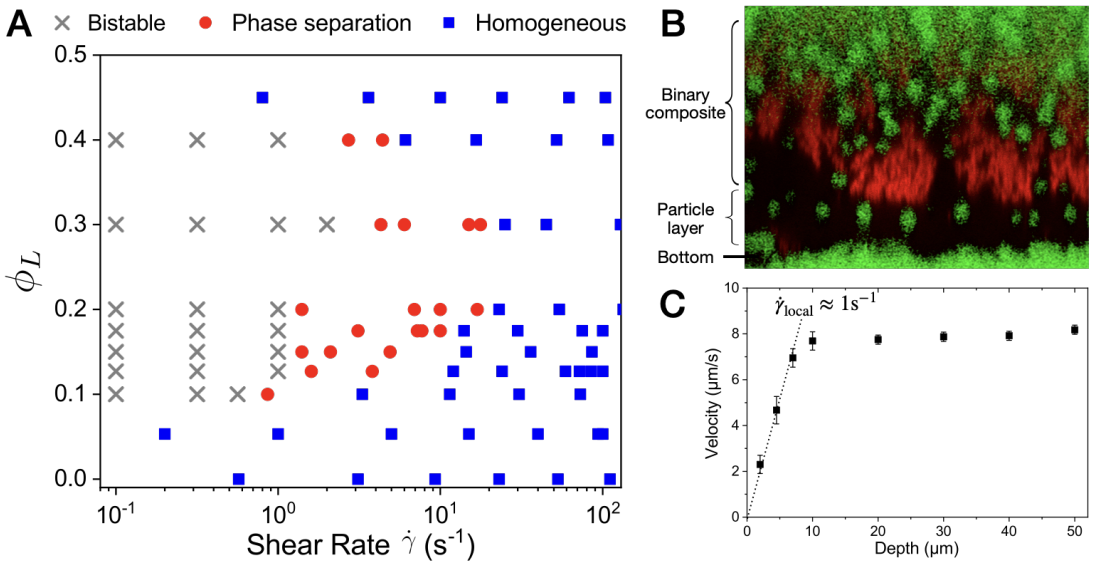

Figure 5.17 A. $\dot{\gamma}$–ϕ_L state diagram, determined by controlling the shear rate $\dot{\gamma}$. We prepared an H state by preshear $\sigma_{pre} = 100\,\text{Pa}$ in the sample of $\phi_S = 10\,\%$ and $\phi_L = 20\,\%$, and then imposed a low shear rate $\dot{\gamma} = 0.1\,\text{s}^{-1}$. B. Confocal snapshot in the velocity-gradient plane taken after 1 min shear. C. Velocity profile under $\dot{\gamma} = 0.1\,\text{s}^{-1}$ shear. Through particle image velocimetry (PIV) on MATLAB, the velocity of each data point was determined from the time-lapsed confocal images in the velocity-vorticity plane. The dashed line indicates a local shear rate $\dot{\gamma}_{local} \approx 1\,\%$ in the particle layer.

In practice, however, we still observed the bistable low shear regime when controlling the shear rate $\dot{\gamma}$, Figure 5.17A. At low-rate shear, the 'droplets' in the PS state persist, whereas the homogeneous gel in the H state can also 'survive' by means of slipping. Such slipping results from large particle segregation. When the gel matrix of an H state is sheared at low rate ($\dot{\gamma} = 0.1\,\text{s}^{-1}$), one or a few layers of large particles quickly form at the bottom, Figure 5.17B. While most of the applied shear is localised in the particle layer, the binary composite on the top is

barely sheared, Figure 5.16C. By 'sacrificing' a small fraction of large particles, the bulk homogeneous structure could persist under low-rate shear. This slipping, or equivalently the low shear rate regime, usually occurs at $\dot{\gamma} \lesssim 1\,\mathrm{s}^{-1}$, Figure 5.17A.

In this way, reporting in either stress σ or rate $\dot{\gamma}$ results in three shear regimes with the lowest one being bistable. Compared with the two rate boundaries, the physical meaning of σ_y and σ_b, corresponding to the yield stress and breaking stress respectively (see Sec. 5.4.1), are more clear. In addition, by changing the environment temperature, we found that the stress boundaries are more robust than the rate boundaries.

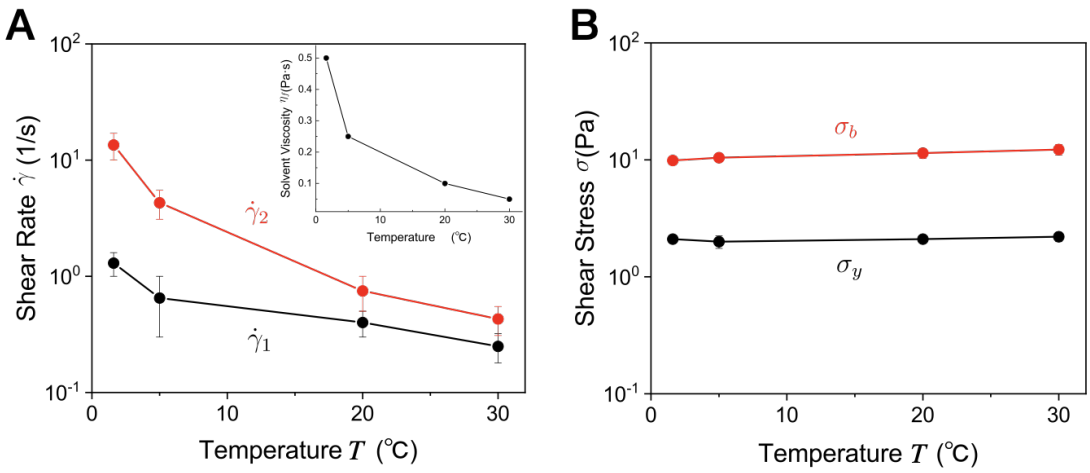

Figure 5.18 Transition boundaries in the sample of $\phi_S = 10\,\%$ and $\phi_L = 20\,\%$ at different temperatures. A. Two critical shear rates vary as functions of temperature. Inset: relation of temperature and solvent viscosity η. B. Two critical shear stresses vary as functions of temperature.

When we changed the environment temperature ranging from 1.5 °C to 30 °C, the solvent viscosity η_f varies by almost an order of magnitude, Figure 5.18A (inset). At different temperatures[3], we probed the three shear regimes at $\phi_S = 10\,\%$ and $\phi_L = 20\,\%$. Both the two critical rates strongly depend on the environment temperature, Figure 5.18A. By contrast, the critical stresses $\sigma_y \approx 2.5\,\mathrm{Pa}$ and $\sigma_b \approx 10\,\mathrm{Pa}$ remain almost constant, Figure 5.18B.

Throughout the thesis, therefore, we control either stress σ or rate $\dot{\gamma}$ in experiments according to the specific situation, but only report in stress σ unless otherwise stated.

[3]Theoretically, hydrophobic interaction is an entropic effect and thereby depends on the temperature. Yet here the temperature change in Kelvin unit K is sufficiently small ($\Delta T/T \sim 5\,\%$) so that the impact on the hydrophobic interaction between small particles is neglectable.

Other ϕ_S

The state diagram was further explored at four different small particle volume fraction ϕ_S, Figure 5.19. For the ease of comparison, we still report the diagram in ϕ_L–σ plot, with different symbols representing different states.

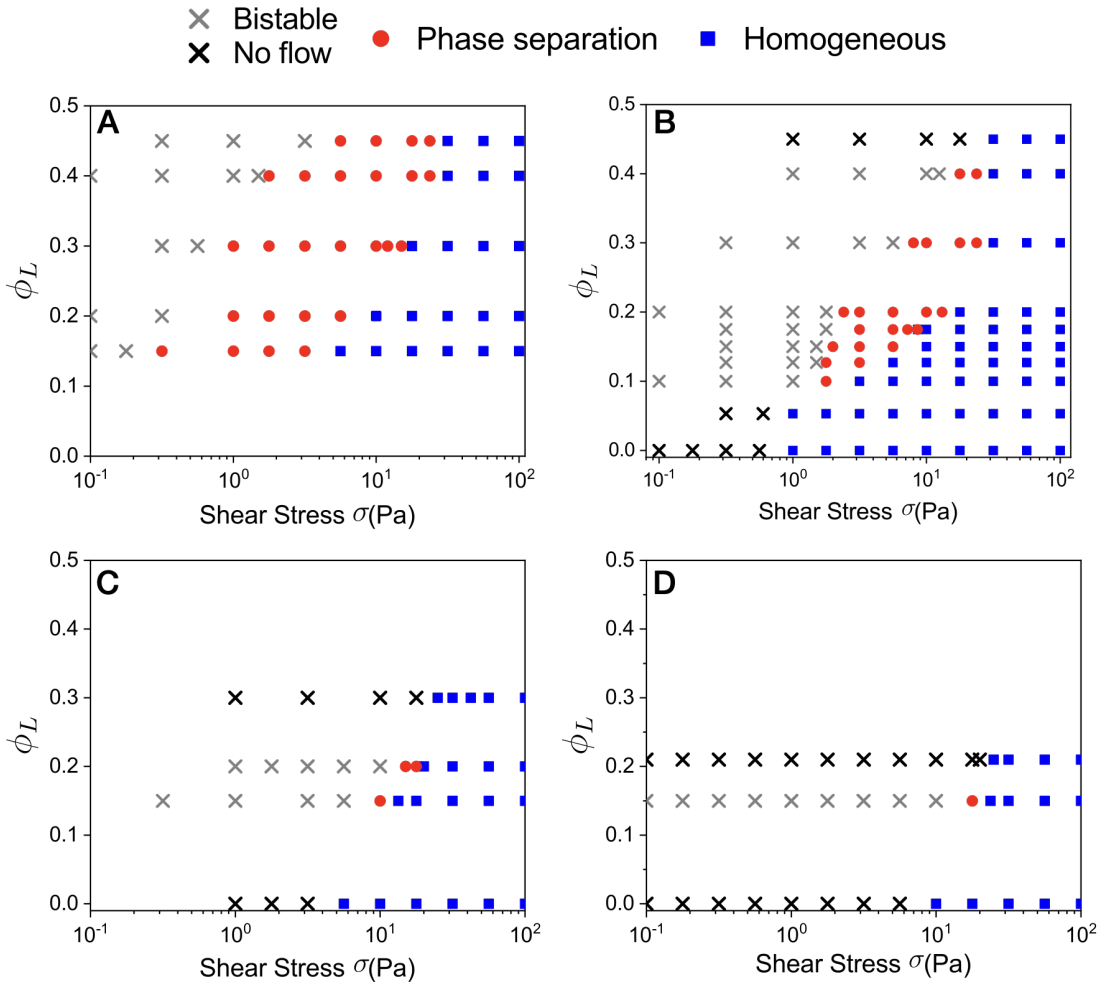

Figure 5.19 Slices of state diagram at four different ϕ_S. A. $\phi_S = 5\,\%$. B. $\phi_S = 10\,\%$, reproduced from Figure 5.18. C. $\phi_S = 15\,\%$. D. $\phi_S = 20\,\%$.

In each diagram, both σ_y and σ_b increases with ϕ_L. In the diagrams at $\phi_S = 10\,\%$, $15\,\%$ and $20\,\%$, the sample presents a re-entrant transition as ϕ_L increases: it switches from a monostable gel to a bistable suspension and finally turns back into a monostable gel. This indicates that σ_y increases more rapidly than σ_b with ϕ_L.

If we consider a fixed ϕ_L (e.g. $\phi_L = 20\,\%$), we will find that σ_y and σ_b both increases with ϕ_S and σ_y appears to increase more rapidly. As ϕ_S increases, the

medium shear regime progressively narrows down. In the $\phi_S = 20\,\%$ diagram, Figure 5.19D, there is only one data point exhibiting phase-separated 'droplets'. So there may be a critical $\phi_S^{\max} \gtrsim 20\,\%$ at which σ_y catches up σ_b. No phase separation is expected with $\phi_S > \phi_S^{\max}$.

5.5 Conclusions

In this chapter, we explored our binary suspension in depth and demonstrated a unique flow-switched transition. We showed that the rheology of a binary suspension is bistable and can be switched from a solid state to a liquid state (or vice versa) by external shear flow. We designed a series of measuring protocol to quantitatively demarcate different flow regimes and identify the physical meaning of regime boundaries.

Differing from thixotropy in general gels, this transition indicates a new effect from the additional large particles. Rheo-confocal microscopy reveals a clear structural difference between the solid and liquid states. To better determine the system state, we quantified the structural heterogeneity by means of Moran's I and propose a critical I_c to distinguish H and PS state. In the end, we mapped out the shear regimes at different particle compositions and thereby constructed a state diagram which enables dynamical control on the binary suspensions.

However, the fundamental understanding on the flow-switched transition is hitherto poor. For example, we have no clue about why the transition boundaries (σ_y and σ_b) vary with particle compositions (ϕ_S and ϕ_L). According to the physical meanings of the two boundaries, σ_y and σ_b are closely related to the property of H and PS state. In the next chapter, we will further explore the macroscopic properties of different states.

Chapter 6

Macroscopic Properties of the Two States

In our binary suspensions, a unique solid-liquid transition, exhibiting both reversibility and memory, is triggered by shear flow. In the last chapter, we demonstrated that this transition in the rheology could be attributed to a clear change in the microstructure. Applying a shear with high stress (or rate) homogenises the suspension, so that upon shear cessation the system quickly re-gels into a solid with the small particles forming a ramified network with large particles embedded inside. In contrast, flow at moderate shear stresses/rates causes the small particles to collapse into disjoint 'droplets' surrounded by the large particles. Without the gel network, the system instead flows like a liquid. These changes in the microstructure define two distinct states for our system: a homogeneous (H) state and a phase-separated (PS) state. In the previous chapter we mapped out the state behaviour, varying the applied shear and particle concentrations. We found three distinct three shear regimes. They correspond to high and medium shear regimes where the system ultimately evolves into either the H or PS state given sufficient time, as well as a bistable low-shear regime where the suspension remains in its initial state.

In this chapter, we examine the characteristics of the two different states in more depth. In particular, for the H state we focus on the how the composite rheology (e.g. yield stress and viscoelasticity) varies with the presence of large particles. For the PS state, we explore the microstructure, packing density and morphology of the small-particle 'droplets' which form under medium shear, as well as how

these ‘droplets’ fail and rupture at high shear. From a better understanding the nature of these two different states, we can begin to unravel the factors controlling the state boundaries in the diagram.

6.0.1 Methods

Here we briefly discuss the methods we used when investigating the two states. To prepare a well-developed state before measurement, we applied high and medium shears on samples, both lasting for sufficiently long until reaching a steady state. For H-state samples, we then waited at rest for 30 min so that the small particles have time to diffuse and aggregate and finally form a gel matrix. To prevent possible sedimentation, we did not do so for PS-state samples from medium preshear; instead we measured them immediately after preshear.

We mainly study the rheology of H state and the structure of PS state. Measurement on the H-state samples, i.e. particle-filled gels, has been introduced in previous chapters. We used creep test to measure the yield stress and small-amplitude oscillatory shear to explore the linear viscoelasticity.

As for the PS state, we mainly used dual-channel confocal imaging to study the structure, as well as cryo-SEM as a supplement to explore the interior of ‘droplets’. Besides Moran’s I which has been introduced in the last chapter, we also used other methods to quantify our observations. Image processing on 3D confocal stacks enables us to identify individual ‘droplets’ and measure their properties one by one. Specifically, we used mean-shift clustering to characterise each ‘droplets’ in terms of size and shape and thereby did the statistics. We also proposed a method to estimate the internal volume fraction of ‘droplets’ by simply thresholding and dilating/eroding.

Details of these methods we used can be found in the corresponding sections.

6.1 H state: particle-filled gel

From the structural perspective, an H state can be decomposed into isolated large particles of size $d_L = 4\,\mu\text{m}$ and a ramified network of small particles ($d_S = 482\,\text{nm}$), Figure 6.1A–C. Both qualitative visual demonstration and rheological measurement confirm the yield stress in our binary suspensions when prepared

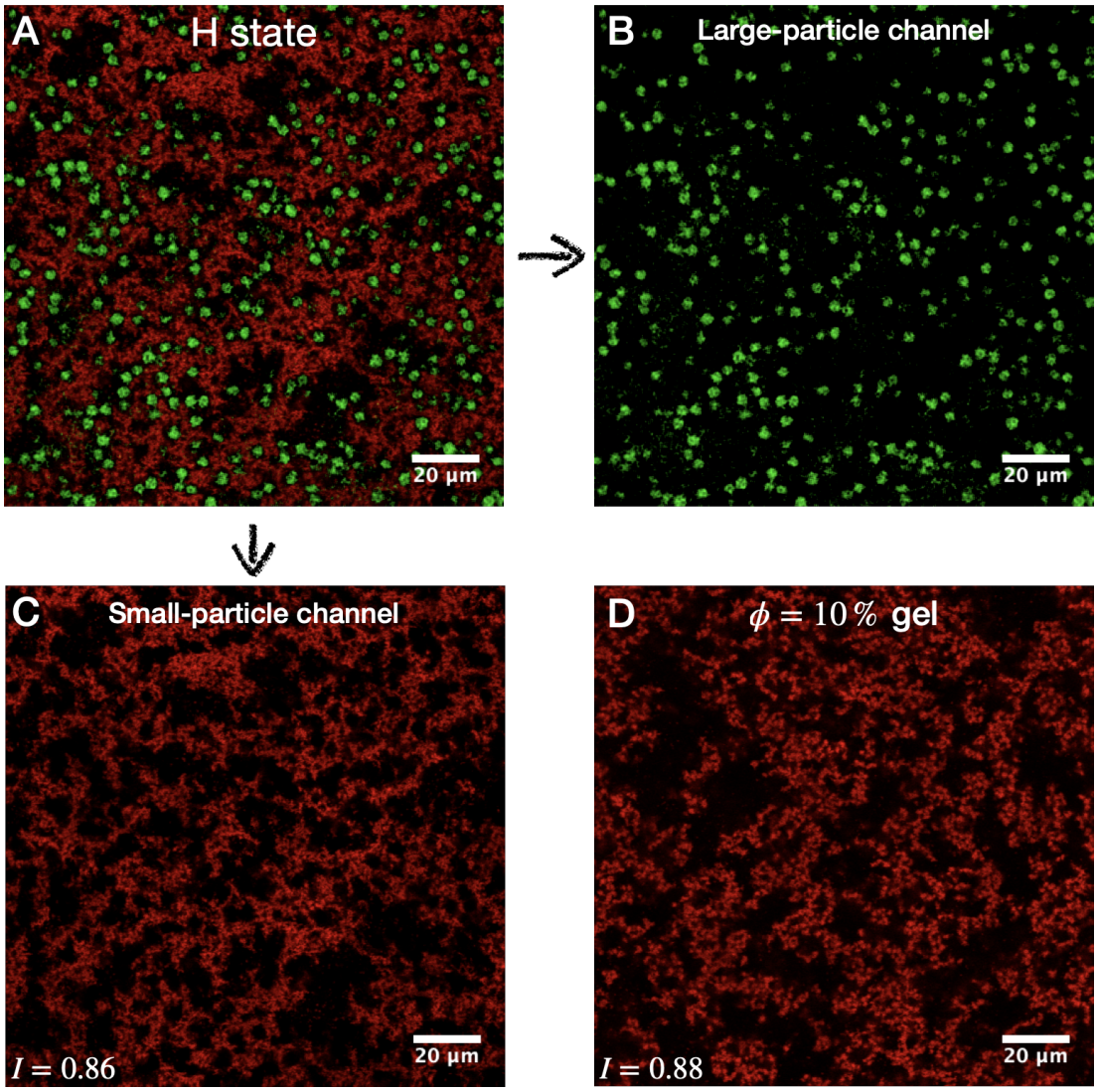

Figure 6.1 Comparison of an H state (particle-filled gel) and a colloidal gel (unfilled gel). After high-shear rejuvenation at $\dot{\gamma}_{\mathrm{rej}} = 1000\,\mathrm{s}^{-1}$, the H state was prepared in binary suspension at $\phi_S = 10\,\%$ and $\phi_L = 20\,\%$. Confocal images were then taken at a height of $\sim 30\,\mu\mathrm{m}$. A. Two-channel confocal image of the binary sample, which can be decomposed into large-particle channel (B) and small-particle channel (C). D. Confocal image of colloidal gel at $\phi = 10\,\%$, taken from Figure 4.7B in Chapter 4. Calculated Moran's Is (based on 2D slices) were shown in the bottom-left corner.

in the H state. From the solid-like response, we infer that the small-particle network therein, which can carry stresses, percolates the entire system. So an H state is composed of a gel matrix and dispersed large particles as fillers, i.e. a particle-filled gel.

After high-shear homogenisation, the small particles re-gel with the large particles embedded inside. Compared with the PS state, either the gel matrix or the configuration of large particles in H state is relatively homogeneous, Figure 6.1B and C. Visually, the gel matrix of H state resembles that in an unfilled gel. Figure 6.1C and D compare their confocal snapshots at an identical $\phi_S = 10\,\%$, which are hard to distinguish visually. The calculation of Moran's I (Fig. 6.1C-D, bottom-left corner) indicates comparable degree of spatial heterogeneity as well. Therefore, we may expect a binary suspension in H state and a colloidal gel to have similar rheology. At least, the measurement on yield stress suggests that they are both soft solids.

We compared a binary sample and a colloidal gel at $\phi_S = 10\,\%$. They consist of the same amount of small particles while the former additionally includes $\phi_L = 20\,\%$ large particles. We first measured the flow curve of the binary sample by step-down shear protocol (see caption in Fig. 6.2A), which enables us to measure the response of H state before the gel matrix collapses into 'droplets'. For consistency, we used the same protocol to measure the colloidal gel.

The two flow curves in Figure 6.2A have similar shape, yet at the same shear rate $\dot{\gamma}$, the binary sample always exhibits higher stress σ than the colloidal gel. Since the total solid volume fraction is higher in the binary sample ($\phi_{\text{tot}} = \phi_S + \phi_L = 30\,\%$), such behaviour is expected at high shear. As shear rate decreases, the stress appears to approach a low-shear plateau in both cases. Herschel-Bulkley fitting (Fig. 6.2A, solid lines) suggests that the binary sample has a higher yield stress ($\sigma_y = 2.6\,\text{Pa}$) than the unfilled gel ($\sigma_y = 0.8\,\text{Pa}$). Even though the gel network is composed of the same amount of attractive colloids ($\phi_S = 10\,\%$), a particle-filled gel is stronger than an unfilled gel: the addition of large particles seems to strengthen the whole system.

Such strengthening also manifests in oscillatory rheology. The result of dynamic frequency sweep at small strain $\gamma = 0.1\,\%$ shows that the binary sample has higher dynamic modulus, Figure 6.2B. In the two samples, the modulus scales with frequency ω in a similar manner. The elastic modulus G' slowly increases with frequency ω, whereas the viscous modulus G'' presents a broad minimum at

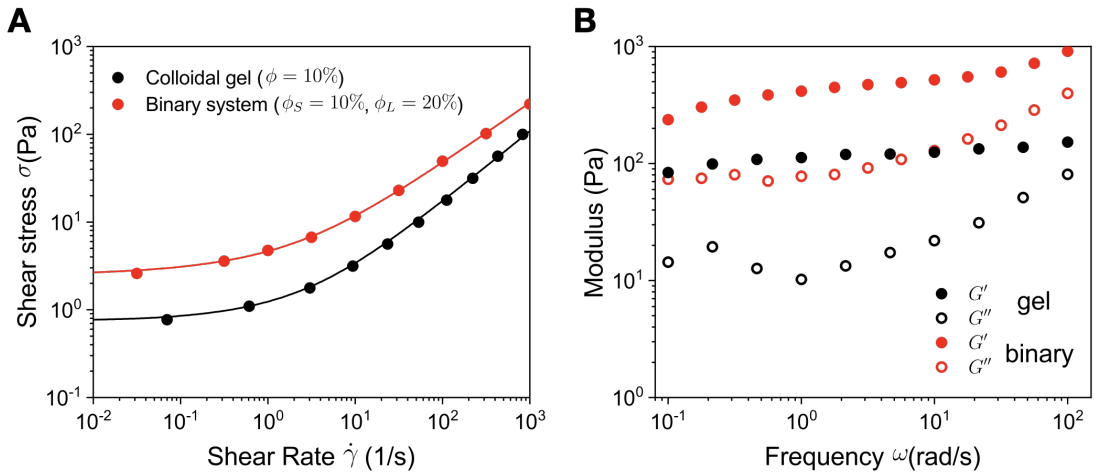

Figure 6.2 Comparison of rheology between an unfilled gel ($\phi = 10\,\%$, black) and a binary suspension in H state ($\phi_S = 10\,\%$ and $\phi_L = 20\,\%$, red). A. Flow curves measured by step-down shear protocol. After rejuvenation at $\dot{\gamma}_{\text{rej}} = 1000\,\text{s}^{-1}$, a lower shear rate $\dot{\gamma}$ was applied and the transient stress σ was measured for 30 s. Such procedure was repeated for various shear rates $\dot{\gamma}$. The solid lines are Herschel-Buckley fits. Red: $\sigma_y = 2.6\,\text{Pa}$, $k = 1.8\,\text{Pas}^{\text{n}}$ and $n = 0.7$; Black: $\sigma_y = 0.8\,\text{Pa}$, $k = 0.4\,\text{Pas}^{\text{n}}$ and $n = 0.8$. B. Dynamic frequency sweep at small strain amplitude $\gamma = 0.1\,\%$. After rejuvenation at $\dot{\gamma}_{\text{rej}} = 1000\,\text{s}^{-1}$ and waiting for 30 min, the frequency ω was ramped down and each data point was measured for $\gtrsim 10$ cycles of oscillation.

$\omega \approx 1\,\text{rad}\,\text{s}^{-1}$ and then increases with ω more rapidly than G' at high frequency. Both moduli are higher in binary sample than they are in gel, approximately by a factor of 5. Despite having the same $\phi_S = 10\,\%$, the binary sample exhibits higher elasticity. This is consistent with its higher yield stress as shown in Figure 6.2A.

6.1.1 Yield stress σ_y

The results above imply that the addition of large particles reinforces the gel strength. To better understand the relation between yield strength and large particles, we prepared binary suspensions at various compositions. In particular, we grouped these sample into four different ϕ_S (5 %, 10 %, 15 %, 20 %) with ϕ_L varying from 0 to 45 %. Figure 6.3A summarises their yield stresses in a σ_y-ϕ_L plot, where different ϕ_S groups are labelled by different symbols.

At $\phi_L = 0$, i.e. unfilled gels, the yield stress σ_y increases with ϕ_S as previously reported in Chapter 4. For each ϕ_S group, the yield stress σ_y

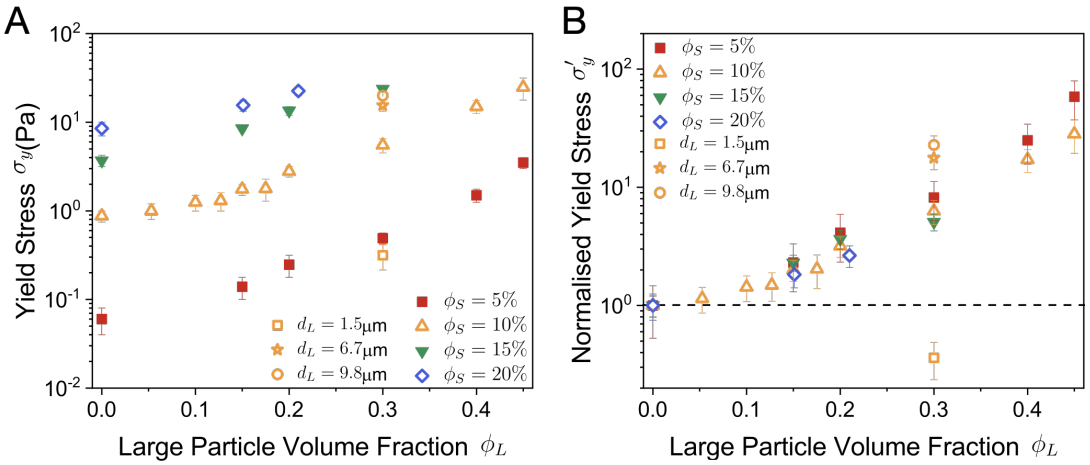

Figure 6.3 Yield strength of binary suspensions (H state) at various compositions. Unless otherwise stated, the large particle size $d_L = 4\,\mu m$. We also prepared three samples at $\phi_S = 10\,\%$ and $\phi_L = 30\,\%$ using silica with other d_L. For each sample, the yield stress σ_y was determined by creep test, before which the sample was rejuvenated at high shear stress $\sigma_{pre} = 100\,Pa$. A. Yield stress σ_y varies as a function of large particle concentration ϕ_L. For each ϕ_S group, we normalised the yield stress σ_y by that of unfilled gel ($\phi_L = 0$), see Eq. 6.2. B. Normalised yield stress σ'_y varies as a function of large particle concentration ϕ_L. The dashed line denotes $\sigma'_y = 1$.

monotonically increases with the large particle concentration ϕ_L in a similar manner. Significantly, at $\phi_S = 5\,\%$ and $\phi_S = 10\,\%$, the addition of $\phi_L = 40\,\%$ large particles can increase the yield stress σ_y by almost an order of magnitude. The strengthening effect by large particles generically occurs in binary suspensions regardless of ϕ_S and ϕ_L. This is consistent with the state diagrams (Figure 5.19 in Chapter 5), where the lower shear boundary σ_y increases with ϕ_L in each diagram.

Such strengthening is size-dependent. While the results presented so far are from samples using $d_L = 4\,\mu m$ silica as large particles, we also used silica with different d_L to prepare samples at $\phi_S = 10\,\%$ and $\phi_L = 30\,\%$. At fixed composition, the yield stress σ_y monotonically increases with the large particle size d_L, from $\sigma_y = 0.3\,Pa$ ($d_L = 1.5\,\mu m$) to $\sigma_y = 25.3\,Pa$ ($d_L = 9.8\,\mu m$), Figure 6.3A.

The result above shows that the yield stress of a particle-filled gel is a function of concentrations of both species of particles:

$$\sigma_y = \sigma_y\left(\phi_S, \phi_L\right). \tag{6.1}$$

To quantitatively study their relation, we normalised the yield stress σ_y by that of unfilled gel for each ϕ_S group:

$$\sigma_y' = \frac{\sigma_y(\phi_S, \phi_L)}{\sigma_y(\phi_S, \phi_L = 0)}, \tag{6.2}$$

where σ_y' is the normalised yield stress, and $\sigma_y(\phi_S, \phi_L = 0)$ is the yield stress of gel at ϕ_S. We then plot σ_y' versus ϕ_L in Figure 6.3B. Such normalisation appears to collapse the data from Figure 6.3A (except those at different d_L) on a master curve.

Not surprisingly, the normalised yield stresses of different ϕ_S groups converge to $\sigma_y' = 1$ at $\phi_L = 0$, Figure 6.3B (dashed line). For each group, σ_y' increases with ϕ_L in an almost identical manner, Figure 6.3B. The collapsed data implies a universal law for the relation of σ_y' and ϕ_L:

$$\sigma_y' = f\left(\phi_L\right), \tag{6.3}$$

where $f(\phi_L)$ is a monotone increasing function with $f(0) = 1$. Combining Eq. 6.2 and Eq. 6.3, we can decompose the contribution to the yield stress of particle-filled gel (or equivalently binary suspension in H state) in the form of:

$$\sigma_y(\phi_S, \phi_L) = \sigma_y^{\text{gel}}(\phi_S) \cdot f(\phi_L), \tag{6.4}$$

where σ_y^{gel} refers to the yield stress of unfilled gel, scaling with ϕ_S as power law (see Figure 11B in Chapter 4). For a colloidal gel at ϕ_S, the addition of ϕ_L large particles amplifies its yield stress $\sigma_y^{\text{gel}}(\phi_S)$ by a factor of $f(\phi_L)$. Yet again, data from samples using different d_L do not collapse on the master curve of $d_L = 4\,\mu\text{m}$ samples, Figure 6.3B. Remarkably, adding $d_L = 1.5\,\mu\text{m}$ silica to a gel causes weakening rather than strengthening, as the normalised yield stress σ_y' falls below 1, Figure 6.3B.

Effective volume fraction

We attempt to explain the variation in yield stress in terms of reduced free volume available to the small particles. On their own, attractive colloids diffuse and stick to each other and finally form a spanning network whose yield strength is determined by the volume fraction ϕ [126]. The volume fraction is defined as $\phi = V_{\text{particle}}/V_{\text{total}}$ since the total system volume is accessible. In binary suspensions,

the small particles still form a percolated gel matrix as shown in Figure 6.1C, yet the accessible volume, i.e. the free volume ϕ_{free}, decreases with the presence of large particles. This effectively drives up the concentration of small particles.

A simple way to account for the free volume reduction is to directly deduct the large particle volume. In this way, the small particle concentration increases from ϕ_S to $\phi_S/(1-\phi_L)$ in a binary suspension. We replot the yield stress data from Figure 6.3A against $\phi_S/(1-\phi_L)$ in Figure 6.4A. For samples using 4-µm silica, data points are quite scattered and do not collapse on the power-law fit of yield stress of colloidal gels (Fig. 6.4A, dashed line). In particular, for each ϕ_S group, the deviation becomes more significant at higher ϕ_L. Data of different d_L are even more scattered.

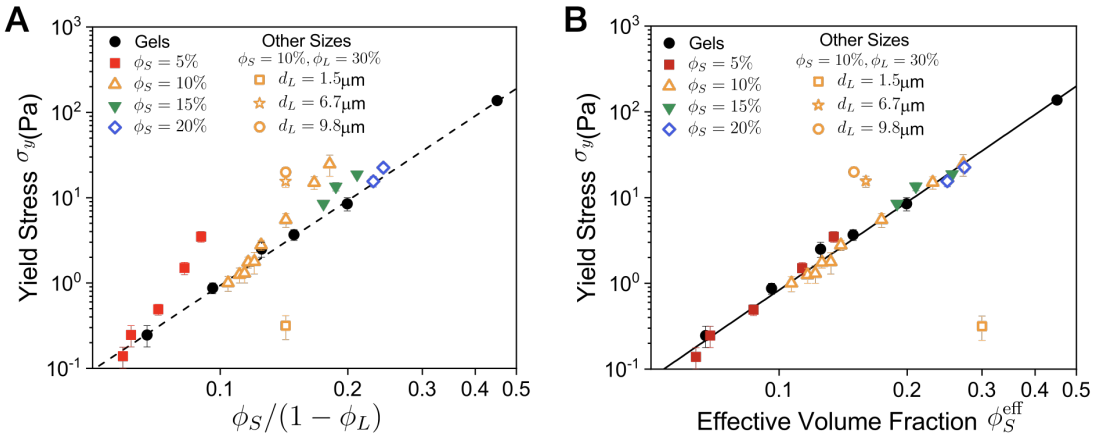

Figure 6.4 Yield stress varies as a function of effective volume fraction estimated by two different approach. Raw data are from Figure 6.3A. A. Yield stress σ_y versus $\phi_S/(1-\phi_L)$. The free volume reduction is considered by directly deducting the large particle volume. The dashed line is the power-law fit ($\sigma_y = \sigma_0\phi^\nu$) on data of colloidal gels: $\sigma_0 = 1870\,\text{Pa}$ and $\nu = 3.3$. B. Yield stress σ_y versus ϕ_S^{eff}, where the effective volume fraction is determined by Eq. 6.5 and Eq. 6.6 . The solid line is the power-law fit ($\sigma_y = \sigma_0(\phi_S^{\text{eff}})^\nu$) on the data of samples using $d_L = 4\,\mu\text{m}$ silica, giving $\sigma_0 = 2089\,\text{Pa}$ and $\nu = 3.4$.

The failure of this estimation is expected as it neglects the depletion shell (with thickness $d_S/2$) around large particles. Here we adapt an analytic expression, originally used to estimate the free volume of non-absorbing polymers in polymer-colloids mixtures [63], to estimate the effective volume fraction ϕ_S^{eff} in our binary suspensions:

$$\begin{aligned} \phi_{\text{free}} &= (1-\phi_L)\cdot e^{-A\gamma - B\gamma^2 - C\gamma^3} \\ \phi_S^{\text{eff}} &= \frac{\phi_S}{\phi_{\text{free}}} \end{aligned} \tag{6.5}$$

with

$$\begin{aligned}\gamma &= \phi_L/(1-\phi_L)\\ A &= 3\alpha + 3\alpha^2 + \alpha^3\\ B &= 9\alpha^2/2 + 3\alpha^3\\ C &= 3\alpha^3,\end{aligned} \tag{6.6}$$

where $\alpha = d_S/d_L \approx 0.12$ is the size ratio. Given a specific composition (ϕ_S and ϕ_L), we can estimate the effective volume fraction ϕ_S^{eff} by Eq. 6.5 and Eq. 6.6.

We replot the yield stress data from Figure 6.3A against ϕ_S^{eff} in Figure 6.4B. For samples using $d_L = 4\,\mu\text{m}$ silica, data points, of either binary suspensions or colloidal gels, all collapse on an identical curve. We used power law $\sigma_y = \sigma_0(\phi_S^{\text{eff}})^\nu$ to fit these data, giving $\sigma_0 = 2089\,\text{Pa}$ and $\nu = 3.4$. The fitting result is comparable to the power-law fit on gel samples ($\sigma_0 = 1870\,\text{Pa}$ and $\nu = 3.3$).

For binary samples with $d_L = 4\,\mu\text{m}$, the effective volume fraction enables us to predict the yield stress of particle-filled gels. In this way, we may treat a binary system at ϕ_S and ϕ_L (H state) as a colloidal gel with ϕ_S^{eff} determined by Eq. 6.5 and Eq. 6.6.

Inconsistency

We now explore whether the treatment using effective volume fraction ϕ_S^{eff} applies to all binary suspensions with different d_L. While such treatment appears to work for $d_L = 4\,\mu\text{m}$ large particles, the data of other sizes d_L deviates from that of 4-µm silica, Figure 6.4B. At the same composition ($\phi_S = 10\,\%$ and $\phi_L = 30\,\%$), the yield stress σ_y increases with d_L, which is in conflict with the prediction from ϕ_S^{eff}, Figure 6.4B. Specifically, according to Eq. 6.5 and Eq. 6.6, the $d_L = 1.5\,\mu\text{m}$ sample has an effective volume fraction $\phi_S^{\text{eff}} = 30\,\%$, yet its yield stress $\sigma_y \approx 0.3\,\text{Pa}$ is around two orders of magnitude lower than that of $d_L = 9.8\,\mu\text{m}$ sample whose effective volume fraction $\phi_S^{\text{eff}} = 16\,\%$.

So far we do not understand such deviations. However, they are not a total surprise since the approach we used (Eq. 6.5 and Eq. 6.6) relies on several assumptions. As described in [63, 203], Eq. 6.5 is derived by comparing the chemical potential of a dilute gas of non-interacting 'test spheres' [204] to expressions for the chemical potential of hard sphere mixtures [205]. While these assumptions may be appropriate for colloid-polymer mixtures, applying this equilibrium calculation using solid attractive colloids in a sea of non-Brownian

particles is less justified, particularly at higher values of ϕ_S and ϕ_L.

A plausible explanation on the size dependence regards a particle-filled gel as a defective gel [193]. When non-sticky large particles are introduced into small-particle gel, some of them are kinetically trapped in the gel network and act as defects to weaken the gel strength. This may explain why the particle-filled gel with $d_L = 1.5\,\mu\text{m}$ is even weaker than the unfilled gel. The size of large particles d_L may play a role in this scenario, as it controls the area of non-sticky surface at fixed ϕ_L. However, this interpretation needs to be further verified.

6.1.2 Elastic modulus G'

Oscillatory rheology reveals further differences between binary samples and unfilled gels. Again, we prepared samples at various compositions and different d_L, and measured the elastic modulus G' at $\gamma = 0.1\,\%$ and $\omega = 10\,\text{rad}\,\text{s}^{-1}$.

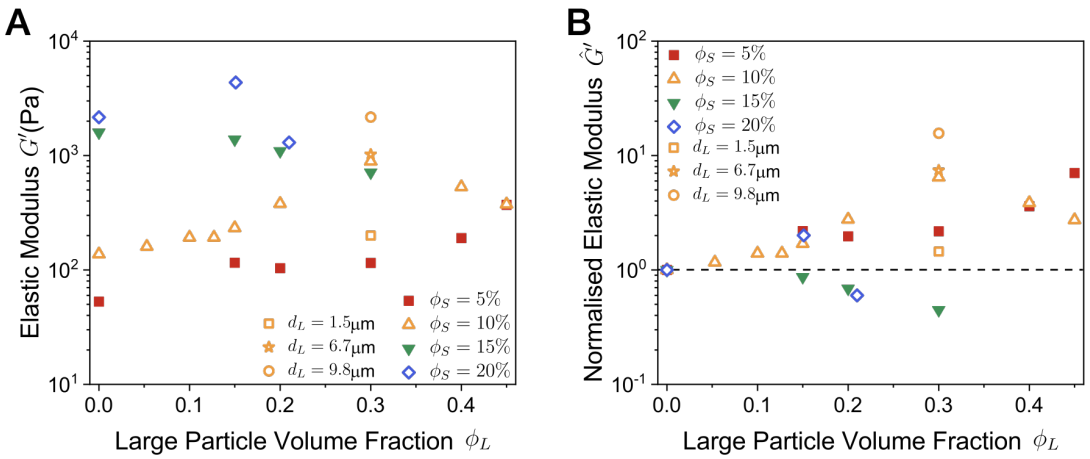

Figure 6.5 Elastic modulus G' of binary suspensions at various compositions. Unless otherwise stated, the large particle size $d_L = 4\,\mu\text{m}$. We also prepared three additional samples using silica with other d_L, with $\phi_S = 10\,\%$ and $\phi_L = 30\,\%$. The elastic modulus G' was measured at $\gamma = 0.1\,\%$ and $\omega = 10\,\text{rad}\,\text{s}^{-1}$, before which the sample was rejuvenated at high shear stress $\sigma_{\text{rej}} = 100\,\text{Pa}$ and then left undisturbed for 30 min. A. Elastic modulus G' varies as a function of large particle concentration ϕ_L. For each ϕ_S group, we normalised G' by that of unfilled gel ($\phi_L = 0$). B. The normalised elastic modulus $\hat{G}'$ versus large particle concentration ϕ_L. The dashed line denotes $\hat{G}' = 1$.

For colloidal gels ($\phi_L = 0$), the elastic modulus G' increases with ϕ_S as indicated in Figure 6.5A. As ϕ_L increases, however, G' does not always exhibit monotonic

increase like yield stress σ_y does in Figure 6.3A. At $\phi_S = 5\,\%$, G' generally increases with ϕ_L. By contrast, for the $\phi_S = 10\,\%$ group, G' initially increases and then starts to decrease above $\phi_L = 30\,\%$. At $\phi_S = 15\,\%$ and $20\,\%$, binary samples even exhibit G' lower than that of unfilled gels.

Similar to the treatment on yield stress σ_y, we normalised the elastic modulus G' by that of unfilled gels at the same ϕ_S. For samples using $d_L = 4\,\mu\text{m}$ silica, while the normalised yield stresses σ'_y collapse on the same curve when plotting σ'_y versus ϕ_L, the data points of normalised $\hat{G}'$ are greatly scattered in Figure 6.5B. Some data points at $\phi_S = 15\,\%$ and $\phi_S = 20\,\%$ even fall below $\hat{G}' = 1$ (Fig. 6.5B, dashed line). Consistent with the size dependence in σ_y, the elastic modulus G' increases with d_L at $\phi_S = 10\,\%$ and $\phi_L = 30\,\%$.

Our previous result shows that the denser colloidal gels are, the higher elastic modulus G' they have. If a binary system can be treated as a gel by means of effective volume fraction ϕ_S^{eff}, as indicated by the data collapse in Figure 6.4B, we also expect the elastic modulus G' monotonically increases with ϕ_S^{eff} and fall on an identical curve. When plotted against ϕ_S^{eff} (determined by Eq. 6.5 and Eq. 6.6), the elastic modulus G' of different samples only collapses on a master curve at low ϕ_S^{eff} ($\lesssim 15\,\%$). As ϕ_S^{eff} increases, the elastic modulus G' even drops at high ϕ_S^{eff}, Figure 6.6 (dashed lines). Not surprisingly, samples with other d_L deviate from those with $d_L = 4\,\mu\text{m}$.

The scattered G' data (including the modulus drop) and the failure of data collapse for different d_L both demonstrate the limitation of an effective volume fraction approach. Here we examine the case at $\phi_S = 10\,\%$ in depth. At $\phi_S = 10\,\%$, the yield stress σ_y shows monotonic increase with ϕ_L in Figure 6.3A. By contrast, the elastic modulus G' initially grows and then decreases with ϕ_L beyond $30\,\%$, Figure 6.5A. Weakening and strengthening occur at the same time. Such conflict cannot be simply explained by the problematic ϕ_S^{eff} estimation, since adding large particles definitely increases ϕ_S^{eff} and is supposed to enhance the elasticity. The failure of data collapse in G' invalidates the treatment using ϕ_S^{eff}, indicating a more interesting role for the large particles than merely confining the small-particle gel to a smaller volume.

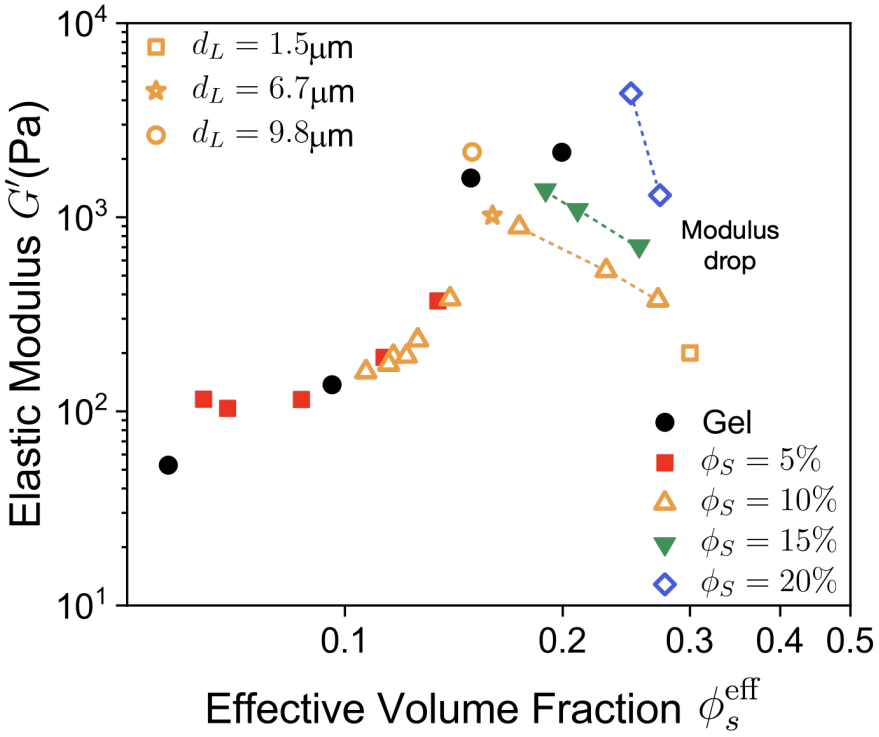

Figure 6.6 Elastic modulus G' versus effective volume fraction ϕ_S^{eff} estimated by Eq. 6.5 and Eq. 6.6. Raw data are taken from Figure 6.5A. The dashed lines indicate modulus drop in the dense regime.

6.1.3 Yielding behaviour

The difference between filled gels and unfilled gels manifests during yielding. We have already known that adding large particles can effectively increase the yield strength (Fig. 6.3A). To better understand the yielding behaviour, we performed dynamic strain sweep on various samples. We fixed the concentration of small particles at $\phi_S = 10\,\%$ and varied that of large particles ϕ_L from 0 to 45 %. Figure 6.7 compares the strain sweep result by plotting the moduli (A – elastic modulus G'; B – viscous modulus G'') versus oscillation strain γ.

In all samples, the linear viscoelasticity (i.e. modulus plateau) is confined to small strains and the elastic modulus G' starts to deviate from the linear response beyond about 0.1 %, Figure 6.7A. This indicates yielding, with the small strain implying the short range of hydrophobic attraction between small particles. Below $\phi_L = 30\,\%$, both G' and G'' increase with the amount of large particles ϕ_L. Consistent with our result in Figure 6.5A, both moduli reach their maximum at $\phi_L = 30\,\%$, beyond which G' and G'' decreases with ϕ_L.

As ϕ_L increases, the two moduli G' and G'' start to exhibit 'bulges' at large strain

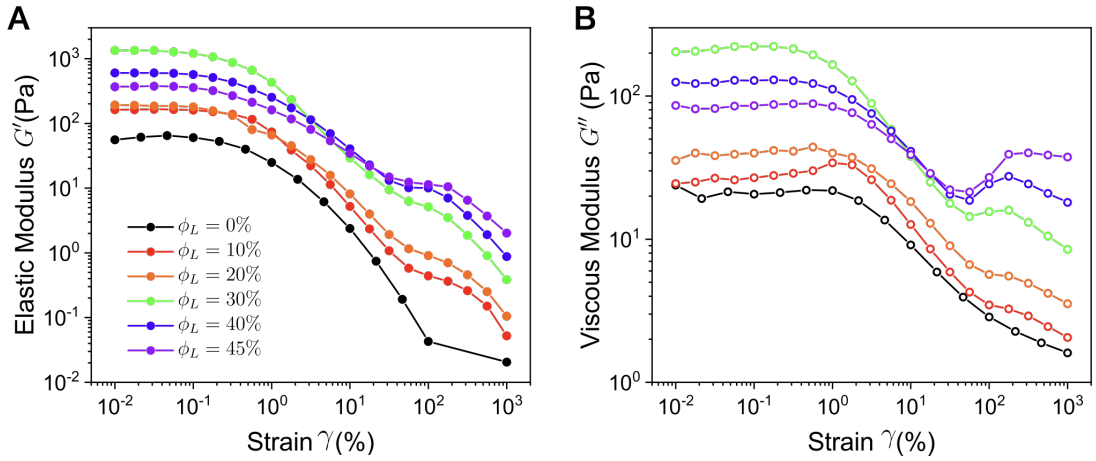

Figure 6.7 Dynamic strain sweep at frequency $\omega = 10\,\mathrm{rad\,s^{-1}}$. We fixed $\phi_S = 10\,\%$ and varied ϕ_L from 0 to 45 %. Before each measurement, high-stress rejuvenation ($\sigma_{\mathrm{pre}} = 100\,\mathrm{Pa}$) was applied and followed by waiting for 30 min. The strain γ was ramped up from $\gamma = 0.01\,\%$ to 1000 %, while each data point was measured for 100 s. The plots of elastic modulus G' and viscous modulus G'' versus strain γ are shown in A and B separately. Lines are drawn to guide the eye.

$\gamma \sim 100\,\%$. The higher ϕ_L is, the more significant the 'bulges' are. In particular, at $\phi_L = 45\,\%$, the elastic modulus G' drops with γ after initial yielding until reaching a second plateau at $\gamma \approx 100\,\%$, and then continue to decrease with γ. At $\phi_L = 30\,\%$, 40 % and 45 %, the viscous modulus G'' even present a peak at $\gamma \sim 200\,\%$. This G'' peak, typically presented during yielding, is absent when the two moduli first deviate from linear response at smaller strain. Such behaviour was not observed in the unfilled gel (Fig. 6.7, black), implying that a particle-filled gel yields in a different manner from a colloidal gel.

To better illustrate the yielding behaviour, we plot the elastic stress $\sigma' = G'\gamma$ versus strain γ in Figure 6.8A. The elastic stress σ' was determined from the data in Figure 6.7A. As the strain γ increases, the elastic stress first σ' linearly increases and reaches a maximum (Fig. 6.8A, large filled circles) at $\gamma \sim 1\,\%$ strain unit. While the colloidal gel only presents one peak, we observed a second peak at large strains $\gamma \sim 500\,\%$ in other binary samples. As ϕ_L becomes higher, the peak becomes less prominent and then turns into a point of inflection at $\phi_S = 40\,\%$ and 45 %.

From the dynamic strain sweep result, we can identify two yielding points in particle-filled gels, denoted by the large filled circles as well as the gray areas in Figure 6.7A. The first yielding, corresponding to the peak (or inflection) in σ'-γ plot, occurs in all samples and is confined to small strains $\gamma \lesssim 1\,\%$. The second

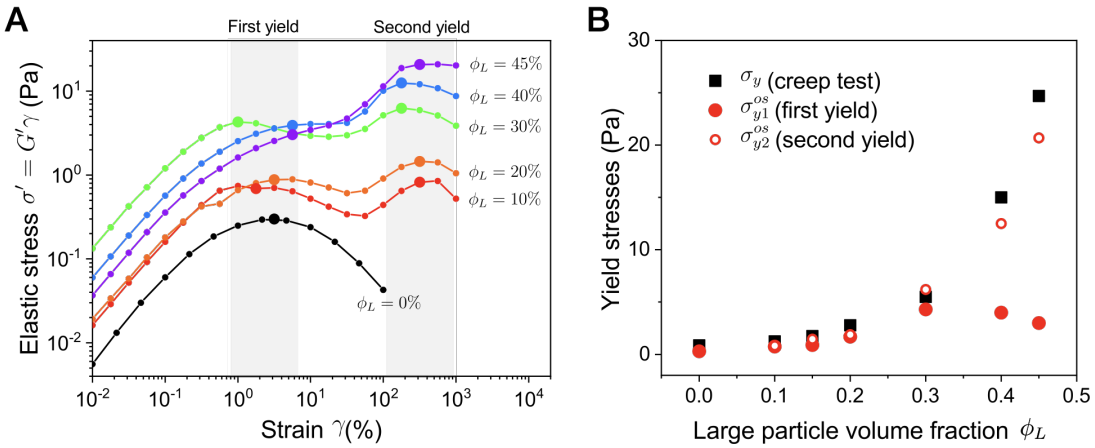

Figure 6.8 A. Elastic stress $\sigma' = G'\gamma$ versus oscillation strain γ, for the same data in Figure 6.7A. Large filled circles within the gray areas represent the yield points. Lines are drawn to guide the eye. B. Yield stresses vary as functions of large particle concentration ϕ_L. Black squares are yield stresses σ_y from creep test (taken from Figure 6.3A). Red filled circles and open circles are yield stresses under oscillatory shear, respectively corresponding to the first yield point (σ_{y1}^{os}) and the second yield point (σ_{y2}^{os}) in A.

yielding is indicated by the second peak (or inflection) in elastic stress σ', which occurs only in binary suspensions at large strains. From Figure 6.7A, we can extract two oscillatory shear yield stresses, σ_{y1}^{os} (the first yield point) and σ_{y2}^{os} (the second yield point).

There exists two concentration regimes, Figure 6.8B. Below $\phi_L = 30\,\%$, the three yield stresses agree with each other and all increase with ϕ_L. As ϕ_L increases above 30 %, the second peak in Figure 6.8A becomes higher than the first peak. Accordingly, the second yield stress σ_{y2}^{os} remains comparable to the steady shear yield stress σ_y and monotonically increases with ϕ_L. By contrast, the first yield stress σ_{y1}^{os} deviates from σ_y and σ_{y2}^{os} and exhibits slight decrease instead, Figure 6.8B.

For colloidal gels, it is typically the first yielding corresponding to the mechanical yielding [7, 127]. If the same applies here, we may expect that σ_{y1}^{os} should be comparable to σ_y. However, our result in Figure 6.8B suggests that, with the presence of large particles, the second yielding manifests and determines the yielding under steady shear at high ϕ_L. Moreover, the critical volume fraction $\phi_L = 30\,\%$, demarcating two concentration regimes, is consistent with the point above which elastic modulus G' decreases with ϕ_L. This implies different physics behind the yielding of particle-filled gels.

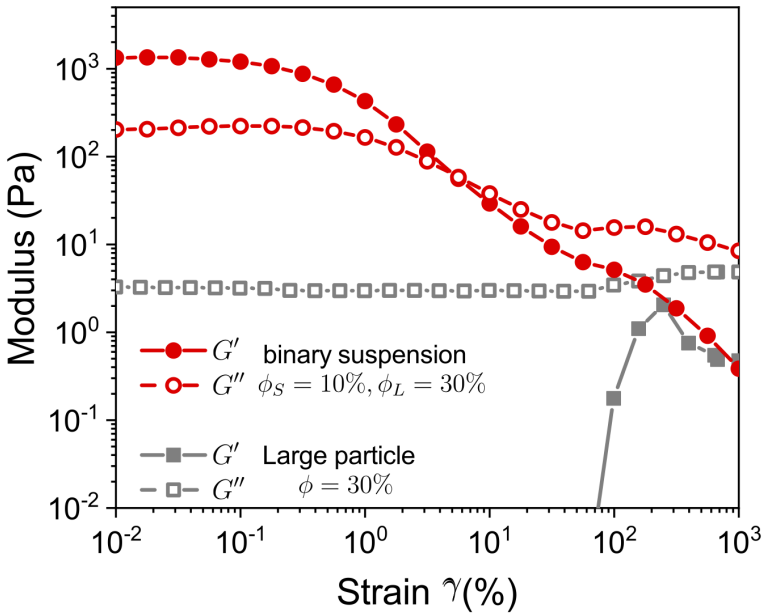

Figure 6.9 Dynamic strain sweep of binary suspension (red) and large particle suspension (gray), with compositions noted in legend. The data of binary sample are from Figure 6.7. For the large particle suspension, we performed strain sweep by ramping up strain γ at frequency $\omega = 10\,\mathrm{rad\,s^{-1}}$. Each data point was measured for 10 s.

The monotonic increase in σ_y (Fig. 6.3A) occurs as a result of the rise in the second peak in σ'–γ plot (Fig. 6.8A), which in turn results from the addition of large particles. Our large particles shear thicken on their own, and $\phi = 30\,\%$ suspension of large particles presents a abrupt increase in G' at $\gamma \sim 100\,\%$, Figure 6.9 (gray). Such strain scale is comparable to strain where the modulus 'bulge', i.e. the second yielding, occurs in binary suspensions, Figure 6.9 (red). Moreover, both the second yield stress $\sigma_{y2}^{\mathrm{os}}$ and shear thickening manifest at high ϕ_L. These results suggest a possible relation between the second yielding in particle-filled gels and the shear thickening in large particles.

As discussed in Chapter 3, shear thickening results from interparticle friction. In this sense, the agreement between σ_y and $\sigma_{y2}^{\mathrm{os}}$ in Figure 6.8B implies the role of friction in yield resistance. A recent study has revealed the connection between friction and yield stress in adhesive non-Brownian suspensions [12]. Combining the modulus drop above $\phi_L = 30\,\%$ (Fig. 6.6), we infer that large particles may contribute to the yield resistance under steady shear without increasing the viscoelasticity under oscillatory shear.

Here we propose a conjecture. The hard particles start to percolate at intermediate volume fractions [206]. However, such percolation is so transient

that it has little effect on rheology. In our binary suspension, the percolation of large particles may be reinforced by the gel matrix and thereby resists yielding. Such resistance mainly manifests under steady shear, where system-spanning force chains develop in the compressive direction. Under oscillatory shear, the contact percolation is broken upon reversal in each oscillation and thereby contributes little to the modulus. Remarkably, the percolation of non-Brownian particles in [206], as well as the modulus drop (Fig. 6.6) and the discrepancy in yield stresses (Fig. 6.8B), all start to occur at $\phi_L \approx 30\,\%$.

Understanding the macroscopic property of H state in our binary suspensions is important, as it closely relates to the lower shear boundary which demarcates bistable low shear and monostable medium shear. So far, we have shown that particle-filled gels behave differently from unfilled colloidal gels. Such difference cannot be simply captured by the reduction in free volume. The results from oscillatory rheology revealed a second yielding, which may occur as a result of interparticle friction. In addition, the size dependence on either yield stress or dynamic modulus still remains unclear. There exists tremendous scope for future research based on our findings above.

6.1.4 Conclusions

In this section, we studied colloidal gels with granular fillers, i.e. our binary suspensions in the H state. In the presence of large particles, attractive colloids still form a gel network which is visually indistinguishable from a pure colloidal gel. Rheology measurement shows that both particle-filled gel and pure colloidal gel are solid-like. Compared with unfilled gel, however, filled gel seems to possess higher yield stress σ_y and modulus G'. Such strengthening effect is then systematically investigated, yet so far we do not understand the physics behind it. We exclude the reduction in the free volume as a strengthening mechanism, and suspect that the interparticle friction may somehow contribute to the yield strength. Potential research lines are listed in Chapter 8.

6.2 PS state: Phase-separated 'droplets'

An H state yields when sheared beyond its yield stress σ_y. As we described in the previous chapter, if the applied stress happens to be in the intermediate regime ($\sigma_y < \sigma < \sigma_b$), the gel component will collapse and finally phase separate into disjoint 'droplets'. While these 'droplets' occasionally trap a few large particles, the vast majority of large particles are dispersed outside the 'droplets'. We define this phase-separated (PS) state by this change in the microstructure. Without the percolated gel network, binary suspensions in the PS state lack a yield stress and flow like a liquid.

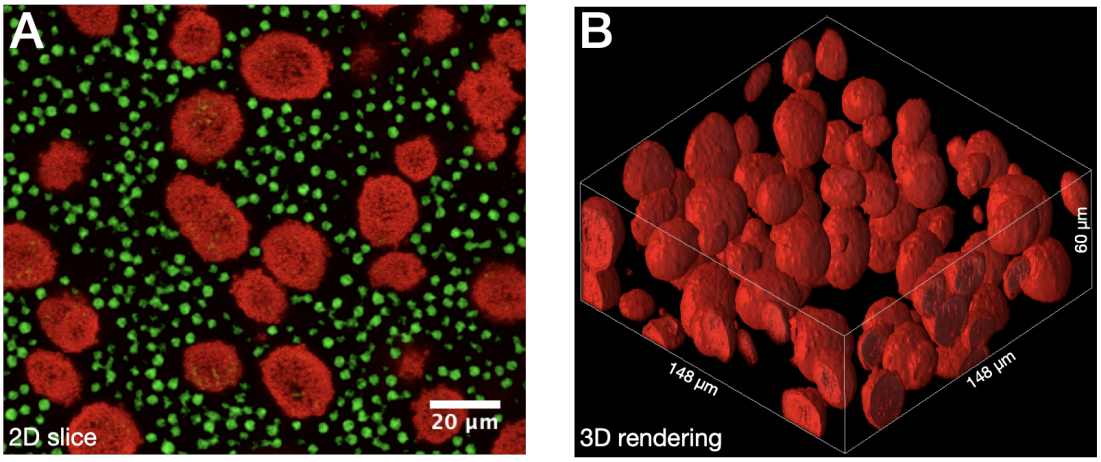

Figure 6.10 Confocal image of binary sample in PS state. The sample composition is $\phi_S = 10\,\%$ and $\phi_L = 20\,\%$. The PS state was prepared by prolonged preshear at stress $\sigma_{\text{pre}} = 5\,\text{Pa}$, after which imaging was carried out in 3D ($148\,\mu\text{m} \times 148\,\mu\text{m} \times 60\,\mu\text{m}$). A. 2D slice on the velocity-vorticity plane at depth of 30 µm from bottom. B. 3D rendering of the small-particle channel.

Figure 6.10A shows an example confocal image of a binary suspension in the PS state. We confirm the disjoint and compact nature of the 'droplets' evident in the 2D confocal slices using a 3D rendering of the small-particle channel for the full confocal stack. Visually, the PS state resembles a a collection of isolated large particles and polydispersed 'droplets'. While the large particles have been characterised in detail in Chapter 4, the property of phase-separated 'droplets' hitherto remains unclear. In this section, we mainly characterise the external morphology and internal structure of 'droplets'.

6.2.1 External morphology

At first glance, the 'droplets' in PS state are globules with similar sizes. To quantitatively measure the 'droplets', we segmented 3D confocal stacks using binary thresholding and the mean shift clustering algorithm to identify individual 'droplets' (see Appendix B for further processing details). Figure 6.11 shows a demonstration using 2D confocal slice, in which clusters of pixels are labelled by different colours. Visually, this method can effectively identify the 'droplets' in PS state.

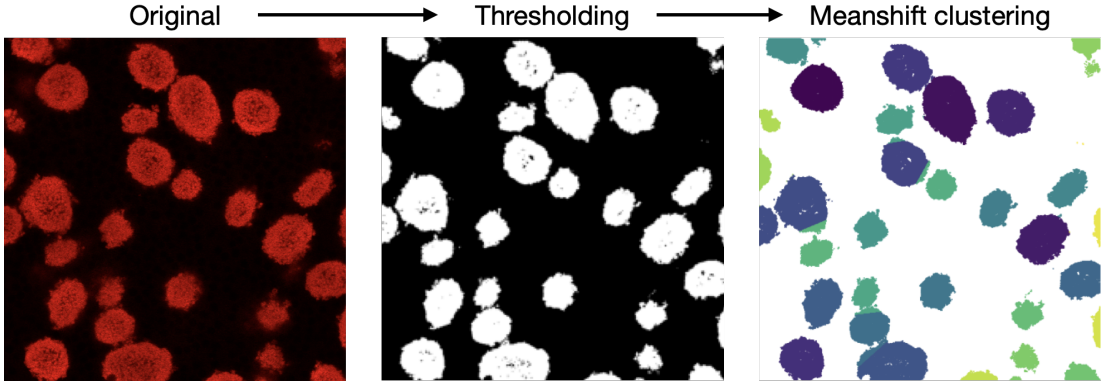

Figure 6.11 A 2D demonstration of mean shift clustering algorithm. The original confocal image (small-particle channel) was taken in sample of $\phi_S = 10\,\%$ and $\phi_L = 20\,\%$ after $\sigma_{\text{pre}} = 5\,\text{Pa}$ preshear. We binarised the original image by thresholding (threshold: 100), and then applied mean shift clustering (bandwith: 30 pixels). Non-zero pixels in the binarised image were classified into different regions, which are labelled by different colours.

From the regions identified using this method, we can extract a 'droplet' size d_{drop} for each region. Due to the globular shape, we use the sphere of equivalent volume to define d_{drop}:

$$d_{\text{drop}} = \left(\frac{6V_{\text{drop}}}{\pi}\right)^{\frac{1}{3}}, \tag{6.7}$$

where V_{drop} is the 'droplet' volume, derived from the number of non-zero pixels within a region (voxel size: $0.3 \times 0.3 \times 0.3\mu\text{m}^3$).

The distribution of d_{drop} is shown for a sample at $\phi_S = 10\,\%$ and $\phi_L = 20\,\%$, Figure 6.12A, where the PS state was prepared by prolonged preshear at $\sigma_{\text{pre}} = 5\,\text{Pa}$. We find that the distribution resembles a normal distribution with a well-defined mean size $\langle d_{\text{drop}} \rangle = 22.7 \pm 3.7\,\mu\text{m}$, Figure 6.12A. This roughly agrees with the confocal image shown in Figure 6.10.

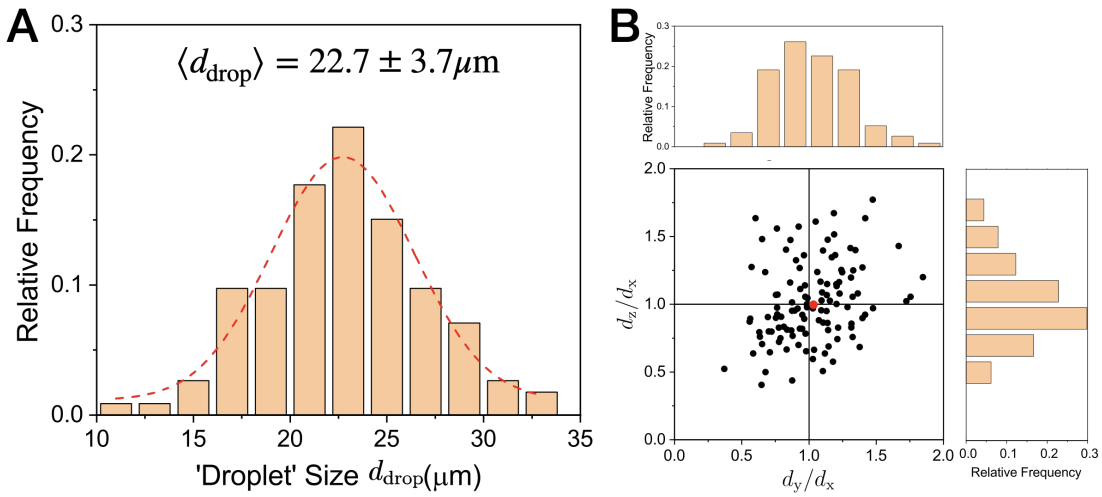

Figure 6.12 External morphology of 'droplets' in PS state. Here we used sample at $\phi_S = 10\,\%$ and $\phi_L = 20\,\%$, where the PS state was prepared by prolong medium preshear ($\sigma_{pre} = 5\,Pa$). We counted 116 'droplets' in four confocal 3D stacks, identified by the mean shift clustering described in Figure 6.11. A. 'Droplet' size distribution. Normal distribution fitting (red dashed line) gives the mean size $\langle d_{drop} \rangle = 22.7\,\mu m$ and standard deviation $\Delta d_{drop} = 3.7\,\mu m$. B. Scatter plot of the aspect ratios d_y/d_x and d_z/d_x. Bar plots above and to the right show histograms of the same data. The average values are shown by the red filled circle, giving $d_x \approx d_y \approx d_z$.

Based on the clustering result, we can also determine the characteristic length along different directions for each 'droplet'. Here we denote the lengths in flow, vorticity and gradient directions as d_x, d_y and d_z respectively. For better presentation, we normalised d_y and d_z by d_x, giving the aspect ratios d_z/d_x and d_y/d_x. Figure 6.12B shows the scatter plot of the two aspect ratios, where the data are quite scattered around the centre (1,1). This is confirmed by the histograms in Figure 6.12B (top and right). On average, 'droplets' do not show obvious elongation along any specific direction, since the mean aspect ratios are both close to unity, Figure 6.12B (red filled circles). This is consistent with the globular shape that we observed in confocal images (Fig. 6.10).

6.2.2 Internal structure

Apart from the external morphology, we also explored the internal structure of phase-separated 'droplets'. Since we cannot fully resolve individual small particles using confocal microscopy, we used cryo-SEM to image the 'droplets' at higher resolution. Before imaging, the PS state was prepared by prolonged roller mixing

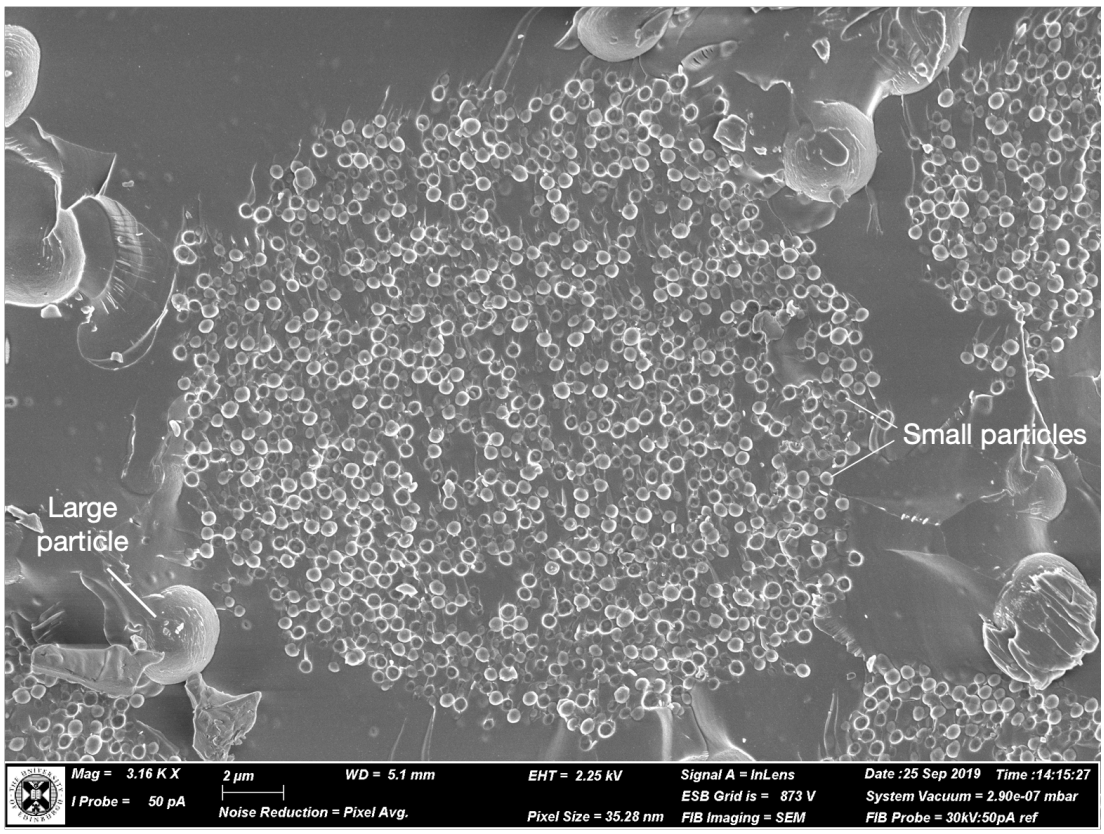

Figure 6.13 Cryo-SEM image of 'droplet' in binary sample of $\phi_S = 10\,\%$ and $\phi_L = 20\,\%$. Before loading, the sample was put on roller mixer for 1 h to achieve the PS state. Basic imaging parameters and a scale bar are shown at the bottom of the image.

in a binary sample with $\phi_S = 10\,\%$ and $\phi_L = 20\,\%$. The sample was then slowly loaded on the cryo-SEM sample holder via pipette, and then rapidly frozen in liquid nitrogen and cleaved by a cold blade in the cryo chamber. The ice was then sublimed by brief heating at $T = -90\,°\mathrm{C}$.

While there is a risk of disrupting the PS state during the loading process, we nevertheless found clear small-particle 'droplets' in the cryo-SEM images. Figure 6.13 shows a 2D profile of 'droplet' in sample of $\phi_S = 10\,\%$ and $\phi_L = 20\,\%$. Large particles are distributed outside the 'droplet', whereas small particles appear as either dark craters or bright spots (see annotation in Fig. 6.13). The SEM image suggests that 'droplets' are densely packed internally ($\gg \phi_S$), yet still far from random close packing $\phi_{\mathrm{rcp}} \approx 64\,\%$. Visually, the interior of 'droplet' is amorphous and plausibly homogeneous despite of few empty voids.

Intra-droplet volume fraction ϕ_S^{int}

To quantitatively characterise the interior of 'droplets', we developed a method to estimate the concentration of small particles inside 'droplets', which we denote as the intra-droplet volume fraction ϕ_S^{int}. While we initially considered using cryo-SEM imaging for more precise analysis, we found the SEM images too heterogeneous to robustly locate particle positions and the cryo samples too large and unstable for 3D FIB sectioning.

Instead, we calculate ϕ_S^{int} by first estimating the total volume occupied by the 'droplets' V_{drop} within a 3D confocal stack of volume V_{stack}. Then, assuming all small particles are contained within 'droplets' and that the concentration of small particles within the stack is identical to the bulk value ϕ_S, we compute ϕ_S^{int} from the number conservation of small particles:

$$\phi_S^{\text{int}} = \phi_S \frac{V_{\text{stack}}}{V_{\text{drop}}}. \tag{6.8}$$

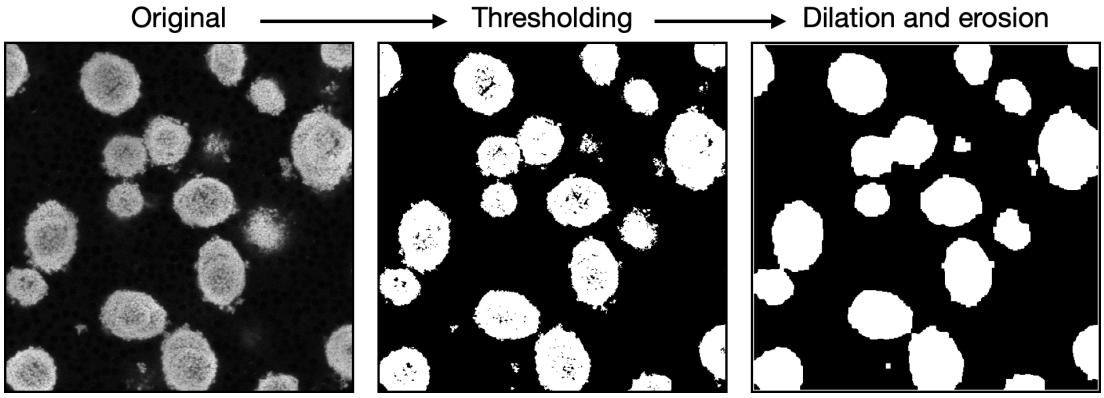

Figure 6.14 A 2D demonstration of image processing. To measure the 'droplet' volume V_{drop}, the confocal image is first binarised by thresholding (threshold: 100). Dilation (kernel size: 7 pixels $\sim 2\,\mu\text{m}$) is then applied to fill up the interstice within 'droplets', after which erosion with the same kernel size is applied to eliminate the dilation on the 'droplet' interfaces.

To estimate V_{drop}, we first extract the small particle channel and binarise it by thresholding. Using a sequence of dilation and erosion, we fill up the interstice inside 'droplets' without changing the morphology much. Figure 6.14 shows an example where the outlines of 'droplets' are clearly shown after image processing. The 'droplet' volume V_{drop} is then given by the total number of white voxels in these 3D binary stacks, enabling us to compute ϕ_S^{int} by Eq. 6.8. This estimation

of V_{drop} depends slightly on the choice of threshold and size of dilation/erosion kernel. We estimate our uncertainty in V_{drop}, and hence ϕ_S^{int}, by varying these parameters until the processed image is far from the original image (by visual inspection).

Using the above method, we compute $\phi_S^{\text{int}} = 50\,\% \pm 5\,\%$ in the sample of $\phi_S = 10\,\%$ and $\phi_L = 20\,\%$, where the PS state was prepared by prolonged preshear at $\sigma_{\text{pre}} = 5\,\text{Pa}$. Visually, such an estimate does not appear to be inconsistent with the cryo-SEM image (Fig. 6.13).

Solid-like 'droplets'

Liquid drops are spherical because of surface tension. For a collection of liquid droplets, coalescence is favoured as it can lower the surface energy. Throughout this thesis, we refer to the blobs of small particles as 'droplets' to connote the globular shape. However, we note that our particulate 'droplets' are solid-like rather than liquid-like, evident by the absence of 'droplet' coalescence. For a well-developed PS state, the 'droplet' size does not increase after left undisturbed for 2 h, Figure 6.14. The absence of coalescence at rest indicates solid-like 'droplets'.

Apart from the absence of coalescence, the lack of deformation under flow (shown in Sec. 6.2.4) also suggests the solid-like nature of our 'droplets'. Given the amorphous microstructure (Fig. 6.13), the high packing volume fraction ($\phi_S^{\text{int}} = 50\,\% \pm 5\,\%$) and the solid-like dynamics (no coalescence in Fig. 6.15), we speculate that the small particles in 'droplets' are in the attractive glass regime; at least they are kinetically arrested.

6.2.3 'Droplets' under different conditions

Different preshears

Methods introduced above, mean shift clustering and ϕ_S^{int} estimation, enable us to quantitatively characterise the 'droplets'. As shown in the last chapter, PS states containing phase-separated 'droplets' can be induced by preshears in the medium shear regime. To study the impact of preshear on 'droplets', we measured several PS states in the binary sample of $\phi_S = 10\,\%$ and $\phi_L = 20\,\%$.

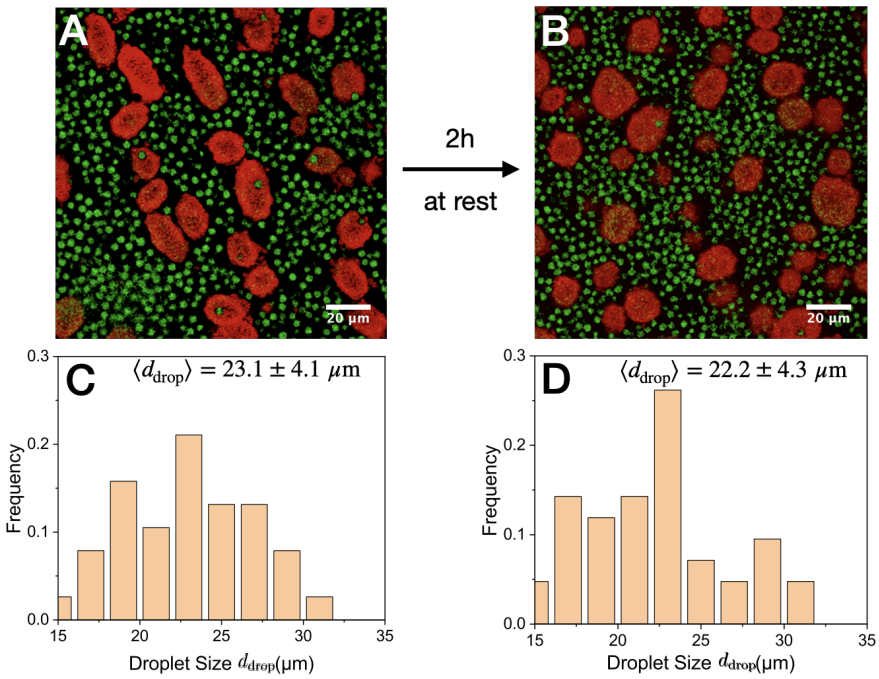

Figure 6.15 Absence of 'droplet' coalescence a sample of $\phi_S = 10\,\%$ and $\phi_L = 20\,\%$. We first prepared a PS state by preshear $\sigma_{\text{pre}} = 5\,\text{Pa}$ for 20 min, and then left it undisturbed for 2 h. Confocal images of the initial stage and final stage were taken in 3D, while A and B display 2D confocal slice before and after waiting at rest. The corresponding size distributions (determined by mean shift clustering results) were shown in C and D respectively.

Detailed analysis was based on four confocal stacks of PS states induced by four preshear stresses. From the 3D renderings in Figure 6.16, we do not identify significant differences between these PS states: globular 'droplets' with $d_{\text{drop}} \sim 20\,\mu\text{m}$ are always presented. Quantitative analysis on the size distribution (Fig. 6.16I–L), aspect ratios (Fig. 6.16M–P) and intra-droplet volume fraction ϕ_S^{int} (Fig. 6.17A) shows that the characters of 'droplets' barely vary with preshear strength. This agrees with our visual observation: the PS states induced by different preshears resemble each other. That is, in a specific binary sample, PS states induced by different shear flows are essentially indistinguishable.

Different ϕ_L

At various ϕ_L, we further explored the 'droplets' in PS states with ϕ_S fixed at 10 %. As the state diagram (Fig. 5.16A in Chapter 5) indicates, the range of medium shear varies with ϕ_L. Therefore, while the PS state in one sample was prepared by a specific preshear, the imposed stress σ_{pre} varies from sample to

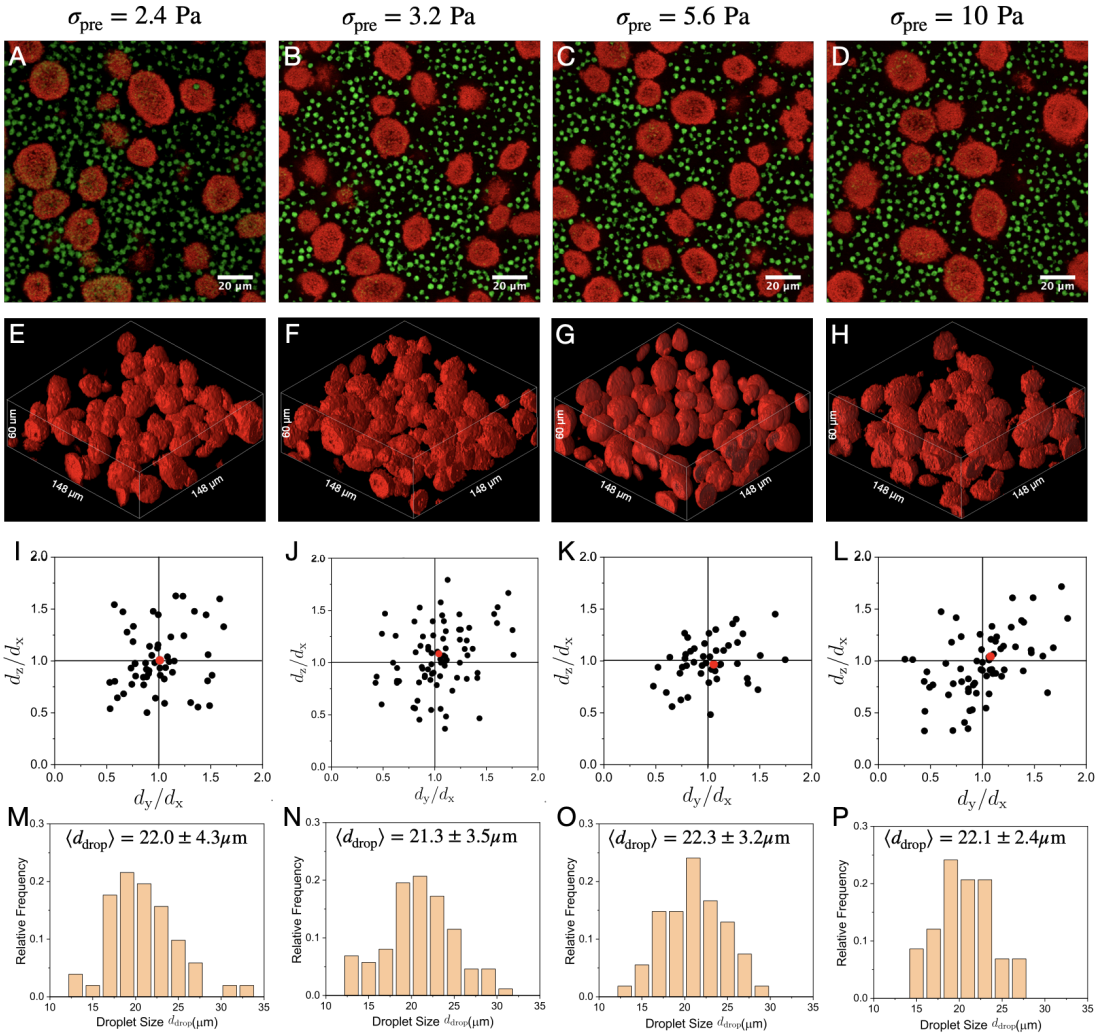

Figure 6.16 PS states prepared by different preshears in the sample of $\phi_S = 10\,\%$ and $\phi_L = 20\,\%$. The imposed preshear stress σ_{pre} is shown on the top of each column. A-D: Confocal images at depth of $\sim 30\,\mu\mathrm{m}$. E-H: 3D renderings of confocal stacks (small-particle channel). Based on the confocal stacks, we counted ~ 50 'droplets' for each σ_{pre}, identified by the mean shift clustering algorithm. I-L: Scatter plots of the aspect ratios $d_{\mathrm{y}}/d_{\mathrm{x}}$ and $d_{\mathrm{z}}/d_{\mathrm{x}}$. The red filled circle represents average values. M-P: 'Droplet' size distribution. The mean sizes $\langle d_{\mathrm{drop}} \rangle$ are noted on the top.

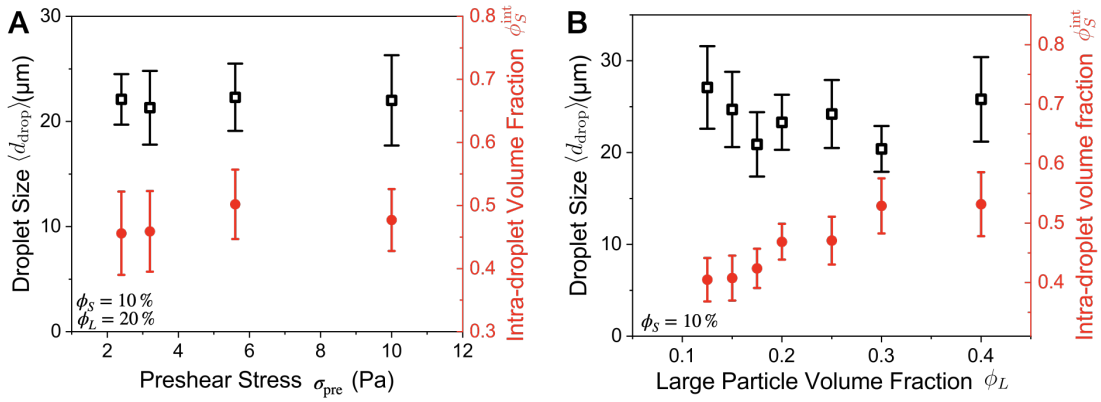

Figure 6.17 A. Mean 'droplet' size $\langle d_{\text{drop}} \rangle$ (black) and intra-droplet volume fraction ϕ_S^{int} (red) as functions of preshear stress σ_{pre} in binary sample of $\phi_S = 10\,\%$ and $\phi_L = 20\,\%$. B. Mean 'droplet' size $\langle d_{\text{drop}} \rangle$ (black) and intra-droplet volume fraction ϕ_S^{int} (red) as functions of large particle volume fraction ϕ_L. The small particle concentration $\phi_S = 10\,\%$ was fixed. To induce PS states, the imposed stress σ_{pre} varies from sample to sample to ensure a medium preshear in each sample. The imposed σ_{pre} are (ϕ_L from low to high): 3.2 Pa, 3.2 Pa, 5.6 Pa, 5.6 Pa, 10 Pa, 10 Pa, 17.8 Pa. Lines are drawn to guide the eye.

sample to ensure a medium preshear.

In samples with different ϕ_L, we did not observe significant variation in the 'droplet' size. The mean 'droplet' size $\langle d_{\text{drop}} \rangle$, determined from the result of mean shift clustering, fluctuates between 20 µm to 30 µm, Figure 6.17B (black). But there is no obvious trend, and we conclude that $\langle d_{\text{drop}} \rangle$ does not depend on ϕ_L.

By contrast, the intra-droplet volume fraction ϕ_S^{int} increases with ϕ_L even though the global $\phi_S = 10\,\%$ is fixed, Figure 6.17B (red). The addition of more large particles leads to 'droplets' with denser internal packing, ranging from roughly 40 % to 54 %. This is consistent with the positive correlation between σ_b and ϕ_L in the state diagrams (Fig. 5.16A in Chapter 5). As ϕ_L increases, 'droplets' become denser and thereby more rigid so that higher stress is required to break them.

6.2.4 Formation and breakage

In the PS region of our state diagram, the attractive particles collapse into globular 'droplets' with a characteristic size that seems to be independent of

both the applied stress σ and the large particle concentration ϕ_L. This implies generic physics in the formation of 'droplets'. Here investigation was carried out on the 'droplet' formation and breakup dynamics as the system transitions back and forth between the H and PS states.

Formation

The 'droplet' formation resembles phase separation: the sparse vapour phase of attractive colloids condenses into 'droplets' of dense liquid phase. By imposing moderate shears on an H state and simultaneously imaging the sample via rheo-confocal, we studied such phase separation in a sample at $\phi_S = 10\,\%$ and $\phi_L = 20\,\%$.

We focus on the structural behaviour of small particles. After cessation of a high preshear ($\sigma_{\text{pre}} = 100\,\text{Pa}$), small particles form a homogeneous gel matrix, Figure 6.18A. The imposed medium shear yields such matrix and quickly ruptures it into small pieces[1], Figure 6.18B. These pieces move with the flow and re-assemble into dense clusters which grows over time, Figure 6.18C-F. During this period, Moran's I increases as the structure becomes progressively heterogeneous. Once growing up to a characteristic size $\sim 20\,\mu\text{m}$, these clusters seem to stop growing (Fig. 6.18F-H); instead they gradually rearrange themselves under flow until turning into globular 'droplets', Figure 6.18I.

After the accumulated strain $\gamma \gtrsim 10^3$, the driven binary suspension reaches a steady PS state of 'droplets' with size $d_{\text{drop}} \sim 20\,\mu\text{m}$. Such structure does not continue to evolve if subsequently sheared for another 20 min (a further strain $\gamma \sim 5000$), Figure 6.19A-B. Since our 'droplets' are solid 'droplets', we do not expect coalescence during shear. The comparison of size distribution confirms our expectation, as the mean size $\langle d_{\text{drop}} \rangle$ barely changes before and after 20-minute shear, Figure 6.19C-D.

The formation of 'droplets' corresponds to the transition from the H to the PS state, during which the viscosity η decreases over time under medium shears, Figure 6.20A. To further confirm the strain scale $\gamma \sim 10^3$ beyond which a driven binary system becomes steady, we imposed different shear stresses σ, all in the medium shear regime, on H states and studied the evolution of viscosity. We plot viscosity η versus strain γ rather than time t. While the viscosity η decreases

[1] This process (matrix $\rightarrow$ pieces) is more apparent in the movie.

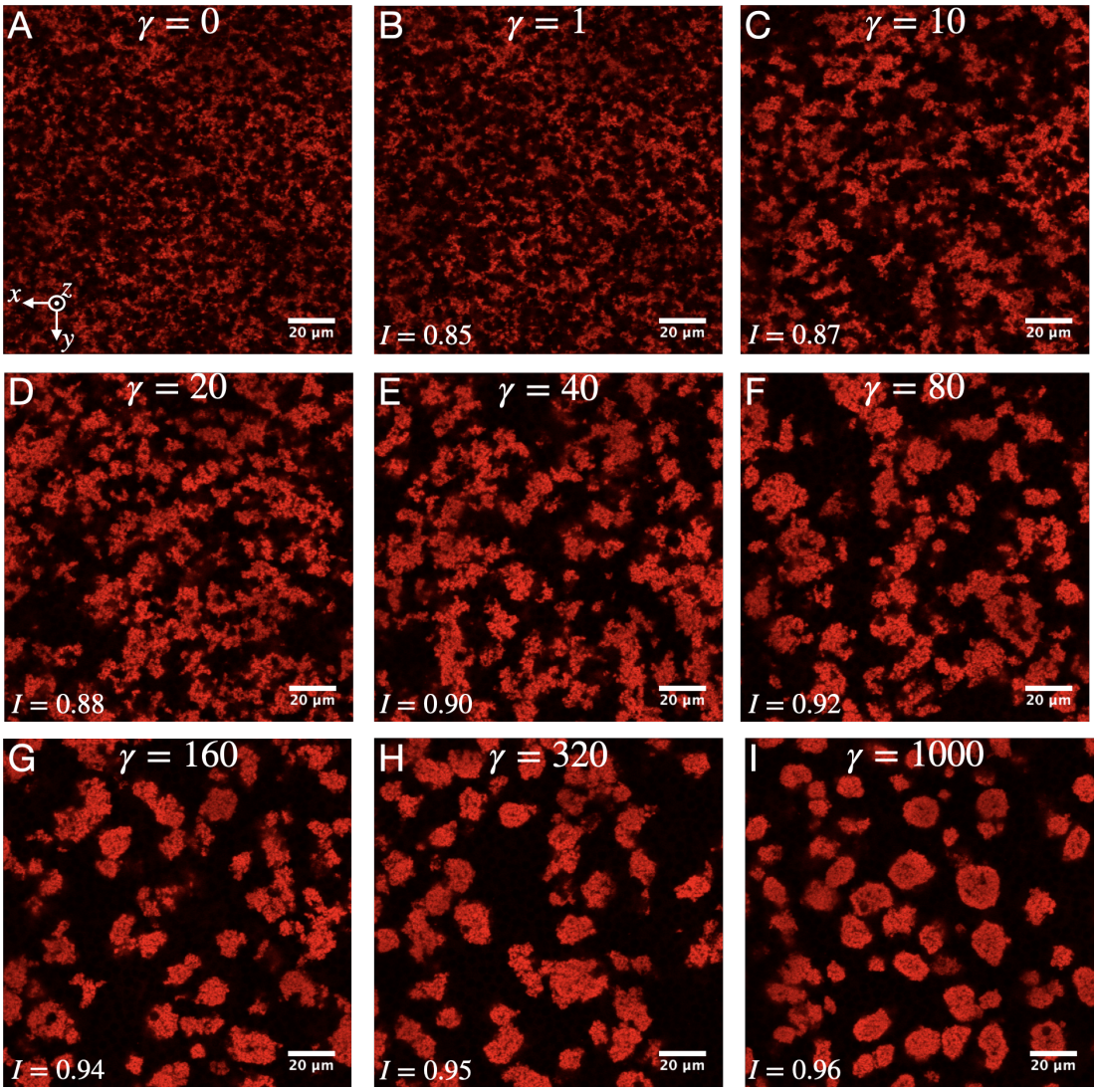

Figure 6.18 Confocal snapshots (small-particle channel) of phase separation at different stages. Here we used a sample of $\phi_S = 10\,\%$ and $\phi_L = 20\,\%$, and prepared an initial H state by preshear $\sigma_{\text{pre}} = 100\,\text{Pa}$. We imposed a medium shear stress $\sigma = 5\,\text{Pa}$ and simultaneously imaged the sample at height of 30 μm from the bottom plate. The axes of x, y and z in Figure A (bottom-left corner) refer to the flow, vorticity, gradient directions respectively. The accumulated strains γ are shown on the top, while the calculated Moran's Is are shown in the bottom-left corner.

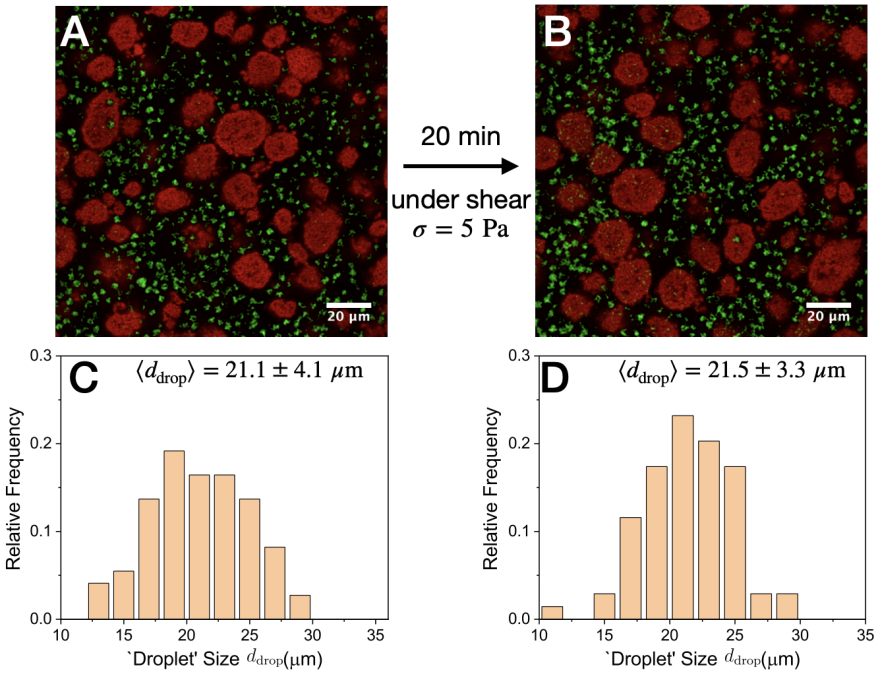

Figure 6.19 Evolution of PS state under medium shear. We prepared a PS state in sample of $\phi_S = 10\,\%$ and $\phi_L = 20\,\%$ by preshear $\sigma_{\mathrm{pre}} = 5\,\mathrm{Pa}$ for 20 min. After confocal imaging, we continued to shear the sample at $\sigma = 5\,\mathrm{Pa}$ for another 20 min and again imaged the sample upon shear cessation. A and B are confocal snapshots before and after the second shear, while corresponding size distributions (determined from 3D stacks) are shown below.

from different initial values to different final values, they appear to reach plateaus at similar strain scales $\gamma \sim 10^3$ regardless of shear strength, Figure 6.20A.

We also revealed the strain dependence in microstructure. At different medium shear stresses, the evolution of Moran's I roughly collapses on an identical curve when plotted versus strain γ, Figure 6.20B. Yet unlike viscosity η, Moran's I seems to stabilise at a smaller strain $\gamma \sim 200$ and then slightly increase over time. This is consistent with our visual observation in Figure 6.18, where heterogeneous clusters are first formed within a small strain ($\gamma \lesssim 80$), after which subtle rearrangement occurs until irregular clusters turn into globular 'droplets' upon $\gamma \sim 10^3$.

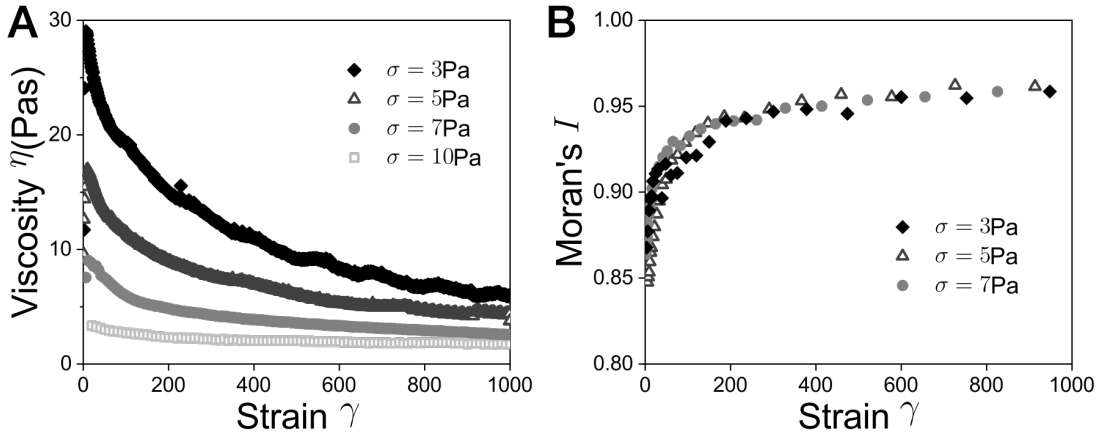

Figure 6.20 Evolutions of rheology and structure under medium shear. To induce phase separation in the sample of $\phi_S = 10\,\%$ and $\phi_L = 20\,\%$, we sheared an H state (prepared by preshear $\sigma_{\text{pre}} = 100\,\text{Pa}$) at different medium shear stresses. A. Viscosity η versus strain γ. B. Moran's I versus strain γ. Moran's I is determined from 2D slice movies

The results above establish that the shear-induced phase separation is strain dependent, and after a critical accumulated strain of $\gamma \sim 10^3$, the driven system turns into a steady PS state. We further compare the viscosity evolution in samples with various ϕ_L. Due to the difference in the range of medium shear, the imposed stress σ varies from sample to sample. For each ϕ_L, the viscosity η decreases under shear until reaching a lower plateau as the accumulated strain $\gamma \gtrsim 10^3$, Figure 6.21. Despite of different stresses σ and ϕ_L, we did not observe a significant change in the strain scale.

To summarise, we find that the steady state structure of the PS state seems to depend solely on accumulated strain, and is independent on the applied stress σ and the large particle concentration ϕ_L. Since using Moran's I to measure

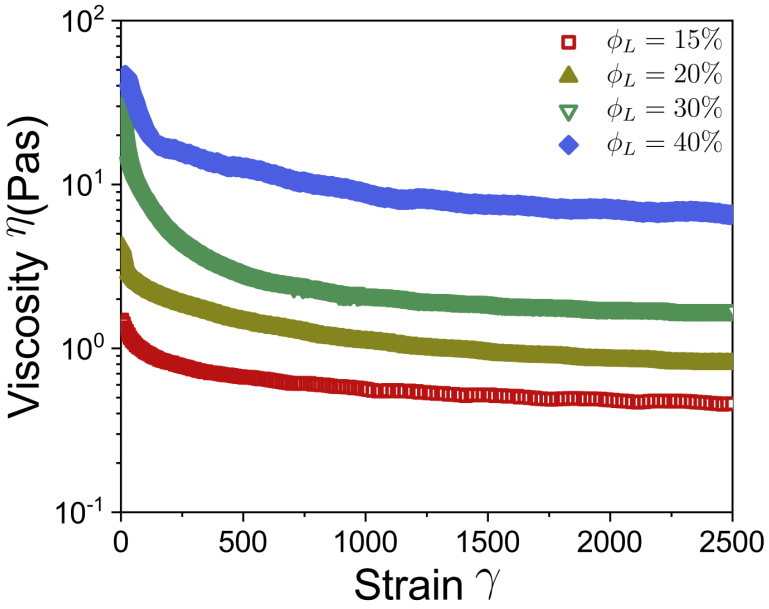

Figure 6.21 Evolutions of viscosity η in samples with different ϕ_L. For each sample, we initially imposed a high preshear $\sigma_{\text{pre}} = 100\,\text{Pa}$ to prepare H states, and then sheared the sample with stress σ in its medium shear regime. The imposed stresses are: $\sigma = 3.2\,\text{Pa}$ ($\phi_L = 15\,\%$), $\sigma = 5.6\,\text{Pa}$ ($\phi_L = 20\,\%$), $\sigma = 10\,\text{Pa}$ ($\phi_L = 30\,\%$), $\sigma = 17.8\,\text{Pa}$ ($\phi_L = 40\,\%$). For better illustration, the viscosity data of $\phi_L = 15\,\%$ sample was shifted by a factor of 0.5.

the global structure obscures important local information (such as the subtle rearrangement at the later stage under shear, Fig. 6.18F-I), further verification may require detailed analysis at the single-particle level.

Breakage

We have shown that moderate shear stresses cause our binary suspensions to phase separate into globular 'droplets' with a characteristic size. However, as the shear stress is further increased beyond σ_b, these 'droplets' eventually rupture and become re-dispersed into a homogeneous state.

We might expect this breakup stress σ_b to reflect the mechanical strength of the 'droplets'. However, extrapolating the colloidal gel yield stress out to our measured ϕ_S^{int} at different ϕ_L, Figure 6.22, we find that the breaking stress σ_b is almost always an order of magnitude lower than the gel yield stress σ_y. That is, these 'droplets' can be readily ruptured by a stress which cannot even make them yield. To attempt to understand this discrepancy, we investigate this breakup process in more depth.

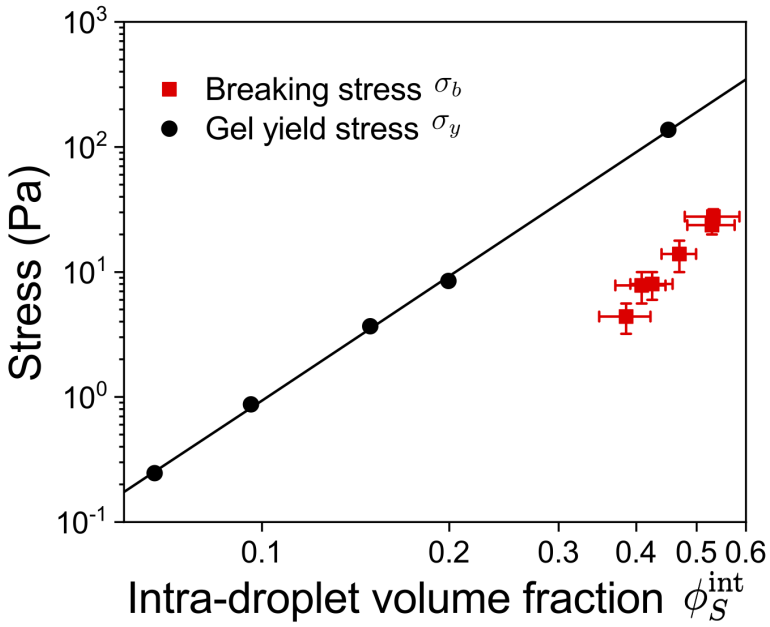

Figure 6.22 Breaking stress σ_b varies as a function of intra-droplet volume fraction ϕ_S^{int}. Using the method described in Figure 6.14, we determined ϕ_S^{int} in samples with different ϕ_L (from low to high): 12.5 %, 15 %, 17.5 %, 20 %, 30 %, 40 %. Black filled circles are yield stresses of colloidal gel at volume fraction $\phi = \phi_S^{\text{int}}$. Solid line: power-law fit ($\sigma_y = \sigma_0 \phi^\nu$) of gel yield stress, giving $\sigma_0 = 1870\,\text{Pa}$ and $\nu = 3.3$.

We imposed a high shear $\sigma = 20\,\text{Pa}$ to a PS state and simultaneously imaged the microstructure. To avoid motion blurring and distortions that result from imaging fast moving objects with a line scanning sensor, we increased the solvent viscosity η_f by reducing the temperature ($T = 5\,^\circ\text{C}$) so that the consequent rate $\dot{\gamma} \sim 10\,\text{s}^{-1}$ is sufficiently low. Figure 6.23 displays confocal slices at different accumulated strains during breakage.

For a liquid droplet under shear, the competition between surface tension and viscous force stretches it into an oval-ish shape before breakage [207]. We have previously shown that our 'droplets' are solid 'droplets' as they do not coalesce. In Figure 6.23, we did not observe visible elongation in the flow direction until complete rupture. This further confirms that the 'droplets' in PS state are solid-like 'droplets', where surface tension plays no role.

Under high shear, the 'droplets' move with flow while their constituents, the small particles, are gradually peeled off, Figure 6.23. Such ablation appear to starts from the interfaces and the 'droplet' cores become smaller, Figure 6.23E-G. At the same time, there are more isolated small particles and flocs as flow proceeds.

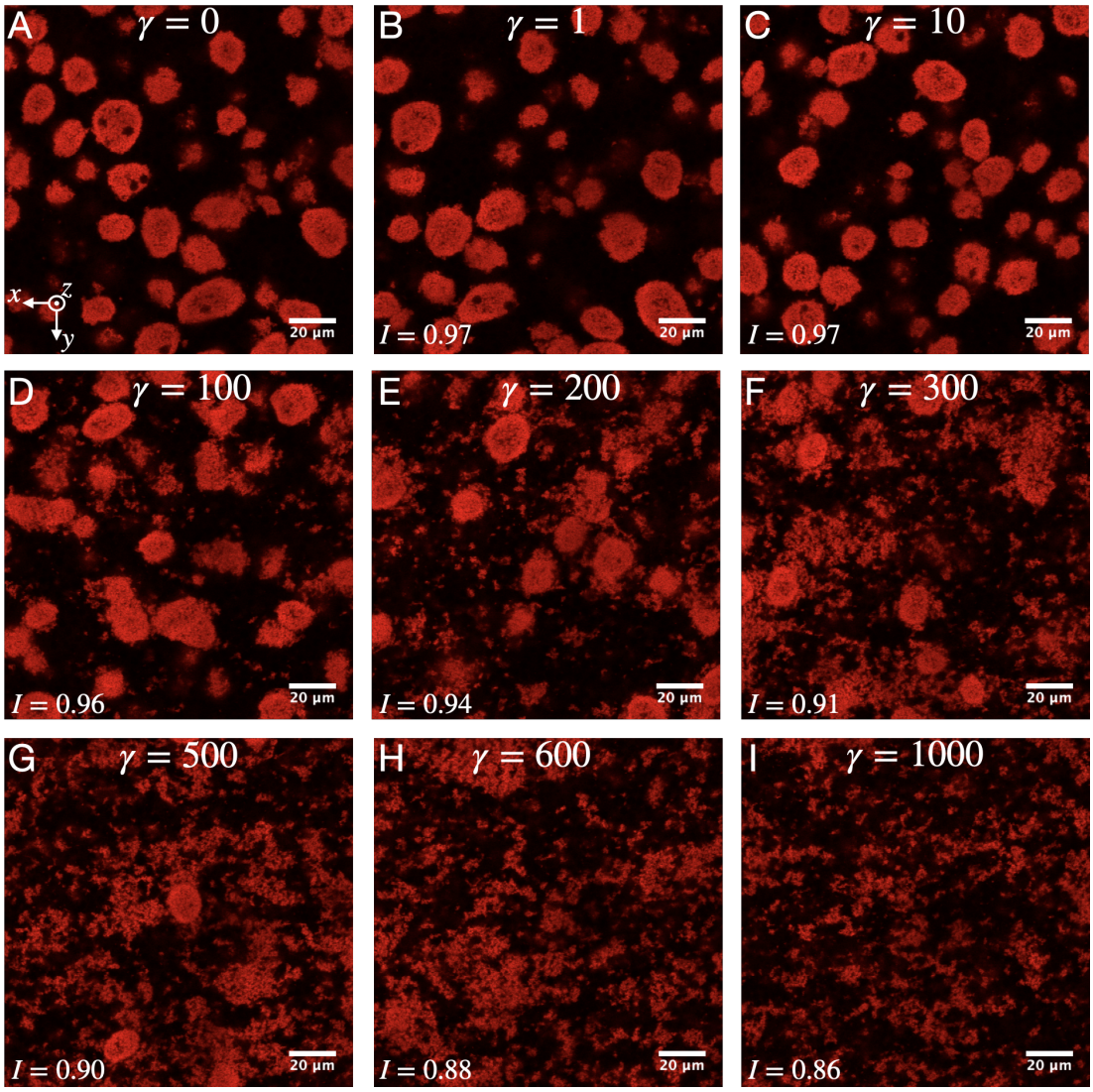

Figure 6.23 Confocal snapshots (small-particle channel) of 'droplet' rupture at different stages. Here we used a sample of $\phi_S = 10\,\%$ and $\phi_L = 20\,\%$, and prepared an initial PS state by preshear $\sigma_{\text{pre}} = 5\,\text{Pa}$. To prevent imaging distortion, we minimise the shear rate by imposing a high shear stress $\sigma = 20\,\text{Pa}$ at a low temperature $T = 5\,^{\circ}\text{C}$. Time-lapsed confocal images were taken at the height of $30\,\mu\text{m}$ simultaneously. The axes of x, y and z in Figure A (bottom-left corner) refer to the flow, vorticity, gradient directions respectively. The accumulated strains γ are shown on the top, while the calculated Moran's Is are shown in the bottom-left corner.

Upon around 1000 strain units, 'droplets' are mostly ruptured and the driven system reaches a steady H state. Such strain scale is roughly verified by the evolutions of Moran's I and viscosity η in Figure 6.24B.

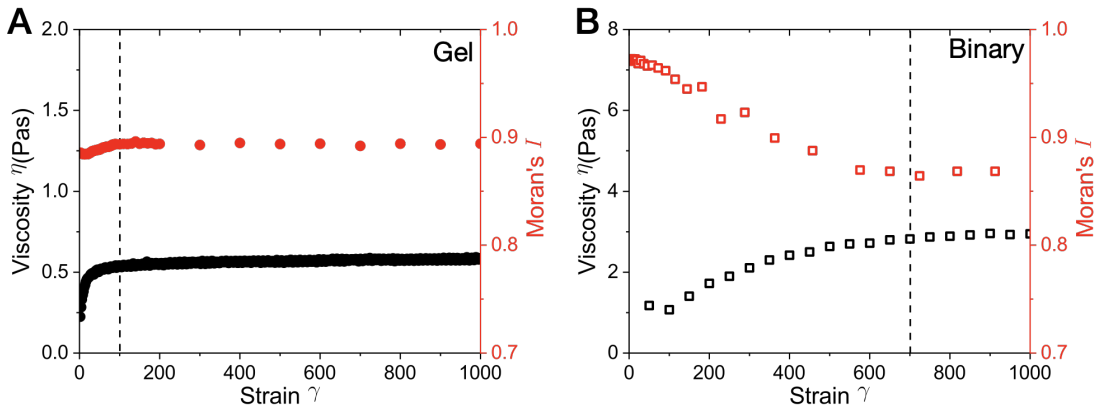

Figure 6.24 A. Evolutions of viscosity η (black) and Moran's I in a $\phi = 10\,\%$ gel under shear with stress $\sigma = 10\,\text{Pa}$. The dashed line ($\gamma = 100$) denotes the strain scale after which the gel reaches a steady state under shear. B. Evolutions of viscosity η (black) and Moran's I in a binary sample ($\phi_S = 10\,\%$ and $\phi_L = 20\,\%$) under shear. We first prepared a PS state by preshear at $\sigma_{\text{pre}} = 5\,\text{Pa}$, and then imposed shear stress $\sigma = 20\,\text{Pa}$ at temperature $T = 5\,^{\circ}\text{C}$. The dashed line ($\gamma = 700$) denotes the strain scale after which the binary sample reaches a steady state under shear.

.

For a small-particle gel under shear, it starts to yields within 1 strain unit (see dynamic strain sweep in Fig. 6.7) while the bulk system reaches a steady state within approximately 100 strain units, Figure 6.24A. Compared with a sheared gel, the breakage of 'droplets' appears to require much more strain units. For an initial PS state, both the viscosity η and Moran's I reach steady states upon $\gamma \gtrsim 700$ under high shear, Figure 6.24B. The difference in the strain scale suggests that the 'droplets' are ruptured in a peeling rather than yielding manner, which is also consistent with our visual observation (Fig. 6.23). In this way, the dominance of local shear force over attraction may be responsible to the 'droplets' breakage. This plausibly explains the discrepancy between the extrapolated yield stress of gel σ_y and the breaking stress σ_b in Figure 6.22.

Breaking stress σ_b

Apart from the interest in microscopic mechanism, the 'droplet' breakage also correlates with macroscopic properties. As previously stated, the medium and

high shear regimes are demarcated by the breaking stress σ_b, beyond which 'droplets' are ruptured. As an important parameter in the state diagram, σ_b varies as a function of both ϕ_S and ϕ_L, Figure 6.25A.

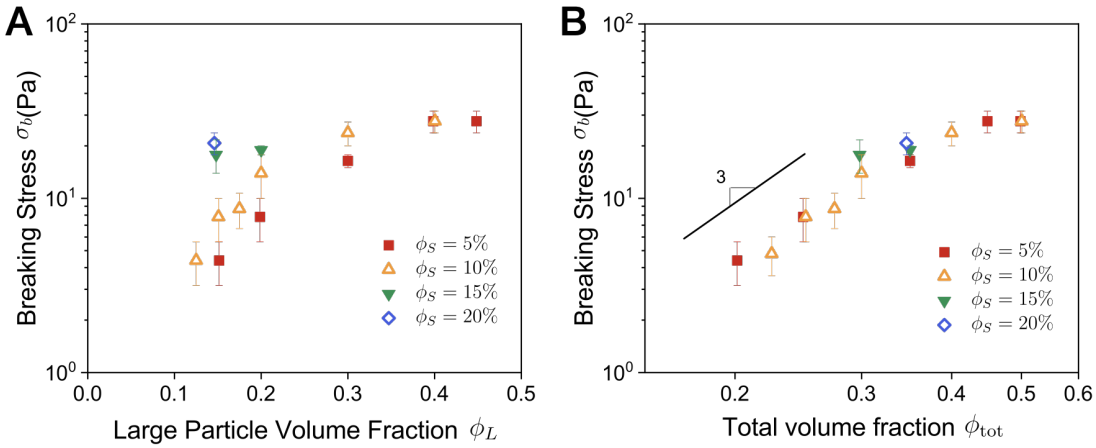

Figure 6.25 Breaking stress σ_b (i.e. the upper shear boundary) in samples of different compositions. A. Breaking stress σ_b versus large particle concentration ϕ_L. Small particle concentrations ϕ_S are labelled by different symbols (see legend). B. Breaking stress σ_b versus total volume fraction $\phi_{tot} = \phi_S + \phi_L$ for the same data in A. The solid line indicates a slope of 3.

Analogous to the effective volume fraction ϕ_S^{eff}, we may expect a unified parameter to collapse σ_b data on a master curve just like the yield stress σ_y does in the σ_y-ϕ_S^{eff} plot (Fig. 6.4B). A few attempts were made and we found that using the total solid volume fraction $\phi_{tot} = \phi_L + \phi_S$ produces the best result, Figure 6.25B. Plotted versus ϕ_{tot}. the breaking stress σ_b at different compositions roughly reduces to an identical curve. As ϕ_{tot} increases, the breaking stress σ_b first appears to increase in a power-law manner with an exponent of 3 and then saturates at around 30 Pa beyond $\phi_{tot} \approx 40\,\%$, Figure 6.25B. We do not understand this collapse, yet it may be used to predict the state transition at a specific composition.

6.2.5 Conclusions

In this section, we investigated the PS state of our binary system, with the focus mostly on the compact 'droplets' of small particles. Through image processing, we quantitatively studied the external morphology of these 'droplets' and confirmed that they are mostly globular and have a size scale $\sim 20\,\mu m$ which barely varies with the applied shear and large particle concentration. These 'droplets' are solid-like as they do not coalesce either at rest or under moderate flow. This

is consistent with the internal structure from SEM which plausibly indicates a glassy state inside the 'droplets'. We also recorded their formation and breakage process under shear by rheo-imaging, and identified the important role of the accumulated strain γ.

However, our understanding on the binary suspension is still poor. Both the discrepancy between the 'droplet' yield stress and the breaking stress (Fig. 6.22), and the microscopic mechanism of phase separation, the most important phenomenology in this work, still remain open questions. To get broader insights into fundamental physics, in the next chapter, we will further explore the parameter space of our binary suspension.

Chapter 7

Beginning to Explore Parameter Space

Controlling parameters is an effective way to enhance understanding on a phenomena or a system. For example, through tuning particle surface roughness, a recent experimental study verified the role of interparticle friction in shear thickening [145]. Hence to better understand our binary suspension, it is vital to fully explore the parameter space. Although we have just begun to explore it, the present results have already identified the importance of particle composition. Further tuning other parameters, therefore, may contribute towards answering fundamental questions like 'how/why does phase separation occur under flow?'.

Apart from the intrinsic interest, exploring the parameter space also sets the stage for improving structural and rheological control, which is of practical significance [208]. Though the flow-switched transition enables one to tune the flow property of binary suspensions, the tunability is somewhat limited. According to the state diagrams from Chapter 5 (Fig. 5.19), the solid states of bistable samples are soft: the yield stress σ_y can only be tuned within a narrow range (0 Pa to $\sim$ 30 Pa). In industrial applications, however, greater tunability is favoured, such as the transition from an adaptive liquid to a rigid solid ($\sigma_y \gtrsim 1\,\mathrm{kPa}$) in mould casting [209]. To improve the rheological performance of our system, it is instructive to individually study the impact from different parameters.

The parameter space of our binary suspension is huge, and so far we have only explored a small part of it. In Chapter 5, we mapped out slices of the state diagram by tuning the mixture composition (ϕ_S and ϕ_L) and imposed shear

stress σ. To completely describe such binary mixture, one still needs to specify three pair interactions (small-small, small-large and large-large) and two particle sizes (d_S and d_L). In this chapter, we tune the pair interactions and particle sizes, and investigate how the state transition varies with these parameters. We summarise the relation between state boundaries and these parameters in the end. Our results imply that the small-small attraction U_{att} and the large particle size d_L are two key factors. This finding may fill important gaps for fundamental understanding on the shear-induced phase separation.

7.1 Tuning pair interactions

Three pair interactions exist in our binary system: small-small U_{SS}, small-large U_{SL} and large-large U_{LL}. In this thesis so far, U_{SS} is hydrophobic attraction (denoted by U_{att}) and U_{LL} is electrostatic repulsion (denoted by U_{rep}). The mixed interactions U_{SL} are not well characterised, but the lack of visible small-large binding indicates repulsion, or at most attraction of the order of k_BT. Through changing the surface chemistry, here we probe the relation between phase separation and these interactions. Since precise measurement on interparticle force is challenging in practice, we only qualitatively discuss the influence of pair interactions unless otherwise stated.

7.1.1 Making large particles attractive

We tuned U_{LL} and U_{SL} by making large particles hydrophobic. The large silica particles were functionalised by the same protocol as small particles (see Chapter 4), with the same mass ratio of silica: ethanol: HMDS: ammonia = 1: 40: 3: 7. After functionalisation, both species of particles are hydrophobic and expected to attract each other. In this way, our binary composite becomes a bidisperse attractive suspension.

Confocal imaging shows that, in contrast to binary mixtures with bare large particles, halos of small particles form around the hydrophobic silica spheres (Fig. 7.1A), indicating significantly increased small-large attraction. Though we did not directly observe aggregation amongst large particles, we can confirm large-large attraction by comparing the rheology of bare and hydrophobic large particle suspensions (Fig. 7.1B). At a moderate volume fraction ($\phi \simeq 25\,\%$), the

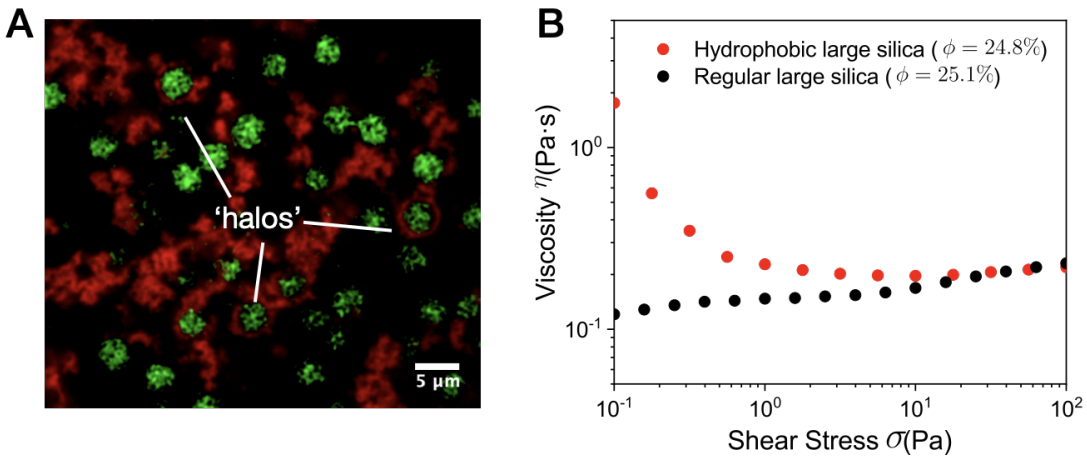

Figure 7.1 Demonstration of attractions between small-small, small-large and large-large. A. Confocal image of binary sample ($\phi_S = 10\,\%$; $\phi_L = 20\,\%$) using hydrophobic large silica. The red aggregates and 'halo' structure confirm the U_{SS} attraction and U_{SL} attraction respectively. B. Flow curves of suspensions of bare large silica (black) and hydrophobic large silica (red) at a moderate concentration $\phi \simeq 25\,\%$. The shear thinning behaviour implies that U_{LL} is attractive [210, 211].

suspension of bare large silica is nearly Newtonian. In contrast, the hydrophobic large silica exhibits clear shear thinning at low applied stress ($\sigma \lesssim 1\,\mathrm{Pa}$), and possibly even possesses a very weak yield stress. At high stress $\sigma > 10\,\mathrm{Pa}$, the two viscosities converge. Such a change from a Newtonian or thickening rheology to shear thinning in non-Brownian suspensions has been shown in both experiments [210] and simulations [211] to result from the addition of inter-particle attraction.

Using these hydrophobic particles, we can examine the behaviour of binary suspensions where we know that all three interactions, U_{SS}, U_{SL} and U_{LL}, are attractive. Though we can verify attraction, we cannot directly quantify the absolute magnitude of these attractive interactions without more advanced characterisation methods (e.g. colloidal probe AFM).

Though the hydrophobic coating alters both the rheology of large particle suspensions (Fig. 7.1B) and the microstructure of the binary mixture (Fig. 7.1A), we still observe the same shear-induced phase separation that we found with the repulsive large particles. Figure 7.2 compares the binary samples (with the same composition) using bare large silica and hydrophobic large silica. A and B are confocal images of each state, with the two transition boundaries (σ_y and σ_b) noted on the top. Visually, there is no obvious difference in the microstructure. In either sample, the H state consists of gel matrix of small particles with large

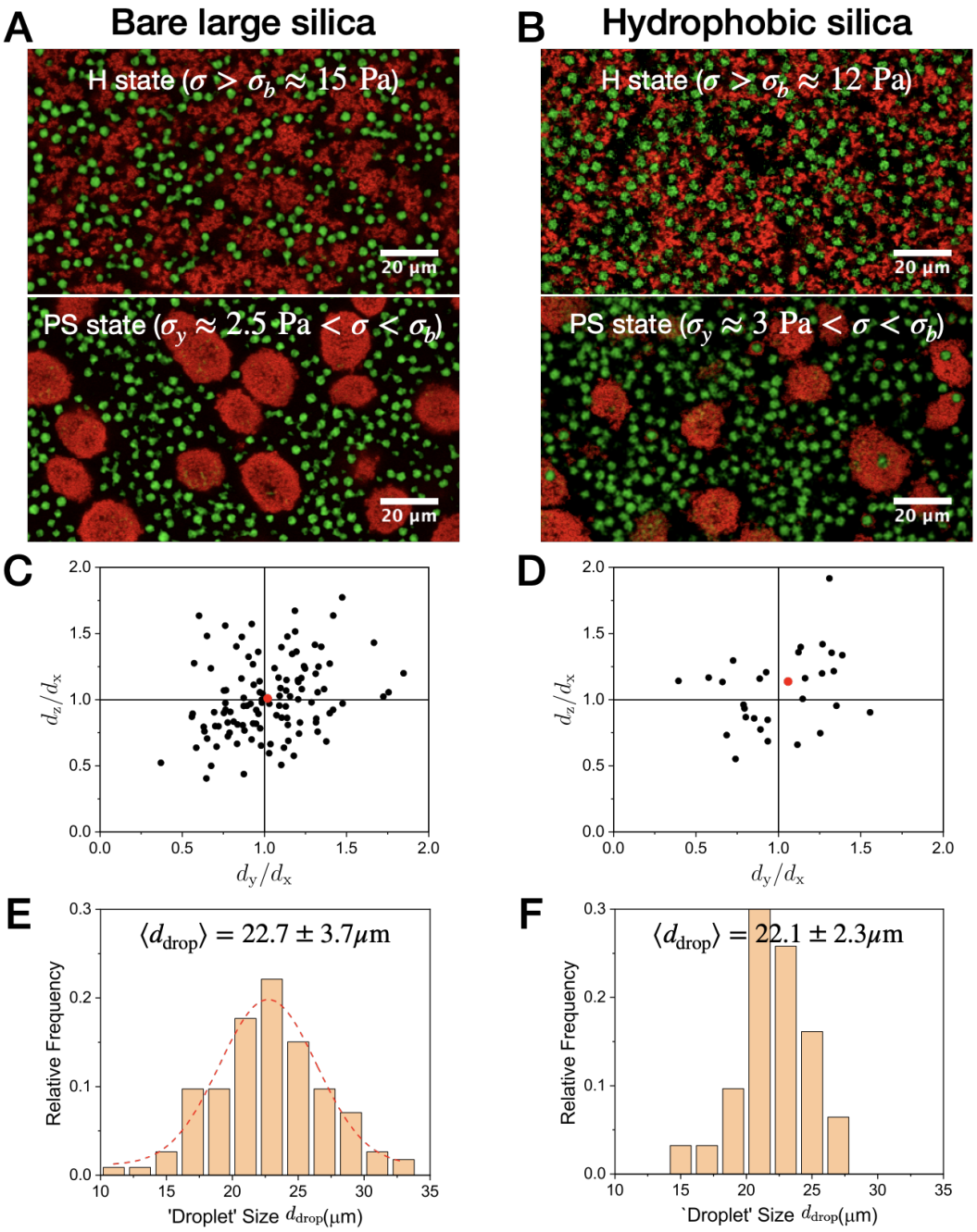

Figure 7.2 Comparison of binary samples ($\phi_S = 10\,\%$ and $\phi_L = 20\,\%$) using bare silica (A, C, E) and hydrophobic silica (B, D, F) as large particles. A-B: Confocal images of H states (top) and PS states (bottom). The shear boundaries are noted on the top of each image. Based on the 3D confocal stacks, we counted 'droplets' in PS states using the mean-shift clustering algorithm. C-D: Scatter plots of the aspect ratios (d_y/d_x and d_z/d_x). The red filled circles represent average values. C is taken from Chapter 6 (Fig. 6.12B). E-F: 'Droplet' size distributions. The mean sizes $\langle d_{\mathrm{drop}} \rangle$ are shown on the top. E is taken from Chapter 6 (Fig. 6.12A).

particles embedded inside, whereas the PS state consists of globular 'droplets' with a characteristic size $\sim 20\,\mu m$. Apart from the similar microstructure, the two transition boundaries remain almost unchanged as well.

Quantitative analysis based on 3D stacks confirms the globular shape and similar size of 'droplets'. The scatter plots of the aspect ratios d_y/d_x and d_z/d_x, Figure 7.2 C and D, show wide distributions with the average values ≈ 1 (red filled circles) in both cases. The size distributions, Figure 7.2E and F, suggest similar mean 'droplet' sizes $\langle d_{\mathrm{drop}} \rangle$ as well. These results imply that making large particles attractive appears to have little effect on our binary suspensions. The shear-driven phase separation that we have discovered in this work is not restricted to composites with repulsive large particles.

7.1.2 Tuning small-small attraction

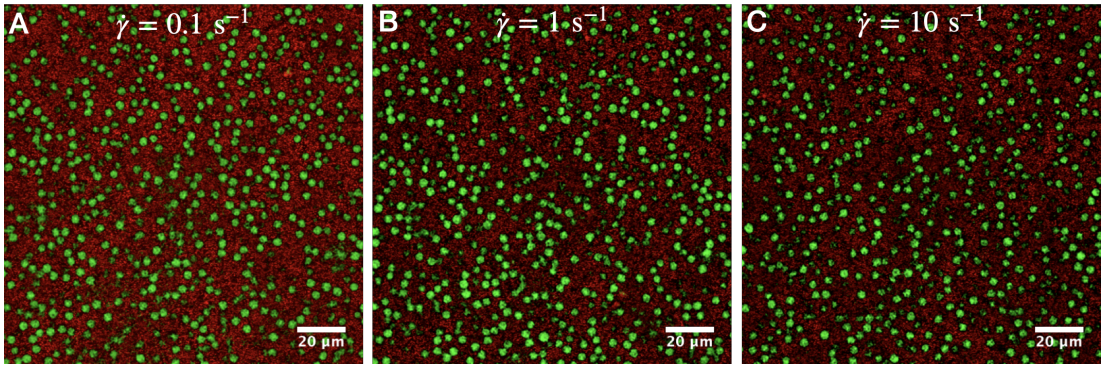

Figure 7.3 Confocal images of a binary suspension without small-small attraction U_{att}. We used unfunctionalised silica colloids as small particles, and prepared the sample at $\phi_S = 10\,\%$ and $\phi_L = 20\,\%$. We imposed different shear rates $\dot{\gamma}$ (see the top of each image) and imaged the sample upon shear cessation. The shear with rate $\dot{\gamma} = 0.1\,s^{-1}$ lasted for 30 min, whereas other shear rates were applied up to the accumulated strain $\gamma \gtrsim 1000$.

Not surprisingly, the small-small attraction plays an important role in the phase separation. Without such attraction, our binary mixture becomes a bidisperse suspension of hard particles, in which neither gelation nor phase separation is observed [15, 212]. We confirmed this by using unfunctionalised (hydrophilic) silica colloids as small particles so that they do not hydrophobically attract each other. Again, we prepared the binary sample at $\phi_S = 10\,\%$ and $\phi_L = 20\,\%$. Without small-small attraction, the yield stress is absent as expected in such a collection of bidisperse hard-particles. Moreover, upon cessation of moderate

shear with rate $\dot{\gamma}$ ranging from $0.1\,\mathrm{s}^{-1}$ to $10\,\mathrm{s}^{-1}$, we did not observe any visible aggregates or density variations in the small particle phase, Figure 7.3. The absence of 'droplets' suggests that the small-small attraction is essential for phase separation.

To further understand the role of attraction, we varied the attraction strength U_{att}. For a small-particle gel, as previously shown in Chapter 4, its yield stress σ_y slowly (over the course of weeks) decreases with time after the small particles are dispersed into the solvent, Figure 7.4A (black). Such ageing effect, also observed in binary suspensions (Fig. 7.4A), suggests that the hydrophobic attraction U_{att} decreases over time. While the majority of measurements in this thesis were taken at a fixed sample age ($t_{\mathrm{age}} = 3\,\mathrm{d}$) to compensate for this, we can actually exploit the ageing effect to vary U_{att} by simply letting samples age for different time periods.

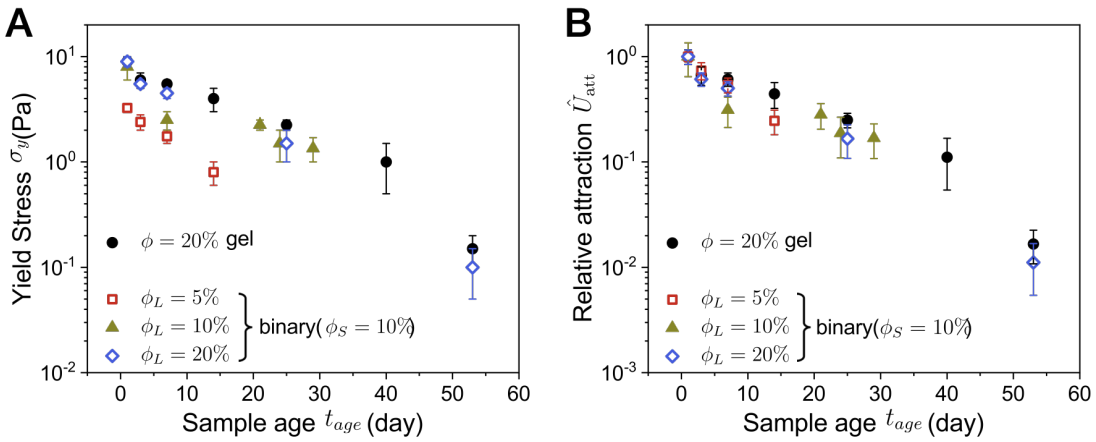

Figure 7.4 A. Yield stress σ decreases with time after sample preparation. Such ageing effect was observed in a $\phi = 20\,\%$ gel (black, taken from Fig. 4.14B in Chapter 4) as well as in binary samples with different ϕ_L. See legend for detailed composition. B. Relative attraction $\hat{U}_{\mathrm{att}}$, i.e. the scaled yield stress (see Eq. 7.1), varies as a function of sample age t_{age}. For the same data in A.

While, as noted before, we cannot directly measure U_{att}, we can indirectly infer the relative change in U_{att} from the decrease in yield stress $\sigma_y(t_{\mathrm{age}})$ since we expect $\sigma_y \propto U_{\mathrm{att}}$ [213]. Specifically, we first prepared a sample (either binary or pure gel) and let it age in a well-sealed vial. After one day, we extracted a small portion of the sample and measured its yield stress $\sigma_y(t_{\mathrm{age}} = 1\,\mathrm{d})$ as a reference. For the sample at age t_{age}, we normalise its yield stress $\sigma_y(t_{\mathrm{age}})$ to define the relative attraction $\hat{U}_{\mathrm{att}}$:

$$\hat{U}_{\mathrm{att}} = \frac{\sigma_y(t_{\mathrm{age}})}{\sigma_y(t_{\mathrm{age}} = 1\,\mathrm{d})}. \tag{7.1}$$

In either colloidal gels or binary suspensions, the relative attraction $\hat{U}_{\text{att}}$ decreases with the sample age t_{age} in a similar manner, Figure 7.4B. In this way, we can vary and quantify the attraction strength $\hat{U}_{\text{att}}$ in an arbitrary sample.

Fixing $\phi_S = 10\,\%$, we prepared three binary samples at $\phi_L = 5\,\%$, $10\,\%$ and $20\,\%$ and measured them at different ages (i.e. different attraction strength). Their state diagrams as functions of the relative attraction strength $\hat{U}_{\text{att}}$ are shown in Figure 7.5A-C, whereas the relation between the two shear boundaries and $\hat{U}_{\text{att}}$ is shown in Figure 7.5E-F.

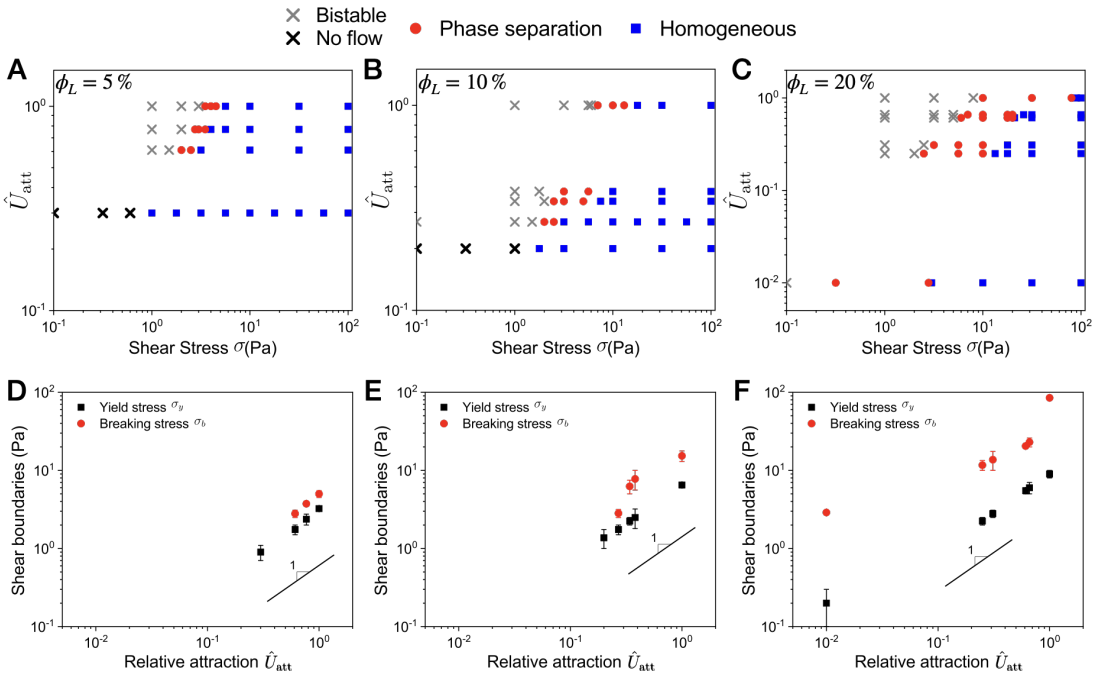

Figure 7.5 Varying the small-small attraction affects state diagrams. We fixed $\phi_S = 10\,\%$ and prepared three binary samples with different ϕ_L. A-C. State diagrams vary as functions of relative attraction strength $\hat{U}_{\text{att}}$ at different ϕ_L (noted in the top-left corner). D-F. Two shear boundaries (determined from A-C) vary as functions of relative attraction $\hat{U}_{\text{att}}$.

Consistent with the definition of $\hat{U}_{\text{att}}$ (Eq. 7.1), the lower boundary σ_y between low and medium shear regimes linearly increases with $\hat{U}_{\text{att}}$ in each case, Figure 7.5D-F. Meanwhile, the breaking stress σ_b, which demarcates medium and high shear regimes, increases with $\hat{U}_{\text{att}}$ as well. As the small-small attraction becomes weaker, the medium shear regime progressively narrows down. In particular, at $\phi_L = 5\,\%$ and $10\,\%$ (Fig. 7.5A and B), the phase separation region (red filled circles) vanishes below a critical $\hat{U}_{\text{att}}$. By contrast, we still observed phase separation in the $\phi_L = 20\,\%$ sample even when $\hat{U}_{\text{att}}$ drops by two orders of

magnitude (Fig. 7.5C). Though the medium shear regime appears to be still broad in the log-log plot, the range of medium stress actually becomes quite narrow on a linear scale.

In the state diagram at $\phi_S = 10\,\%$ (Fig. 5.16A in Chapter 5), phase separation is completely absent below $\phi_L = 10\,\%$. It seems like increasing attraction strength can effectively lower this concentration threshold. At the strongest attraction we achieved, the addition of 5 % large particles is sufficient to enable PS state, Figure 7.5A. Broadening the medium shear regime as well as lowering the concentration threshold, stronger attraction U_{att} between small particles makes their phase separation more readily.

Even though varying the small-small attraction U_{att} has a significant effect on the state diagram, surprisingly, it has little impact on the phase-separated structure. Figure 7.6 compares the PS structure at different attraction strength $\hat{U}_{\mathrm{att}}$. Here we fixed $\phi_S = 10\,\%$ and $\phi_L = 20\,\%$ and varied sample age t_{age}. With t_{age} ranging from 1 day to 53 days, the 'droplets' with sharp interfaces, as shown in Figure 7.6A-C, always occur under moderate shear.

Visually, the phase-separated 'droplets' are similar in all cases. We then quantitatively analysed these 'droplets' based on 3D stacks. The scatter plots of the aspect ratios all show that the length of 'droplets' in each direction is comparable on average ($d_{\mathrm{x}} \approx d_{\mathrm{y}} \approx d_{\mathrm{z}}$), Figure 7.6D-F. The size distributions in Figure 7.6G-I indicate that these 'droplets' have similar sizes, except that the weakest attraction $\hat{U}_{\mathrm{att}} = 0.01$ exhibits slightly smaller 'droplets' (Fig. 7.6G). Overall, while the two shear boundaries vary as functions of the small-small attraction U_{att}, the microstructure in PS state exhibits little dependence on U_{att}.

7.2 Varying particle sizes

In our results presented thus far, regardless of the composition, shear strength and pair interactions, the 'droplets' in PS state are globular with well-defined average size $d_{\mathrm{drop}} \sim 20\,\mu\mathrm{m}$. This implies generic physics behind the phase separation. Using silica with different sizes, we show that the size of large particles d_L sets the size of the resulting 'droplets'.

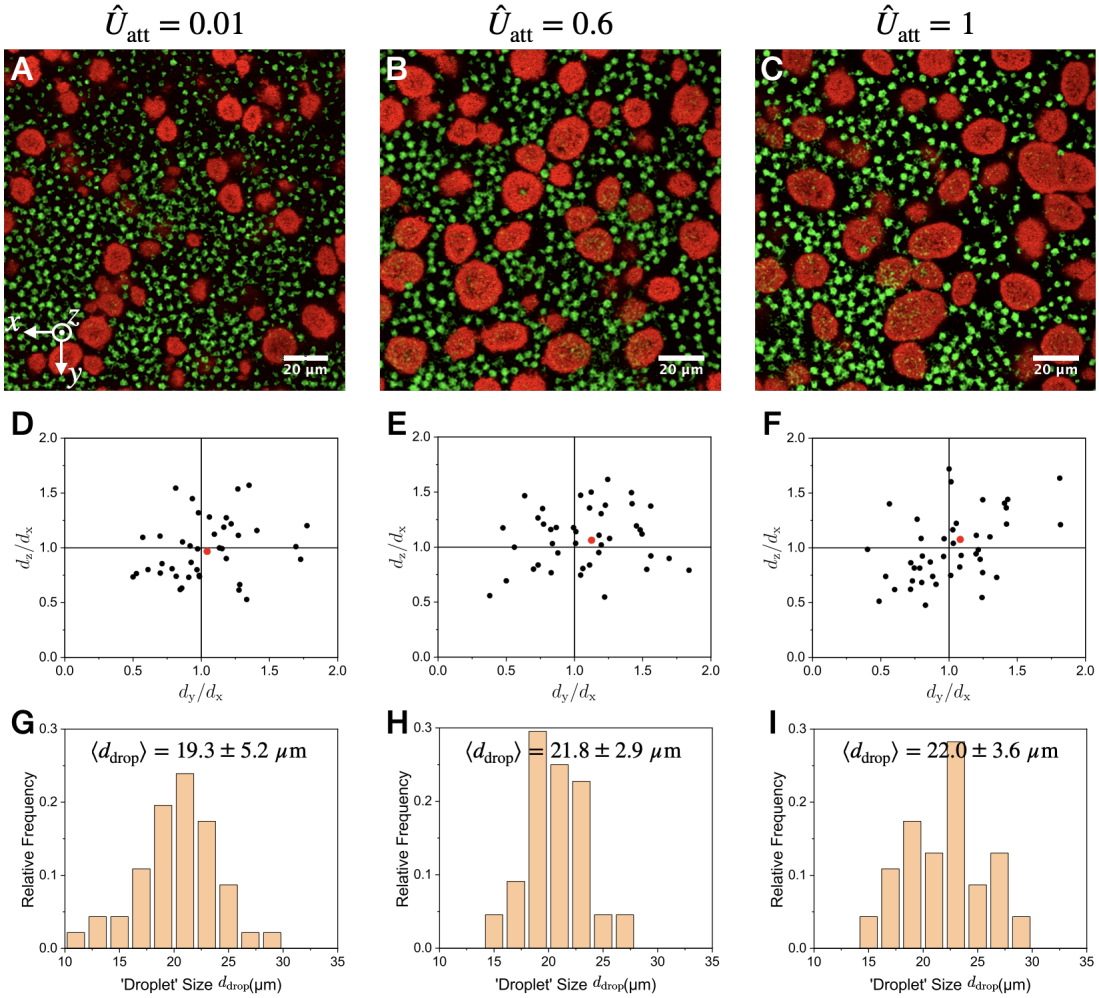

Figure 7.6 PS structure in a binary suspension ($\phi_S = 10\,\%$; $\phi_L = 20\,\%$) with varying attraction. We measured the same sample at different ages (from old to young): 53 days ($\hat{U}_{att} = 0.01$), 7 days ($\hat{U}_{att} = 0.6$) and 1 day ($\hat{U}_{att} = 1$). The relative attraction $\hat{U}_{att}$ is noted on the top of each column. A-C: Confocal images after cessation of medium shear. The imposed stresses are (from left to right): 0.32 Pa, 10 Pa and 31.6 Pa. D-F: Scatter plots of the aspect ratios (d_y/d_x and d_z/d_x) of the 'droplets'. The red filled circles represent average values. G-I: 'Droplet' size distribution. The mean sizes $\langle d_{drop} \rangle$ are shown on the top of each graph.

7.2.1 Small particle size d_S

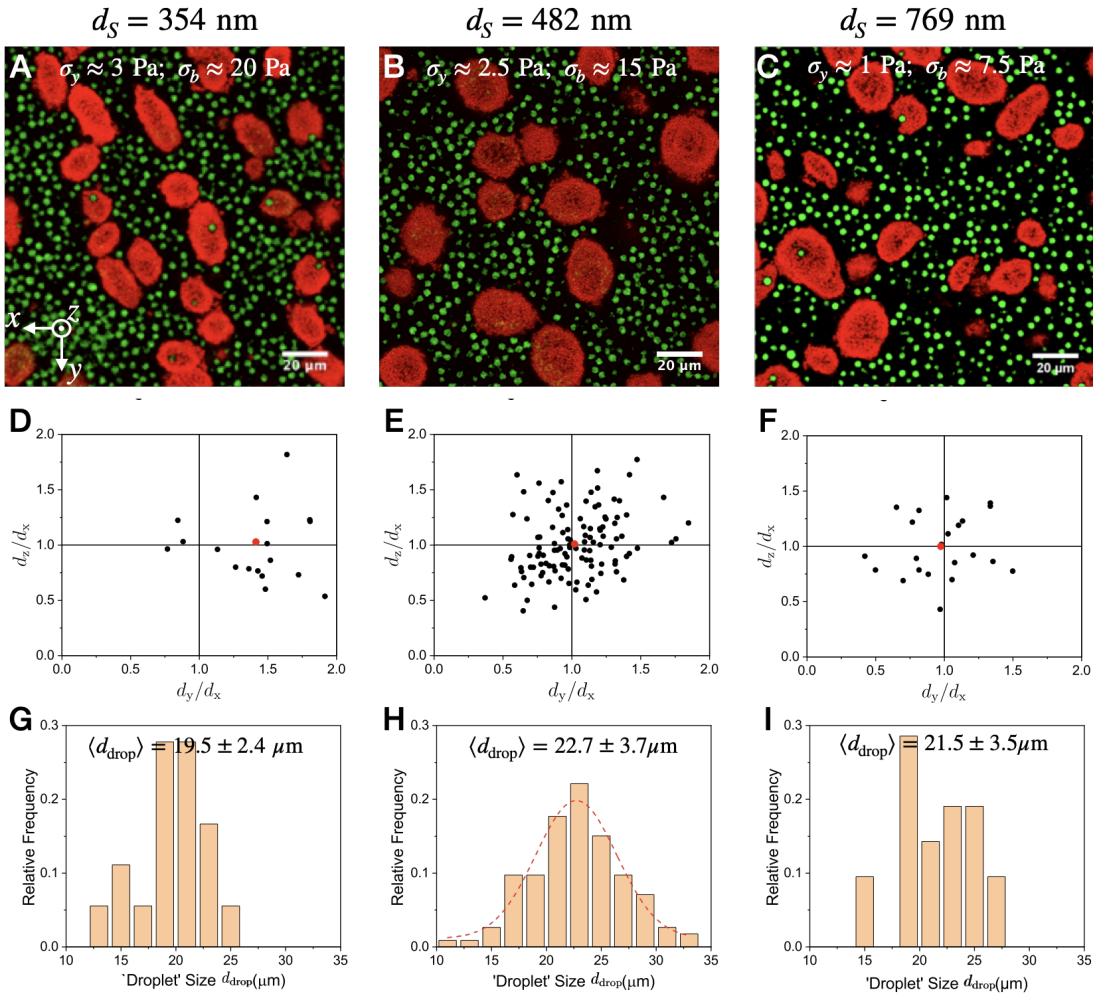

Figure 7.7 PS structure in a binary suspension ($\phi_S = 10\,\%$; $\phi_L = 20\,\%$) with different small particle size d_S (noted on the top of each volume). A-C: Confocal images after cessation of medium shear rate $\dot{\gamma} = 5\,\mathrm{s}^{-1}$. The two shear boundaries σ_y and σ_b are shown on the top of each image. D-F: Scatter plots of the aspect ratios ($d_\mathrm{y}/d_\mathrm{x}$ and $d_\mathrm{z}/d_\mathrm{x}$) of the 'droplets'. The red filled circles represent average values. G-I: 'Droplet' size distribution. The mean sizes $\langle d_\mathrm{drop} \rangle$ are shown on the top of each graph.

To vary the small particle size d_S, we used different recipe to synthesise several batches of silica colloids with the size ranging from approximately 300 to 800 nm. After synthesis, these silica colloids were functionalised by the same protocol described in Chapter 4. Using the same large particles ($d_L = 4\,\mu\mathrm{m}$) and small particles with various d_S, we studied binary suspensions at $\phi_S = 10\,\%$ and $\phi_L = 20\,\%$ through rheo-confocal microscopy.

Again, we observed phase separation in these samples. Figure 7.7A-C show PS states of samples using small particles with $d_S = 354\,\text{nm}$, $d_S = 482\,\text{nm}$ and $d_S = 769\,\text{nm}$ (all determined by DLS) respectively. The PS states were prepared by shearing at a fixed rate $\dot{\gamma} = 5\,\text{s}^{-1}$ up to an accumulated strain of $\gamma \gtrsim 1000$. Visually, there are slight differences in the 'droplet' morphology. The droplets formed by the smallest particles ($d_S = 354\,\text{nm}$) are noticeably elongated on the vorticity y-direction (Fig. 7.7A and D). This slight anisotropy seems to occur in all samples using the same batch of hydrophobic silica. Since we only examined the PS microstructure at three different d_S, we cannot confirm if this elongation results from the reduced particle size or from surface chemistry. Besides, we also observed a slight excess of smaller 'droplets' in samples with $d_S = 354\,\text{nm}$ and $d_S = 769\,\text{nm}$, Figure 7.7G and I. However, overall these variations in the 'droplet' size and shape are relatively minor considering that the small particle size has been varied by over a factor of two.

Smaller particles lead to stronger gels [187]. Hence we expect that smaller d_S leads to increases in both σ_y, the H-state yield stress, and σ_b, the breaking stress which correlates with the mechanical strength of 'droplets'. Our results do agree with this expectation (see the shear boundaries σ_y and σ_b on the top of Fig. 7.7A-C). However, direct measurements of the particle interactions would be needed account for likely variations in the particle surface chemistry, and hence interaction strength, to truly distinguish the role of small particle size d_S.

Based on these results, we may conclude that the size d_S of small particles, the constituents of 'droplets', plays a minor role in the shear-induced phase separation. At least, this applies within the size range we probed ($300 \sim 800\,\text{nm}$).

7.2.2 Large particle size d_L

Using several batches of silica microspheres, we varied the size of repulsive particles d_L from 10 µm down to 0.5 µm. Specifically, the silica microspheres with d_L =0.5 µm, 1.5 µm and 4.0 µm are from Amstrongsphere®, whereas those with d_L =6.7 µm and 9.8 µm are from Whitehouse Scientific Ltd. Using the same small attractive particles ($d_S = 482\,\text{nm}$) and repulsive particles with different d_L, we prepared binary samples at $\phi_S = 10\,\%$ and $\phi_L = 30\,\%$ and studied their structural behaviour via rheo-confocal microscopy. Note that we keep the same notation as elsewhere in the thesis, using d_L and ϕ_L to refer to the repulsive particles, even though we approach $d_L \approx d_S$.

Remarkably, we did not observe phase separation or even significant aggregation in the sample with $d_L = 0.5\,\mu\text{m} \approx d_S$. To completely confirm the absence of phase separation, we imposed shear rates $\dot{\gamma}$ ranging from $0.1\,\text{s}^{-1}$ to $100\,\text{s}^{-1}$. After cessation of shear, the small particles exhibit homogeneous configuration in all cases, Figure 7.8. However, unlike binary suspensions with larger repulsive particles, here we were unable to resolve a measurable yield stress (Fig. 7.8), indicating that the small particles were unable to form a gel even though the suspensions appear homogeneous.

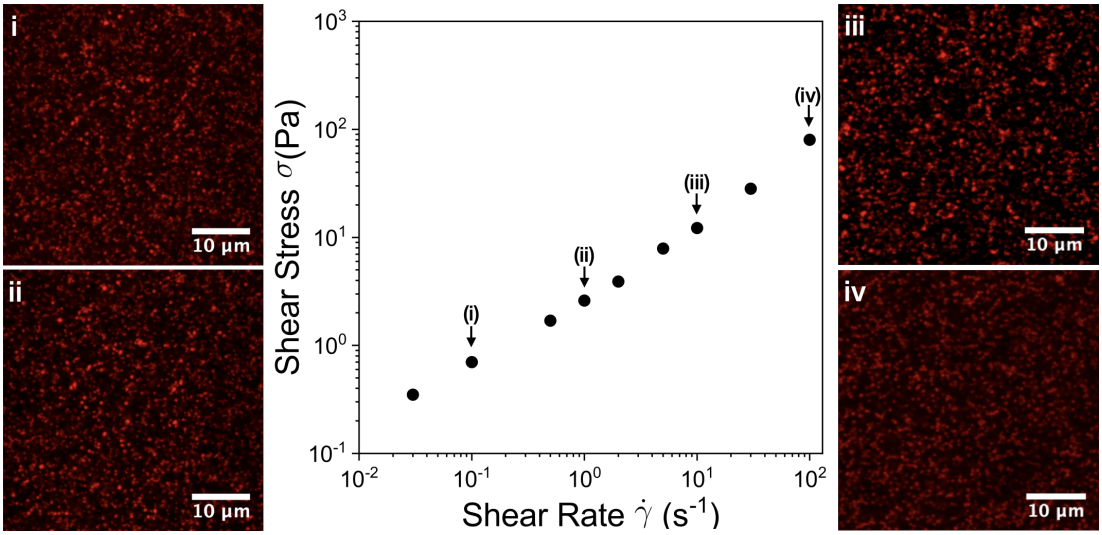

Figure 7.8 Flow curve of a binary sample ($\phi_S = 10\,\%$; $\phi_L = 30\,\%$) with $d_L = 0.5\,\mu\text{m}$, along with confocal images (small-particle channel) after cessation of shear with rates indicated using arrows in the main figure. Before imaging, we performed the $0.1\,\text{s}^{-1}$ shear (i) for 30 min, while the other shear rates (i-iv) were performed up to the accumulated strain of $\gamma \gtrsim 1000$.

Holding the composition fixed, samples with $d_L \gtrsim 1.5\,\mu\text{m}$ exhibited the same shear-driven transition (between homogeneous gel and phase-separated 'droplets') that we observed with the $4\,\mu\text{m}$ repulsive particles, though the 'droplets' in the $1.5\,\mu\text{m}$ case are noticeably smaller and less globular, Figure 7.9A. As d_L increases, 'droplets' with sharp interfaces are formed under moderate shear, and there is a clear increase in the 'droplets' size (Figures 7.9 and 7.10B). In particular, the size of 'droplets' approaches $40\,\mu\text{m}$ for the largest repulsive particles we used ($d_L = 9.8\,\mu\text{m}$). In such case, we used a plate-plate geometry with a large gap height ($500\,\mu\text{m}$) so that the 'droplet' growth is not artificially limited. This result, as well as the absence of phase separation when $d_L \approx d_S$, demonstrates that the large particle size plays a key role controlling the microstructure.

In addition to setting the 'droplet' size, d_L also affects the stress boundaries for

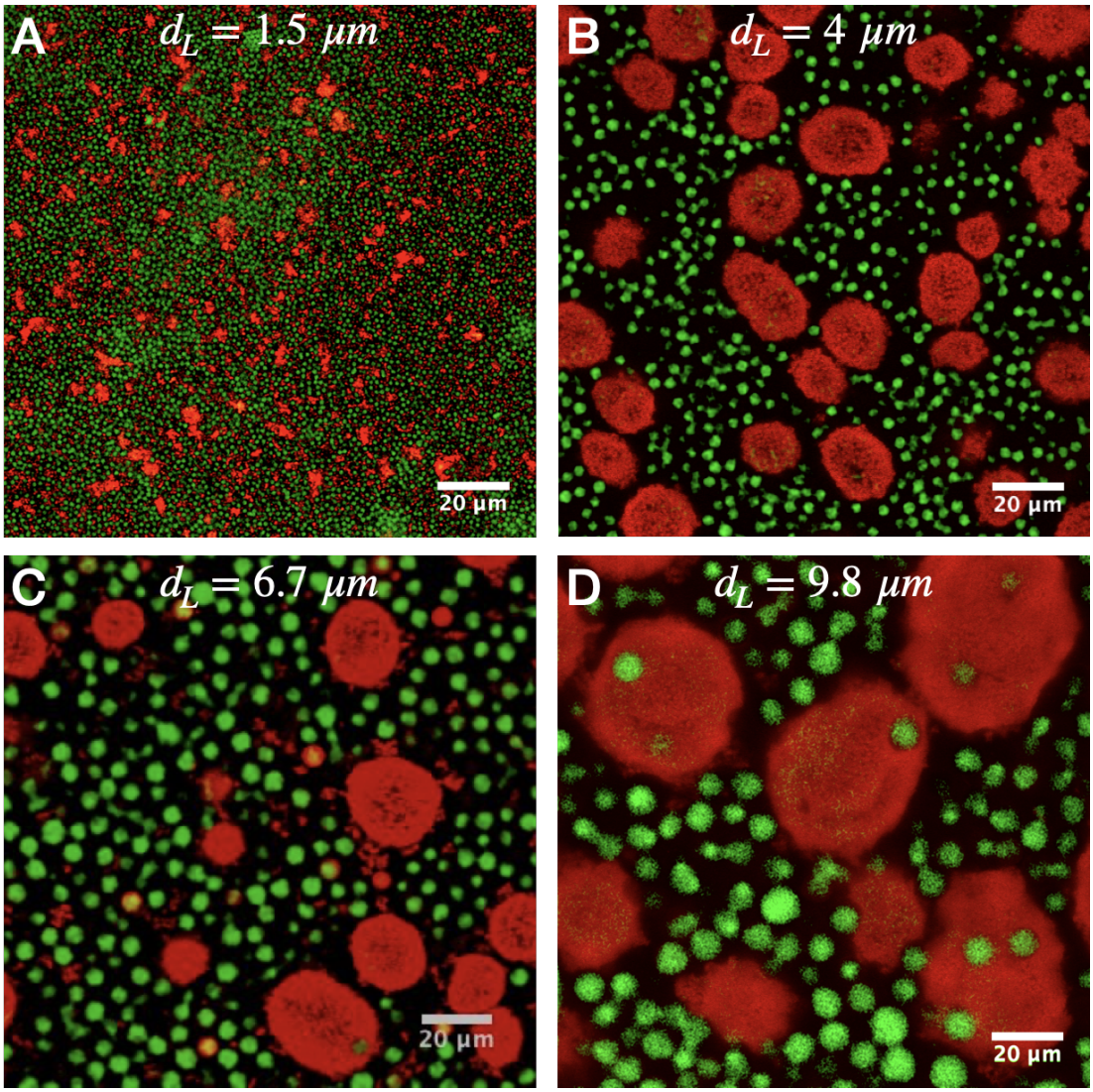

Figure 7.9 PS states of binary samples with different d_L (noted on the top of each image). Here we fixed $\phi_S = 10\,\%$ and $\phi_L = 30\,\%$, and prepared the PS states by imposing prolonged medium shear ($\dot{\gamma} = 5\,\mathrm{s}^{-1}$) until the accumulated strain $\gamma \gtrsim 1000$.

the state diagram. Holding the composition ($\phi_S = 10\,\%$, $\phi_L = 30\,\%$) fixed, we plot the state diagram as a function of d_L in Figure 7.10A. The H-state yield stress σ_y, which sets the low bound for the PS region, increases with d_L drastically and drops below our rheometer resolution ($\sigma_y < 0.1\,\text{Pa}$) for $d_L \approx d_S$. As d_L increases from 1.5 µm to 9.8 µm, the lower boundary σ_y increases by almost two orders of magnitude. As discussed in Chapter 6, such correlation may offer important insights into the yielding behaviour of particle-filled gels.

By contrast, the upper boundary σ_b, also referred to as the breaking stress beyond which 'droplets' are ruptured, shows little dependence on d_L. While the shear-induced 'droplets' are ubiquitous at $d_L \gtrsim 1.5\,\mu\text{m}$, the range of medium stress can become quite narrow as d_L increases. Figure 7.10B summarises the influence of large particle size d_L.

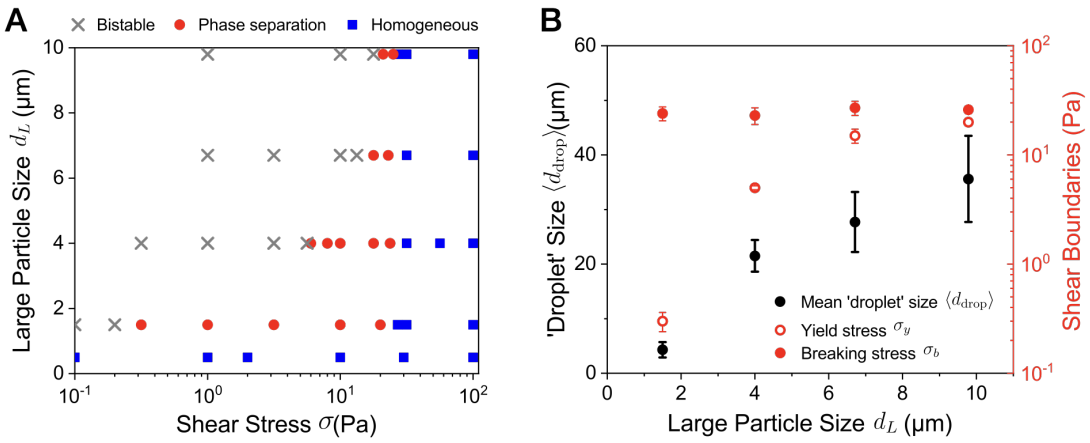

Figure 7.10 Binary samples ($\phi_S = 10\,\%$; $\phi_L = 30\,\%$) with varying d_L. A. State diagram as a function of large particle size d_L. Since the PS structure at $d_L = 1.5\,\%$ is not as heterogeneous as other samples that exhibit clear phase separation (see Fig. 7.9), we determined the state of the $d_L = 1.5\,\%$ sample by visual judgement. B. The relation between large particle size d_L and microstructure and shear boundaries. Black: mean 'droplet' size $\langle d_{\text{drop}} \rangle$, determined by the mean-shift clustering. Red open circles: the lower shear boundary, i.e. yield stress σ_y. Red filled circles: the upper boundary, i.e. breaking stress σ_b.

7.3 Tuning state diagram and microstructure

The state diagram of our binary suspension is mainly characterised by the two shear boundaries σ_y and σ_b. Our results in this chapter demonstrate that the

Table 7.1 *Dependence of shear boundaries on different parameters*

	The lower boundary σ_y	The upper boundary σ_b
Large particle concentration ϕ_L	↑	↑
Small particle concentration ϕ_S	↑	↑
Large particle size d_L	↑	—
Small particle size d_S	↓ (to be verified)	↓ (to be verified)
Small-small attraction U_{att}	↑	↑
L-L and S-L interactions	No significant effect	

shear-driven phase separation described in this thesis can be observed over a wide range of both large and small particle sizes, and even when the large particle interactions switch from repulsive to attractive. This ubiquity suggests that this phenomenon is likely possible in other types of granular-gel composites, including even real industrial materials. We have moreover demonstrated that the phase separation boundaries and 'droplet' size can be tuned by varying the large and small particle properties. Specifically, the small-small attraction U_{att} and large particle size d_L are two key factors. This suggests routes to exploit and manipulate this phenomena in applications. Here we summarise the dependence of shear boundaries on different parameters in Table 7.1. The upwards arrow ↑ indicates a positive correlation, whereas the downwards arrow ↓ means the opposite. The hyphen – refers to little dependence. These results not only enrich the empirical paradigm for structural and rheological control, but also fill important gaps for fundamental understanding on multi-component suspensions.

So far, we have only begun to explore the parameter space of our binary suspension. We do not yet understand the physics controlling the phase separation process, but have empirically identified key factors controlling the state diagram and 'droplet' size in the PS state. Our results here can at least constrain and guide future experimental, computational and theoretical efforts to understand this phenomena. In particular, the key role played by the large particle size in setting the 'droplet' size suggests that local dynamics will be key in any future models. There remains tremendous scope for future work exploring this phase separation phenomena, and binary mixtures in general.

Chapter 8

Conclusions, Applications and Future Work

Suspensions containing large grains dispersed in a viscoelastic gel are widely encountered in industry. However, due to the lack of proper model systems, there are few studies on such class. We mixed two species of particles with disparate sizes and interactions to establish a model system. Its rheology, as well as its structural behaviour under flow, was investigated in this work.

In such binary suspensions, we highlighted a flow-switched state transition. While a vigorous flow results in a yield-stress solid upon flow cessation, a gentle flow can fluidise it into a liquid state which persists when left undisturbed. Rheo-confocal microscopy correlated this solid-liquid transition with a clear change in the microstructure. Based on the structural signature, we identified two states (homogeneous – H; phase-separated – PS) and accordingly mapped out a state diagram. We illustrated the physical meanings of state boundaries, and by extension discussed the macroscopic property of each state. In the end, we further explored the parameter space of our binary system.

8.0.1 Establishing a model system

Our model system is composed of two species of particles: large repulsive grains and small attractive colloids. To achieve disparate interactions in one system, we dispersed two batches of silica particles in the mixture of ethanol, water

and glycerol (1:1:9 by mass). The first batch consists of charge-stabilised silica microspheres with diameter $d_L = 4\,\mu\text{m}$, corresponding to the large repulsive grains. The second batch consists of hydrophobically-functionalised silica colloids ($d_S = 482\,\text{nm}$) which attract each other as a hydrophobic effect. The nearly-matched refractive index as well as the fluorescence labelling (small particles – rhodamine B; solvent – fluorescein sodium salt) enables confocal microscopy.

We individually characterised each species of particles in Chapter 4. Physical properties of particles (e.g. size, density and refractive index) were measured. On their own, small particles attract each other (confirmed by confocal imaging) and form yield-stress gels at low concentrations. By contrast, suspensions of large particles exhibit shear thickening when $\phi \gtrsim 40\,\%$, suggesting interparticle repulsions. The magnitude of interaction was roughly estimated in each species.

We developed a standardised procedure to prepare binary suspension samples, from which the concentration of each species of particles can be derived. Based on confocal images, we classified the small-large interaction as 'non-sticky', while the small-small attraction and large-large repulsion appear to remain unchanged in the mixture. Our model system is well-characterised, tunable and transparent. It sets the stage for further study on suspensions disparate in particle size and interaction.

8.0.2 A flow-switched transition

One of the most important findings of this thesis is the flow-switched transition. For a binary suspension, moderate flow produces a liquid state that, upon brief vigorous flow, switches into a solid state. Through laboratory mixing operations, we demonstrated that this transition is reversible and has memory.

To quantitatively characterise the transition, extensive studies were performed on a binary sample at $\phi_S = 10\,\%$ and $\phi_L = 20\,\%$. Consistent with the lab demonstration, the rheological result identified two shear regimes demarcated by a critical stress. Respectively, high shear leads to solidification after shear cessation while moderate shear leads to fluidisation. Detailed comparison differentiates this novel phenomenology from generic thixotropy.

We examined the *in-situ* microstructure via rheo-confocal microscopy and correlates the rheological transition with a structural change. After cessation

of high preshear, small particles form a gel matrix with large particles embedded inside. Such structure is referred to as the homogeneous (H) state. Upon lower preshear, by contrast, small particles aggregate into large, disjoint 'droplets', termed as the phase-separated (PS) state. To precisely determine the system state, we proposed a quantifying method using Moran's I.

While there exists two states, detailed observation identified three shear regimes. The low, medium and high shear regimes are demarcated by two stress boundaries σ_y and σ_b. The high shear ($\sigma > \sigma_b$) and medium shear regimes ($\sigma_y < \sigma < \sigma_b$), leading to H and PS states respectively, are monostable. In contrast, the low shear regime ($\sigma < \sigma_y$) is too weak to change the state and thereby bistable: two stable states exist and the final state is the same as the initial state. Based on the three-regimes scenario, slices of state diagram were mapped out at four different ϕ_S.

8.0.3 Macroscopic property of each state

Understanding the macroscopic property of each state, which correlates with the state diagram, is important. For example, the H-state yield stress σ_y demarcates the low and medium shear regimes, whereas the breaking stress of 'droplets' σ_b represents the transition boundary between phase separation and homogenisation.

In binary suspensions, an H state consists of a gel matrix with embedded large particles, i.e. a particle-filled gel. The gel network spans and thereby solidifies the entire system. Compared with an unfilled gel with the same ϕ_S, a particles-filled gel exhibits a higher strength. We demonstrate that this strengthening effect cannot be simply interpreted by the reduction in free volume. In particular, the large particle size d_L plays a vital role. Oscillatory rheology implies different yielding behaviours in binary composites and single-component gels.

A PS state resembles a collection of isolated large particles and globular 'droplets' with a characteristic size $\sim 20\,\mu\text{m}$. Confirmed by the absence of coalescence, such 'droplets' are solid-like with the interior kinetically arrested. The SEM image shows an amorphous and homogeneous internal structure of 'droplets'. While the 'droplet' morphology shows little dependence on both the applied stress σ and the large particle concentration ϕ_L, we found that more large particles leads to denser 'droplets'. To a certain extent, this explains the positive correlation between the breaking stress σ_b and ϕ_L in the state diagram.

8.0.4 Exploring parameter space

To better understand the phase separation in binary suspensions, we further explored the parameter space by varying several parameters. Our results show that the small-small attraction U_{att} and the large particle size d_L are two key factors.

The two transition boundaries were both found positively correlated with the attraction strength U_{att}. By making small particles more attractive, one may enable phase separation at $\phi_L = 5\,\%$ or even lower concentrations. The large particle size d_L greatly affects the lower boundary σ_y. Moreover, we revealed a strong dependence between the 'droplet' size d_{drop} and the large particle size d_L. As d_L decreases, the 'droplets' become smaller until completely absent when the two particle sizes are comparable ($d_S \approx d_L$).

These results illuminate tunability in both macroscopic rheology and microscopic structure, which is summarised in the final section of Chapter 7. Our binary suspension has a huge parameter space. So far we have just begun to explore it. Further exploration may fill important gaps for fundamental understanding and is thereby expected.

8.1 Applications

8.1.1 Industrial slurries

Considerable progress has been made in describing single-component suspensions in recent years. However, most realistic suspensions consist of multiple species of particles which differ in size, shape and interaction. A generic class contains large grains suspended in a gel background. Such multi-component slurries occur widely in industry, e.g. lithium-ion batteries (LIB), concretes and toothpastes [16–18].

Here we detail the case in LIB. A typical LIB electrode consists of active material particles (e.g. $LiFePO_4$ and $LiCoO_2$) and conductive additives (e.g. carbon black nanoparticles) [60]. During manufacturing, the components are mixed in a solvent and coated on the metal substrate through slot dies. Understanding the slurry rheology and correlating it to the microstructure are important, since

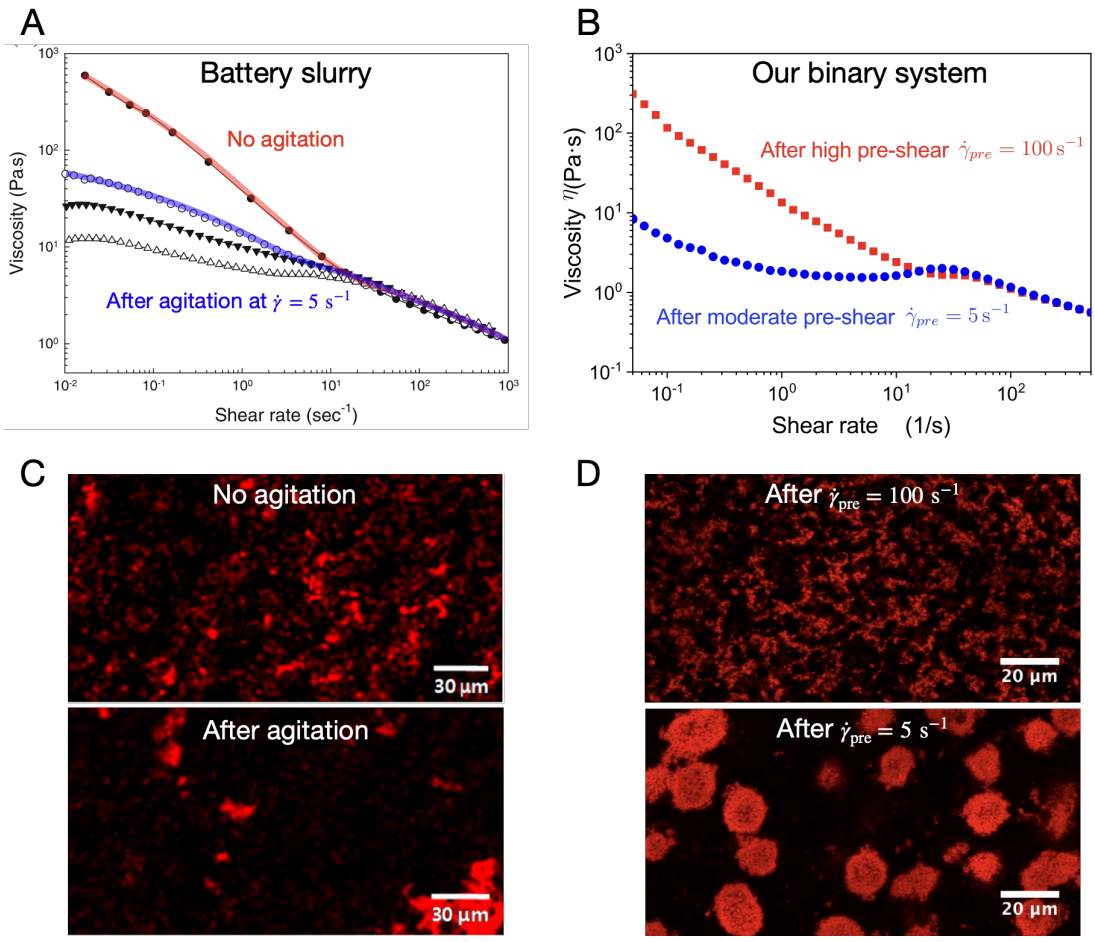

Figure 8.1 Comparison between a real battery slurry (A and C) and our binary system (B and D). The battery slurry contains active material ($LiCoO_2$, $\sim$ 10 µm), conductive additive (carbon black, $\sim$ 30 nm) and polymeric binder (polyvinylidenefluoride) in a N-methylpyrrolidone solvent [16]. The solid weight fraction in battery slurry $\phi_{\text{wt}} = 70\,\%$ [16], whereas our binary system has $\phi_S = 10\,\%$ and $\phi_L = 30\,\%$. A (adapted from [16]) and B are flow curves measured after different agitations (or preshears). C. EDS mapping of carbon before and after agitation at $\dot{\gamma} = 5\,\text{s}^{-1}$. Taken from [16]. D. Confocal images of the small-particle channel after different preshears.

the rheology controls the efficiency of slot-die coating and the microstructure decisively influences the electrical performance of the final product.

The LIB slurry resembles our binary suspension: granular active material ($\sim 10\,\mu m$) dispersed in a conductive nanoparticle network. In Figure 8.1, we compare a specific battery slurry [16] with our binary system. Similarities are found in both rheology and microstructure. The flow curves of the two systems exhibit dependence on the previous treatment. Moderate agitation (preshear) at $\dot{\gamma} = 5\,s^{-1}$ can effectively decrease the low-shear viscosity. As the shear rate $\dot{\gamma}$ increases, the diverged branches of viscosity overlap at $\dot{\gamma} \gtrsim 10\,s^{-1}$ in both cases. In the battery slurry, the EDS mapping of carbon indicates a more heterogeneous microstructure after moderate agitation. This is similar to the phase-separated PS state in our binary suspension.

Understanding the flow in our system offers effective reference for LIB manufacture. Apart from battery slurries, fresh concrete, a dispersion of coarse aggregates in a cementicious background of smaller particulates [160], is another example of binary suspensions. Similar effect of continuous agitation had also been reported in concretes [17]. In addition, silica particles are often added to thicken the background matrix suspending large particulate abrasives in toothpastes [18]. Our model system, as well as the results presented in this thesis, illustrates a strong and extensive implication in industrial formulation and processing.

8.1.2 Mechano-rheological (McR) fluids

Smart fluids are of considerable interest in industry and applied research, because their flow property can be manipulated via external stimuli [214]. Electrorheological (ER) and magnetorheological (MR) fluids are two prototypical examples: switching on the relevant field causes transition into a solid state and removal of the applied field refluidises the solid [215, 216]. Such field responsive rheology has already been used in commercial applications like automotive industry, dampers and shock absorbers [214]. Yet ER and MR fluids are occasionally restricted by the environment, as external magnetic or electric fields are not always applicable in practical processes. Meanwhile, as they do not have 'memory', the applied field has to be kept on to maintain the state, which is costly and unsustainable. Therefore, new strategies to control smart fluids are desired.

Here we conceptually propose a new type of smart fluids named mechanorheological (McR) fluids, whose rheology is tuneable by mechanical stimuli. Technically, most complex fluids are McR fluids in this sense. They may shear thin or shear thicken, i.e. the viscosity varies with the applied shear. Dry granular materials, which can be fluidise when vibrated, can also be seen as a McR material [217]. However, these conventional McR fluids are without memory, so it is interesting to develop memory in such smart fluids.

The solid-liquid transition we have demonstrated suggests that our binary suspension is a memory McR material. It is switchable between solid and liquid states, and 'remembers' the state into which it has been switched. The memory could help maintain the state even after the removal of stimuli. Also, compared with ER and MR fluids, the response to mechanical stimuli makes it more convenient to manipulate the flow property in practice. Besides the shear field from rheometers, other mechanical operations (e.g. shaking, stirring, vibration and sonication) are all supposed to trigger the transition.

Memory McR materials open up the possibility of new applications. Mould casting refers to a manufacturing process. Adaptive casting material is poured into a mould with designed cavity, and then allowed to solidify. For our memory McR suspension, the liquid state can fully adapt to the mould and then quickly solidify by strong mechanical agitation. Such casting does not require extreme temperature (e.g. metals [218]), prolonged ageing (e.g. concretes) and complex procedures (e.g. plastic resins), and it applies to moulds with arbitrary shapes. As a simple, safe and sustainable casting material, our memory McR suspension may be preferably used in extreme situations such as outer space. Applications in free form concrete [219] and 3D printing are also promising.

Soft robotics is another potential field for memory McR materials [220]. Rigid underlying structure of traditional robots limits their interaction with environment. Hence they encounter difficulty when operating in an irregular or highly congested or restricted room. Soft structure, by contrast, provides sufficient degrees of freedom and enables robots to accomplish delicate tasks in complex environment. Using memory McR material, the rigidity can be controlled by simple mechanical stimuli. For instance, by embedding vibrators internally, the robot (or part of it) can be either rigid or soft at will.

8.2 Future work

In this work, we explored the rheology of a binary suspension and highlighted a flow-switched transition. While some of questions raised have been answered, there still remains several unanswered questions which suggest tremendous scope for future study. Based on the presented results, here we detail three possible lines for future work.

8.2.1 Understanding state transitions

The flow-switched transition is the most important phenomenon in this thesis. Fundamentally understanding the state transition is not only of intrinsic interest to statistical physics, but also opens up the possibility of manipulating the transition boundaries. However, the mechanism of either the phase separation under medium shear or the 'droplet' breakage under high shear is still unclear.

In the presence of large particles, small attractive colloids phase separate into condensed 'droplets' under medium shear. As the accumulated strain increases up to $\gamma \sim 10^3$, such phase separation process reaches a steady PS state in which the 'droplets' no longer grow if further sheared (Fig. 6.19). The strain scale $\gamma \sim 10^3$ does not depend on the applied shear and the large particle concentration (Fig. 6.20 and 6.21). The issue of what sets the strain scale and how it can be tuned is an intriguing one. If the strain scale can be shortened by an order of magnitude, we can then quickly fluidise the sample by roller mixing within 2 min rather than 20 min.

Though polydispersed, the 'droplets' in the PS state always have a characteristic size $d_{\text{drop}} \sim 20\,\mu\text{m}$. We have hinted in Chapter 7 that d_{drop} depends, and only depends, on the large particle size d_L. This naturally raises the question that whether d_{drop} will infinitely grow with d_L or it will saturate at a specific size. Together with another interesting fact that the breaking stress σ_b remains constant at different d_L (Fig. 7.9), we therefore propose to investigate the role of large particles in the 'droplet' formation. In analogy with the size correlation between 'droplets' and large particles, one may expect to find interesting results in the shape correlation: will using cubic/ellipsoid large particles result in different 'droplet' morphology?

We have reminded the reader of the importance of small-small attraction in Chapter 7. As the attraction strength U_{att} increases, we induced phase-separated 'droplets' at a pretty low concentration $\phi_L = 5\,\%$ (Fig. 7.5). It is therefore of great interest to see whether infinitely increasing U_{att} will enable phase separation at arbitrary low ϕ_L. Moreover, quantitatively studying the relation between the attraction U_{att} and the phase separation, as well as the two boundaries σ_y and σ_b, can improve fundamental understanding on binary systems.

The PS $\rightarrow$ H transition is essentially the breakage of 'droplets' at high shear $\sigma > \sigma_b$, where the breaking stress σ_b represents the mechanical strength of 'droplets'. In chapter 6, we have shown that adding more large particles leads to denser 'droplets' (Fig. 6.17B) and thereby higher σ_b (Fig. 6.22). It is nevertheless unclear how ϕ_L affects the 'droplet' formation. The data collapse in the σ_b–ϕ_{tot} plot (Fig. 6.25) implies the role of large particle compression, so that the breaking stress σ_b may be quantitatively related to the particle pressure which also scales with ϕ_{tot} [221]. Another intriguing finding is that the breaking stress σ_b is always an order of magnitude lower than the extrapolated yield stress of 'droplets' (Fig. 6.22). This may result from the discrepancy between the imposed bulk shear and the local shear, which is worth further verification.

8.2.2 New model systems

Another point of interest is to study the phase separation in various model systems. If the globular 'droplets' with similar size occur in binary suspensions regardless of the raw materials, we can then confirm the generic physics behind the shear-driven phase separation.

In a more industrially-relevant system which uses Aerosil (primary aggregate size $\sim 220\,\text{nm}$, functionalised by TMS groups) as small particles and polyethylene glycol (PEG, Mw = 200) as solvent, similar flow-switched transition was observed, Figure 8.2. This result has profound implications for practical applications as Aerosil are widely used as a industrial material [222]. However, in this Aerosil system as well as our system, the small-small attractions are realised by hydrophobicity. An alternative way to induce attraction is using microgel colloids, which become attractive with increasing the temperature in water [223]. In addition, dispersing hydrophilic fumed silica and PMMA spheres in organic solvents (such as decalin) also results in disparate interactions in one system.

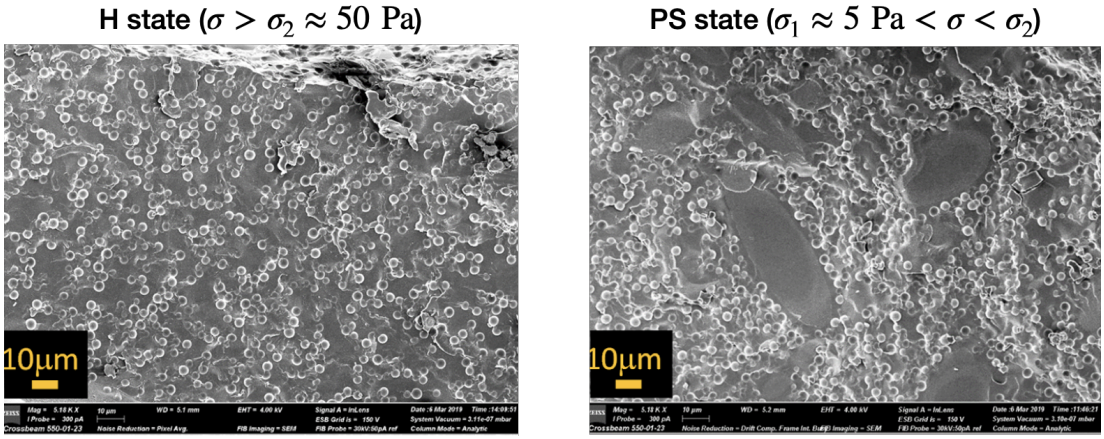

Figure 8.2 Cryo-SEM images of a binary system using functionalised Areosil as small particles ($d_S \sim 220\,\text{nm}$ and PEG (Mw = 200) as solvent. As in this thesis, the large particles are 4-µm silica microspheres. The particle composition is $\phi_S \approx 2\,\%$ and $\phi_L = 30\,\%$. The H (left) and PS (right) states were induced by shear stress $\sigma = 100\,\text{Pa}$ and $\sigma = 10\,\text{Pa}$ respectively. Provided by Soichiro Makino.

Despite of the great tunability, our system has limitations. Even though the small-small attraction is important to the phase separation, it is still challenging to precisely measure it. Besides, our small particles cannot be resolved as single particles in practice, which greatly restricts the structure analysis. By developing new model systems, we expect better characterisations (e.g. the calculable depletion in colloids-polymer mixtures [224]) which can improve the fundamental understanding.

8.2.3 Particles-filled gels

Another research line involves with the particles-filled gel. Following the results in chapter 6, here we propose a whole series of possibilities for additional work.

The first line concerns about *gelation dynamics*. On one hand, adding large particles effectively drives up the concentration of small particles, which, in principle, should shorten the gelation time [225]. On the other hand, the presence of large particles hinders the Brownian diffusion of small colloids and thereby prolongs the gelation. Hence it is interesting to examine the gelation dynamics in the binary mixture.

We also expect that the presence of large particles to have an effect on the *gel structure*. During the gelation in a particle-filled gel, the small-particle network

is constantly perturbed by the existence of large particles. Compared with an unfilled gel, on one hand the addition of large particles leads to a higher effective volume fraction, on the other it introduces defects to the gel matrix [193]. We revealed a size dependence in Chapter 6. Hold the composition fixed at $\phi_S = 10\,\%$ and $\phi_L = 30\,\%$, 4-µm large particles strengthen the gel whereas 1.5-µm large particles weaken the gel (Fig. 6.3). We suspect that such deviation results from the perturbed gel structure.

We regard the *rheology* of particle-filled gels as the third interesting line. In Chapter 6, we have already pointed out the conflict between the increasing yield stress σ_y and the decreasing elastic modulus G' as ϕ_L increases to the dense regime ($\phi_L \gtrsim 30\,\%$). The discrepancy between the yield stresses from oscillatory rheology and steady shear rheology (Fig. 6.8B) also tells important physics in the yielding behaviour. In addition, the second yielding peak in the dynamic strain sweep (Fig. 6.8A) may imply the role of interparticle friction, which can be further verified by experimental techniques like tuneable surface roughness [145]. We also suggest numerical simulation to study the local dynamics at the single particle level.

Appendix A

Estimating attraction strength U_{att}

We use two approaches to individually estimate the attraction strength U_{att} between our hydrophobic silica. They consistently point to a magnitude $U_{\mathrm{att}} \sim 100\ k_B T$.

A.1 The first approach

We consider the finite binding energy as the potential depth U_{att}. As a reference, the work density required to separate two adhered hydrocarbon surfaces in water is $W \approx 100\,\mathrm{mJ\,m^{-2}}$ [74]. For a pair of hydrophobic spheres with diameter d_S in contact, as shown in Figure A.1, the attraction only manifests in the shaded dome with area $S \sim \pi d_S \xi/2$, where the separation is always shorter than the interaction range ξ. Since the gap between spheres varies from 0 to ξ within the shaded region, we use $W/2$ as the average separating work density. The total separation work is then the product of area S and average work density $W/2$:

$$W_{\mathrm{h/w/h}} \sim S \cdot \frac{W}{2} = \pi d_S \xi W/4. \tag{A.1}$$

The surface of our functionalised silica is not as hydrophobic as hydrocarbon surfaces, since only part of silanol groups are coated by TMS groups. The functionalisation recipe we used is comparable to that in [93]. Based on their magic angle spinning nuclear magnetic resonance (MAS NMR) results, the

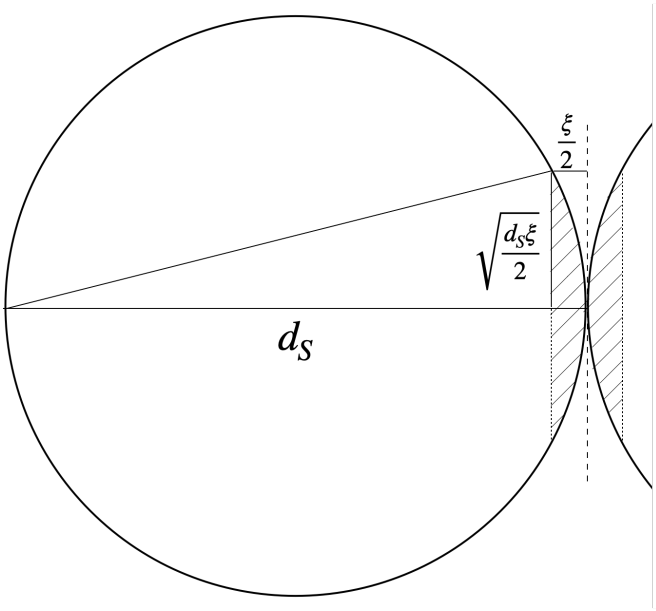

Figure A.1 Two hydrophobic spheres in contact. Short-ranged hydrophobic attraction only manifests within the shaded region.

coverage of TMS group [1] is around 3 %.

This coverage roughly agrees with the decrease in ζ-potential: from $-80\,\mathrm{mV}$ (before functionalisation) to $-72\,\mathrm{mV}$ (after functionalisation). According to the grahame equation [74], the electric potential is proportional to the surface charge density σ_s. The 10 % drop in ζ-potential thus implies that $\sim 10\,\%$ silanol groups, originally disassociated and charged, are replaced by TMS groups after functionalisation. Since silanol groups take up around 20 % of total surface groups [168], the TMS coverage is then approximately 2 %. Here we simply assume that the separating work density between our functionalised silica is $\sim 2\,\%$ of that of hydrocarbon surfaces. Given the attraction range $\xi \sim 1\,\mathrm{nm}$ (see Sec. 4.4 in Chapter 4), we then estimate $U_{\mathrm{att}} \sim 2\,\% W_{\mathrm{h/w/h}} \approx 200\ k_B T$.

A.2 The second approach

The attraction depth can also be estimated from the result of direct force measurement in other literatures. Figure A.2B shows the force (measured by atomic force microscope) between silanated glass sphere and silica plate with different contact angles in water [90]. Based on the general relation $F = -\mathrm{d}U/\mathrm{d}r$, the force $F(r)$ as a function of spearation r can be converted into the potential

[1] The percentage of Si atoms in the colloid that have TMS groups attached.

depth U_{att}.

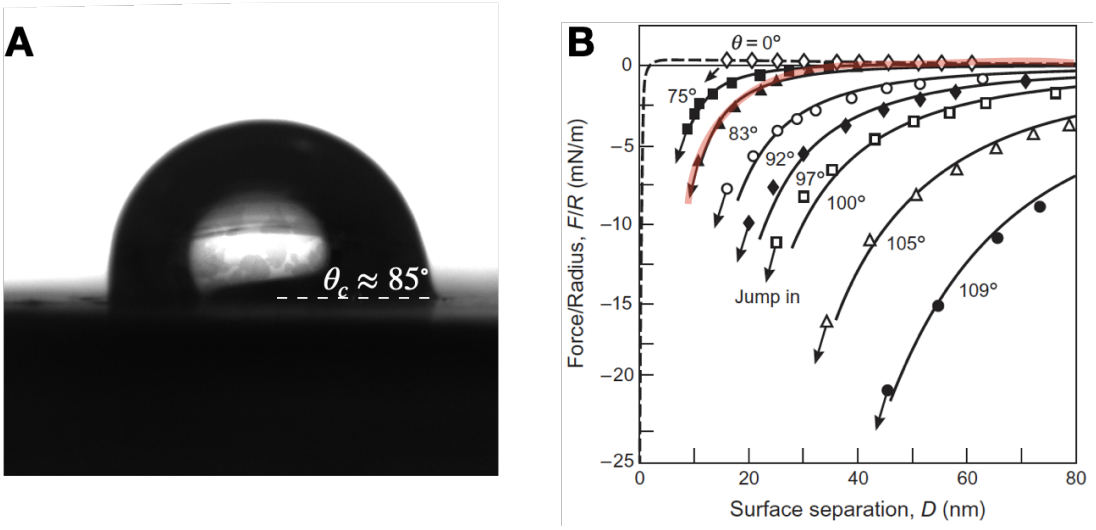

Figure A.2 A. Contact angle measurement of a particle-laiden slide. Reproduced from Figure 4.13A. B. Direct force measurement between surfaces (a sphere and a plate) in water with different hydrophobicity. Taken from [90]. The red line refers to the surfaces with a contact angle similar to our particles.

According to Figure A.2A, our small particles have a contact angle $\theta_c \approx 85°$. Therefore, we assume their attraction to be comparable to the force curve with 83° contact angle in Figure A.2B (red). Based on these information and taking the Derjaguin approximation [226] into consideration, we then give an estimation of $U_{\text{att}} \sim 500 k_B T$ for our hydrophobic silica. Since the roughness of the dried slab of particles makes the measured θ_c higher than the real contact angle, the real attraction should be lower than this estimate: $U_{\text{att}} \lesssim 500 k_B T$.

Note that the two methods here are crude and quantitatively problematic, since they rely on numerous assumptions and approximations. For example, the surface roughness is not considered in both cases, despite that it can reduce the separating work W as well as effectively increase the contact angle θ_c. However, the two methods here, as well as the estimate from yield stress (see Sec. 4.1.3 in Chapter 4), consistently point to a potential depth with similar magnitude $U_{\text{att}} \sim 10^2\ k_B T \gg k_B T$.

Bibliography

[1] Charles Kittel, Paul McEuen, and Paul McEuen. *Introduction to solid state physics*, volume 8. Wiley New York, 1996.

[2] Richard Anthony Lewis Jones, R Jones, Richard AL Jones, et al. *Soft condensed matter*, volume 6. Oxford University Press, 2002.

[3] Taewoo Lee, Bohdan Senyuk, Rahul P Trivedi, and Ivan I Smalyukh. Optical microscopy of soft matter systems. *Fluids, Colloids and Soft Materials: An Introduction to Soft Matter Physics*, pages 165–185, 2016.

[4] Jan Mewis and Norman J Wagner. *Colloidal suspension rheology*. Cambridge University Press, 2012.

[5] Khoa N Pham, Antonio M Puertas, Johan Bergenholtz, Stefan Ulrich Egelhaaf, A Moussaid, Peter N Pusey, Andrew B Schofield, Michael E Cates, Matthias Fuchs, and Wilson CK Poon. Multiple glassy states in a simple model system. *Science*, 296(565):104–106, 2002.

[6] Peter J Lu, Emanuela Zaccarelli, Fabio Ciulla, Andrew B Schofield, Francesco Sciortino, and David A Weitz. Gelation of particles with short-range attraction. *Nature*, 453(7194):499–503, 2008.

[7] N Koumakis and G Petekidis. Two step yielding in attractive colloids: transition from gels to attractive glasses. *Soft Matter*, 7(6):2456–2470, 2011.

[8] Joseph M Brader, Thomas Voigtmann, Matthias Fuchs, Ronald G Larson, and Michael E Cates. Glass rheology: From mode-coupling theory to a dynamical yield criterion. *Proceedings of the National Academy of Sciences*, 106(36):15186–15191, 2009.

[9] Matthieu Wyart and ME Cates. Discontinuous shear thickening without inertia in dense non-brownian suspensions. *Physical review letters*, 112(9):098302, 2014.

[10] John R Royer, Daniel L Blair, and Steven D Hudson. Rheological signature of frictional interactions in shear thickening suspensions. *Physical review letters*, 116(18):188301, 2016.

[11] BM Guy, JA Richards, DJM Hodgson, E Blanco, and WCK Poon. Constraint-based approach to granular dispersion rheology. *Physical review letters*, 121(12):128001, 2018.

[12] James A Richards, Ben M Guy, Elena Blanco, Michiel Hermes, Guilhem Poy, and Wilson CK Poon. The role of friction in the yielding of adhesive non-brownian suspensions. *Journal of Rheology*, 64(2):405–412, 2020.

[13] PN Pusey. The effect of polydispersity on the crystallization of hard spherical colloids. 1987.

[14] David John Fairhurst. Polydispersity in colloidal phase transitions, 1999.

[15] Ben M Guy, Christopher Ness, Michiel Hermes, Laura J Sawiak, Jin Sun, and Wilson CK Poon. Testing the wyart–cates model for non-brownian shear thickening using bidisperse suspensions. *Soft matter*, 16(1):229–237, 2020.

[16] Young Il Kwon, Jong Dae Kim, and Young Seok Song. Agitation effect on the rheological behavior of lithium-ion battery slurries. *Journal of Electronic Materials*, 44(1):475–481, 2015.

[17] Leslie J Struble and Chun-Tao Chen. Effect of continuous agitation on concrete rheology. *Journal of ASTM International*, 2(9):1–19, 2005.

[18] Frank Lippert. An introduction to toothpaste-its purpose, history and ingredients. In *Toothpastes*, volume 23, pages 1–14. Karger Publishers, 2013.

[19] Xiang Cheng, Jonathan H McCoy, Jacob N Israelachvili, and Itai Cohen. Imaging the microscopic structure of shear thinning and thickening colloidal suspensions. *Science*, 333(6047):1276–1279, 2011.

[20] Yu Ling Wu, Didi Derks, Alfons van Blaaderen, and Arnout Imhof. Melting and crystallization of colloidal hard-sphere suspensions under shear. *Proceedings of the National Academy of Sciences*, 106(26):10564–10569, 2009.

[21] Nick Koumakis, Esmaeel Moghimi, Rut Besseling, Wilson CK Poon, John F Brady, and George Petekidis. Tuning colloidal gels by shear. *Soft Matter*, 11(23):4640–4648, 2015.

[22] Christopher W Macosko and Ronald G Larson. Rheology: principles, measurements, and applications. 1994.

[23] Daniel TN Chen, Qi Wen, Paul A Janmey, John C Crocker, and Arjun G Yodh. Rheology of soft materials. *Annu. Rev. Condens. Matter Phys.*, 1(1):301–322, 2010.

[24] Paul A Janmey, Penelope C Georges, and Søren Hvidt. Basic rheology for biologists. *Methods in cell biology*, 83:1–27, 2007.

[25] MJ Unsworth, Alan G Jones, Wenbo Wei, G Marquis, SG Gokarn, and JE Spratt. Crustal rheology of the himalaya and southern tibet inferred from magnetotelluric data. *Nature*, 438(7064):78–81, 2005.

[26] Gary Christensen. Modelling the flow of fresh concrete: The slump test. 1992.

[27] Ben Bloys, Neal Davis, Brad Smolen, Louise Bailey, Otto Houwen, Paul Reid, John Sherwood, Lindsay Fraser, Mike Hodder, and France Montrouge. Designing and managing drilling fluid. *Oilfield Review*, 6(2):33–43, 1994.

[28] Peter Fischer and Erich J Windhab. Rheology of food materials. *Current Opinion in Colloid & Interface Science*, 16(1):36–40, 2011.

[29] John M Dealy and Kurt F Wissbrun. *Melt rheology and its role in plastics processing: theory and applications*. Springer Science & Business Media, 2012.

[30] Morton E Gurtin, Eliot Fried, and Lallit Anand. *The mechanics and thermodynamics of continua*. Cambridge University Press, 2010.

[31] Arash Koocheki, Amir Ghandi, Seyed MA Razavi, Seyed Ali Mortazavi, and Todor Vasiljevic. The rheological properties of ketchup as a function of different hydrocolloids and temperature. *International journal of food science & technology*, 44(3):596–602, 2009.

[32] AJ Reuvers. Control of rheology of water-borne paints using associative thickeners. *Progress in Organic Coatings*, 35(1-4):171–181, 1999.

[33] Shu Chien, SHUNICHI Usami, Harry M Taylor, John L Lundberg, and Magnus I Gregersen. Effects of hematocrit and plasma proteins on human blood rheology at low shear rates. *Journal of Applied Physiology*, 21(1):81–87, 1966.

[34] Norman J Wagner and John F Brady. Shear thickening in colloidal dispersions. *Physics Today*, 62(10):27–32, 2009.

[35] Daniel Bonn and Morton M Denn. Yield stress fluids slowly yield to analysis. *Science*, 324(5933):1401–1402, 2009.

[36] Howard A Barnes. The yield stress—a review or '$\pi\alpha\nu\tau\alpha$ $\rho\varepsilon\iota$'—everything flows? *Journal of Non-Newtonian Fluid Mechanics*, 81(1-2):133–178, 1999.

[37] Marco Caggioni, Veronique Trappe, and Patrick T Spicer. Variations of the herschel–bulkley exponent reflecting contributions of the viscous continuous phase to the shear rate-dependent stress of soft glassy materials. *Journal of Rheology*, 64(2):413–422, 2020.

[38] Roseanna N Zia, Benjamin J Landrum, and William B Russel. A micro-mechanical study of coarsening and rheology of colloidal gels: Cage building, cage hopping, and smoluchowski's ratchet. *Journal of Rheology*, 58(5):1121–1157, 2014.

[39] Christophe Daniel, Christoph Dammer, and Jean-Michel Guenet. On the definition of thermoreversible gels: the case of syndiotactic polystyrene. *Polymer*, 35(19):4243–4246, 1994.

[40] Yongxiang Gao, Juntae Kim, and Matthew E Helgeson. Microdynamics and arrest of coarsening during spinodal decomposition in thermoreversible colloidal gels. *Soft Matter*, 11(32):6360–6370, 2015.

[41] Jan Mewis and Norman J Wagner. Thixotropy. *Advances in Colloid and Interface Science*, 147:214–227, 2009.

[42] Rafael Mendes, Guillaume Vinay, Guillaume Ovarlez, and Philippe Coussot. Reversible and irreversible destructuring flow in waxy oils: An mri study. *Journal of Non-Newtonian Fluid Mechanics*, 220:77–86, 2015.

[43] Daniel Bonn, Sorin Tanase, Bérengère Abou, Hajime Tanaka, and Jacques Meunier. Laponite: Aging and shear rejuvenation of a colloidal glass. *Physical review letters*, 89(1):015701, 2002.

[44] Paulo R de Souza Mendes, Alexandra A Alicke, and Roney L Thompson. Parallel-plate geometry correction for transient rheometric experiments. *Applied Rheology*, 24(5):1–10, 2014.

[45] Chang Dae Han. *Rheology and processing of polymeric materials: Volume 1: Polymer Rheology*, volume 1. Oxford University Press on Demand, 2007.

[46] Esmaeel Moghimi, Alan R Jacob, Nick Koumakis, and George Petekidis. Colloidal gels tuned by oscillatory shear. *Soft Matter*, 13(12):2371–2383, 2017.

[47] P Coussot. Experimental procedures and problems in paste viscometry. *Rheometry of Pastes, Suspensions, and Granular Materials: Applications in Industry and Environment*, pages 81–152, 2005.

[48] Ann S Yoshimura and Robert K Prud'homme. Wall slip effects on dynamic oscillatory measurements. *Journal of Rheology*, 32(6):575–584, 1988.

[49] HJ Walls, S Brett Caines, Angelica M Sanchez, and Saad A Khan. Yield stress and wall slip phenomena in colloidal silica gels. *Journal of Rheology*, 47(4):847–868, 2003.

[50] Pierre Ballesta, Nick Koumakis, Rut Besseling, Wilson CK Poon, and George Petekidis. Slip of gels in colloid–polymer mixtures under shear. *Soft Matter*, 9(12):3237–3245, 2013.

[51] Michiel Hermes, Ben M Guy, Wilson CK Poon, Guilhem Poy, Michael E Cates, and Matthieu Wyart. Unsteady flow and particle migration in dense, non-brownian suspensions. *Journal of Rheology*, 60(5):905–916, 2016.

[52] Peter D Olmsted. Perspectives on shear banding in complex fluids. *Rheologica Acta*, 47(3):283–300, 2008.

[53] Norman J Wagner. Rheo-optics. *Current opinion in colloid & interface science*, 3(4):391–400, 1998.

[54] Nicolas Huang and Daniel Bonn. Viscosity of a dense suspension in couette flow. *Journal of fluid mechanics*, 590:497, 2007.

[55] Rut Besseling, Lucio Isa, Eric R Weeks, and Wilson CK Poon. Quantitative imaging of colloidal flows. *Advances in colloid and interface science*, 146(1-2):1–17, 2009.

[56] EW Errill. Rheology of blood. *Physiological reviews*, 49(4):863–888, 1969.

[57] F Varela López and M Rosen. Rheological effects in roll coating of paints. *Latin American applied research*, 32(3):247–252, 2002.

[58] Mei-Chun Li, Qinglin Wu, Kunlin Song, Yan Qing, and Yiqiang Wu. Cellulose nanoparticles as modifiers for rheology and fluid loss in bentonite water-based fluids. *ACS applied materials & interfaces*, 7(8):5006–5016, 2015.

[59] Elena Blanco, Daniel JM Hodgson, Michiel Hermes, Rut Besseling, Gary L Hunter, Paul M Chaikin, Michael E Cates, Isabella Van Damme, and Wilson CK Poon. Conching chocolate is a prototypical transition from frictionally jammed solid to flowable suspension with maximal solid content. *Proceedings of the National Academy of Sciences*, 116(21):10303–10308, 2019.

[60] Marcel Schmitt, Ralf Diehm, Philip Scharfer, and Wilhelm Schabel. An experimental and analytical study on intermittent slot die coating of viscoelastic battery slurries. *Journal of Coatings Technology and Research*, 12(5):927–938, 2015.

[61] CK Wilson et al. Gelation in colloid–polymer mixtures. *Faraday Discussions*, 101:65–76, 1995.

[62] Peter N Pusey and W Van Megen. Phase behaviour of concentrated suspensions of nearly hard colloidal spheres. *Nature*, 320(6060):340–342, 1986.

[63] Henk NW Lekkerkerker, WC-K Poon, Peter N Pusey, A Stroobants, and PB 0 Warren. Phase behaviour of colloid+ polymer mixtures. *EPL (Europhysics Letters)*, 20(6):559, 1992.

[64] G Bossis and JF Brady. The rheology of brownian suspensions. *The Journal of chemical physics*, 91(3):1866–1874, 1989.

[65] Albert Einstein. Über die von der molekularkinetischen theorie der wärme geforderte bewegung von in ruhenden flüssigkeiten suspendierten teilchen. *Annalen der physik*, 322(8):549–560, 1905.

[66] Dongdong Jia, Jonathan Hamilton, Lenu M Zaman, and Anura Goonewardene. The time, size, viscosity, and temperature dependence of the brownian motion of polystyrene microspheres. *American Journal of Physics*, 75(2):111–115, 2007.

[67] Cx K Batchelor and GK Batchelor. *An introduction to fluid dynamics*. Cambridge university press, 2000.

[68] John F Brady. The long-time self-diffusivity in concentrated colloidal dispersions. *Journal of Fluid Mechanics*, 272:109–134, 1994.

[69] Jan KG Dhont. *An introduction to dynamics of colloids*. Elsevier, 1996.

[70] Romain Mari, Ryohei Seto, Jeffrey F Morris, and Morton M Denn. Discontinuous shear thickening in brownian suspensions by dynamic simulation. *Proceedings of the National Academy of Sciences*, 112(50):15326–15330, 2015.

[71] BM Guy, Michiel Hermes, and Wilson CK Poon. Towards a unified description of the rheology of hard-particle suspensions. *Physical review letters*, 115(8):088304, 2015.

[72] Wilson Poon. Colloids as big atoms. *Science*, 304(5672):830–831, 2004.

[73] Sébastien Wiederseiner, Nicolas Andreini, Gaël Epely-Chauvin, and Christophe Ancey. Refractive-index and density matching in concentrated particle suspensions: a review. *Experiments in fluids*, 50(5):1183–1206, 2011.

[74] Jacob N Israelachvili. *Intermolecular and surface forces*. Academic press, 2015.

[75] Jonas Paul, Stefan Romeis, Jürgen Tomas, and Wolfgang Peukert. A review of models for single particle compression and their application to silica microspheres. *Advanced Powder Technology*, 25(1):136–153, 2014.

[76] Evgenni Mikhailovich Lifshitz, M Hamermesh, et al. The theory of molecular attractive forces between solids. In *Perspectives in Theoretical Physics*, pages 329–349. Elsevier, 1992.

[77] Joseph M Monti, Patricia M McGuiggan, and Mark O Robbins. Effect of roughness and elasticity on interactions between charged colloidal spheres. *Langmuir*, 35(48):15948–15959, 2019.

[78] Ralph K Iler. *The colloid chemistry of silica and silicates*, volume 80. LWW, 1955.

[79] David C Grahame. Diffuse double layer theory for electrolytes of unsymmetrical valence types. *The Journal of Chemical Physics*, 21(6):1054–1060, 1953.

[80] Hajime Tanaka, Jacques Meunier, and Daniel Bonn. Nonergodic states of charged colloidal suspensions: Repulsive and attractive glasses and gels. *Physical Review E*, 69(3):031404, 2004.

[81] Robert J Hunter. *Zeta potential in colloid science: principles and applications*, volume 2. Academic press, 2013.

[82] H Ohshima and T Kondo. Electrophoresis of large colloidal particles with surface charge layers. position of the slipping plane and surface layer thickness. *Colloid and Polymer Science*, 264(12):1080–1084, 1986.

[83] DJA Williams and KP Williams. Electrophoresis and zeta potential of kaolinite. *Journal of Colloid and Interface Science*, 65(1):79–87, 1978.

[84] Barry W Ninham. On progress in forces since the dlvo theory. *Advances in colloid and interface science*, 83(1-3):1–17, 1999.

[85] Henk NW Lekkerkerker and Remco Tuinier. *Colloids and the depletion interaction*, volume 833. Springer, 2011.

[86] PN Pusey, Wilson CK Poon, SM Ilett, and P Bartlett. Phase behaviour and structure of colloidal suspensions. *Journal of Physics: Condensed Matter*, 6(23A):A29, 1994.

[87] Wilson CK Poon. Phase separation, aggregation and gelation in colloid-polymer mixtures and related systems. *Current opinion in colloid & interface science*, 3(6):593–599, 1998.

[88] Henry S Frank and Marjorie W Evans. Free volume and entropy in condensed systems iii. entropy in binary liquid mixtures; partial molal entropy in dilute solutions; structure and thermodynamics in aqueous electrolytes. *The Journal of Chemical Physics*, 13(11):507–532, 1945.

[89] Emily E Meyer, Kenneth J Rosenberg, and Jacob Israelachvili. Recent progress in understanding hydrophobic interactions. *Proceedings of the National Academy of Sciences*, 103(43):15739–15746, 2006.

[90] Roe-Hoan Yoon, Darrin H Flinn, and Yakov I Rabinovich. Hydrophobic interactions between dissimilar surfaces. *Journal of colloid and interface science*, 185(2):363–370, 1997.

[91] RS Hebbar, AM Isloor, and AF Ismail. Contact angle measurements. In *Membrane characterization*, pages 219–255. Elsevier, 2017.

[92] Hugo K Christenson and Per M Claesson. Direct measurements of the force between hydrophobic surfaces in water. *Advances in Colloid and Interface Science*, 91(3):391–436, 2001.

[93] TI Suratwala, ML Hanna, EL Miller, PK Whitman, IM Thomas, PR Ehrmann, RS Maxwell, and AK Burnham. Surface chemistry and trimethylsilyl functionalization of stöber silica sols. *Journal of non-crystalline solids*, 316(2-3):349–363, 2003.

[94] Elisabeth Guazzelli and Jeffrey F Morris. *A physical introduction to suspension dynamics*, volume 45. Cambridge University Press, 2011.

[95] Neil YC Lin, Ben M Guy, Michiel Hermes, Chris Ness, Jin Sun, Wilson CK Poon, and Itai Cohen. Hydrodynamic and contact contributions to continuous shear thickening in colloidal suspensions. *Physical review letters*, 115(22):228304, 2015.

[96] Jacques Duran. *Sands, powders, and grains: an introduction to the physics of granular materials*. Springer Science & Business Media, 2012.

[97] Ryohei Seto, Romain Mari, Jeffrey F Morris, and Morton M Denn. Discontinuous shear thickening of frictional hard-sphere suspensions. *Physical review letters*, 111(21):218301, 2013.

[98] Nikolai V Brilliantov, Frank Spahn, Jan-Martin Hertzsch, and Thorsten Pöschel. Model for collisions in granular gases. *Physical review E*, 53(5):5382, 1996.

[99] Ben Michael Guy. Physics of the flow of concentrated suspensions, 2017.

[100] John P Pantina and Eric M Furst. Elasticity and critical bending moment of model colloidal aggregates. *Physical review letters*, 94(13):138301, 2005.

[101] Peter B Laxton and John C Berg. Investigation of the link between micromechanical interparticle bond rigidity measurements and macroscopic shear moduli of colloidal gels. *Colloids and Surfaces A: Physicochemical and Engineering Aspects*, 301(1-3):137–140, 2007.

[102] D Hankins, JW Moskowitz, and FH Stillinger. Water molecule interactions. *The Journal of Chemical Physics*, 53(12):4544–4554, 1970.

[103] Berni Julian Alder and Thomas Everett Wainwright. Phase transition for a hard sphere system. *The Journal of chemical physics*, 27(5):1208–1209, 1957.

[104] Emanuela Zaccarelli and Wilson CK Poon. Colloidal glasses and gels: The interplay of bonding and caging. *Proceedings of the National Academy of Sciences*, 106(36):15203–15208, 2009.

[105] JD Bernal and J_ Mason. Packing of spheres: co-ordination of randomly packed spheres. *Nature*, 188(4754):910–911, 1960.

[106] Peng Tan, Ning Xu, and Lei Xu. Visualizing kinetic pathways of homogeneous nucleation in colloidal crystallization. *Nature Physics*, 10(1):73–79, 2014.

[107] Ch Beck, W Härtl, and R Hempelmann. The glass transition of charged and hard sphere silica colloids. *The journal of chemical physics*, 111(17):8209–8213, 1999.

[108] Paul M Chaikin, Tom C Lubensky, and Thomas A Witten. *Principles of condensed matter physics*, volume 10. Cambridge university press Cambridge, 1995.

[109] Eric R. Weeks. what is the pair correlation function g(r)?

[110] Hiroshi Yoshida, Kensaku Ito, and Norio Ise. Colloidal crystal growth. *Journal of the Chemical Society, Faraday Transactions*, 87(3):371–378, 1991.

[111] MD Haw, Wilson CK Poon, and PN Pusey. Structure factors from cluster-cluster aggregation simulation at high concentration. *Physica A: Statistical Mechanics and its Applications*, 208(1):8–17, 1994.

[112] Daan Frenkel. Colloidal encounters: a matter of attraction. *Science*, 314(5800):768–769, 2006.

[113] Marjolein Dijkstra. Phase behavior of hard spheres with a short-range yukawa attraction. *Physical Review E*, 66(2):021402, 2002.

[114] Wilson CK Poon. Colloidal suspensions. In *The Oxford Handbook of Soft Condensed Matter*. 2012.

[115] AE Bailey, Wilson Che Kei Poon, Rebecca J Christianson, Andrew B Schofield, Urs Gasser, Vikram Prasad, Suliana Manley, Phil N Segre, Luca Cipelletti, William V Meyer, et al. Spinodal decomposition in a model colloid-polymer mixture in microgravity. *Physical review letters*, 99(20):205701, 2007.

[116] Pierre-Gilles de Gennes. Dynamics of fluctuations and spinodal decomposition in polymer blends. *The Journal of Chemical Physics*, 72(9):4756–4763, 1980.

[117] James S Langer. Theory of spinodal decomposition in alloys. *Annals of Physics*, 65(1):53–86, 1971.

[118] Hiroshi Furukawa. Dynamics-scaling theory for phase-separating unmixing mixtures: Growth rates of droplets and scaling properties of autocorrelation functions. *Physica A: Statistical Mechanics and its Applications*, 123(2-3):497–515, 1984.

[119] PN Pusey. Liquids, freezing and the glass transition, 1991.

[120] Rim Harich, TW Blythe, Michiel Hermes, Emanuela Zaccarelli, AJ Sederman, Lynn F Gladden, and Wilson CK Poon. Gravitational collapse of depletion-induced colloidal gels. *Soft Matter*, 12(19):4300–4308, 2016.

[121] T Van De Laar, R Higler, K Schroën, and J Sprakel. Discontinuous nature of the repulsive-to-attractive colloidal glass transition. *Scientific reports*, 6(1):1–7, 2016.

[122] Lilian C Hsiao, Michael J Solomon, Kathryn A Whitaker, and Eric M Furst. A model colloidal gel for coordinated measurements of force, structure, and rheology. *Journal of Rheology*, 58(5):1485–1504, 2014.

[123] DA Weitz and M Oliveria. Fractal structures formed by kinetic aggregation of aqueous gold colloids. *Physical review letters*, 52(16):1433, 1984.

[124] H Sedgwick, K Kroy, A Salonen, MB Robertson, SU Egelhaaf, and WCK Poon. Non-equilibrium behavior of sticky colloidal particles: beads, clusters and gels. *The European Physical Journal E*, 16(1):77–80, 2005.

[125] Peter J Lu, Jacinta C Conrad, Hans M Wyss, Andrew B Schofield, and David A Weitz. Fluids of clusters in attractive colloids. *Physical Review Letters*, 96(2):028306, 2006.

[126] Wilson CK Poon and MD Haw. Mesoscopic structure formation in colloidal aggregation and gelation. *Advances in Colloid and Interface Science*, 73:71–126, 1997.

[127] M Laurati, SU Egelhaaf, and G Petekidis. Nonlinear rheology of colloidal gels with intermediate volume fraction. *Journal of Rheology*, 55(3):673–706, 2011.

[128] Marina Carpineti and Marzio Giglio. Spinodal-type dynamics in fractal aggregation of colloidal clusters. *Physical review letters*, 68(22):3327, 1992.

[129] Emanuela Zaccarelli. Colloidal gels: equilibrium and non-equilibrium routes. *Journal of Physics: Condensed Matter*, 19(32):323101, 2007.

[130] Ivo R Peters, Sayantan Majumdar, and Heinrich M Jaeger. Direct observation of dynamic shear jamming in dense suspensions. *Nature*, 532(7598):214–217, 2016.

[131] Irvin M Krieger. Rheology of monodisperse latices. *Advances in Colloid and Interface science*, 3(2):111–136, 1972.

[132] John F Brady. The rheological behavior of concentrated colloidal dispersions. *The Journal of Chemical Physics*, 99(1):567–581, 1993.

[133] Andrew P Shapiro and Ronald F Probstein. Random packings of spheres and fluidity limits of monodisperse and bidisperse suspensions. *Physical review letters*, 68(9):1422, 1992.

[134] Hans Martin Laun. Rheological properties of aqueous polymer dispersions. *Die Angewandte Makromolekulare Chemie: Applied Macromolecular Chemistry and Physics*, 123(1):335–359, 1984.

[135] SP Meeker, WCK Poon, and PN Pusey. Concentration dependence of the low-shear viscosity of suspensions of hard-sphere colloids. *Physical Review E*, 55(5):5718, 1997.

[136] Alan A Catherall, John R Melrose, and Robin C Ball. Shear thickening and order–disorder effects in concentrated colloids at high shear rates. *Journal of Rheology*, 44(1):1–25, 2000.

[137] Martin Van Hecke. Running on cornflour. *Nature*, 487(7406):174–175, 2012.

[138] Eric Brown and Heinrich M Jaeger. The role of dilation and confining stresses in shear thickening of dense suspensions. *Journal of Rheology*, 56(4):875–923, 2012.

[139] François Boyer, Élisabeth Guazzelli, and Olivier Pouliquen. Unifying suspension and granular rheology. *Physical Review Letters*, 107(18):188301, 2011.

[140] Nicolas Fernandez, Roman Mani, David Rinaldi, Dirk Kadau, Martin Mosquet, Hélene Lombois-Burger, Juliette Cayer-Barrioz, Hans J Herrmann, Nicholas D Spencer, and Lucio Isa. Microscopic mechanism for shear thickening of non-brownian suspensions. *Physical review letters*, 111(10):108301, 2013.

[141] Romain Mari, Ryohei Seto, Jeffrey F Morris, and Morton M Denn. Shear thickening, frictionless and frictional rheologies in non-brownian suspensions. *Journal of Rheology*, 58(6):1693–1724, 2014.

[142] Leonardo E Silbert. Jamming of frictional spheres and random loose packing. *Soft Matter*, 6(13):2918–2924, 2010.

[143] Chaoming Song, Ping Wang, and Hernán A Makse. A phase diagram for jammed matter. *Nature*, 453(7195):629–632, 2008.

[144] Neil YC Lin, Christopher Ness, Michael E Cates, Jin Sun, and Itai Cohen. Tunable shear thickening in suspensions. *Proceedings of the National Academy of Sciences*, 113(39):10774–10778, 2016.

[145] Chiao-Peng Hsu, Shivaprakash N Ramashna, Michele Zanini, Nicholas D Spencer, and Lucio Isa. Roughness-dependent tribology effects on discontinuous shear thickening. *Proceedings of the National Academy of Sciences*, 115(20):5117–5122, 2018.

[146] John. R. Royer. Private communication. 2018.

[147] David R Foss and John F Brady. Brownian dynamics simulation of hard-sphere colloidal dispersions. *Journal of Rheology*, 44(3):629–651, 2000.

[148] Abdoulaye Fall, Anael Lemaitre, François Bertrand, Daniel Bonn, and Guillaume Ovarlez. Shear thickening and migration in granular suspensions. *Physical review letters*, 105(26):268303, 2010.

[149] William J Frith, P d'Haene, R Buscall, and Joannes Mewis. Shear thickening in model suspensions of sterically stabilized particles. *Journal of rheology*, 40(4):531–548, 1996.

[150] Ronald G Larson. *The structure and rheology of complex fluids*, volume 150. Oxford university press New York, 1999.

[151] Matthew E Helgeson, Yongxiang Gao, Shannon E Moran, Jinkee Lee, Michael Godfrin, Anubhav Tripathi, Arijit Bose, and Patrick S Doyle. Homogeneous percolation versus arrested phase separation in attractively-driven nanoemulsion colloidal gels. *Soft matter*, 10(17):3122–3133, 2014.

[152] Matthias Fuchs and Kenneth S Schweizer. Structure and thermodynamics of colloid-polymer mixtures: A macromolecular approach. *EPL (Europhysics Letters)*, 51(6):621, 2000.

[153] Vladimir Kobelev and Kenneth S Schweizer. Nonlinear elasticity and yielding of depletion gels. *The Journal of chemical physics*, 123(16):164902, 2005.

[154] Kunimasa Miyazaki, Hans M Wyss, David A Weitz, and David R Reichman. Nonlinear viscoelasticity of metastable complex fluids. *EPL (Europhysics Letters)*, 75(6):915, 2006.

[155] Hubert K Chan and Ali Mohraz. Two-step yielding and directional strain-induced strengthening in dilute colloidal gels. *Physical Review E*, 85(4):041403, 2012.

[156] Lilian C Johnson, Benjamin J Landrum, and Roseanna N Zia. Yield of reversible colloidal gels during flow start-up: release from kinetic arrest. *Soft Matter*, 14(24):5048–5068, 2018.

[157] Jader Colombo and Emanuela Del Gado. Stress localization, stiffening, and yielding in a model colloidal gel. *Journal of rheology*, 58(5):1089–1116, 2014.

[158] PA Arp and SG Mason. Orthokinetic collisions of hard spheres in simple shear flow. *Canadian Journal of Chemistry*, 54(23):3769–3774, 1976.

[159] Guillaume Ovarlez, Laurent Tocquer, François Bertrand, and Philippe Coussot. Rheopexy and tunable yield stress of carbon black suspensions. *Soft Matter*, 9(23):5540–5549, 2013.

[160] Nicolas Roussel, Guillaume Ovarlez, Sandrine Garrault, and Coralie Brumaud. The origins of thixotropy of fresh cement pastes. *Cement and Concrete Research*, 42(1):148–157, 2012.

[161] Mohamed Youssry, Lénaïc Madec, Patrick Soudan, Manuella Cerbelaud, Dominique Guyomard, and Bernard Lestriez. Non-aqueous carbon black suspensions for lithium-based redox flow batteries: rheology and simultaneous rheo-electrical behavior. *Physical Chemistry Chemical Physics*, 15(34):14476–14486, 2013.

[162] Cor Van Loveren. *Toothpastes*, volume 23. Karger Medical and Scientific Publishers, 2013.

[163] SM Olhero and JMF Ferreira. Influence of particle size distribution on rheology and particle packing of silica-based suspensions. *Powder Technology*, 139(1):69–75, 2004.

[164] Andrew B Schofield. Private communication. 2019.

[165] Nynke AM Verhaegh and Alfons van Blaaderen. Dispersions of rhodamine-labeled silica spheres: synthesis, characterization, and fluorescence confocal scanning laser microscopy. *Langmuir*, 10(5):1427–1438, 1994.

[166] Werner Stöber, Arthur Fink, and Ernst Bohn. Controlled growth of monodisperse silica spheres in the micron size range. *Journal of colloid and interface science*, 26(1):62–69, 1968.

[167] Wikipedia contributors. Stöber process — Wikipedia, the free encyclopedia, 2020. [Online; accessed 30-May-2020].

[168] Horacio E Bergna. Colloid chemistry of silica: An overview. ACS Publications, 1994.

[169] Ajeet Kumar and Chandra Kumar Dixit. Methods for characterization of nanoparticles. In *Advances in nanomedicine for the delivery of therapeutic nucleic acids*, pages 43–58. Elsevier, 2017.

[170] Katherine A Rumble. Private communication. 2017.

[171] Alfons Van Blaaderen and A Vrij. Synthesis and characterization of colloidal dispersions of fluorescent, monodisperse silica spheres. *Langmuir*, 8(12):2921–2931, 1992.

[172] Kristine M Smith and Lilian C Hsiao. Migration and morphology of colloidal gel clusters in cylindrical channel flow. *Langmuir*, 2021.

[173] Rory E O'Neill, John R Royer, and Wilson CK Poon. Liquid migration in shear thickening suspensions flowing through constrictions. *Physical review letters*, 123(12):128002, 2019.

[174] Leica microsystems. *Microscopy Today*, 22(S1):7–7, 2014.

[175] Motoharu Tanaka, Manami Komagata, Mayumi Tsukada, and Hidehiro Kamiya. Evaluation of the particle–particle interactions in a toner by colloid probe afm. *Powder Technology*, 183(2):273–281, 2008.

[176] Yuncheng Liang, Nidal Hilal, Paul Langston, and Victor Starov. Interaction forces between colloidal particles in liquid: Theory and experiment. *Advances in colloid and interface science*, 134:151–166, 2007.

[177] David G Grier. Optical tweezers in colloid and interface science. *Current opinion in colloid & interface science*, 2(3):264–270, 1997.

[178] Jung Min Kim, Jun Fang, Aaron PR Eberle, Ramón Castañeda-Priego, and Norman J Wagner. Gel transition in adhesive hard-sphere colloidal dispersions: The role of gravitational effects. *Physical review letters*, 110(20):208302, 2013.

[179] KN Pham, G Petekidis, D Vlassopoulos, SU Egelhaaf, WCK Poon, and PN Pusey. Yielding behavior of repulsion-and attraction-dominated colloidal glasses. *Journal of Rheology*, 52(2):649–676, 2008.

[180] Caroline Derec, Guylaine Ducouret, Armand Ajdari, and François Lequeux. Aging and nonlinear rheology in suspensions of polyethylene oxide–protected silica particles. *Physical Review E*, 67(6):061403, 2003.

[181] Saikat Roy and Mahesh S Tirumkudulu. Micro-mechanical theory of shear yield stress for strongly flocculated colloidal gel. *Soft matter*, 16(7):1801–1809, 2020.

[182] Frank Bossler, Johannes Maurath, Katrin Dyhr, Norbert Willenbacher, and Erin Koos. Fractal approaches to characterize the structure of capillary suspensions using rheology and confocal microscopy. *Journal of rheology*, 62(1):183–196, 2018.

[183] WP Cox and EH Merz. Correlation of dynamic and steady flow viscosities. *Journal of Polymer Science*, 28(118):619–622, 1958.

[184] Wei-Heng Shih, Wan Y Shih, Seong-Il Kim, Jun Liu, and Ilhan A Aksay. Scaling behavior of the elastic properties of colloidal gels. *Physical review A*, 42(8):4772, 1990.

[185] CJ Rueb and CF Zukoski. Viscoelastic properties of colloidal gels. *Journal of Rheology*, 41(2):197–218, 1997.

[186] Madhu Priya and Th Voigtmann. Nonlinear rheology of dense colloidal systems with short-ranged attraction: A mode-coupling theory analysis. *Journal of Rheology*, 58(5):1163–1187, 2014.

[187] Richard Buscall, Paul DA Mills, James W Goodwin, and DW Lawson. Scaling behaviour of the rheology of aggregate networks formed from colloidal particles. *Journal of the Chemical Society, Faraday Transactions 1: Physical Chemistry in Condensed Phases*, 84(12):4249–4260, 1988.

[188] Daniel Y Kwok and August W Neumann. Contact angle measurement and contact angle interpretation. *Advances in colloid and interface science*, 81(3):167–249, 1999.

[189] Eric Brown and Heinrich M Jaeger. Shear thickening in concentrated suspensions: phenomenology, mechanisms and relations to jamming. *Reports on Progress in Physics*, 77(4):046602, 2014.

[190] Valeria Tohver, James E Smay, Alan Braem, Paul V Braun, and Jennifer A Lewis. Nanoparticle halos: A new colloid stabilization mechanism. *Proceedings of the National Academy of Sciences*, 98(16):8950–8954, 2001.

[191] Teng-Sing Wei, Frank Y Fan, Ahmed Helal, Kyle C Smith, Gareth H McKinley, Yet-Ming Chiang, and Jennifer A Lewis. Biphasic electrode suspensions for li-ion semi-solid flow cells with high energy density, fast charge transport, and low-dissipation flow. *Advanced Energy Materials*, 5(15):1500535, 2015.

[192] Samantha L Morelly, Maureen H Tang, and Nicolas J Alvarez. The impotence of non-brownian particles on the gel transition of colloidal suspensions. *Polymers*, 9(9):461, 2017.

[193] Di Jia, Javoris V Hollingsworth, Zhi Zhou, He Cheng, and Charles C Han. Coupling of gelation and glass transition in a biphasic colloidal mixture—from gel-to-defective gel-to-glass. *Soft matter*, 11(45):8818–8826, 2015.

[194] Priya Varadan and Michael J Solomon. Shear-induced microstructural evolution of a thermoreversible colloidal gel. *Langmuir*, 17(10):2918–2929, 2001.

[195] Nathan C Keim, Joseph D Paulsen, Zorana Zeravcic, Srikanth Sastry, and Sidney R Nagel. Memory formation in matter. *Reviews of Modern Physics*, 91(3):035002, 2019.

[196] Ronald G Larson and Yufei Wei. A review of thixotropy and its rheological modeling. *Journal of Rheology*, 63(3):477–501, 2019.

[197] G Ovarlez and P Coussot. Physical age of soft-jammed systems. *Physical Review E*, 76(1):011406, 2007.

[198] J Keith Ord and Arthur Getis. Local spatial autocorrelation statistics: distributional issues and an application. *Geographical analysis*, 27(4):286–306, 1995.

[199] Emma S Thompson, Pieter Saveyn, Marc Declercq, Joris Meert, Vincenzo Guida, Charles D Eads, Eric SJ Robles, and Melanie M Britton. Characterisation of heterogeneity and spatial autocorrelation in phase separating mixtures using moran's i. *Journal of colloid and interface science*, 513:180–187, 2018.

[200] Emma S Thompson, Marc Declercq, Pieter Saveyn, Vincenzo Guida, Eric SJ Robles, and Melanie M Britton. Phase separation and collapse in almost density matched depletion induced colloidal gels in presence and absence of air bubbles: An mri imaging study. *Journal of Colloid and Interface Science*, 582:201–211, 2020.

[201] Kathryn A Whitaker, Zsigmond Varga, Lilian C Hsiao, Michael J Solomon, James W Swan, and Eric M Furst. Colloidal gel elasticity arises from the packing of locally glassy clusters. *Nature communications*, 10(1):1–8, 2019.

[202] Ryotaro Shimizu and Hajime Tanaka. A novel coarsening mechanism of droplets in immiscible fluid mixtures. *Nature communications*, 6(1):1–11, 2015.

[203] HNW Lekkerkerker. Osmotic equilibrium treatment of the phase separation in colloidal dispersions containing non-adsorbing polymer molecules. *Colloids and surfaces*, 51:419–426, 1990.

[204] Ben Widom. Some topics in the theory of fluids. *The Journal of Chemical Physics*, 39(11):2808–2812, 1963.

[205] Joel L Lebowitz, Eugene Helfand, and Eigil Praestgaard. Scaled particle theory of fluid mixtures. *The journal of chemical physics*, 43(3):774–779, 1965.

[206] Stany Gallier, Elisabeth Lemaire, Francois Peters, and Laurent Lobry. Percolation in suspensions and de gennes conjectures. *Physical Review E*, 92(2):020301, 2015.

[207] M Kaganyuk and A Mohraz. Shear-induced deformation and interfacial jamming of solid-stabilized droplets. *Soft matter*, 16(18):4431–4443, 2020.

[208] Ahmad K Omar, Yanze Wu, Zhen-Gang Wang, and John F Brady. Swimming to stability: structural and dynamical control via active doping. *ACS nano*, 13(1):560–572, 2018.

[209] Ernest Paul DeGarmo, J Temple Black, Ronald A Kohser, and Barney E Klamecki. *Materials and process in manufacturing*. Prentice Hall Upper Saddle River, 1997.

[210] Eric Brown, Nicole A Forman, Carlos S Orellana, Hanjun Zhang, Benjamin W Maynor, Douglas E Betts, Joseph M DeSimone, and Heinrich M Jaeger. Generality of shear thickening in dense suspensions. *Nature materials*, 9(3):220–224, 2010.

[211] Abhinendra Singh, Sidhant Pednekar, Jaehun Chun, Morton M Denn, and Jeffrey F Morris. From yielding to shear jamming in a cohesive frictional suspension. *Physical review letters*, 122(9):098004, 2019.

[212] Sidhant Pednekar, Jaehun Chun, and Jeffrey F Morris. Bidisperse and polydisperse suspension rheology at large solid fraction. *Journal of Rheology*, 62(2):513–526, 2018.

[213] William Bailey Russel, WB Russel, Dudley A Saville, and William Raymond Schowalter. *Colloidal dispersions*. Cambridge university press, 1991.

[214] R Stanway. Smart fluids: current and future developments. *Materials science and technology*, 20(8):931–939, 2004.

[215] Thomas C Halsey. Electrorheological fluids. *Science*, 258(5083):761–766, 1992.

[216] Juan De Vicente, Daniel J Klingenberg, and Roque Hidalgo-Alvarez. Magnetorheological fluids: a review. *Soft matter*, 7(8):3701–3710, 2011.

[217] Gianfranco D'Anna, P Mayor, A Barrat, V Loreto, and Franco Nori. Observing brownian motion in vibration-fluidized granular matter. *Nature*, 424(6951):909–912, 2003.

[218] John Campbell. *Complete casting handbook: metal casting processes, metallurgy, techniques and design*. Butterworth-Heinemann, 2015.

[219] Will J Hawkins, Michael Herrmann, Tim J Ibell, Benjamin Kromoser, Alexander Michaelski, John J Orr, Remo Pedreschi, Arno Pronk, H Roel Schipper, Paul Shepherd, et al. Flexible formwork technologies–a state of the art review. *Structural Concrete*, 17(6):911–935, 2016.

[220] Deepak Trivedi, Christopher D Rahn, William M Kier, and Ian D Walker. Soft robotics: Biological inspiration, state of the art, and future research. *Applied bionics and biomechanics*, 5(3):99–117, 2008.

[221] Jeffrey F Morris and Fabienne Boulay. Curvilinear flows of noncolloidal suspensions: The role of normal stresses. *Journal of rheology*, 43(5):1213–1237, 1999.

[222] Sheldon K Friedlander and David YH Pui. Emerging issues in nanoparticle aerosol science and technology. *Journal of nanoparticle research*, 6(2):313–320, 2004.

[223] Di Jia, He Cheng, and Charles C Han. Interplay between caging and bonding in binary concentrated colloidal suspensions. *Langmuir*, 34(9):3021–3029, 2018.

[224] Henk NW Lekkerkerker and Remco Tuinier. Depletion interaction. In *Colloids and the depletion interaction*, pages 57–108. Springer, 2011.

[225] Simon B Ross-Murphy. Concentration dependence of gelation time. In *Food polymers, gels and colloids*, pages 357–368. Elsevier, 1991.

[226] Boris Derjaguin. Untersuchungen über die reibung und adhäsion, iv. *Kolloid-Zeitschrift*, 69(2):155–164, 1934.